

Electrochemical Synthesis of Silver Nanoparticles for Applications in Nitrate Detection, Catalysis and Antibacterial Activity



A thesis submitted to the National University of Ireland in fulfilment of the requirements for the degree of

Doctor of Philosophy

By

Catherine M. Fox, B.Sc.

Department of Chemistry,
Maynooth University,
Maynooth, Co. Kildare,
Éire.

2014

Research Supervisor: Prof. Carmel Breslin

Head of Department: Dr. John Stephen

Table of Contents

Declaration.....	v
Acknowledgements.....	vi
Abstract.....	viii
List of Abbreviation.....	x
Chapter 1: Introduction.....	12
1.1 Nanoparticles.....	1
1.1.1 Stability of Colloidal Nanoparticles.....	2
1.1.2 Size Dependence of the Plasmon Absorption of Colloidal Nanoparticles.....	3
1.1.3 Electrochemical Deposition of Nanoparticles.....	5
1.2 Hydrogels.....	10
1.2.1 Polyacrylamide Hydrogels.....	13
1.3 Silver Nanoparticles in Catalysis.....	17
1.3.1 Hydrogel Nanoparticle Composites as Heterogeneous Catalysts.....	18
1.4 Biological Activity of Silver.....	19
1.4.1 Hydrogel Nanoparticle Composites and Antibacterial Activity.....	23
1.5 Nitrate.....	23
1.5.1 Nitrate and Our Environment.....	23
1.5.2 Mechanistic Features of Nitrate Electroreduction.....	26
1.5.3 Current Research in Nitrate Sensors.....	30
1.6 References.....	32
Chapter 2: Experimental.....	41
2.1 Introduction.....	42
2.2 Experimental Set-up.....	42
2.2.1 Electrochemical Apparatus.....	42
2.2.1 The Electrochemical Cell.....	43
2.2.3 Electrode Materials and Preparation.....	44
2.3 Experimental Techniques.....	45
2.3.1 Cyclic Voltammetry.....	45
2.3.2 Potentiostatic Measurements.....	48

2.3.3 Rotating Disc Voltammetry	49
2.3.4 Ultraviolet-Visible Spectroscopy	53
2.3.5 Infrared Spectroscopy	53
2.3.6 Scanning Electron Microscopy and Energy Dispersive X-Ray Analysis	54
2.3.7 Measuring Nanoparticle Size	59
2.3.8 Instrumentation, Software and Ancillary Equipment	60
2.4 Chemicals and Synthesis	61
2.4.1 Chapter 3 – Electrochemical Synthesis of PVP-Protected Silver Nanoparticles and Immobilisation in a Hydrogel Matrix	61
2.4.1.1 Electrochemical Synthesis of PVP-Protected Silver Nanoparticles	61
2.4.1.2 UV-Vis Spectroscopy of PVP-Protected Silver Nanoparticle Solution	62
2.4.1.3 Immobilisation of PVP-Protected Silver Nanoparticles onto a Glassy Carbon Electrode for the Electrochemical Detection of Nitrate	62
2.4.1.4 Polyacrylamide-PVP-Protected Silver Nanoparticle Composite	63
2.4.1.5 Biological Preparation for Anti-Bacterial Testing	64
2.4.2 Chapter 4 – Silver Particles Electrochemically Deposited on a Glassy Carbon Electrode for the Electrochemical Detection of Nitrates	66
2.4.2.1 Electrodeposition of Silver Nanoparticles on a Glassy Carbon Electrode	66
2.4.2.2 Lead Underpotential Deposition at a Bulk Silver and a Silver-Modified Glassy Carbon Electrode	66
2.4.2.3 Nitrate Detection at a Bulk Silver and a Silver-Modified Glassy Carbon Electrode	67
2.5 References	68
Chapter 3: Synthesis and Applications of PVP-Protected Silver Nanoparticles	69
3.1 Introduction	70
3.2 Experimental	71
3.3 Results	71
3.3.1 PVP and Silver	71
3.3.2 Voltammetric Characterisation of Silver-PVP Solution	74
3.3.3 Electrochemical Synthesis of Silver Nanoparticles	77
3.3.3.1 Effect of Applied Potential	77
3.3.3.2 Effect of Silver Concentration	82
3.3.3.3 Effect of PVP Concentration	83
3.3.3.4 Length of Potentiostatic Pulse	84

3.3.3.5 Optimum Condition for Electrochemical Synthesis of PVP-Protected Silver Nanoparticles	87
3.3.3.6 Size of PVP-Protected Silver Nanoparticles	88
3.3.3.7 Stability of PVP-Protected Silver Nanoparticle Solution	89
3.3.3.8 Stability of PVP-Protected Nanoparticles in the Presence of Added Ions	92
3.3.4 Immobilisation of the PVP-Protected Nanoparticles onto a Glassy Carbon Electrode for the Electrochemical Detection of Nitrate	100
3.3.5 Synthesis of a Polyacrylamide-PVP-Protected Silver Nanoparticle Composite	102
3.3.6 Application of Polyacrylamide-PVP-Protected Silver Nanoparticle Composite.....	104
3.3.6.1 Polyacrylamide-PVP-Protected Silver Nanoparticle composite as an Electrode ..	104
3.3.6.2 Polyacrylamide-PVP-Protected Silver Nanoparticle Composite for Use as a Heterogeneous Catalyst in the Reduction of 4-Nitrophenol	107
3.3.6.3 Anti-Bacterial Activity of Polyacrylamide-PVP-Protected Silver Nanoparticle Composite	120
3.3.7 Characterisation of the Polyacrylamide-PVP-Protected Silver Nanoparticle Composite	132
3.3.7.1 Physical Appearance of Polyacrylamide-PVP-Protected Silver Nanoparticle Composite	132
3.3.7.2 SEM and EDX Analysis of the Polyacrylamide-PVP-Protected Silver Nanoparticle Composite	133
3.3.7.3 Leaching of Silver Nanoparticles from the Hydrogel Matrix.....	134
3.4 Summary of Results	135
3.5 References	138
Chapter 4: Silver-Modified Glassy Carbon Electrode for the Electrochemical Detection of Nitrate.....	142
4.1 Introduction	143
4.2 Experimental	144
4.3 Results and Discussion	144
4.3.1 Electrodeposition of Silver on Glassy Carbon	144
4.3.1.1 Double Pulse Method	144
4.3.1.2 Single Pulse Method	159
4.3.2 Modelling of Nanoparticle Growth	168
4.3.3 Size and Surface Area of the Electrodeposited Nanoparticles	174
4.3.3.1 Introduction	174
4.3.3.2 Pb Underpotential Deposition on a Bulk Silver Electrode	178

4.3.3.3 Pb Underpotential Deposition on a Silver-Modified Glassy Carbon Electrode	187
4.3.3.4 Surface Area by Reduction of Surface Oxides using Cyclic Voltammetry	198
4.3.3.5 Size of the Electrodeposited Nanoparticles as Determined by SEM and ImageJ .	202
4.3.4 Nitrate Calibration Curves.....	203
4.3.4.1 Nitrate Detection at a Silver-Modified Glassy Carbon Electrode by Cyclic Voltammetry	204
4.3.4.2 Nitrate Detection at a Bulk Silver Electrode by Cyclic Voltammetry	207
4.3.4.3 Nitrate Detection at a Silver-Modified Glassy Carbon Electrode by Constant Potential Amperometry	210
4.3.5 Influence of pH on Nitrate Reduction Peak	212
4.3.6 Effect of Electrolyte on Nitrate Reduction Peak	214
4.3.7 Kinetics and Reaction Mechanism of Nitrate Reduction	217
4.3.7.1 Influence of Scan Rate on Peak Current	217
4.3.7.2 Evaluation of the Charge Transfer Coefficient.....	219
4.3.7.3 Diffusion Coefficient for Nitrate Reduction	224
4.3.7.4 Number of Electrons in Rate Determining Step of Nitrate Reduction.....	225
4.3.7.5 The Current Function	227
4.3.7.6 Standard Rate Constant for Nitrate Reduction.....	229
4.3.7.7 Reaction Order	230
4.3.7.8 Reaction Hydrodynamics	232
4.3.8 Shape of Nitrate Reduction Peak with Cycling.....	235
4.3.9 Long-term Cycling	246
4.3.10 Interferences.....	248
4.3.10.1 Nitrite Interference	248
4.3.10.2 Chloride Interference	250
4.4 Summary of Results	253
4.5 References	258
Chapter 5: Conclusions.....	264
5.1 Conclusion.....	267

Declaration

I hereby certify that this thesis has not been submitted before, in whole or in part, to this or any university for any degree and is, except where otherwise stated, the original work of the author.

Signed: _____

Date: _____

Maynooth University

Acknowledgements

The completion of this thesis would not have been possible without the help of a number of people that deserve a special mention. First and foremost, my supervisor Prof. Carmel Breslin, one of the most brilliant minds I've ever encountered, with the patience of a saint, thanks for putting up with my incessant questioning. I have learned so much from you and I'm very grateful.

A special thank you to Dr. Denise Rooney and Prof. John Lowry, two people that have helped and supported me throughout my time here in Maynooth. To Dr. Kevin Kavanagh for the use of his biological lab and Dr. Louise Gallagher for showing me the ropes. The biological results obtained during my time in the mycology lab have enriched this body of work. Thanks to the Irish Research Council for financial support.

To the technical staff. Ollie, it took a while but the SEM is eventually up and running. Ria, you've a heart of gold. Noel, you're a genius and always up for a good aul rant. Maryanne, you're an excellent addition to the team. To Barbara, Anne, Orla, Carol and Donna for keeping this place running smoothly. Thank you to all the teaching staff and Department Head, Dr. John Stephens, for giving me the opportunity to learn from you since undergraduate level all the way through to postgraduate.

What makes a place is the people. I've seen a lot of people come and go during my time here and many will remain lifelong friends. I literally couldn't have done this without Roisin O'Flaherty. You never gave up on me, even when I didn't make the ridiculous deadlines you set for me. Thank you so much for all the support and love. Lorna, you are one of the most cheerful people I have ever meet and always there to pick me up. Rob, thanks for the slaggin's, the banter and the straight talking, they've have been good for my soul. Valeria, I hope you continue to allow me to invite myself over. Seems like a lifetime ago now but thanks to Carmel's electrochem girls, Gillian, Claire and Eimear for all the great memories. Every time we meet up it's like no time has passed. To all the "older" postgrads Dec, Denis, Owen, Richard and Sinead. Thanks for all the good times and hopefully all the

curries/Christmas dinners to come. To Jursula, you come as a pair now, but thanks for all the help, especially over the last hurdle. To all the postgrads that I've shared my time in Maynooth with, you have made that time special. Drunken roost nights out and coffee room memories will always be with me.

To my family, who are so important to me. James you light up my life, I couldn't have asked for a better son and I hope I've made you proud. To my parents, sisters and brother, for your patience, support and unconditional love. I'm very lucky to have such a close, loving and supportive family and I know I really couldn't have done this without you.

Abstract

In this thesis results are presented and discussed on the formation and characterisation of silver nanoparticles. The potential applications of the silver nanoparticles are investigated using the reduction of 4-nitrophenol and the detection of nitrates. In addition, data are presented on the antibacterial activity of the silver nanoparticles.

The silver nanoparticles were synthesized as colloidal particles protected with polyvinylpyrrolidone (PVP) with a diameter of 5.73 nm. The colloidal silver nanoparticles were generated in solutions containing $0.05 \text{ mol dm}^{-3} \text{ AgNO}_3$, $0.1 \text{ mol dm}^{-3} \text{ KNO}_3$ and $423.75 \text{ g dm}^{-3} \text{ PVP}$ with an electrochemical pulse of -6.0 V vs Ag^+/Ag . The PVP-protected silver nanoparticles showed excellent stability over a 30 day period and instability was only observed on the addition of AgNO_3 or KNO_3 . The PVP-protected nanoparticles were successfully immobilised in a polyacrylamide hydrogel and employed in the reduction of 4-nitrophenol in the presence of NaBH_4 . The 4-nitrophenol was completely reduced after a 60 min period with a first order rate constant of $7.4 \times 10^{-4} \text{ s}^{-1}$. The activity of the hydrogel composite was maintained on dehydrating and rehydrating and following repeated reactions. The hydrogel composite showed antibacterial activity for *Staphylococcus aureus*, *MRSA*, *Escherichia coli* and *Pseudomonas aeruginosa* and very good antibacterial activity was observed on loading the composite with mobile Ag^+ ions. However, the composite showed poor detection of nitrates, due to diffusion limitations.

The silver nanoparticles were successfully deposited at a glassy carbon electrode using a double pulse or a single pulse technique. For the double pulse technique, a pulse at a potential of E_1 was applied to instantaneously nucleate nanoparticle seeds. Then, a longer pulse at E_2 was applied to grow the seeds into established particles. In the single pulse technique a potential sufficient to nucleate and grow the particles was applied for the entire period, giving a much higher density of silver particles consistent with a progressive nucleation and 3D growth model with a narrow size distribution. The deposited silver nanoparticles were successfully

used in the electrochemical detection of nitrates. The limit of detection was obtained as $2.0 \times 10^{-5} \text{ mol dm}^{-3}$ using cyclic voltammetry and the performance was increased using constant potential amperometry, giving a limit of detection of $9.8 \times 10^{-6} \text{ mol dm}^{-3}$, which falls well below the maximum concentration of $8.0 \times 10^{-4} \text{ mol dm}^{-3}$ as set out by the EPA under the Nitrate Directive (91.676/EEC). However, significant interference was observed on the addition of nitrites and chloride anions. The rate constant for the reduction of nitrate was calculated as $9.79 \times 10^{-3} \text{ s}^{-1}$, while the reaction order was computed as 0.736, consistent with the adsorption of nitrates. Higher peak currents were observed at lower pH values between 2.0 and 4.0, indicating that the adsorption of H^+ ions facilitates the reduction of the nitrate anion.

List of Abbreviation

°C	degree Celsius
2-D	two dimensional
3-D	three dimensional
A	absorbance
AAm	acrylamide
A cm ⁻²	current density-amps per centimetre squared
AP	ammonium persulfate
CPA	constant potential amperometry
CV	cyclic voltammetry
dm ³	cubic decimetre
E _{1/2}	half-wave potential
E _{app}	applied potential
<i>E. coli</i>	<i>Escherichia coli</i>
EDX	energy dispersive X-Ray
GC	glassy carbon electrode
H	Plank's constant
IN2D	instantaneous nucleation and two dimensional growth
IN3D	instantaneous nucleation and three dimensional growth
IR	infrared
λ _{max}	wavelength at maximum absorbance
MBA	N,N'-methylenebisacrylamide
mL	millilitre
mol	mole
MIC	minimal inhibitory concentration
min	minute
MRSA	methicillin resistant <i>Staphylococcus aureus</i>
mV	millivolt
nm	nanometre

OCP	open circuit potential
PAAm-PVP	polyacrylamide-PVP
PAAm-PVP-Ag-np	polyacrylamide-PVP-protected silver nanoparticle
PbCl ₂	lead(II)chloride
pH	logarithmic scale of concentration of hydronium ions
PN2D	progressive nucleation and two dimensional growth
PN3D	progressive nucleation and three dimensional growth
<i>P. aeruginosa</i>	<i>Pseudomonas aeruginosa</i>
PVP	poly(N-vinylpyrrolidone)
RDE	rotating disc electrode
RDV	rotating disc voltammetry
RPM	revolutions per minute
s	seconds
SCE	saturated calomel electrode
SEM	scanning electron microscopy
<i>S. aureus</i>	<i>Staphylococcus aureus</i>
TEMED	tetramethylethylenediamine
UV-Vis	ultraviolet-visible
UPD	underpotential deposition
v	scan rate
V	volt

Chapter 1

Introduction

1.1 Nanoparticles

The field of nanoscience is one of the most rapidly expanding areas of research across all disciplines. This is due largely to a wide range of applications for nanoparticles, such as electronic devices, sensors and biomedical devices. The synthesis of nanoparticles was carried out long before their nature was understood. Back as far as the 17th century, nano gold was used in stained glass windows to produce a ruby red colour while a lemon-yellow colour is typical of silver nanoparticles. The properties of nanoparticles are strongly dependent on their size and shape. The optical properties of nanoparticles is caused by oscillation of the free conduction electrons and this can be described by Mie theory ⁽¹⁾. These resonances are often referred to as surface plasmons. There are many different methods employed to generate nanoparticles but broadly speaking, solution phase chemical reduction using a reducing agent, vapour-phase condensation, laser ablation of a metal target, photoreduction and electrochemical deposition are the most common. The Creighton method to synthesize nanosized silver uses NaBH₄ to reduce AgNO₃ and gives particles of around 10 nm with a narrow size distribution ⁽²⁾. This method has been adapted for the synthesis of other metal nanoparticles such as Pt, Pd, Ru and Cu ⁽³⁾. In high ionic strength solutions a protecting or capping agent is employed to prevent aggregation of the particles in solution. Sodium citrate is one of the most commonly used protecting agents but poly(N-vinylpyrrolidone) (PVP) is also widely used ⁽⁴⁾. The large positive reduction potential of Ag means that nanoparticles are quite thermodynamically stable to oxidation in low-ionic strength aqueous and alcoholic suspensions. For this reason, apart from gold, the synthesis of silver nanoparticles is the most researched of all the nanomaterials. In this study, both colloidal and electrodeposited silver nanoparticles are synthesised. The application of these materials as antibacterial agents, heterogeneous catalysts and as a nitrate sensor is then investigated.

1.1.1 Stability of Colloidal Nanoparticles

While the synthesis of silver nanoparticles is relatively straight forward, the challenge lies in preventing aggregation once formed. The surfaces of nanoparticles are dynamic and are strongly influenced by the local environment. An understanding of the mechanism and conditions that lead to aggregation is a developing field. A protecting agent is usually required for colloidal particles to prevent aggregation, particularly in high ionic strength solutions. The influence of simple mono and di-valent electrolytes on colloidal stability can be explained by the Derjaguin-Landau-Verwey-Overbeek (DLVO) theory where aggregation is induced by screening of the surface charge ⁽⁵⁻⁷⁾. The DLVO theory explains colloidal stability based on the balance between the van der Waals forces and the electrostatic repulsion forces within the diffuse double layer that surrounds colloidal particles in solution. Aggregation is typically averted using two main approaches. Electrostatic repulsion between particles is achieved using anions such as citrate and borohydride that are weakly bound to the nanoparticle core ⁽⁸⁻¹⁰⁾ producing a charged layer that serves as an electrostatic barrier to aggregation. Steric repulsion is achieved using bulky organic polymers such as polyethylene glycol (PEG) and poly(N-vinylpyrrolidone) (PVP), effectively isolating the particles from one another ^(4,11). These protecting groups are more difficult to displace than citrate and borohydride but offer a greater degree of stability ⁽⁴⁾.

The stability of colloidal nanoparticles is often examined with the addition of salts that increase the ionic strength of the solution ⁽¹²⁾. For example, the effect of adding extra salts was studied by Espinoza and co-workers whereby the kinetics of halide-induced decomposition and aggregation of citrate protected silver nanoparticles was measured ⁽¹³⁾. They discussed how the capping agent works by producing a charged layer that surrounds the nanoparticles and serves as an electrostatic barrier to aggregation and proposed that by increasing the ionic strength of the solution this decreases the effective electric field between the charged nanoparticles and consequently lowers this barrier. The double layer contracts and the surface potential decreases with increasing ionic strength. The particles coagulate when the ionic strength exceeds the critical coagulation concentration (c.c.c.) ⁽¹⁴⁾.

Because PVP acts sterically to prevent aggregation, one would expect the particles to be unaffected by changes to the solution ionic strength. However, Zhang showed how both PVP and citrate protected silver nanoparticles suffered from particle aggregation at high ionic strength although citrate particles were more susceptible to aggregation ⁽¹⁵⁾.

1.1.2 Size Dependence of the Plasmon Absorption of Colloidal Nanoparticles

Nanoparticles have fascinated scientists as far back as the 17th century when gold particles were used in the pigment of ruby stained glass. It was Faraday that recognised that the red colour was due to colloidal gold particles ⁽¹⁶⁾ and Mie was the first to understand that the colour was attributed to the collective oscillation of the free conduction electrons induced by an incident electromagnetic field. Also called surface plasmons, Mie described them quantitatively by solving Maxwell's equations with the appropriate boundary conditions for a spherical particle ⁽¹⁾. The theory describes the total extinction cross section composed of absorption and scattering as a summation of all the electric and magnetic multipole oscillations. Therefore, the electronic and optical properties of nanoparticles are intrinsically linked to their size and shape and these theories can be utilised to understand the connection applicable to many different systems ⁽¹⁷⁾. In this study, it allows for the determination of the size of the particles through the UV-Visible absorption band.

When particles are small compared to the wavelength, λ , of the incident light ($\lambda \gg 2R$, e.g., for gold $2R < 25$ nm) only the electric dipole absorption contributes to the extinction cross section of the nanoparticles ⁽¹⁸⁾ and the optical absorption coefficient, α , of a solution of uniform spheres embedded in a medium of refractive index, n_d , can be described by the Mie scattering theory in the electric dipole approximation given by Equation 1.1. Above a certain particle size, the absorption band shifts to longer wavelengths because additional magnetic-dipole terms must be added to Equation 1.1.

$$\alpha = p \frac{18\pi n_d^3 \varepsilon_m''}{\lambda [(\varepsilon_m' + 2n_d^2)^2 + \varepsilon_m'']} \quad 1.1$$

In Equation 1.1, p is the volume fraction of the spheres, ε_m' and ε_m'' , are the real and imaginary parts of the dielectric constant of the metal. The mean free path of the conduction electrons in the particles is limited by the particles boundary or size and is therefore much smaller than the path in the bulk metal. Changes to the size and hence the mean free path of the electrons, modify the surface plasmon resonance frequency through the dielectric constant. When the effect of the particle size on the mean free path of the electrons is taken into account, the complete expression for the dielectric constant as determined by free electrons is substituted into Equation 1.1 to give Equation 1.2 ⁽¹⁹⁾.

$$\alpha = \frac{9\pi p n_d^3 c}{\sigma} \frac{\lambda^2}{(\lambda_m^2 - \lambda^2)^2 + \lambda^2 \lambda_m^4 / \lambda_a^2} \quad 1.2$$

Here, $\lambda_m = \lambda_c(\varepsilon_0 + 2n_d^2)^{1/2}$ is the wavelength at which the maximum absorption takes place, $\lambda = (2\pi c)^2 m / 4\pi N_e \varepsilon_m^2$ and $\lambda_a = 2\lambda_c^2 \sigma / c$. Equation 1.2 gives a band of Lorentzian shape, if the band is narrow, the width, w , at half maximum absorption (FWHM) is λ_m^2 / λ_a and is given by Equations 1.3 and 1.4. The d.c. conductivity, σ , is given by Equation 1.5.

$$w = \lambda_m^2 / \lambda_a \quad 1.3$$

$$w = (\varepsilon_0 + 2n_d^2) c / 2\sigma \quad 1.4$$

$$\sigma = (N_e e^2 R) m u_F \quad 1.5$$

In Equation 1.5, R is the particle radius, $u_F \left[= (2E_F/m)^{1/2} \right]$ is the electron velocity at the Fermi energy $E_F \left[= (3n/8\pi)^{2/3} (h^2/2m) \right]$ and N_e is the number of electrons

per unit volume. The final expression that describes the relationship between bandwidth and particle radius, is shown in Equation 1.6

$$w = \frac{(\epsilon_0 + 2n_d^2)cmu_F}{2N_e e^2 R} \quad 1.6$$

From Equation 1.6 the bandwidth has a $1/R$ dependence. At larger particle sizes, where the wavelength of the incident light becomes comparable to the particle size, greater than roughly 10 nm or 25 nm for gold, there are magnetic-dipole terms which peak at different energies. These terms are not accounted for in the Mie theory electric dipole approximation, Equation 1.1. These extrinsic size effects are size dependent and require the use of the full expression of the Mie theory. Their contribution means that now the extinction coefficient explicitly depends on the particle size. Additionally, the plasmon bandwidth increases with increasing particle size due to inhomogeneous polarization of the nanoparticle often referred to as retardation effects ⁽²⁰⁾.

1.1.3 Electrochemical Deposition of Nanoparticles

Electrochemical deposition is the process whereby a thin layer of metal, a metal alloy and more recently conducting polymers are deposited on a surface. Electrodeposition of a metal via reduction of metal ions from an electrolyte can be accomplished by two different processes, (a) electrons are provided by an external power supply or (b) the process is electroless and deposition is achieved due to the presence of a reducing agent in solution ⁽²¹⁾.

The field of electrochemical deposition has evolved over the decades, finding applications in an ever increasing number of areas in science and engineering. Fine tuning of electrochemical deposition techniques has been driven by the explosion of the electronics industry in recent decades. The desire to create a unique structure that may infer specific properties useful in microelectronics, optics and

sensors has seen this technique move far beyond simple electroplating. With the emerging interest in nanostructured materials, the virtues of electrochemical deposition are particularly evident. The technique provides a route to a variety of new nanomaterials including nanowires, nanotubes and nanoprisms with the inherent advantage of direct electrical contact with a conducting surface.

Much of the attractiveness of the technique stems from the ease with which the direction of the growth of the nanomaterials can be managed by varying parameters such as overpotential, time and solution composition. Despite its versatility, achieving dimensional uniformity remains a challenge. In order to investigate the size-dependent properties of small nanoparticles, distributions with low size dispersions need to be obtained. For example, Zoval and co-workers found the heterogeneity of platinum nanocrystals deposited on basal plane oriented graphite increased with deposition time from a relative standard deviation of 35% to 44% for potentiostatic pulse durations of 10 ms to 100 ms ⁽²²⁾. Additionally, Burton and co-workers in 1951 realised that crystalline surfaces have imperfections and therefore a variety of growth sites ⁽²³⁾. Electrodeposition at defected sites, like scratches or edges, requires a lower overpotential to deposit metals and this can also lead to a large size distribution ^(24,25). The focus of many studies has therefore been to minimise heterogeneity by varying the electrochemical parameters, namely potential pulse energy and duration. Of course an understanding of the nucleation process of metal particles is essential in order to design experiments that would likely achieve particles with as narrow a size distribution as possible. The number density of metal centres follows first-order kinetics and is given by Equation 1.7.

$$N(t) = N_0\{1 - \exp(-At)\} \quad 1.7$$

Here, N_0 is the total number of sites where nucleation is possible, A is the first order nucleation rate constant, which is a function of a number of parameters like potential, concentration and the nature of the substrate, and t is time. There are

two limiting cases which describe the initial stages of nucleation. When A is large and all the sites are available for nucleation, Equation 1.8 is obtained. This describes the situation of instantaneous nucleation. At small A and small t Equation 1.7 is reduced to Equation 1.9. In this case the number of nuclei is a function of time and is described as progressive. Since the rate is determined by experimental parameters the mode of nucleation can be directed by varying the experimental conditions.

$$N(t) \cong N_0 \quad 1.8$$

$$N(t) \cong AN_0t \quad 1.9$$

The growth of the nuclei into stable metal clusters can proceed by two different mechanisms. Two-dimensional (2D) growth proceeds via adatoms attaching to the edge of existing nuclei. If growth is allowed to continue unabated eventually nuclei will coalesce to form a complete layer on the electrode. Nucleation can then occur on this first layer and the process can be repeated indefinitely. Three-dimensional (3D) growth occurs when adatoms attach to nuclei at any point resulting in upward and lateral growth at similar rates. A commonly referred to model for the potentiostatic current-time transients under diffusion controlled 2D and 3D growth is the Scharifker and Hills model ⁽²⁶⁾. In this model the processes of instantaneous and progressive nucleation and 2D and 3D growth are combined to yield the following four equations, Equations 1.10, 1.11, 1.12 and 1.13, which describe the early stages of deposition and growth.

Progressive nucleation and 2D growth (PN2D) is given by Equation 1.10, while instantaneous nucleation and 2D growth (IN2D) is described by Equation 1.11. Equation 1.12 describes progressive nucleation and 3D growth (PN3D) and instantaneous nucleation and 3D growth (IN3D) is given as Equation 1.12.

$$\frac{I}{I_{max}} = \left(\frac{t}{t_{max}}\right)^2 \exp\left\{-\frac{2}{3}\left(\frac{t^3 - t_{max}^3}{t_{max}^3}\right)\right\} \quad 1.10$$

$$\frac{I}{I_{max}} = \left(\frac{t}{t_{max}}\right) \exp\left\{-\frac{1}{2}\left(\frac{t^2 - t_{max}^2}{t_{max}^2}\right)\right\} \quad 1.11$$

$$\left(\frac{I}{I_{max}}\right)^2 = \frac{1.2254}{\left(\frac{t}{t_{max}}\right)} \left\{1 - \exp\left[-2.3367\left(\frac{t}{t_{max}}\right)^2\right]\right\}^2 \quad 1.12$$

$$\left(\frac{I}{I_{max}}\right)^2 = \frac{1.9542}{\left(\frac{t}{t_{max}}\right)} \left\{1 - \exp\left[-1.2564\left(\frac{t}{t_{max}}\right)^2\right]\right\}^2 \quad 1.13$$

In these equations I_{max} represents the maximum current which is recorded at time, t_{max} . These equations can be applied to the potentiostatic current-time transients to identify the nucleation mode for a given set of experimental conditions.

To achieve monodispersed nanoparticles, instantaneous nucleation is essential so that all nuclei appear at the same time. Ngo and Williams found that a very narrow particle size distribution could be achieved by temporally separating the nucleation and growth phase irrespective of the rate law which applies provided every particle on the surface grows in accordance with the same rate law ^(27,28). Narrow distribution during the growth phase was achieved by manipulating the following growth conditions, i) the flux of the monomer to the surface was high, ii) the sample temperature was low and iii) the nucleation density was low. It was hoped that by following these principles that nucleation would end quickly and the nuclei would grow independently from its neighbour in an uncoupled manner. The system studied by Ngo and Williams was particles grown from a gas flux of monomers. Penner and co-workers believed the same principle could be applied

to the electrochemical deposition of nanoparticles. In their work they described how interparticle diffusional coupling leads to a large size distribution of electrochemically deposited nanoparticles ^(29,30). Although a large overpotential favours instantaneous nucleation, it leads to polydispersity when the growth of particles switches from kinetic control to diffusion control. The concentration of metal ions around growing nuclei is depleted as deposition proceeds. The size of the depletion layer, also known as the diffusion zone is a function of overpotential. If the diffusion layers around neighbouring particles overlap or “couple” the growth of these particles is further limited in comparison to particles which grow independently of one another. Penner provided a schematic representation of this process and this is shown in Figure 1.1.

In theory, eliminating diffusional zone coupling should allow particles to grow independently of one another and exhibit a higher degree of monodispersity. This is realised by a two-step approach, which is an extension of the Ngo and Williams’s concept of separating the nucleation and growth. Two separate pulses of different overpotential are employed. An initial pulse of high overpotential is applied for a very short time with a view to instantaneously seed nuclei. A second pulse, applied over a longer timescale and at a much lower overpotential is designed to grow these seed nuclei in an uncoupled fashion. This double pulse technique has been utilised by many other groups since with great effect ⁽³¹⁻³⁶⁾. Although Penner extensively investigated the fundamental principles behind the technique, it was utilized by Sheludko and Bliznakov to electrodeposit Pb and Ag on Pt microelectrodes as early as 1952 ⁽³⁷⁾.

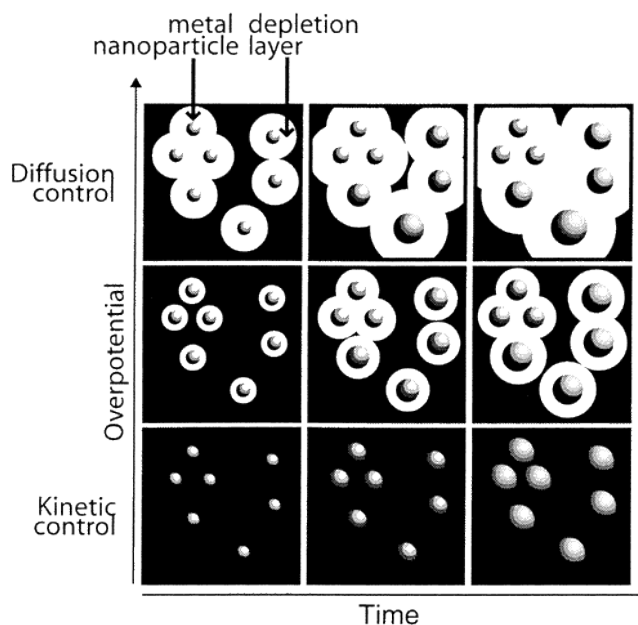


Figure 1.1: Depiction of the effect of interparticle diffusion coupling on the particle size as a function of overpotential and time ⁽³⁰⁾.

1.2 Hydrogels

Hydrogels are a class of polymers that have the ability to gradually swell in aqueous media and retain large amounts of water ⁽³⁸⁾. Examples of some synthetic and natural hydrogels polymers are shown in Figure 1.2. Many derivatives of these polymers and others have been synthesised in order to improve the properties of these gels or to tune them for specific applications. The polymer chains of these gels may or may not be connected via crosslinking molecules and this ultimately dictates whether the gels will maintain the structure of a 'solid-like solution' of polymer and water or eventually dissolve over time.

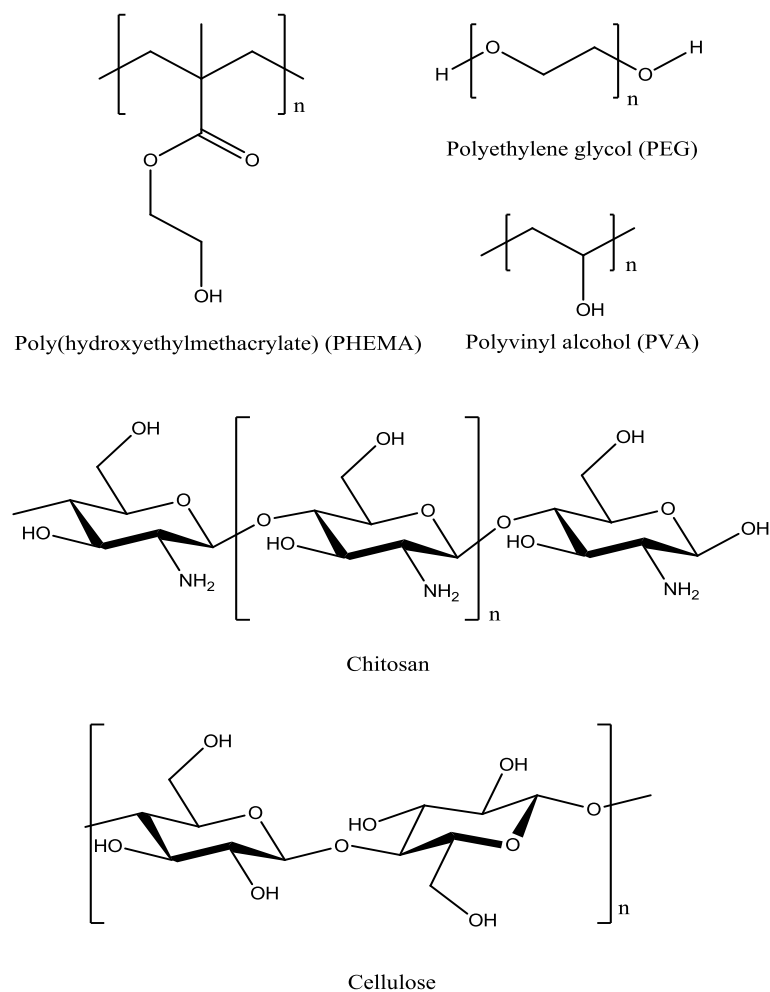


Figure 1.2: Examples of some synthetic hydrogels.

Depending on the desired application, biodegradability may be preferred ⁽³⁹⁾ or, at the other end of the spectrum, long term durability may be required ⁽⁴⁰⁾. The amount of water retained by the hydrogel depends on the structure of the polymer network and on the properties of the swelling media, such as the temperature, pH and ionic strength ⁽⁴¹⁾. Hydrogels are often divided into three classes depending on the nature of their network, namely entangled networks ⁽⁴²⁾, covalently cross-linked networks and networks formed by physical interactions ⁽⁴³⁾.

Since the development of the first hydrogels based on poly(hydroethylmethacrylate) (PHEMA) by Wichterle and Lim ⁽⁴⁴⁾ in the 1950's the types of hydrogels and the range of applications have expanded immensely. Innovative gels based on synthetic, natural or hybrid materials have been

developed to try and optimise the swelling properties, the biocompatibility and physical properties of the hydrogels with a view to increasing the range of applications of these useful materials ⁽⁴⁵⁻⁴⁷⁾. The range of applications is far reaching, for example in personal hygiene products as superabsorbents for disposable nappies and sanitary towels or as stomach bulking agents to help tackle the growing problem of obesity ⁽³⁹⁾. One of the most common applications of hydrogels is in the field of drug delivery ⁽⁴⁸⁾. These materials are ideally suited for drug delivery as they are highly porous materials that have a high affinity for aqueous environments and they can be formulated in a variety of physical forms including slabs, micro and nanoparticles, coatings and films. Nochi and co-workers showed successfully how cationic, self-assembled, cholesteryl group-bearing pullulan nanogels (a polysaccharide polymer) could be used as an antigenic protein-delivery system that could be administered intranasally as an alternative to traditional injections ⁽⁴⁹⁾. They used a non-toxic fragment of *Clostridium botulinum* BoHc/A as a prototype vaccine antigen and found that nasal administrations of BoHc/A entrapped in the pullulan nanogels resulted in prolonged retention of the antigen in the nasal tissue compared to naked administration of the BoHc/A. Also, histochemical studies showed that significantly more mucosal IgA antibodies were produced in mice immunized with the BoHc/A nanogels compared to mice immunized with naked BoHc/A. Many hydrogels are also biocompatible particularly in the case of carbohydrate-based polymers as they resemble the native extracellular matrix. Fricain and co-workers implanted cellulose and phosphorylated cellulose into the femoral bone of rabbits and found no inflammatory response and observed bone cell regeneration along with integration of both types of implants ⁽⁵⁰⁾. The antibacterial properties of hydrogels have also been studied. Primarily, they involve the incorporation of an antibacterial agent ⁽⁵¹⁾ or silver ⁽⁵²⁾ but some hydrogels have antibacterial properties without any antibacterial additives. Saha and co-workers investigated the antibacterial properties of four hydrogels, some of which were synthetic and some were biopolymers. They found that gelatin and sodium alginate hydrogel possessed natural antimicrobial properties ⁽⁵³⁾. Yang and co-workers prepared chitosan and poly(vinyl alcohol) hydrogels for wound dressing that showed good

antibacterial activity against *Escherichia coli* ⁽⁵⁴⁾. Hydrogels have also been utilized as a matrix for heterogeneous catalysis. They provide a stable environment for the catalysis but importantly provide a convenient method to remove the catalyst once the reaction is complete ⁽⁵⁵⁾.

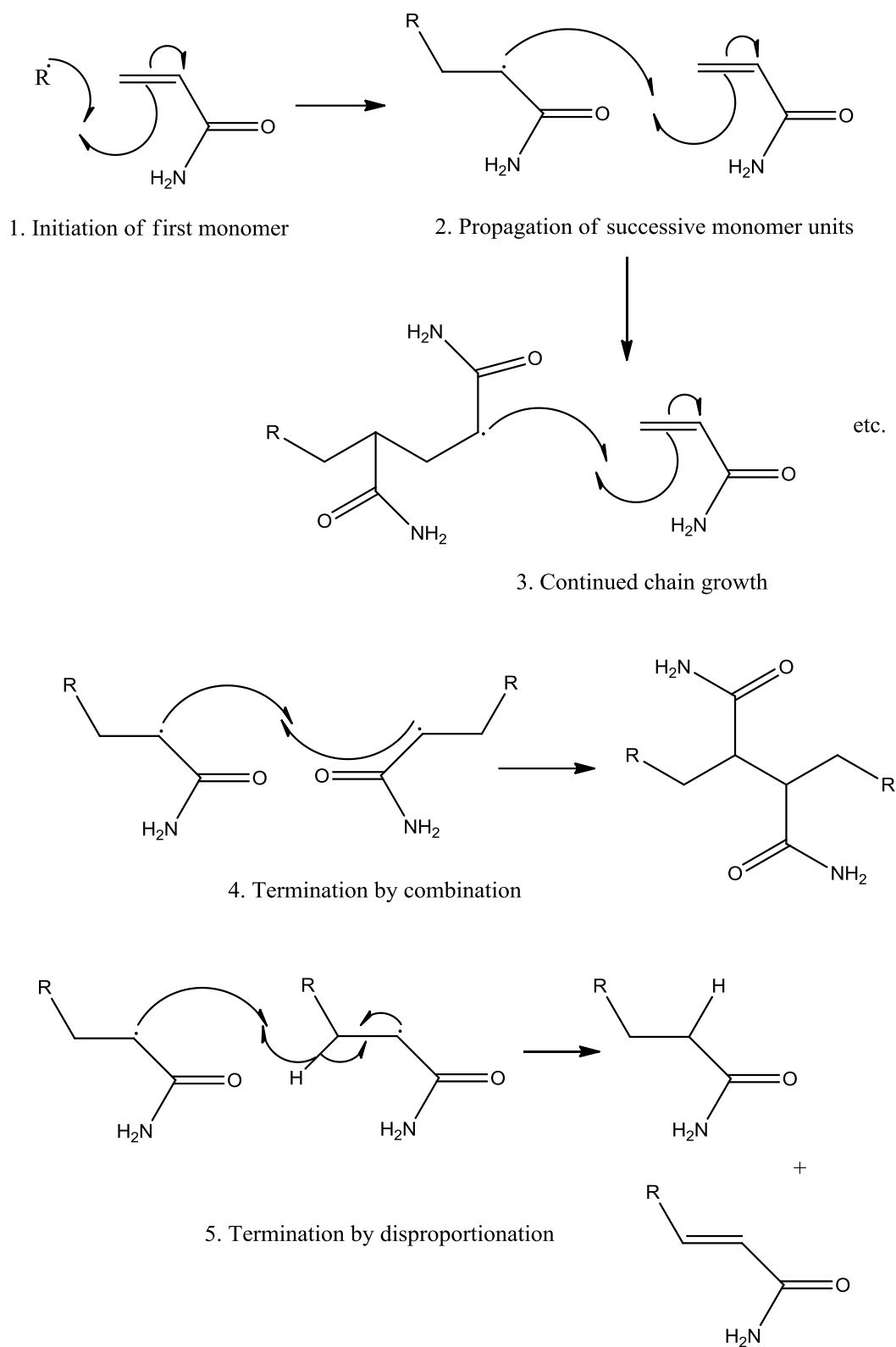
1.2.1 Polyacrylamide Hydrogels

Polyacrylamide is a very widely used and functional polymer. While polyacrylamide is non-toxic the monomer, acrylamide, is a neurotoxin and therefore extensive washing of the polymer is required in order to render it safe for use, in particular for biomedical applications. The range of applications for this material is extensive. It has the ability to form high purity clear gels leading to its earliest use in gel electrophoresis in 1959 ⁽⁵⁶⁾. Because the gels pore size is uniform and can be tuned by controlling the concentrations of acrylamide and bisacrylamide it makes this material ideal for the separation of proteins and DNA fragments. Polyacrylamide has also been used in the agricultural industry as a soil conditioner ⁽⁵⁷⁾. Anionic polyacrylamide is effective at causing clay particles to aggregate through cation bridging therefore leaving the soil less susceptible to erosion. Additionally, soil applied pesticides and fertilizers remain on the soil as opposed to being washed away with the runoff water.

Polyacrylamide can be synthesised in the straight chain form or cross linked usually with *N,N*-methylenebisacrylamide. The reaction mechanism for the polymerisation of acrylamide is a vinyl addition polymerisation initiated by free radicals generated from ammonium persulfate and tetramethylethylenediamine (TEMED) for chemical polymerisation or in photochemical polymerisation riboflavin is also introduced. While the polymerisation reaction is widely used the reaction mechanism for the generation of the initiating free radical has not been studied by many groups. Generally, the reaction is described as being initiated by the persulfate radical while TEMED catalyses the formation of the radicals ⁽⁵⁸⁾. The persulfate radical alone is sufficient to initiate polymerisation but usually heating is required to break the weak O-O bond of persulfate ^(59,60). The most comprehensive study on the reaction mechanism was carried out by Feng and

co-workers⁽⁵⁸⁾. They proposed the initiation mechanism of peroxydisulfate/TEMED by the formation of a contact charge transfer complex (CCT) and a cyclic transition state (CTS) that subsequently produced $(\text{CH}_3)_2\text{NCH}_2\text{CH}_2(\text{CH}_3)\text{NCH}_2\cdot$, $\text{HSO}_4\cdot$ and $\text{HO}\cdot$ free radicals. All these free radicals combined are responsible for the initiation of the vinyl polymerisation.

The suggested reaction scheme for the generation of these radicals is shown in Scheme 1.1. A general mechanism for acrylamide polymerisation is presented in Scheme 1.2 where bisacrylamide is randomly incorporated to crosslink the growing chains. The actual polymerisation reaction is a free radical vinyl polymerisation and is described by three steps, chain initiation, propagation and termination. Chain initiation involves two steps, the generation of the free radicals as described in Scheme 1.1 and the second step involves the addition of this radical to the first monomer unit to produce the chain initiating species, as shown in Scheme 1.3, step 1. Chain propagation then occurs by the successive addition of large numbers of monomer molecules to the chain initiating species. Both of these additions occur when the radical uses one of the electrons from the π system of the vinyl group to form a more stable bond. The remaining electron transfers to the beta carbon turning the molecule into a radical, Scheme 1.3, steps 2 and 3. The process continues as the chain grows until the monomer is used up or termination occurs, step 4 and 5.



Scheme 1.3: Free radical vinyl polymerisation mechanism for acrylamide.

Termination of the growing chains can occur by various methods, including combination and disproportionation. Combination arises where two propagating radicals react with each other by coupling to form a dead polymer and disproportionation occurs when a hydrogen radical that is beta to one radical centre transfers to another radical centre to form two dead polymer chains (one saturated and one unsaturated) ⁽⁶¹⁾, as illustrated in Scheme 1.3.

1.3 Silver Nanoparticles in Catalysis

The use of silver nanoparticles in catalysis first appeared in the 19th century in photography ⁽⁶²⁾. The unique catalytic properties of nanoparticles can be understood by notable changes in reactivity as the size of the clusters decrease. Clearly, the large surface area of nanoparticles increases the activity but additionally the reduction potential becomes progressively more negative as the size of the metal particles approaches the nanodomain ⁽⁶³⁾. The redox potential of the particle for a particular metal depends on the agglomeration number ⁽⁶⁴⁾. The redox potential of these small particles, Equation 1.14



becomes more positive as the particle grows. For $n=1$ (free silver atom) the potential is -1.8 V vs NHE. As the number of atoms within a cluster increases, ($n \rightarrow \infty$), the reduction potential approaches the value of a conventional silver electrode, 0.79 V vs NHE. Henglein described very small particles as “microelectrodes”. Electrons are transferred across the particle-solution interface in much the same way as they are in electrochemistry. When nucleophiles, such as BH_4^- , I^- and PhS^- adsorb on the surface of nanoparticles, the Fermi potential is significantly increased as the nucleophile donates its electron density onto the surface of the particle. In this way the particle mediates the electron transfer for the reduction reaction ^(65,66). Zhang showed how the reaction rate for 4-nitrophenol reduction increased as the size of silver particle on electrospun silica nanotubes decreased ⁽⁶⁷⁾. In another study the activation energy for the

electron transfer reaction between hexacyanoferrate(III) ion and thiosulphate ions was different for different shaped platinum nanoparticle catalysts (tetrahedral, cubic and spherical) ⁽⁶⁸⁾.

The catalytic activity of silver nanoparticles is often accessed by observing the rate of a model reaction. The model reaction should be first order with respect of the reactants, have no side products and should be easy to monitor. A prime example of this is the reduction of 4-nitrophenol to 4-aminophenol by NaBH_4 . The characteristic absorption band at 400 nm for the 4-nitrophenolate anion gradually decreases as reduction occurs while a new absorption band at 300 nm appears ⁽⁶⁹⁾. The reduction of 4-nitrophenol to 4-aminophenol by NaBH_4 does not occur without the presence of a catalyst ⁽⁷⁰⁾. The nanoparticle catalyses the reaction by efficiently mediating the electron transfer from a BH_4^- ion to 4-nitrophenol ⁽⁶⁶⁾.

1.3.1 Hydrogel Nanoparticle Composites as Heterogeneous Catalysts

One of the challenges of using silver nanoparticles for any practical application is the recovery of the material post treatment. Release of silver into water or solution is also a concern. Hydrogels are just one of many types of substrates that have been used to encapsulate or immobilise metal nanoparticles. Patel used electrospun porous silica nanofibers containing silver nanoparticles ⁽⁷¹⁾. Silver-magnetite nanoparticles offer a means of removing particles with a magnet ⁽⁷²⁾. The high surface area afforded by zeolites is a commonly used support for metallic nanoparticles ⁽⁷³⁾. Three important characteristics dictate the catalytic performance of metal nanocomposites. The substrate should have a high surface area, the chemical reagents should have easy access to the nanoparticles inside the substrate and the size and distribution of the nanoparticle within the substrate should be uniform ⁽⁷¹⁾.

There are two main approaches used to successfully generate hydrogel networks containing homogeneous silver nanoparticles. In the first method, often referred to as the breath-in breath-out method, preformed hydrogels are dehydrated then placed in a silver nanoparticle solution where uptake occurs ⁽⁷⁴⁾. In the second approach, reduction of silver salt to metallic nanoparticles occurs within the polymer matrix ⁽⁷⁵⁾. Citrate stabilised silver nanoparticles have been successfully

prepared, in situ, during the photoinduced polymerisation of acrylamide cross-linked with bisacrylamide ⁽⁷⁶⁾. PVP can also form hydrogels if physically cross-linked with ionizing radiation. Obradovic and co-workers electrochemically synthesized alginate protected silver nanoparticles and successfully produced hydrogel microdiscs that could be blended with PVP and PVA ⁽⁷⁷⁾. The composition of the hydrogel matrix can also be used to direct the size and shape of the nanostructures that form within the gel. Mohan found that polyacrylamide/poly(ethylene glycol) gels with increasing crosslinking density resulted in a continuous decrease in silver nanoparticle size ⁽⁷⁸⁾.

1.4 Biological Activity of Silver

Medical research is in a continuous battle with microorganisms such as bacteria, viruses and fungi to prevent infectious diseases in human and animals. The advent of antibiotics over 70 years ago revolutionized the treatment of infectious disease changing the course of medicine. Jubilation was short lived as within a few years the emergences of the first strains resistant to penicillin were identified. Spontaneous and rapid mutations in bacterial DNA confer resistance to antibiotics. Most frighteningly however is the ability of bacteria to transfer DNA coding for this resistance from one species to another through plasmid sharing ⁽⁷⁹⁾. The emergence of methicillin-resistant *Staphylococcus aureus* (MRSA) is probably the most publicised occurrence of bacterial resistance due to its prevalence in hospitals where already immuno compromised patients are at very high risk. The first strain of MRSA was isolated in the UK in 1960, just one year after the use of methicillin as an alternative to penicillin started.

Bacteria confer resistance through mutations of their genome. Methicillin is one of a group of narrow-spectrum β -lactam antibiotics widely used to treat infections. Resistant to methicillin is related to the gene *mecA*, which codes for the low affinity penicillin-binding protein 2A (PBP2A) which can still function as a trans-peptidase in the presence of high concentrations of β -lactam antibiotics. Trans-peptidase is a bacterial enzyme that crosslinks the peptidoglycan chains of the cell wall. In this way MRSA can maintain normal cell function in the presence of methicillin and

other β -lactam antibiotics⁽⁸⁰⁾. Alternatives to β -lactam antibiotics where resistance cannot develop have received tremendous attention as more and more resistant strains are discovered yearly. This has resulted in a resurging interest in silver as an antimicrobial agent^(81,82).

The antimicrobial activity of silver has been known for well over 2000 years. During the middle ages the Greeks and Roman placed silver coins in water containers to prevent microbial spoilage⁽⁸³⁾. Of all the metals ionic silver is known to have the largest antimicrobial activity. Whether bacteria have the potential to develop resistance to silver based drugs, to the same extent as they have to antibiotics like penicillin, is a much debated topic⁽⁸⁴⁾. Certainly, the fact that silver has been used as an antimicrobial agent for thousands of years suggests that resistance is much more difficult to acquire. This is attributed to the silver having several modes of attack, whereas traditional antibiotics bind to specific cell antigens giving bacteria the opportunity to develop gene mutations to counteract these specific binding interactions. An in depth review of the molecular genetics of silver resistance was performed by Silver⁽⁸⁵⁾.

Nevertheless, silver has been incorporated into many medical products such as plasters and wound dressing and is a rapidly growing industry. Suspensions of colloidal silver, which can be sprayed directly onto skin to aid in the healing of a burn, are also commercially available. While silver does not appear to be an accumulative poison and the World Health Organisation does not regulate the amount of silver in drinking water, high levels of silver can lead to conditions such as argyria. Argyria manifests as a bluish/grey discoloration of the skin as silver compounds accumulate in the dermis and other membranes. The condition is not life-treating however the discoloration is normally permanent⁽⁸⁶⁾. Silver does not appear to have a physiological role and is therefore of little clinical or toxicological significance. However, as the use of silver and silver nanoparticles in everyday household items such as clothing, children's toys, water filters and cosmetics becomes more prevalent, more detailed studies on the trophic transfer of silver and its effect on higher organisms is needed. In particular, little is known of the ecological impact that silver nanoparticles may have. Silver nanoparticles were

found in some cases to accumulate in the liver and lungs and penetrate the blood-brain barrier of rodents ⁽⁸⁷⁾.

The number of papers illustrating the beneficial antimicrobial effects of silver is vastly growing. Despite this, few attempts to elucidate the mechanism by which silver imparts its antibacterial activity have been carried out. The mechanism therefore remains not widely understood. However, metallic silver is inert in the presence of human and bacteria cells, it is the silver ion that is biologically active and readily binds to cell surface receptors and metal carrier proteins like albumins ⁽⁸⁴⁾. The most commonly proposed mechanism of silver toxicity is described in the following ways (i) uptake of free silver ions followed by disruption of ATP production and DNA replication (ii) silver nanoparticles and silver ions generate reactive oxygen species and (iii) silver nanoparticles causing direct damage to the cell membranes ⁽⁸¹⁾. A synergistic effect has been observed when some antibiotics have been coupled to silver nanoparticles. Shahverdi and co-workers found that the antibacterial activities of many common antibiotics were enhanced when tested against *S. aureus* and *E. coli* when used in combination with silver nanoparticles ⁽⁸⁸⁾. The production of reactive oxygen species and disruption of disulfide bond formation caused by the presence of silver severely weakens the structural integrity of the cell wall making it more permeable to antibiotics ⁽⁸⁹⁾. TEM images of silver treated *E. coli* showed drastic morphological changes in the cell membrane as a result of protein aggregation. As a result, the potency of β -lactam, aminoglycosides and quinolone antibiotics was increased a 1000 fold in some cases. Morones and co-workers demonstrated that the size of the nanomaterial impacted on the resulting antibacterial activity. Only silver particles smaller than 10 nm were able to directly interact with the bacterial membrane ⁽⁹⁰⁾. Pal and co-workers demonstrated a shape-dependent interaction between *E. coli* and silver nanomaterials. They found that truncated triangular silver nanoplates possessing (111) planes displayed better biocidal activity compared to spherical and rod-shaped nanoparticles as well as silver ions as AgNO_3 ⁽⁹¹⁾. Lack of a standardised method to test the effectiveness of silver compounds and nanoparticles makes literature comparisons difficult. Additionally, Lalueza, Chopra and co-workers highlighted that describing the real bioavailability

of silver has led to disparity in values of MIC (minimal inhibitory concentration) for around a hundred strains of *S. aureus*. Values between 8 to 80 mg/L silver nitrate have been reported ^(82,92).

In this work, plate assays were used to assess the anti-bacterial activity, if any, of polyacrylamide-PVP-protected silver nanoparticle composite on five strains of bacteria. Gram-positive bacteria; *S. aureus* and methicillin-resistant *S. aureus* (MRSA), and gram-negative bacteria; *Pseudomonas aeruginosa* (ATCC 27853), *Pseudomonas aeruginosa* (ATCC 10145) and *Escherichia coli* (*E.coli*) were the five strains studied.

The hydrophilic nature of Ag⁺ means gram-negative bacteria such as *E. coli* are more susceptible to the biocidal properties of silver containing compounds. There are many reports on the efficacy of silver nanoparticles suppression of *E. coli* growth. Rastogi found that total suppression of *E. coli* growth was achieved when the bacteria were incubated for 24 hours with colloidal silver nanoparticles ⁽⁹³⁾.

Silver nanoparticles biosynthesised from the bioreduction of Ag⁺ by *S. aureus* showed promising results when tested for antimicrobial activity by a well-diffusion method against MRSA and methicillin-resistant *Staphylococcus epidermis* (MRSE) ⁽⁹⁴⁾. As the research area expands, materials with silver in various forms with more unusual morphologies are being tested for antibacterial activity. Silver vanadate nanowires decorated with silver nanowires were tested on three strains of *S. aureus* and promising antimicrobial activity was found. The MIC value against MRSA was found to be ten times lower compared to concentrations for the antibiotic, oxacillin ⁽⁹⁵⁾.

The other bacteria species used in this study were two strains of *Pseudomonas aeruginosa* (*P. aeruginosa*). Again there are many studies illustrating the effectiveness of silver to kill and suppress the growth of this bacterium. Kora and co-worker showed a dose dependent relationship between the amount of silver nanoparticles and the measured zones of inhibition for well diffusion assays for *P. aeruginosa* ⁽⁹⁶⁾.

1.4.1 Hydrogel Nanoparticle Composites and Antibacterial Activity

The low solubility of silver salts in biological media, due to the presence of chloride anions, significantly limits the use of silver. Immobilizing silver salts and nanoparticles in a polymer matrix offers a number of advantages. Nanoparticles easily aggregate, which diminishes the chemical and physical properties that make them unique. With the aid of a polymer matrix, precipitation is prevented and silver is stabilised long enough to be delivered to its desired site when the particles are placed in a protective environment. The slow release of silver ions is also achieved by employing a polymer matrix.

Polymeric, biomaterial-based hydrogels offer an immobilising matrix suitable for silver nanoparticles. Examples of antibacterial studies on silver nanoparticle impregnated hydrogels are available in the literature ^(52,74,76,97,98). The experimental approach to anti-bacterial testing is quite varied. Some studies supplement the nutrient agar with a hydrogel silver nanoparticle composite ⁽⁹⁹⁾. A testing method most similar to the one employed in this study was also used by Eid and co-workers ⁽¹⁰⁰⁾. Here, hydrogel discs of poly(acrylamide/itaconic acid) containing silver nanoparticles, from the reduction of silver ions using gamma radiation, were investigated for their anti-bacterial activity. They were most effective against *P. aeruginosa*.

1.5 Nitrate

1.5.1 Nitrate and Our Environment

Nitrate is an essential compound for all plant life to proliferate. It is found in chlorophyll, a crucial component of photosynthesis, the nucleic acids that encode for the proteins and enzymes that allow the plant cell to function and grow. Therefore, much of the plants energy and resources serve to fix nitrogen and incorporate it into the cell where it can be utilised. A plant that grows in a soil rich in nitrogen sources generally has more leaves, stems and gives higher yields. Globally, the use of nitrogen fertilisers is vital to meet the huge demands for agriculture crops by the world's population. However, this inevitably leads to its own problems. Nitrate is very soluble and is easily leached by rain from the soil

into natural water systems which eventually leads its way into drinking water. It also increases the amount of atmospheric nitrous oxide, a potent greenhouse gas, which may be of even greater concern. Additionally, the ammonium ion (NH_4^+), which is positively charged and held in soil through electrostatic attraction to negatively charged clay, is converted to nitrate by microbes using a process called nitrification⁽¹⁰¹⁾. The majority of nitrate enters the soil after harvest when these microbes continue to breakdown any remaining residual organic compounds into nitrate that would normally be taken up by the growing plants. It is generally accepted that plants preferentially absorb inorganic forms of nitrogen such as nitrate and ammonium, however, in the last few decades this view is changing⁽¹⁰²⁾ and recent research suggests that dissolved organic nitrogen, in the form of amino acids, can also be directly taken up by plants⁽¹⁰³⁾. The reality is probably that while nitrate is preferentially absorbed, nutrient availability, plant species type, pH and temperature all dictate which type of nitrogen is absorbed, as suggested by Addiscott⁽¹⁰⁴⁾.

In agriculture, the demand for higher productivity over the past fifty years has forced producers to spread ever increasing amounts of fertilizers on crops⁽¹⁰⁵⁾. Figure 1.3 illustrates how Ireland is one of highest users of chemical and manure sources of nitrate. The Nitrate Directive (91/679/EEC), adopted in 1991, has the objective of reducing water pollution caused or induced by nitrates from agricultural sources⁽¹⁰⁶⁾.

Agriculture is not the only source of nitrogen pollution, road traffic and industry produce nitrates directly or compounds that are readily converted to nitrate. The effect of excess nitrate in the environment has significant health risks. For instance, when nitrate is taken in by eating food and drinking water containing nitrate, nitrate is converted in the gut to nitrite, which can bind with haemoglobin, decreasing its ability to carry oxygen around the body. This generally affects infants more than adults and is commonly known as 'blue-baby syndrome' as it causes the skin to turn blue. Other health problems associated with nitrates include diuresis, increased starchy deposits and haemorrhaging of the spleen.

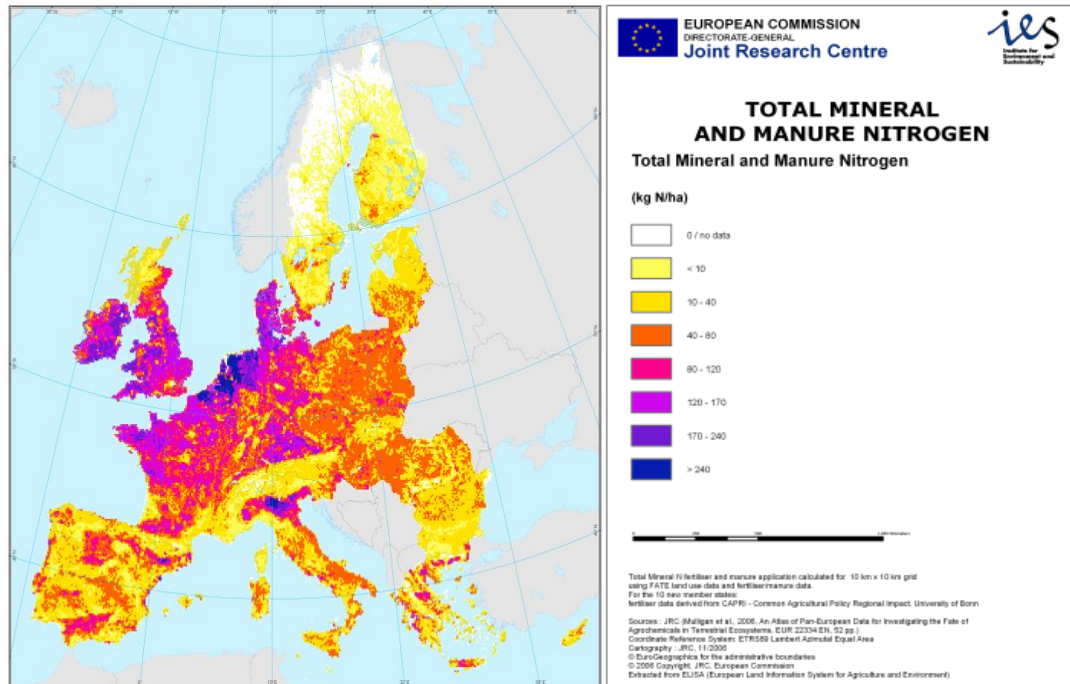


Figure 1.3: Total mineral and manure nitrogen application across the EU (source: JRC, Mulligan and co-worker 2006).

From an environmental point of view excess nitrate can have serious effects on the health of an eco-system. When nitrates are present with phosphates, nitrate leads to eutrophication of water systems causing algae blooms. When these algae blooms biodegrade they drastically deplete the dissolved oxygen content in the water which has detrimental effects on all fish and other animal life that are supported in these ecosystems. For this reason the Environmental Protection Agencies (EPAs) are closely monitoring nitrate levels in water systems and have accordingly set Maximum Contamination Levels (MCLs) for nitrate concentrations. For the EU, the European Communities Drinking Water Regulations 2000 set nitrate levels at 50 ppm ($8.0 \times 10^{-4} \text{ mol dm}^{-3}$) while in the US it is even lower at 10 ppm ($1.6 \times 10^{-4} \text{ mol dm}^{-3}$). Under the EUs Water Framework Directive, all European countries are to have 'good water status' by 2015. Many countries are struggling to meet this target, therefore a means of an effective method to monitor nitrate levels is vitally important.

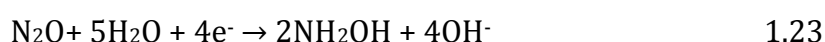
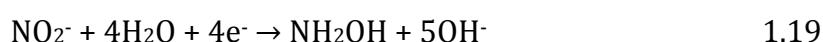
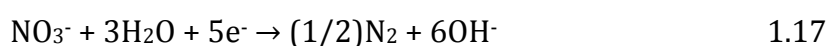
Nitrate is an extremely stable ion and is the most fully oxidised form of nitrogen. In fact, Silvester and co-workers in 2008 believed they were the first to report the oxidation of nitrate to NO_2 electrochemically as a consequence of the wide electrochemical window afforded by using an ionic liquid⁽¹⁰⁷⁾. However, nitrate is a strong oxidizing agent and is therefore readily reduced to nitrite.

1.5.2 Mechanistic Features of Nitrate Electroreduction

The nitrate reduction reaction is a widely studied reaction as more efficient ways of removing this product from waste water are always in demand, particularly as regulations on its discharge into the environment become more stringent. Possible technologies for the treatment of nitrate-containing solutions include biological denitrification⁽¹⁰⁸⁾, ion exchange⁽¹⁰⁹⁾ and heterogeneous catalysis⁽¹¹⁰⁾, but electrochemical reduction is becoming an increasingly attractive alternative since it offers convenience, low cost and does not require additional reagents. Concurrently, research has focussed on how electrochemistry can be used as a nitrate monitoring tool as well as a means of treating nitrate contaminated water. Nitrate reduction has been studied at various metal substrates, including copper⁽¹¹¹⁻¹¹⁴⁾, silver^(115,116), lead⁽¹¹⁷⁾, cadmium⁽¹¹⁸⁾ and boron-doped diamond^(119,120). Alloys and nanomaterials offer a variety of new materials which could be investigated for their ability to reduce and sense nitrate. The catalytic activity of standard macroelectrodes has been shown to increase after modification with a second element^(121,122). For example, the electrocatalytic reduction of nitrate at Rh nanoparticles was improved through modification with Sn⁽¹²³⁾. Understanding the reduction mechanism and how the properties and composition of the electrolyte dictate the products of the reduction reaction is crucial for designing more efficient materials for both the batch electrochemical reduction of nitrate contaminated water and the development of sensors with greater sensitivity. Despite the large number of groups working in this area over many decades, the complex nature of the cathodic reduction of nitrate is still not fully understood. Typically, a mixture of products is produced and it is rarely obvious whether the electron transfer is sequential or whether different reduction reactions are occurring concurrently.

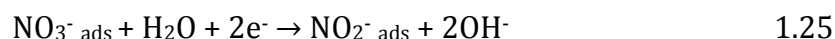
Additionally, there is also evidence that a chemical reaction is coupled to electron transfer as the function $i_p/v^{1/2}$ decreases monotonously with $v^{1/2}$ ⁽¹²⁴⁾.

Equations 1.15 to 1.23 are a list of some of the possible reaction pathways that nitrate and subsequently nitrite undergo as proposed by Plieth ^(125,126). Clearly, the reaction is very complicated but many agree that the rate-determining step is the electron transfer to convert nitrate to nitrite, Equation 1.15. Also, it is clear that the adsorption of nitrate to the surface is essential in order for electron transfer to occur. The importance of adsorption in the reaction mechanism was illustrated by Castella and Gatta when they observed the effects that changing the oxidative potential limit had on the nitrate reduction wave. The current decreased when the oxidative limit, the potential region for nitrate adsorption, was shifted towards more reductive potentials and disappeared completely at values lower than -0.60 V vs SCE ⁽¹²⁷⁾. Adsorption of nitrate can also account for the low values of the charge transfer coefficients quoted in the literature ⁽¹²⁸⁾.

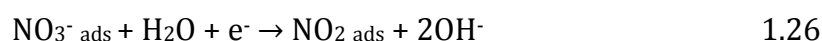


The presence of strongly adsorbing anions, such as sulphate and chloride, indicate the importance of adsorption in the overall rate of nitrate reduction. Molodkina and co-workers found reduction rates were considerably lower in sulphate containing electrolytes compared to perchlorate ⁽¹²⁹⁾.

The rate determining step is often written as Equation 1.25.



Much research has gone into determining the number of electrons in the rate-determining step, producing conflicting results. Reyter and co-workers obtained an α_n' value of 0.98 thus by assuming a charge transfer coefficient of 0.5, most likely two electrons were involved in the rate-determining step ⁽¹¹³⁾. However, another study by De and co-workers ⁽¹²⁸⁾, which compared experimentally obtained Tafel plots and calculated Tafel slopes using Temkin and Frumkin isotherms, found that Equation 1.26 best represented the rate determining step for nitrate reduction in neutral solution.



Dima and co-workers comparison of nitrate reduction at various coinage and transition-metal electrodes in acidic media yielded a similar conclusion. The values of the Tafel slopes suggested that the first electron transfer of the overall reaction of nitrate to nitrite was the rate-determining step ⁽¹³⁰⁾.

The range of products formed is highly dependent on the electrode material as well as the solution composition and pH ^(131,132). For example, Cattarin found that the electrolyses of a nitrate solution a -1.4 V vs SCE at a silver electrode resulted primarily in the production of nitrite, while at a copper electrode ammonia was the end product ⁽¹¹⁵⁾. The current density for nitrate reduction depends strongly on the

nature of the electrode. Dima and co-workers performed an extensive study on the reactivity of nitrate on eight different polycrystalline electrodes (Pt, Pd, Rh, Ru, Ir, Cu, Ag and Au) in acidic media using cyclic voltammetry ⁽¹³⁰⁾. They found that the activity of the metal towards nitrate reduction decreased in the order Rh > Ru > Ir > Pd and Pt for the transition metals and in the order Cu > Ag > Au for the coinage metals. When Molodkina and co-workers investigated the kinetics and mechanism of nitrate and nitrite reduction at a platinum electrode modified by copper adatoms they suggested that the increased activity towards nitrate reduction at copper is largely due to the facilitation of the nitrate adsorption as a result of the partial positive charge of copper adatoms ⁽¹²⁹⁾. More recently, Sn modification of Rh nanoparticles not only increased the nitrate currents but the final products were also dependent on the electrode material ⁽¹²³⁾. Using ion chromatography to determine the products of nitrate reduction, Yang and co-workers found that after Sn modification of a Pt electrode hydroxylamine became the dominant product. Ammonia was the only identifiable product at a Pt electrode ⁽¹³³⁾. The stronger adsorption of nitrate to oxophilic sites on Sn is believed to enhance activity, while differences in the ability to break the N-O bond can give rise to different abilities to form NH_4^+ and NH_3OH^+ ⁽¹²³⁾.

The reduction reaction has been studied in both acidic and basic media and the rate of reduction has been found to be influenced by the pH of the solution. Many research groups choose alkaline media in order to separate the nitrate reduction peaks from the hydrogen evolution reaction since the overpotential for nitrate reduction is high ⁽¹³⁴⁾. Indeed, the reduction rate is favoured at more negative potentials ⁽¹³⁵⁾. Reyter and co-workers studied the electroreduction of copper in alkaline solution and determined that reaction products were dependent on applied potential, with hydroxylamine produced at -1.1 V and ammonia the final product at -1.3 V vs SCE ⁽¹¹³⁾. Groot and Koper determined that the selectivity and the rate of electrocatalytic nitrate reduction at platinum was influenced by nitrate concentration and the pH of the solution ⁽¹³⁶⁾. They described how nitrate undergoes direct reduction at all concentrations but at higher concentrations (> 1.0 mol dm⁻³) and in highly acidic media an indirect, autocatalytic mechanism occurs.

1.5.3 Current Research in Nitrate Sensors

There are several methodologies used to quantify nitrate levels in aqueous solutions. These include UV-Vis spectroscopy, capillary electrophoresis, chromatography and chemiluminescence. HPLC is the most widely used method to quantify nitrate and nitrite in biological samples such as blood, urine and food. Jobgen and co-workers published a comprehensive review comparing HPLC analysis of nitrite and nitrate containing samples using various detectors ⁽¹³⁷⁾. UV-Vis absorbance, electrochemistry and fluorescence are the principle detection techniques used in conjunction with HPLC. Typically, concentrations in the nanomolar range can be detected. For example, Muscara and de Nucci reached a detection limit of 75 nM by performing the Griess reaction post-column on a sample containing nitrate and nitrite ⁽¹³⁸⁾. Interfering compounds such as chloride, proteins and amines are removed on an ion exchange column. Subsequently the nitrate is reduced to nitrite on a second column packed with copper plated cadmium powder. Finally, the diazo-compound from the reaction of nitrite with the Griess reagents, sulphanilamide and N-(1-naphthyl)ethylenediamine, is detected at 540 nm. While the technique offers excellent sensitivity, many of these techniques involve a lot of sample preparation, require expensive materials and skilled operators. Electroanalysis offers several advantages over these techniques, from ease of use and sensitivity to low cost and ease of miniaturisation. The reduction of nitrate is thermodynamically favourable but because the kinetics of the charge transfer is slow, direct detection of nitrate is characterised by poor sensitivity, the need for large overpotentials and electrode fouling ⁽¹³⁹⁾. The electroreduction of nitrate has been extensively studied at traditional electrodes and research is currently focusing on bimetallic alloys, conducting polymers and nanomaterials as potential materials suitable for nitrate sensing. Copper-based materials have received a lot of attention due to its high catalytic ability to reduce nitrate ⁽¹¹¹⁾. Many research groups look to incorporate copper in some form when developing new materials for electrochemical nitrate sensors. A limit of detection of 76 μ M nitrate was obtained at a copper plated, boron-doped, diamond microelectrode ⁽¹⁴⁰⁾. Bimetallic copper-thallium composite films exhibited higher electrocatalytic activity for the reduction of nitrate and nitrite compared to pure

copper and pure thallium electrodeposits ⁽¹²⁷⁾. This bimetallic composite film had detection limits of 190 and 250 μM for nitrate and nitrite, respectively. Nanoparticles offer four main advantages over macroelectrode in electroanalysis: high effective surface area, enhanced mass transport, catalytic activity and control over local microenvironments ⁽¹⁴¹⁾. Simm and co-workers compared the activity of a silver nanoelectrode and a macroelectrode for the electroreduction of halothane and found that although the limits of detection were similar the nanoelectrode displayed greater sensitivity ⁽¹⁴²⁾. Silver nanoparticle deposited on a pure gold electrode allowed detection of nitrate in synthetic seawater at concentrations of 24 and 10 μM in deoxygenated and oxygenated media, respectively ⁽¹⁴³⁾. Besides metals, electrochemically deposited conducting polymers offer an alternative material that has been investigated for the electrochemical detection of nitrate. Doping a conducting polymer, such as polypyrrole, with the analyte to be detected creates chemical recognition sites that are selective for that analyte. Hutchins described how these ionophores are complimentary in size to the target analyte, creating a host cavity for nitrate, thus providing enhanced selectivity in the presence of interfering ions ⁽¹⁴⁴⁾. More recently, nanostructured conducting polymers doped with nitrate further enhance the detection properties of these materials by increasing the surface area. A limit of detection of 4.5 μM was recorded at nitrate doped polypyrrole nanowires within a microfluidic device ⁽¹⁴⁵⁾. Nitrate biosensors have also been developed and have proven to be very sensitive. Nitrate reductase immobilised within a gelatin matrix on a glassy carbon electrode detected nitrate concentrations of 2.2 nM nitrate by monitoring the oxidation current of the redox mediator, methyl violgen ⁽¹⁴⁶⁾. The various techniques have advantages and disadvantages, so choice of technique is very much application driven.

The aim of this thesis was to explore the formation and potential applications of silver nanoparticles in a number of different areas; colloidal silver nanoparticles encapsulated within a hydrogel matrix for use as a heterogeneous catalyst and antibacterial substance and electrodeposited silver particles on a glassy carbon electrode as a sensing material for low levels of nitrate in aqueous solutions.

1.6 References

1. G. Mie, "Beiträge zur Optik trüber Medien, speziell kolloidaler Metallösungen", *Annalen der Physik*, **330**, 377, (1908).
2. J.A. Creighton, C.G. Blatchford, M.G. Albrecht, "Plasma resonance enhancement of Raman scattering by pyridine adsorbed on silver or gold sol particles of size comparable to the excitation wavelength", *Journal of the Chemical Society, Faraday Transactions 2: Molecular and Chemical Physics*, **75**, 790, (1979).
3. D.D. Evanoff, G. Chumanov, "Synthesis and optical properties of silver nanoparticles and arrays", *Chemphyschem*, **6**, 1221, (2005).
4. M. Tejamaya, I. Römer, R.C. Merrifield, J.R. Lead, "Stability of Citrate, PVP, and PEG Coated Silver Nanoparticles in Ecotoxicology Media", *Environmental Science & Technology*, **46**, 7011, (2012).
5. X. Li, J.J. Lenhart, H.W. Walker, "Dissolution-Accompanied Aggregation Kinetics of Silver Nanoparticles", *Langmuir*, **26**, 16690, (2010).
6. E.J.W. Verwey, J.T.G. Overbeek, *Theory of the Stability of Lyophobic Colloids*; Elsevier Amsterdam, 1948.
7. B.V. Derjaguin, L.D. Landau, *Acta Physicochimica U.R.S.S.*, **14**, 633, (1941).
8. T.M. Tolaymat, A.M. El Badawy, A. Genaidy, K.G. Scheckel, T.P. Luxton, M. Suidan, "An evidence-based environmental perspective of manufactured silver nanoparticle in syntheses and applications: A systematic review and critical appraisal of peer-reviewed scientific papers", *Science of The Total Environment*, **408**, 999, (2010).
9. L. Mulfinger, S.D. Solomon, M. Bahadory, A.V. Jeyarajasingam, S.A. Rutkowsky, C. Boritz, "Synthesis and Study of Silver Nanoparticles", *Journal of Chemical Education*, **84**, 322, (2007).
10. T.C. Prathna, N. Chandrasekaran, A. Mukherjee, "Studies on aggregation behaviour of silver nanoparticles in aqueous matrices: Effect of surface functionalization and matrix composition", *Colloids Surf., A*, **390**, 216, (2011).
11. Y.W. Tan, X.H. Dai, Y.F. Li, D.B. Zhu, "Preparation of gold, platinum, palladium and silver nanoparticles by the reduction of their salts with a weak reductant-potassium bitartrate", *Journal of Materials Chemistry*, **13**, 1069, (2003).
12. S.A. Macpherson, G.B. Webber, R. Moreno-Atanasio, "Aggregation of nanoparticles in high ionic strength suspensions: Effect of Hamaker constant and particle concentration", *Advanced Powder Technology*, **23**, 478, (2012).
13. M.G. Espinoza, M.L. Hinks, A.M. Mendoza, D.P. Pullman, K.I. Peterson, "Kinetics of Halide-Induced Decomposition and Aggregation of Silver Nanoparticles", *The Journal of Physical Chemistry C*, **116**, 8305, (2012).
14. M. Zhou, B. Wang, Z. Rozynek, Z. Xie, J.O. Fossum, X. Yu, S. Raaen, "Minute synthesis of extremely stable gold nanoparticles", *Nanotechnology*, **20**, 505606/1, (2009).
15. H. Zhang, C. Zhang, "Transport of silver nanoparticles capped with different stabilizers in water saturated porous media", *J. Mater. Environ. Sci.*, **5**, 231, (2014).
16. M. Faraday, "The Bakerian Lecture: Experimental Relations of Gold (and Other Metals) to Light", *Philosophical Transactions of the Royal Society of London*, **147**, 145, (1857).
17. S. Link, M.A. El-Sayed, "Spectral Properties and Relaxation Dynamics of Surface Plasmon Electronic Oscillations in Gold and Silver Nanodots and Nanorods", *The Journal of Physical Chemistry B*, **103**, 8410, (1999).
18. S. Link, M.A. El-Sayed, "Size and Temperature Dependence of the Plasmon Absorption of Colloidal Gold Nanoparticles", *The Journal of Physical Chemistry B*, **103**, 4212, (1999).

19. P. Chakraborty, "Metal nanoclusters in glasses as non-linear photonic materials", *Journal of Materials Science*, **33**, 2235, (1998).
20. U. Kreibig, M. Vollmer, *Optical Properties of Metal Clusters*; Springer: Berlin, 1995; Vol. 25.
21. M. Paunovic, M. Schlesinger, *Fundamentals of Electrochemical Deposition*; 2nd Edition ed.; Wiley-Interscience, 2006.
22. J.V. Zoval, J. Lee, S. Gorer, R.M. Penner, "Electrochemical Preparation of Platinum Nanocrystallites with Size Selectivity on Basal Plane Oriented Graphite Surfaces", *The Journal of Physical Chemistry B*, **102**, 1166, (1998).
23. W.K. Burton, N. Cabrera, F.C. Frank, "The Growth of Crystals and the Equilibrium Structure of their Surfaces", *Philosophical Transactions of the Royal Society of London. Series A, Mathematical and Physical Sciences*, **243**, 299, (1951).
24. J.V. Zoval, R.M. Stiger, P.R. Biernacki, R.M. Penner, "Electrochemical deposition of silver nanocrystallites on the atomically smooth graphite basal plane", *Journal of Physical Chemistry*, **100**, 837, (1996).
25. R.T. Pötzschke, C.A. Gervasi, S. Vinzelberg, G. Staikov, W.J. Lorenz, "Nanoscale studies of Ag electrodeposition on HOPG (0001)", *Electrochimica Acta*, **40**, 1469, (1995).
26. B. Scharifker, G. Hills, "Theoretical and experimental studies of multiple nucleation", *Electrochimica Acta*, **28**, 879, (1983).
27. J.L. Fransaer, R.M. Penner, "Brownian Dynamics Simulation of the Growth of Metal Nanocrystal Ensembles on Electrode Surfaces from Solution. I. Instantaneous Nucleation and Diffusion-Controlled Growth", *The Journal of Physical Chemistry B*, **103**, 7643, (1999).
28. T.T. Ngo, R.S. Williams, "Kinetic routes to the growth of monodisperse islands", *Applied Physics Letters*, **66**, 1906, (1995).
29. H. Liu, R.M. Penner, "Size-Selective Electrodeposition of Mesoscale Metal Particles in the Uncoupled Limit", *The Journal of Physical Chemistry B*, **104**, 9131, (2000).
30. R.M. Penner, "Brownian Dynamics Simulations of the Growth of Metal Nanocrystal Ensembles on Electrode Surfaces in Solution: 2. The Effect of Deposition Rate on Particle Size Dispersion†", *The Journal of Physical Chemistry B*, **105**, 8672, (2001).
31. R.E. Davila-Martinez, L.F. Cueto, E.M. Sanchez, "Electrochemical deposition of silver nanoparticles on TiO₂/FTO thin films", *Surf. Sci.*, **600**, 3427, (2006).
32. T. Hezard, K. Fajerweg, D. Evrard, V. Colliere, P. Behra, P. Gros, "Influence of the gold nanoparticles electrodeposition method on Hg(II) trace electrochemical detection", *Electrochim. Acta*, **73**, 15, (2012).
33. W. Plieth, H. Dietz, A. Anders, G. Sandmann, A. Meixner, M. Weber, H. Knepe, "Electrochemical preparation of silver and gold nanoparticles: Characterization by confocal and surface enhanced Raman microscopy", *Surf. Sci.*, **597**, 119, (2005).
34. A.A. Rafati, A. Afraz, A. Hajian, P. Assari, "Simultaneous determination of ascorbic acid, dopamine, and uric acid using a carbon paste electrode modified with multiwalled carbon nanotubes, ionic liquid, and palladium nanoparticles", *Microchim. Acta*, Ahead of Print, (2014).
35. M. Ueda, H. Dietz, A. Anders, H. Knepe, A. Meixner, W. Plieth, "Double-pulse technique as an electrochemical tool for controlling the preparation of metallic nanoparticles", *Electrochim. Acta*, **48**, 377, (2002).
36. G. Sandmann, H. Dietz, W. Plieth, "Preparation of silver nanoparticles on ITO surfaces by a double-pulse method", *Journal of Electroanalytical Chemistry*, **491**, 78, (2000).
37. A. Sheludko, G. Bliznakov, "Initial Stages of electrodeposition of metals. II", *Bulg. Acad. Sci. Phys. Inst.*, **2**, 227, (1952).
38. E.H. Schacht, "Polymer chemistry and hydrogel systems", *J. Phys.: Conf. Ser.*, **3**, 22, (2004).

39. A. Sannino, C. Demitri, M. Madaghiele, "Biodegradable Cellulose-based Hydrogels: Design and Applications", *Materials*, **2**, 353, (2009).
40. T. Dai, X. Qing, H. Zhou, C. Shen, J. Wang, Y. Lu, "Mechanically strong conducting hydrogels with special double-network structure", *Synthetic Metals*, **160**, 791, (2010).
41. M. Shibayama, T. Tanaka, "Volume Phase-Transition and Related Phenomena of Polymer Gels", *Advances in Polymer Science*, **109**, 1, (1993).
42. J. Yang, X.-P. Wang, X.-M. Xie, "In situ synthesis of poly(acrylic acid) physical hydrogels from silica nanoparticles", *Soft Matter*, **8**, 1058, (2012).
43. J. Berger, M. Reist, J.M. Mayer, O. Felt, N.A. Peppas, R. Gurny, "Structure and interactions in covalently and ionically crosslinked chitosan hydrogels for biomedical applications", *European Journal of Pharmaceutics and Biopharmaceutics*, **57**, 19, (2004).
44. O. Wichterle, D. Lim, "Hydrophilic Gels for Biological Use", *Nature*, **185**, 117, (1960).
45. M.V. Risbud, R.R. Bhonde, "Polyacrylamide-Chitosan Hydrogels: In Vitro Biocompatibility and Sustained Antibiotic Release Studies", *Drug Delivery*, **7**, 69, (2000).
46. S. Rimdusit, S. Jingjid, S. Damrongsakkul, S. Tiptipakorn, T. Takeichi, "Biodegradability and property characterizations of Methyl Cellulose: Effect of nanocompositing and chemical crosslinking", *Carbohydrate Polymers*, **72**, 444, (2008).
47. A.B. Imran, T. Seki, Y. Takeoka, "Recent advances in hydrogels in terms of fast stimuli responsiveness and superior mechanical performance", *Polym J*, **42**, 839, (2010).
48. Y. Qiu, K. Park, "Environment-sensitive hydrogels for drug delivery", *Advanced Drug Delivery Reviews*, **53**, 321, (2001).
49. T. Nochi, Y. Yuki, H. Takahashi, S.-I. Sawada, M. Mejima, T. Kohda, N. Harada, I.G. Kong, A. Sato, N. Kataoka, D. Tokuhara, S. Kurokawa, Y. Takahashi, H. Tsukada, S. Kozaki, K. Akiyoshi, H. Kiyono, "Nanogel antigenic protein-delivery system for adjuvant-free intranasal vaccines", *Nat Mater*, **9**, 572, (2010).
50. J.C. Fricain, P.L. Granja, M.A. Barbosa, B. De J  So, N. Barthe, C. Baquey, "Cellulose phosphates as biomaterials. In vivo biocompatibility studies", *Biomaterials*, **23**, 971, (2002).
51. M.V. Risbud, A.A. Hardikar, S.V. Bhat, R.R. Bhonde, "pH-sensitive freeze-dried chitosan-polyvinyl pyrrolidone hydrogels as controlled release system for antibiotic delivery", *Journal of Controlled Release*, **68**, 23, (2000).
52. K. Varaprasad, Y.M. Mohan, S. Ravindra, N.N. Reddy, K. Vimala, K. Monika, B. Sreedhar, K.M. Raju, "Hydrogel-Silver Nanoparticle Composites: A New Generation of Antimicrobials", *Journal of Applied Polymer Science*, **115**, 1199, (2010).
53. N. Saha, A. Saarai, N. Roy, T. Kitano, P. Saha, "Polymeric biomaterial based hydrogels for biomedical applications", *J. Biomater. Nanobiotechnol.*, **2**, 85, (2011).
54. X. Yang, Q. Liu, X. Chen, F. Yu, Z. Zhu, "Investigation of PVA/ws-chitosan hydrogels prepared by combined gamma-irradiation and freeze-thawing", *Carbohydrate Polymers*, **73**, 401, (2008).
55. L.H. Ai, J. Jiang, "Catalytic reduction of 4-nitrophenol by silver nanoparticles stabilized on environmentally benign macroscopic biopolymer hydrogel", *Bioresource Technology*, **132**, 374, (2013).
56. S. Raymond, L. Weintraub, "Acrylamide Gel as a Supporting Medium for Zone Electrophoresis", *Science*, **130**, 711, (1959).
57. V.S. Green, D.E. Scott, "Polyacrylamide: Use, effectiveness and cost of soil erosion control amendments", *Selected papers from the 10th International Soil Conservation Organization Meeting May 24-29 1999*, 384, (2001).

58. X.D. Feng, X.Q. Guo, K.Y. Qiu, "Study of the initiation mechanism of the vinyl polymerization with the system persulfate/N,N,N',N'-tetramethylethylenediamine", *Die Makromolekulare Chemie*, **189**, 77, (1988).
59. H.-R. Lin, "Solution polymerization of acrylamide using potassium persulfate as an initiator: kinetic studies, temperature and pH dependence", *European Polymer Journal*, **37**, 1507, (2001).
60. D. Hunkeler, "Mechanism and Kinetics of the Persulfate-Initiated Polymerization of Acrylamide", *Macromolecules*, **24**, 2160, (1991).
61. T.C. Beeskow, W. Kusharyoto, F.B. Anspach, K.H. Kroner, W.D. Deckwer, "Surface Modification of Microporous Polyamide Membranes with Hydroxyethyl Cellulose and Their Application as Affinity Membranes", *Journal of Chromatography A*, **715**, 49, (1995).
62. J.S. Bradley In *Clusters and Colloids*; Wiley-VCH Verlag GmbH: 2007, p 459.
63. A. Henglein, "Small-particle research: physicochemical properties of extremely small colloidal metal and semiconductor particles", *Chemical Reviews*, **89**, 1861, (1989).
64. N.R. Jana, T.K. Sau, T. Pal, "Growing Small Silver Particle as Redox Catalyst", *The Journal of Physical Chemistry B*, **103**, 115, (1998).
65. A. Henglein, "Physicochemical properties of small metal particles in solution: "microelectrode" reactions, chemisorption, composite metal particles, and the atom-to-metal transition", *The Journal of Physical Chemistry*, **97**, 5457, (1993).
66. N. Pradhan, A. Pal, T. Pal, "Silver nanoparticle catalyzed reduction of aromatic nitro compounds", *Colloids and Surfaces a-Physicochemical and Engineering Aspects*, **196**, 247, (2002).
67. Z. Zhang, C. Shao, Y. Sun, J. Mu, M. Zhang, P. Zhang, Z. Guo, P. Liang, C. Wang, Y. Liu, "Tubular nanocomposite catalysts based on size-controlled and highly dispersed silver nanoparticles assembled on electrospun silica nanotubes for catalytic reduction of 4-nitrophenol", *J. Mater. Chem.*, **22**, 1387, (2012).
68. R. Narayanan, M.A. El-Sayed, "Catalysis with transition metal nanoparticles in colloidal solution: Nanoparticle shape dependence and stability", *Journal of Physical Chemistry B*, **109**, 12663, (2005).
69. K. Kuroda, T. Ishida, M. Haruta, "Reduction of 4-nitrophenol to 4-aminophenol over Au nanoparticles deposited on PMMA", *Journal of Molecular Catalysis A: Chemical*, **298**, 7, (2009).
70. H. Wu, Z. Liu, X. Wang, B. Zhao, J. Zhang, C. Li, "Preparation of hollow capsule-stabilized gold nanoparticles through the encapsulation of the dendrimer", *Journal of Colloid and Interface Science*, **302**, 142, (2006).
71. A.C. Patel, S. Li, C. Wang, W. Zhang, Y. Wei, "Electrospinning of Porous Silica Nanofibers Containing Silver Nanoparticles for Catalytic Applications", *Chemistry of Materials*, **19**, 1231, (2007).
72. P. Gong, H. Li, X. He, K. Wang, J. Hu, W. Tan, S. Zhang, X. Yang, "Preparation and antibacterial activity of Fe₃O₄ @ Ag nanoparticles", *Nanotechnology*, **18**, 285604/1, (2007).
73. K. Shameli, M. Bin Ahmad, M. Zargar, W. Yunus, N.A. Ibrahim, "Fabrication of silver nanoparticles doped in the zeolite framework and antibacterial activity", *International Journal of Nanomedicine*, **6**, 331, (2011).
74. V. Thomas, M.M. Yallapu, B. Sreedhar, S.K. Bajpai, "Breathing-in/breathing-out approach to preparing nanosilver-loaded hydrogels: Highly efficient antibacterial nanocomposites", *Journal of Applied Polymer Science*, **111**, 934, (2009).
75. P. Saravanan, M. Padmanabha Raju, S. Alam, "A study on synthesis and properties of Ag nanoparticles immobilized polyacrylamide hydrogel composites", *Materials Chemistry and Physics*, **103**, 278, (2007).

76. M. Uygun, M.U. Kahveci, D. Odaci, S. Timur, Y. Yagci, "Antibacterial Acrylamide Hydrogels Containing Silver Nanoparticles by Simultaneous Photoinduced Free Radical Polymerization and Electron Transfer Processes", *Macromolecular Chemistry and Physics*, **210**, 1867, (2009).
77. B. Obradovic, J. Stojkowska, Z. Jovanovic, V. Miskovic-Stankovic, "Novel alginate based nanocomposite hydrogels with incorporated silver nanoparticles", *J. Mater. Sci.: Mater. Med.*, **23**, 99, (2012).
78. Y. Murali Mohan, K. Vimala, V. Thomas, K. Varaprasad, B. Sreedhar, S.K. Bajpai, K. Mohana Raju, "Controlling of silver nanoparticles structure by hydrogel networks", *Journal of Colloid and Interface Science*, **342**, 73, (2010).
79. J.D. Van Elsas In *Genetic Interactions Among Microorganisms in the Natural Environment*; Elsas, E.M.H.W.D.v., Ed.; Pergamon: Amsterdam, 1992, p 17.
80. M.C. Enright, D.A. Robinson, G. Randle, E.J. Feil, H. Grundmann, B.G. Spratt, "The evolutionary history of methicillin-resistant *Staphylococcus aureus* (MRSA)", *Proc. Natl. Acad. Sci. U. S. A.*, **99**, 7687, (2002).
81. C. Marambio-Jones, E.M.V. Hoek, "A review of the antibacterial effects of silver nanomaterials and potential implications for human health and the environment", *Journal of Nanoparticle Research*, **12**, 1531, (2010).
82. P. Lalueza, M. Monzon, M. Arruebo, J. Santamaria, "Bactericidal effects of different silver-containing materials", *Mater. Res. Bull.*, **46**, 2070, (2011).
83. J.W. Alexander, "History of the medical use of silver", *Surg Infect (Larchmt)*, **10**, 289, (2009).
84. A.B.G. Lansdown, *Silver in Healthcare: Its Antimicrobial Efficacy and Safety in Use*, 2010; Vol. 6.
85. S. Silver, "Bacterial silver resistance: molecular biology and uses and misuses of silver compounds", *FEMS Microbiol. Rev.*, **27**, 341, (2003).
86. P.L. Drake, K.J. Hazelwood, "Exposure-related health effects of silver and silver compounds: A review", *Annals of Occupational Hygiene*, **49**, 575, (2005).
87. S.M. Hussain, K.L. Hess, J.M. Gearhart, K.T. Geiss, J.J. Schlager, "In vitro toxicity of nanoparticles in BRL 3A rat liver cells", *Toxicology in Vitro*, **19**, 975, (2005).
88. A.R. Shahverdi, A. Fakhimi, H.R. Shahverdi, S. Minaian, "Synthesis and effect of silver nanoparticles on the antibacterial activity of different antibiotics against *Staphylococcus aureus* and *Escherichia coli*", *Nanomedicine: Nanotechnology, Biology and Medicine*, **3**, 168, (2007).
89. J.R. Morones-Ramirez, J.A. Winkler, C.S. Spina, J.J. Collins, "Silver Enhances Antibiotic Activity Against Gram-Negative Bacteria", *Science Translational Medicine*, **5**, 190ra81, (2013).
90. J.R. Morones, J.L. Elechiguerra, A. Camacho, K. Holt, J.B. Kouri, J.T. Ramírez, M.J. Yacaman, "The bactericidal effect of silver nanoparticles", *Nanotechnology*, **16**, 2346, (2005).
91. S. Pal, Y.K. Tak, J.M. Song, "Does the antibacterial activity of silver nanoparticles depend on the shape of the nanoparticle? A study of the gram-negative bacterium *Escherichia coli*", *Applied and Environmental Microbiology*, **73**, 1712, (2007).
92. I. Chopra, "The increasing use of silver-based products as antimicrobial agents: a useful development or a cause for concern?", *Journal of Antimicrobial Chemotherapy*, **59**, 587, (2007).
93. S.K. Rastogi, V.J. Rutledge, C. Gibson, D.A. Newcombe, J.R. Branen, A.L. Branen, "Ag colloids and Ag clusters over EDAPTMS-coated silica nanoparticles: synthesis, characterization, and antibacterial activity against *Escherichia coli*", *Nanomedicine: Nanotechnology, Biology and Medicine*, **7**, 305, (2011).

94. A. Nanda, M. Saravanan, "Biosynthesis of silver nanoparticles from *Staphylococcus aureus* and its antimicrobial activity against MRSA and MRSE", *Nanomedicine: Nanotechnology, Biology and Medicine*, **5**, 452, (2009).
95. R.D. Holtz, A.G. Souza, M. Brocchi, D. Martins, N. Duran, O.L. Alves, "Development of nanostructured silver vanadates decorated with silver nanoparticles as a novel antibacterial agent", *Nanotechnology*, **21**, (2010).
96. A.J. Kora, J. Arunachalam, "Assessment of antibacterial activity of silver nanoparticles on *Pseudomonas aeruginosa* and its mechanism of action", *World Journal of Microbiology & Biotechnology*, **27**, 1209, (2011).
97. B.-H. Jun, J.-W. Byun, J.Y. Kim, H. Kang, H.-J. Park, J. Yoon, Y.-S. Lee, "Facile method of preparing silver-embedded polymer beads and their antibacterial effect", *J. Mater. Sci.*, **45**, 3106, (2010).
98. P.S.K. Murthy, Y. Murali Mohan, K. Varaprasad, B. Sreedhar, K. Mohana Raju, "First successful design of semi-IPN hydrogel–silver nanocomposites: A facile approach for antibacterial application", *Journal of Colloid and Interface Science*, **318**, 217, (2008).
99. V. Thomas, M.M. Yallapu, B. Sreedhar, S.K. Bajpai, "A versatile strategy to fabricate hydrogel–silver nanocomposites and investigation of their antimicrobial activity", *Journal of Colloid and Interface Science*, **315**, 389, (2007).
100. M. Eid, E. Araby, "Bactericidal Effect of Poly(Acrylamide/Itaconic Acid)-Silver Nanoparticles Synthesized by Gamma Irradiation Against *Pseudomonas Aeruginosa*", *Appl. Biochem. Biotechnol.*, **171**, 469, (2013).
101. D.S. Hagopian, J.G. Riley, "A closer look at the bacteriology of nitrification", *Aquacultural Engineering*, **18**, 223, (1998).
102. J.P. Schimel, J. Bennett, "Nitrogen mineralization: Challenges of a changing paradigm", *Ecology*, **85**, 591, (2004).
103. A. Weigelt, R. Bol, R.D. Bardgett, "Preferential uptake of soil nitrogen forms by grassland plant species", *Oecologia*, **142**, 627, (2005).
104. T.M. Addiscott, *Nitrate, Agriculture and the Environment*; CABI Publishing, 2005.
105. <http://Psep.Cce.Cornell.Edu/Facts-Slides-Self/Facts/Mod-Ag-Grw85.AspX>.
106. <http://Eur-Lex.Europa.Eu/Lexuriserv/Lexuriserv.Do?Uri=Celex:3199110676:En:Html>.
107. D.S. Silvester, E.I. Rogers, L.E. Barrosse-Antle, T.L. Broder, R.G. Compton, "The electrochemistry of simple inorganic molecules in room temperature ionic liquids", *Journal of the brazilian chemical society*, **19**, 611, (2008).
108. H. Lu, K. Chandran, D. Stensel, "Microbial ecology of denitrification in biological wastewater treatment", *Water Research*, **64**, 237, (2014).
109. A. Pintar, J. Batista, J. Levec, "Integrated ion exchange/catalytic process for efficient removal of nitrates from drinking water", *Chemical Engineering Science*, **56**, 1551, (2001).
110. U. Prüsse, K.-D. Vorlop, "Supported bimetallic palladium catalysts for water-phase nitrate reduction", *Journal of Molecular Catalysis A: Chemical*, **173**, 313, (2001).
111. G.E. Badea, "Electrocatalytic reduction of nitrate on copper electrode in alkaline solution", *Electrochimica Acta*, **54**, 996, (2009).
112. J. Davis, M.J. Moorcroft, S.J. Wilkins, R.G. Compton, M.F. Cardosi, "Electrochemical detection of nitrate and nitrite at a copper modified electrode", *Analyst*, **125**, 737, (2000).
113. D. Reyter, D. Bélanger, L. Roué, "Study of the electroreduction of nitrate on copper in alkaline solution", *Electrochimica Acta*, **53**, 5977, (2008).
114. A.O. Solak, P. Gülser, E. Gökm, F. Gökmeşe, "A New Differential Pulse Voltammetric Method for the Determination of Nitrate at a Copper Plated Glassy Carbon Electrode", *Microchimica Acta*, **134**, 77, (2000).

115. S. Cattarin, "Electrochemical reduction of nitrogen oxyanions in 1 M sodium hydroxide solutions at silver, copper and CuInSe₂ electrodes", *Journal of Applied Electrochemistry*, **22**, 1077, (1992).
116. M. Fedurco, P. Kedzierzawski, J. Augustynski, "Effect of multivalent cations upon reduction of nitrate ions at the Ag electrode", *Journal of the Electrochemical Society*, **146**, 2569, (1999).
117. H.L. Li, J.Q. Chambers, D.T. Hobbs, "Electroreduction of nitrate ions in concentrated sodium hydroxide solutions at lead, zinc, nickel and phthalocyanine-modified electrodes", *Journal of Applied Electrochemistry*, **18**, 454, (1988).
118. Davenport R. J, D.C. Johnson, "Voltammetric Determination of Nitrate and Nitrite ions using a Rotating Cadmium disk Electrode", *Analytical Chemistry*, **45**, 1979, (1973).
119. C. Lévy-Clément, N.A. Ndao, A. Katty, M. Bernard, A. Deneuille, C. Cominellis, A. Fujishima, "Boron doped diamond electrodes for nitrate elimination in concentrated wastewater", *Diamond and Related Materials*, **12**, 606, (2003).
120. A. Manzo-Robledo, C. Lévy-Clément, N. Alonso-Vante, "The interplay between hydrogen evolution reaction and nitrate reduction on boron-doped diamond in aqueous solution: the effect of alkali cations", *Electrochimica Acta*, **117**, 420, (2014).
121. O.S.G.P. Soares, J.J.M. Órfão, M.F.R. Pereira, "Bimetallic catalysts supported on activated carbon for the nitrate reduction in water: Optimization of catalysts composition", *Applied Catalysis B: Environmental*, **91**, 441, (2009).
122. A. Anastasopoulos, L. Hannah, B.E. Hayden, "High throughput optimisation of PdCu alloy electrocatalysts for the reduction of nitrate ions", *Journal of Catalysis*, **305**, 27, (2013).
123. W. Siriwatcharapiboon, Y. Kwon, J. Yang, R.L. Chantry, Z. Li, S.L. Horswell, M.T.M. Koper, "Promotion effects of Sn on the electrocatalytic reduction of nitrate at Rh nanoparticles", *ChemElectroChem*, **1**, 172, (2014).
124. M.R. Gartia, B. Braunschweig, T.-W. Chang, P. Moinzadeh, B.S. Minsker, G. Agha, A. Wieckowski, L.L. Keefer, G.L. Liu, "The microelectronic wireless nitrate sensor network for environmental water monitoring", *Journal of Environmental Monitoring*, **14**, 3068, (2012).
125. A.J. Bard, H. Lund, *Encyclopedia of Electrochemistry of the Elements Vol VIII*; Marcel Dekker Incorporated, 1978.
126. M. Li, C. Feng, Z. Zhang, X. Lei, R. Chen, Y. Yang, N. Sugiura, "Simultaneous reduction of nitrate and oxidation of by-products using electrochemical method", *Journal of Hazardous Materials*, **171**, 724, (2009).
127. I.G. Casella, M. Gatta, "Electrochemical reduction of NO₃⁻ and NO₂⁻ on a composite copper thallium electrode in alkaline solutions", *Journal of Electroanalytical Chemistry*, **568**, 183, (2004).
128. D. De, J.D. Englehardt, E.E. Kalu, "Electroreduction of nitrate and nitrite ion on a platinum-group-metal catalyst-modified carbon fiber electrode - Chronoamperometry and mechanism studies", *Journal of the Electrochemical Society*, **147**, 4573, (2000).
129. E.B. Molodkina, I.G. Botryakova, A.I. Danilov, J. Souza-Garcia, J.M. Feliu, "Kinetics and mechanism of nitrate and nitrite electroreduction on Pt(100) electrodes modified by copper adatoms", *Russian Journal of Electrochemistry*, **49**, 285, (2013).
130. G.E. Dima, A.C.A. De Vooy, M.T.M. Koper, "Electrocatalytic reduction of nitrate at low concentration on coinage and transition-metal electrodes in acid solutions", *Journal of Electroanalytical Chemistry*, **554–555**, 15, (2003).
131. R.K. Kvaratskheliya, T.S. Machavariani, "Role of the nature of the electrode in processes of electroreduction of 'difficultly reduced' anions", *Soviet electrochemistry*, **20**, 284, (1984).

132. O.A. Petrij, T.Y. Safonova, "Electroreduction of nitrate and nitrite anions on platinum metals: A model process for elucidating the nature of the passivation by hydrogen adsorption", *Journal of Electroanalytical Chemistry*, **331**, 897, (1992).
133. J. Yang, Y. Kwon, M. Duca, M.T.M. Koper, "Combining Voltammetry and Ion Chromatography: Application to the Selective Reduction of Nitrate on Pt and PtSn Electrodes", *Analytical Chemistry*, **85**, 7645, (2013).
134. D. Kim, I.B. Goldberg, J.W. Judy, "Chronocoulometric determination of nitrate on silver electrode and sodium hydroxide electrolyte", *Analyst*, **132**, 350, (2007).
135. D. De, E.E. Kalu, P.P. Tarjan, J.D. Englehardt, "Kinetic studies of the electrochemical treatment of nitrate and nitrite ions on iridium-modified carbon fiber", *Chemical Engineering & Technology*, **27**, 56, (2004).
136. M.T. De Groot, M.T.M. Koper, "The influence of nitrate concentration and acidity on the electrocatalytic reduction of nitrate on platinum", *Journal of Electroanalytical Chemistry*, **562**, 81, (2004).
137. W.S. Jobgen, S.C. Jobgen, H. Li, C.J. Meiningner, G. Wu, "Analysis of nitrite and nitrate in biological samples using high-performance liquid chromatography", *Journal of Chromatography B*, **851**, 71, (2007).
138. M.N. Muscará, G. De Nucci, "Simultaneous determination of nitrite and nitrate anions in plasma, urine and cell culture supernatants by high-performance liquid chromatography with post-column reactions", *Journal of Chromatography B: Biomedical Sciences and Applications*, **686**, 157, (1996).
139. M.J. Moorcroft, J. Davis, R.G. Compton, "Detection and determination of nitrate and nitrite: a review", *Talanta*, **54**, 785, (2001).
140. S. Ward-Jones, C.E. Banks, A.O. Simm, L. Jiang, R.G. Compton, "An In Situ Copper Plated Boron-Doped Diamond Microelectrode Array for the Sensitive Electrochemical Detection of Nitrate", *Electroanalysis*, **17**, 1806, (2005).
141. F.W. Campbell, R.G. Compton, "The use of nanoparticles in electroanalysis: an updated review", *Analytical and Bioanalytical Chemistry*, **396**, 241, (2010).
142. A.O. Simm, S. Ward-Jones, C.E. Banks, R.G. Compton, "Novel methods for the production of silver microelectrode-arrays: Their characterisation by atomic force microscopy and application to the electro-reduction of halothane", *Analytical Sciences*, **21**, 667, (2005).
143. K. Fajerwerg, V. Ynam, B. Chaudret, V. Garçon, D. Thouron, M. Comtat, "An original nitrate sensor based on silver nanoparticles electrodeposited on a gold electrode", *Electrochemistry Communications*, **12**, 1439, (2010).
144. R.S. Hutchins, L.G. Bachas, "Nitrate-Selective Electrode Developed by Electrochemically Mediated Imprinting/Doping of Polypyrrole", *Analytical Chemistry*, **67**, 1654, (1995).
145. S. Aravamudhan, S. Bhansali, "Development of micro-fluidic nitrate-selective sensor based on doped-polypyrrole nanowires", *Sensors and Actuators, B: Chemical*, **132**, 623, (2008).
146. E. Dinckaya, E. Akyilmaz, M.K. Sezginturk, F.N. Ertas, "SENSITIVE NITRATE DETERMINATION IN WATER AND MEAT SAMPLES BY AMPEROMETRIC BIOSENSOR", *Preparative Biochemistry & Biotechnology*, **40**, 119, (2010).

Chapter 2 Experimental

2.1 Introduction

In this chapter the experimental techniques and apparatus used in the course of this research are outlined. Firstly, the experimental set-up of the electrochemical apparatus is described, in Section 2.2. The theoretical background for each of the different experimental techniques employed in the preparation and characterisations of the electrodeposited silver nanoparticles and the PVP-protected colloidal nanoparticles is provided in Section 2.3. The chemicals and preparation procedures of the samples are introduced in Section 2.4, while specific details on the concentration and experimental parameters are outlined in the results chapters as the experiments are discussed.

2.2 Experimental Set-up

2.2.1 Electrochemical Apparatus

Electrochemical experiments such as potentiostatic, galvanostatic, cyclic voltammetry (CV), open-circuit potential measurements were carried out using one of two potentiostats; a Solartron (Model SI 1287) or a CHI440 instrument (Model EA160). Each system was controlled by a computer and the various software packages used were CorrWare for Windows™, Version 2.1 and CHI440 software Version 2.06 respectively. A schematic of the electrochemical equipment is shown in Figure 2.1. In all cases, experiments were carried out using a conventional three-electrode system, as described in Section 2.2.2.

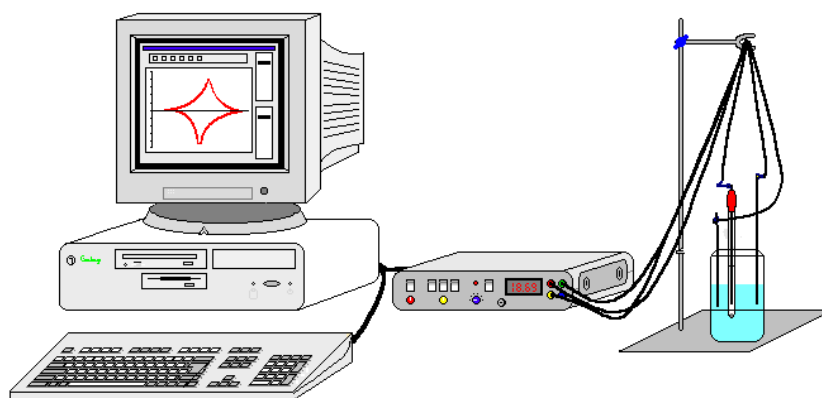


Figure 2.1: Experimental set up used to record all electrochemical measurements.

2.2.1 The Electrochemical Cell

The electrochemical cell is shown in Figure 2.2 is a standard three-electrode cell consisting of a working electrode (WE), an auxiliary or counter electrode (CE) and a reference electrode (RE). Different reference electrodes were utilised throughout this study depending on the nature of the electrolyte solution, namely a silver wire or a standard calomel electrode (SCE). The potential of the silver wire was measured after the experiment. A number of different materials served as the working electrode. Platinum sheet electrodes were employed in Chapter 3 for the synthesis of PVP-protected colloidal silver nanoparticles. A glassy carbon (GC) disc electrode served as the substrate material upon which silver was electrochemically deposited in Chapter 4. The electrochemical reduction of nitrate was also investigated at a silver electrode for comparison. A platinum wire/sheet was used as the auxiliary (counter) electrode in all cases. The electrodes were connected to the potentiostat using insulated wires and the experimental parameters and results were imputed and recorded on a standard PC as shown in Figure 2.1

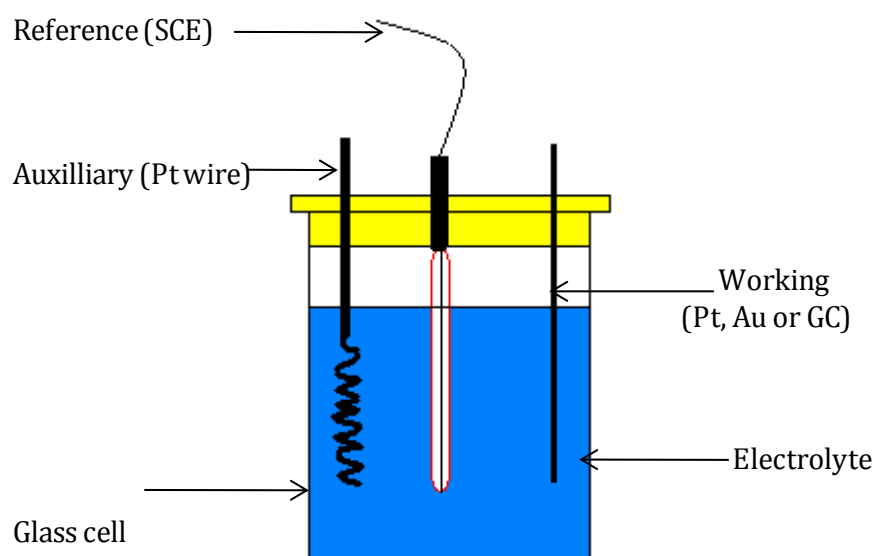


Figure 2.2: Diagram of electrode and electrochemical cell.

2.2.3 Electrode Materials and Preparation

All electrode materials were purchased from Goodfellow or Alfa Aesar. The GC substrate and bulk silver rods were encased in Teflon and set in place using epoxy resin, a schematic of which is illustrated in Figure 2.3. The electrical contact for the electrodes was achieved using a copper wire and conducting silver epoxy. The platinum sheets were connected via a copper hook through a small hole at the top of the platinum sheet itself. The GC was of high purity grade and had a 4 mm or 5 mm diameter. Similarly, the silver was of high purity but 3 mm in diameter. The platinum wire CE and the platinum sheets, WE and CE, were also of high purity, 99.9%, with a diameter of 1 mm for the wire and 1 x 5 cm length x width dimensions for the sheet electrodes. Prior to each experiment the exposed electrode surface was polished using a Metaserv Universal polisher with water lubricated silicon carbide paper. The surfaces were polished to a smooth finish with successively finer grades, ranging from 300 to 1200 grade, rinsed and sonicated in distilled water between each grade. A mirror finish was then achieved by spraying Buehler MetaDi Monocrystalline Diamond suspension of between 1 to 30 μm onto a Buehler polishing cloth and hand polishing using successively finer grades. Again rinsing and sonicated with distilled water between grades.

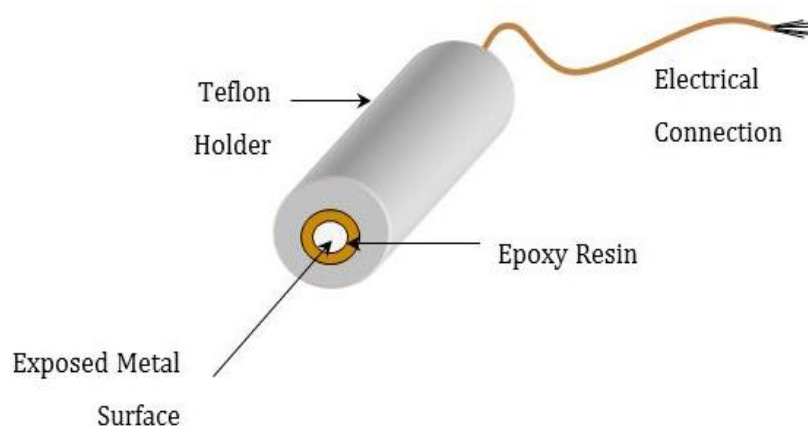


Figure 2.3: Schematic diagram of electrode assembly.

2.3 Experimental Techniques

The principal electrochemical/analytical techniques employed throughout this study were cyclic voltammetry, potentiostatic measurements, rotating disc voltammetry, ultraviolet-visible spectroscopy (UV-Vis) and scanning electron microscopy (SEM) in conjunction with energy dispersive X-ray analysis (EDX). An overview of each of the techniques is given below and other more detailed parameters are discussed in the results chapters.

2.3.1 Cyclic Voltammetry

Cyclic voltammetry (CV) is often the first technique used to characterise an electrochemical reaction, giving vital information on the mechanism of the reaction. CV involves sweeping the applied potential at working electrode between two chosen potential limit while monitoring the current output. The initial applied potential, E_i , is swept to a vertex potential, E_v , the scan is then reversed and swept back to the final potential, E_f , which is usually equal to the initial potential, E_i . These sweeps are typically carried out a number of times and at a constant rate known as the scan rate. The resulting plot is one of applied potential (V vs. ref) versus current ($A\ cm^{-2}$). The WE serves as the surface where the electron transfer of the redox reaction takes place and the electrical current created is known as the faradaic current. The CE balances this faradaic process with an electron transfer in the opposite direction i.e. if oxidation takes place at the WE a reduction reaction takes place at the CE. So, depending of the applied potential at the WE, the electroactive species can be reduced or oxidised.

There are four main CV responses that depend on the reversibility of the redox process and whether the redox species are adsorbed or not on the electrode surface as shown in Figure 2.4. Each response is characterized by the different shape of the corresponding cyclic voltammogram, which is described by three key parameters, the peak current (I_p), the peak potential (E_p) and the potential width at half peak ($|E_p - E_{p/2}|$). The dependence of each parameter on the potential scan rate, v , allows the characterisation of the electrochemical system. The E_p does not

change with v for reversible (Nernstian) systems. The I_p changes linearly with $v^{1/2}$ for reversible and irreversible systems, and with v for reversible adsorbed species. The correlation between I_p and $v^{1/2}$ for *quasi*-reversible systems depends on the scan rate and the electron-transfer rate constant. Generally, there is no correlation between I_p and $v^{1/2}$ at high scan rates and for reactions which display slow electron-transfer kinetics. The exact diagnostic equations used to probe the redox characteristics are described in detail in various electrochemistry textbooks (1,2).

The voltammogram response at different scan rates can reveal kinetic information concerning the electrocatalytic process such as diffusion and adsorption effects. A linear response to scan rate would be evidence of a diffusion controlled reaction as described by the Randles-Sevcik equation with has two forms depending on the behaviour, reversible (Equation 2.1) or irreversible (Equation 2.2) of the reaction taking place at the electrode.

$$i_p = (2.69 \times 10^5)n^{3/2}D^{1/2}v^{1/2}AC_o \quad 2.1$$

$$i_p = -(2.99 \times 10^5)n(\alpha n')^{1/2}D^{1/2}v^{1/2}AC_o \quad 2.2$$

Reversible behaviour is observed when both the oxidation and reduction species are stable and where the kinetics of the electron transfer process is fast (3). In Equation 2.1, i_p is the peak current (A), n is the number of electrons, D is the diffusion coefficient ($\text{cm}^2 \text{s}^{-1}$), v is the scan rate (V s^{-1}) and C_o is the concentration (mol cm^{-3})(4). Equation 2.2, for the irreversible systems, has some additional terms compared to Equation 2.1 namely α , the charge transfer coefficient which is a measure of the symmetry of the energy barrier. The term n' is the number of electrons transferred up to and including the rate determining step. For the purpose of this study, CV was used to study the electrochemical behaviour of the nitrate anion at the modified electrode surface. Since nitrate oxidation is generally

not observed only the reduction process was monitored. Additionally, the effect of all the interfering compounds, the composition of the background electrolyte and the determination of the surface area by lead underpotential deposition were investigated by cyclic voltammetry.

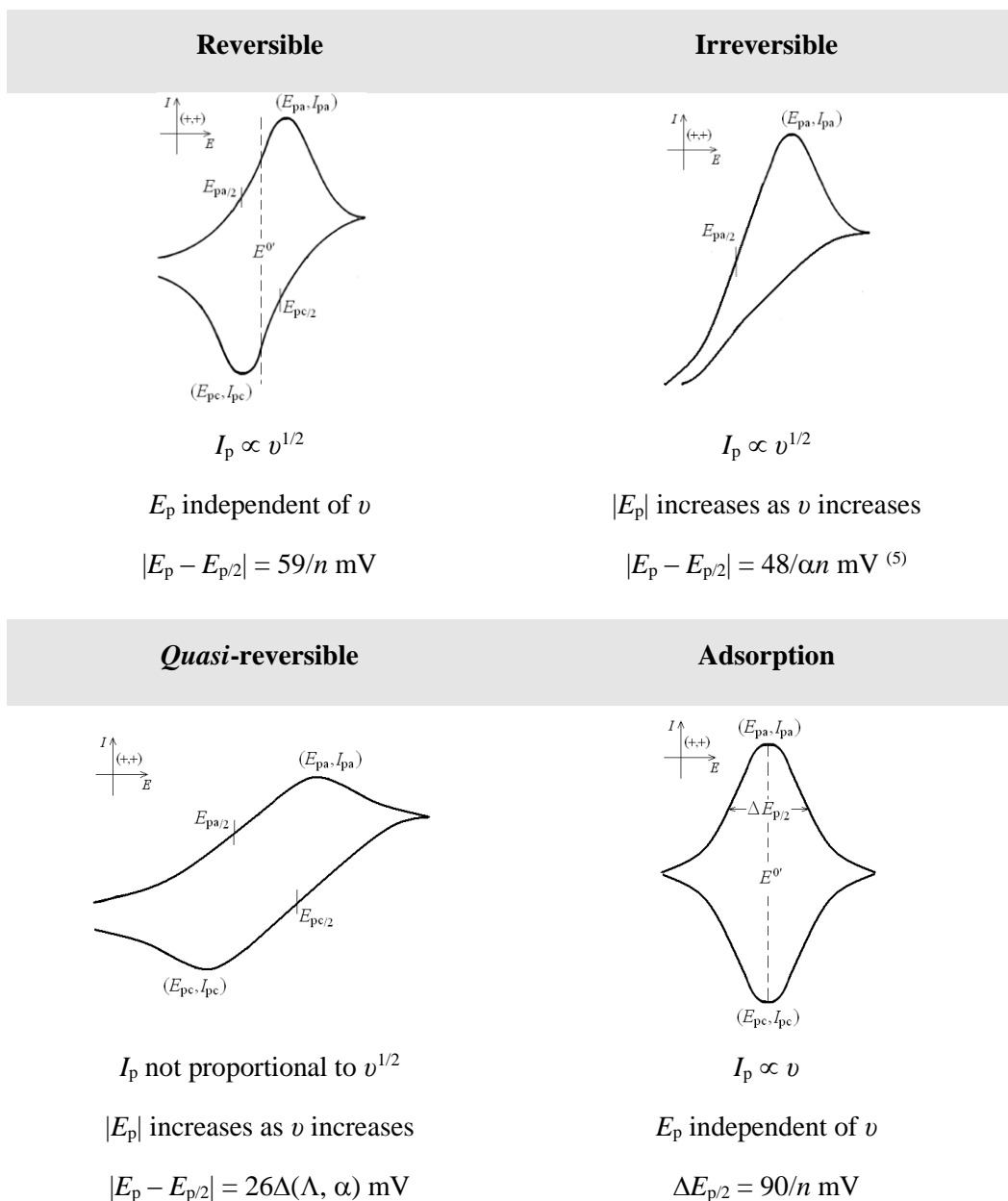


Figure 2.4: Cyclic voltammograms with their respective peak current (I_p) and potential (E_p) characteristics. The electrochemical system is reversible when the concentrations of the electroactive species at the electrode surface are governed at any time by the Nernst equation. The integer, n , is the number of electrons involved in the redox process, and α is the corresponding transfer coefficient. The factor $\Delta(\Lambda, \alpha)$ is a function of α and $\Lambda = k^0 / (vDF/RT)^{1/2}$, where D is the diffusion coefficient of the electroactive species and k^0 is the standard heterogeneous rate constant. The values of this factor are available in the literature. All potentials are expressed at 25 °C.

2.3.2 Potentiostatic Measurements

This versatile technique was utilised in this study for a variety of different processes. A potentiostatic mode was employed to grow silver nanoparticles on the surface of a glassy carbon electrode in Chapter 4. A multi-step approach can be utilised to affect the size of the particles by varying the length of the potential steps. A potentiostatic mode was also utilised to generate poly(N-vinylpyrrolidone) (PVP) protected colloidal silver nanoparticles in Chapter 3. The applied potential was held for either a fixed amount of time or until a desired charge had passed. Potentiostatic measurements were also used as an analytical tool. Constant potential amperometry (CPA) is a technique where a constant potential, sufficient to either oxidise or reduce the analyte of interest, is applied to the electrode and the current is monitored. Current steps are observed as aliquots of analyte are added and these steps can be used to generate a calibration curve to investigate the sensitivity of a surface to changes in analyte concentration, in this case nitrate. The working electrode is usually rotated at high speed, to remove mass transport effects, until the non-faradaic current reaches a stable background level. When basal current levels are achieved, a series of injections of analyte are made to the cell while the working electrode is still being rotated and the changes in the current are monitored. This produces a step-wise pattern of time (s) versus current ($A\text{ cm}^{-2}$), Figure 2.5. This technique is very useful when trying to determine the limit of detection of the electrode material being tested as it allows the charging background current to dissipate to very low levels so that small changes in faradaic or redox current can be detected.

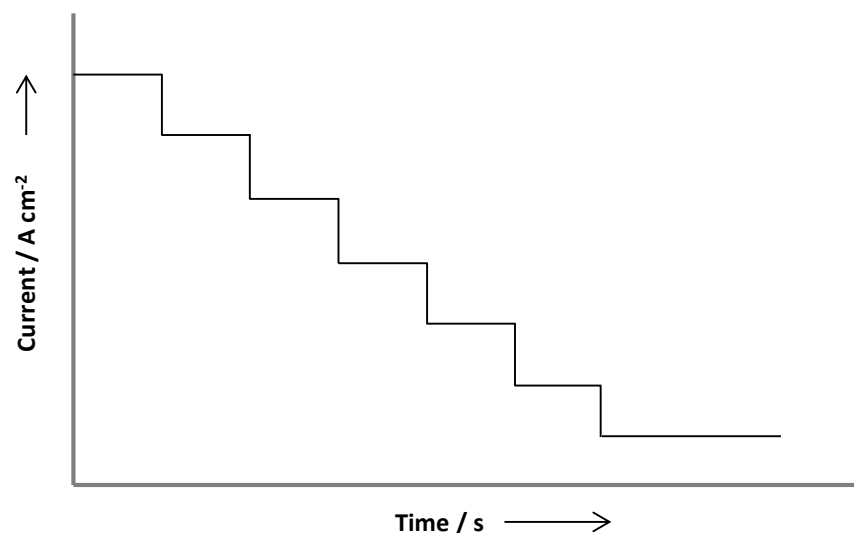


Figure 2.5: Typical constant potential amperometry response.

2.3.3 Rotating Disc Voltammetry

The kinetic and mass transport contribution to the measured current can be separated and examined by essentially controlling the mass transport to the surface through controlled rotation of the electrode. For a reaction such as the complex nitrate reduction reaction where mixed electron and mass transport controls are likely this technique can give useful insight. The rotating disk electrode apparatus was a Princeton Applied Research Model 636 Ring-Disk Electrode System. Rotating disc voltammetry (RDV) is similar to CV in that the potential of the working electrode is swept between two chosen potential limits and the change in current is monitored. However, it differs significantly because the working electrode itself is rotated about its own axis. The rotating disc electrode (RDE) consists of a flat disc of suitable electrode material, in this case GC, centrally embedded in a rod of insulating material. It is attached to a motor by a rotating shaft and subsequently immersed in the electrolyte solution and rotated at a certain frequency, f , where the angular frequency (s^{-1}) is, $\omega = 2\pi f$. A schematic representation of the set-up is shown in Figure 2.6. The current is measured as a function of potential and the resulting voltammograms generally exhibit a sigmoid shaped wave, Figure 2.7, at a sufficiently fast rotation rate.

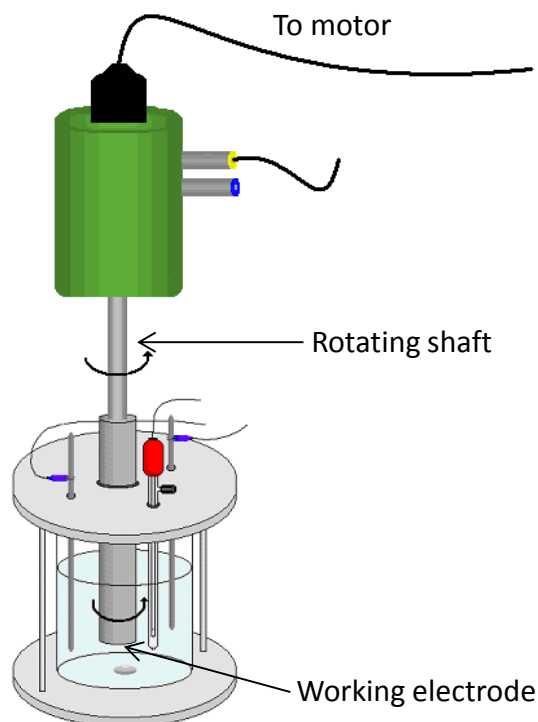


Figure 2.6: Schematic representation of the experimental set-up for rotating disc voltammetry.

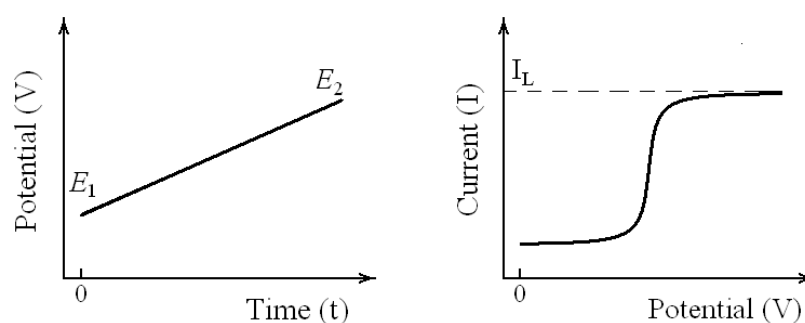


Figure 2.7: Typical rotating disc voltammetry response.

The rotation causes a controlled flux of solution towards and perpendicularly to the electrode surface, which is then radially and evenly distributed on the disk; Figure 2.8(a) and (b). The layer of solution adjacent to the surface of the electrode behaves as if it was stuck to the electrode and appears from the perspective of the rotating electrode to be motionless. The thinner the stagnant layer the faster the analyte can diffuse across it and become quickly oxidised or reduced leading to higher currents. The thickness of the stagnant layer, δ in cm, is inversely

proportional to the square root of the angular frequency, $\omega^{1/2}$, Equation 2.3. And so in general, faster rotation makes the stagnant layer thinner.

$$\delta(\omega) = 1.61 \frac{D^{1/3} \nu^{1/6}}{\omega^{1/2}} \quad 2.3$$

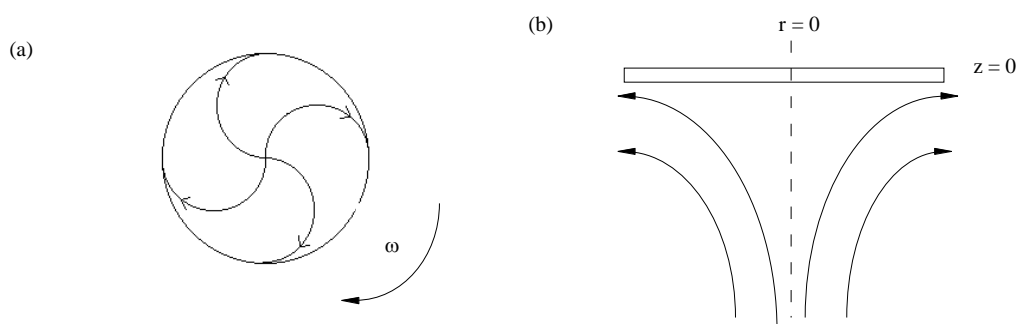


Figure 2.8: Schematic showing the flow pattern from (a) below and (b) a side view.

It is this high rate of mass transport that results in the sigmoid shaped wave. If the rotation rate is not sufficiently fast, voltammograms resembling those of CV are obtained. When the observed current using RDV is limited by diffusion only with no complications due to sluggish kinetics or coupled reactions the voltammograms will be sigmoidal in shape regardless of rotation rate and the limiting current can be related to the rotation rate of the electrode using the Levich equation, Equation 2.4.

$$i_L = (0.62)nFAD^{2/3}\omega^{1/2}\nu^{-1/6}C_o \quad 2.4$$

Where i_L is the limiting current (A), n is the number of electrons transferred, F is the Faraday constant (96485 C mol⁻¹), A is the electrode area (cm²), D is the diffusion coefficient (cm² s⁻¹), ω is the angular frequency, ν is the kinematic viscosity (0.01 cm² s⁻¹) and C is the concentration of the reactant in the solution (mol cm⁻³). It can be seen from this equation that the diffusion coefficient is linearly dependant on the square root of the rotational speed and the limiting current. Therefore, a plot of i_L versus $\omega^{1/2}$ yields a linear plot for a mass transport controlled reaction and the diffusion coefficient can be calculated from the slope of the line. Deviations from linearity and an intercept that doesn't pass through zero is an indication of a reaction having sluggish kinetics and possible coupled chemical reactions.

When there is a kinetic element to the reaction, an extension of the Levich equation, called the Koutecky-Levich Equation, Equation 2.5, can be used to extract the heterogeneous rate constant, i_k , from the intercept.

$$\frac{1}{i} = \frac{1}{i_k} + \frac{1}{0.62nFAD^{2/3}\omega^{1/2}\nu^{-1/6}C} \quad 2.5$$

The parameters are as described above. By extrapolating what the limiting current would be at infinitely high rotation speeds i.e. the y-intercept, one can extract the rate constant, k_0 (cm s⁻¹) from a plot of $1/i$ as a function of $1/\omega^{1/2}$ where the intercept is $1/i_k$. k_0 is related to i_k through the following relationship, Equation 2.6.

$$i_k = nFAk_0C \quad 2.6$$

For the purpose of this study, RDV was used to evaluate the diffusion coefficient and the heterogeneous rate constant for nitrate at the modified electrode under study.

2.3.4 Ultraviolet-Visible Spectroscopy

Ultraviolet-Visible (UV-Vis) spectroscopy is a very useful analytical technique as it can be used to determine very low concentrations of an analyte in a solution by applying the Beer-Lambert law, Equation 2.7,

$$A = \epsilon bc \quad 2.7$$

where, A is the absorbance, ϵ is the extinction coefficient, b is the path length and c is the concentration of the absorbing species. The wavelength at which a material or chemical absorbs light is a function of its electronic structure and also, in the case of colloidal nanoparticles, it's related to the size and size distribution of the particles. A Varian Cary series spectrophotometer was used for all the analysis and a 1 cm wide quartz crystal cuvette was employed. For the purpose of this study, UV-Vis spectroscopy was employed to investigate the concentration, size distribution and stability of the PVP-protected silver nanoparticles.

2.3.5 Infrared Spectroscopy

In this research infrared (IR) spectra were recorded as KBr discs using a Perkin Elmer system FT-IR spectrometer. Samples were finely ground with a pestle and mortar with dry KBr and pressed into a disc under 10 tonne of pressure.

The position of the IR band is specified by its wavelength (λ) and is given by its reciprocal, wavenumber in cm^{-1} . The normal range of IR frequency used is between 4000 and 400 cm^{-1} . Absorption of IR energy causes vibrational energy changes within the molecule in the form of bending and stretching motions. A dipole must be present in the covalent bond for a compound to be IR-active as absorption of IR energy causes oscillation in the dipole moment that are related to specific vibrational modes. The absorption intensity is also proportional to the square of the dipole moment. These vibrational modes correspond to distinct energies and are specific for each functional group and the overall spectrum may be used as a unique fingerprint of a compound. The vibration between two atoms can be approximated by Hooke's law. In this approximation, two atoms and the connecting bond are treated as a simple harmonic oscillator, where the frequency

depends on two quantities, the masses of the atoms and a force constant (i.e. the stiffness of the bond) as given by Equation 2.8.

$$v = \frac{1}{2\pi} \sqrt{\frac{k}{m}} \quad 2.8$$

Where v is the frequency of the vibration, k is the force constant and m is the mass. This explains why heavier atoms vibrate slower than lighter ones and how bonds with a higher degree of saturation vibrate at higher wavenumbers.

2.3.6 Scanning Electron Microscopy and Energy Dispersive X-Ray

Analysis

The scanning electron microscope (SEM) is a microscope that uses electrons rather than light which interact with objects to form an image. It is routinely used to generate high-resolution images of objects to reveal information about morphology and topography. In order to generate such images, the surface of the sample under investigation is bombarded with a high energy beam of electrons (primary electrons) under high vacuum. In response, electrons from the sample (secondary electrons) are emitted and are attracted and collected by a positive detector which amplifies, analyses and translates the electrons into an image. The SEM consists of an electron-optical column mounted on a vacuum chamber ⁽⁶⁾. The gun, placed on top of the column, is typically a thermionic cathode made of tungsten that emits electrons. The electrons are pushed down into the column by an accelerating voltage ranging from 1 to 30 kV. Magnetic lenses and scan coils are used to focus and scan the electron beam on the specimen. The pressure in the specimen chamber is 10^{-3} - 10^{-5} Pa ($\sim 10^{-7}$ mmHg). The specimen is placed on a stage that can move with nanometric precision along the x, y and z axis.

The interaction of the high-energy electrons with the sample generates different types of signals categorized into two groups depending on whether they are generated by elastic or inelastic interactions ⁽⁷⁾. The elastic scattering results from the deflection of incident electrons by atomic nuclei or shell electrons

with similar energy. This, in turns, results in backscattered electrons (BSE) with negligible energy loss and scattering angles larger than 90° . The inelastic scattering results from interactions of the incident electrons with the nuclei and core electrons of the material, and generates signals with substantial energy loss transferred to the sample. Secondary electrons (SE), Auger electrons, X-ray emission and cathodoluminescence belong to this group. The incident beam has a characteristic penetration volume in the sample and each signal originates from a different part of it, Figure 2.9. The BSE electrons have high enough energy (> 50 eV) to emerge from underneath the sample surface. Images made from BSE electrons are characterized by Z contrast, *i.e.*, the brightness of the elements is proportional to the atomic number (Z) as the backscattering yield increases with increasing Z. The resolution of these images is of the order of $1\ \mu\text{m}$ because of the high energy of the BSE electrons. The SE electrons have low energy (< 50 eV) and consequently carry topographical information of the sample surface. The low energy of SE electrons allows a resolution of about 10 nm. Auger electrons are emitted from atoms ionized by the incident electron beam and their energy is characteristic of the elements. The energy of Auger electrons is very low and the resultant escape depth is only of a few nanometres.

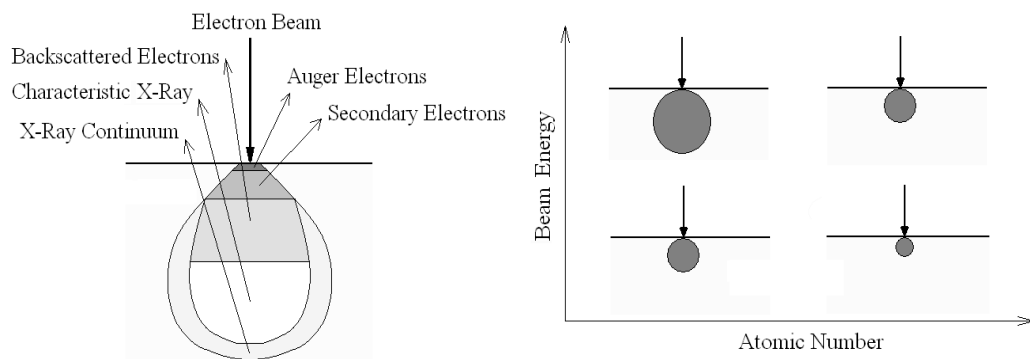


Figure 2.9: Schematic representation of the electron-material interaction in scanning electron microscopy (SEM). (a) Section of the volume of interaction of the electron beam with the sample surface and corresponding areas from which all the different signals originate. (b) Size of the interaction volume as a function of atomic number of the elements in the sample and the energy of the electron beam.

The characteristic X-ray signal is used to perform the chemical microanalysis of the sample surface. This technique is called energy dispersive X-ray (EDX) analysis and is discussed later in greater detail. Cathodoluminescence is produced through electron relaxation emitting infrared, visible and ultraviolet photons. Such a signal can be collected and elaborated to give images with a resolution of 50 nm (7).

The large majority of SEM images are obtained from SE electrons. The image formation is performed by a device made of three components namely a scintillator, a light pipe and a photomultiplier tube. The scintillator converts the SE electrons into light, the light is collected by a light pipe which conveys it into a photomultiplier tube, and here the light is converted back into electrons. The electrons are eventually converted to a visual signal displayed on a cathode ray tube. The brightness and contrast of the image generated are directly dependent on the surface topography, Figure 2.10. The yield of the SE electron emission from the specimen is also dependent on the atomic number of the component in the sample; low atomic number elements naturally emit low yields of SE electrons when excited by an electron source.

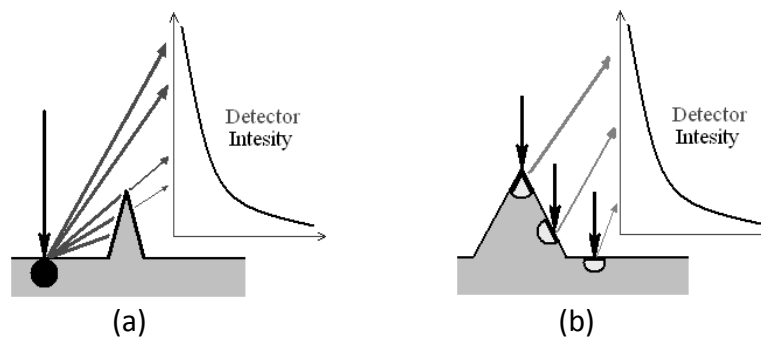


Figure 2.10 Schematic illustration of the effect of surface topography and detector position on the detection of secondary electrons (SE). (a) Effect of surface roughness on the intensity of the collected signal. An obstructing tip is placed in between the beam spot and the detector, the SE electrons emitted behind the tip are gradually absorbed giving the image its 3D appearance. (b) Effect of the emission region on the intensity of the collected signal. The beam focused on the top of the tip has a higher exposure and consequently a more intense associated signal.

Charging phenomena at the surface of non-conductive samples can interfere with the emission of SE electrons. Therefore, in order to improve the yield of SE emission and the surface conductivity, the samples are typically sputter coated with a thin layer of a noble metal, *e.g.*, Au (10 nm).

Energy dispersive X-ray analysis (EDX) is carried out in combination with SEM. EDX allows the localized micro-elemental analysis of the top few micrometres of the sample. X-ray signals are generated when the high-energy electron beam hits the sample surface. A characteristic X-ray signal is produced from the interaction of a beam electron with an inner shell electron of the sample. The inner electron is ejected and replaced by an outer shell electron. This process requires the emission of X-rays with energies corresponding to the energy separation of the levels involved in the electronic transition. Since each element has its characteristic orbital energies, the X-rays emitted by the sample are linked to its chemical composition. An X-ray continuum is also generated through the deceleration of the beam electrons which gives the broad background signal present in all EDX spectra, also referred as Bremsstrahlung. This background has much lower intensity than the elemental peaks and does not represent an issue in the qualitative analysis of the samples.

The transitions involved in the characteristic X-ray emission are labelled after the K, L, M, N electronic shells. The EDX lines are also named α , β or γ depending on which outer shell electrons make the transition to fill the electron vacancy. Transitions of electrons immediately after the emptied level are α , the following level are β and γ in order of increasing energy. An EDX spectrum consists of a series of peaks placed at specific energies depending on the chemical element and with intensity proportional to the number of counts. The number of counts is proportional to both the amount of chemical element in the sample and to the energy carried by the associated X-ray signal. X-rays of higher energy give more intense peaks. This is connected with the working principle of the EDX detectors. The energy of the incoming X-rays is measured in terms of the amount of 'ionization' produced in the detector material. The most common detectors are based on a semiconductor p-n junction where the number of hole/electron pairs

generated by the incoming X-ray signal is roughly the number of times the band-gap fits with the energy carried by the signal. The two main types of detector are the lithium-drift silicon detector, Si(Li), and the silicon drifted detector, SDD. The advantage of the latter is that it does not need to be cryogenically cooled using liquid nitrogen.

The resolution of the EDX probe is given by the size of the volume of interaction of the electron beam with the sample. The size is usually a few microns. Smaller probing spots are achievable at lower energy and with highly collimated beams (feasible conditions with Field-Emission Scanning Electron Microscopes).

The EDX qualitative and quantitative analysis is mainly affected by the surface roughness, Figure 2.11 ^(8,9). The interaction of the BSE electrons with the surrounding zones of the probed point (the beam spot) can cause the emission of X-rays that add up to the signal belonging to the point of analysis. The extent of such interference is a major limitation that affects the quantitative analysis. A quantitative EDX analysis is practicable only with high-quality flat-polished sample surfaces, and it must be performed against a known standard prepared and analysed in the same way. Quantitative analysis is possible by comparison of relative peak heights of the sample and a standard of known composition measured under the same conditions. However various correction factors due to matrix effects must be taken into account in order to obtain reliable data ^(8,9). These correction factors are related to atomic number (Z), absorption (A) and fluorescence (F) effects and are corrected by using a characteristic ZAF factor which correlates the intensity of the peak to the concentration of the element.

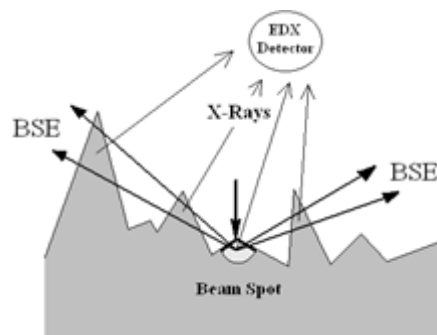


Figure 2.11 Schematic illustration of the effect of the surface roughness on the detection of the X-ray signal. The interaction of the backscattered electrons (BSE) with the surrounding roughness causes the acquisition of a mixed signal by the EDX detector.

2.3.7 Measuring Nanoparticle Size

In order to calculate the size, density and surface area of the electrodeposited nanoparticles and therefore the current density of the nitrate signal, the Java based program ImageJ version 1.45j for Window 7 was utilised. ImageJ is a cross-platform image analysis tool developed by the US NIH. ImageJ can calculate area and pixel value statistics of user-defined selections and intensity threshold objects such as SEM images. The data generated can be used to create size distribution histograms and percentage surface coverage by the particles. ImageJ was used to process SEM images from 6 random sites on a sample and this data was combined and assumed to represent the whole surface of the GC electrode modified with silver particles. The SEM images and hence ImageJ view only the topography of the particles, therefore are viewed as 2D circles, area of πr^2 rather than the hemispherical shape that they most likely are, area $2\pi r^2$. This adjustment of the area data collected by ImageJ is easily achieved using Microsoft Excel.

2.3.8 Instrumentation, Software and Ancillary Equipment

Potentiostatic and CV experiments were carried out using one of two potentiostats; a Solartron (Model SI 1287) or a CHI440 instrument (Model EA160). In the case of the Solartron Potentiostat Model 1287, the electrochemical experiments were performed using Scribner Associates Corrware for windows Version 2.1. The resulting data in all cases were analysed using Scribner Associates CorrView Version 2.3a. CHI440 software Version 2.06 was used to analyse the data generated by the Chi440 instrument. During CPA experiments, the working electrode was rotated using the Princeton Applied Research Model 636 Ring-Disc Electrode System apparatus. UV-Vis spectroscopy was performed in a Varian Cary 50 UV-Vis spectrometer while Infrared scans were performed in a Bruker spectrometer. The SEM and EDX analysis was performed on a Hitachi SEM model S-3200N which was fitted with an Oxford instruments EDX system with a PentaFET Precision INCA X-act detector. General analysis of data and plotting of calibration graphs were performed in Microsoft Excel 2010. An overview of the ancillary equipment used throughout this study is given in Table 2.2.

Table 2.2. Ancillary equipment used with model information

Equipment	Model
Sonicator	Branson 1510
Electronic Balances	Sartorius Models TE612 and TE124S
pH Meter	Orion Model 720A
Conductivity Meter	Jenway 4510
Gold Sputter Coater	Emitech K550x / Agar Scientific

2.4 Chemicals and Synthesis

For all the reagents the highest analytical grade possible was purchased. The chemicals used throughout this study were purchased from Sigma-Aldrich or its subsidiary company Fluka. All chemicals were used as supplied and all solutions were made with distilled water unless stated otherwise. Lithium perchlorate (LiClO_4) was used as a supporting electrolyte for much of this work. This compound was handled with extreme care due to its potentially explosive nature.

2.4.1 Chapter 3 – Electrochemical Synthesis of PVP-Protected Silver Nanoparticles and Their Immobilisation in a Hydrogel Matrix

2.4.1.1 Electrochemical Synthesis of PVP-Protected Silver Nanoparticles

The electrochemical synthesis of poly(N-vinylpyrrolidone) (PVP) protected silver nanoparticles was carried out using a procedure similar to that employed by Yin and co-workers ⁽¹⁰⁾. The voltammetric characterisation was carried out in a conventional three electrode cell where a 4 mm platinum disc electrode served as the working electrode and a platinum and silver wire served as the counter and reference electrode, respectively. A three electrode cell was also employed for the synthesis of the PVP-protected silver nanoparticles but with two platinum sheet electrodes, 1 x 5 cm, serving as the working and counter electrode and a silver wire as a reference electrode. The electrodes were cleaned as outlined in Section 2.2.3 before being placed in a solution containing various amounts of PVP dissolved in 10 mL of $5 \times 10^{-3} \text{ mol dm}^{-3} \text{ AgNO}_3$ and $0.1 \text{ mol dm}^{-3} \text{ KNO}_3$. The PVP content was expressed in g dm^{-3} and had an average molecular weight of 40,000. The electrolysis was carried out using various electrochemical techniques, namely potentiostatic and galvanostatic, for either a fixed amount of time or until a certain total charge had passed. Details are outlined in the results and figure captions. The solution was under constant agitation using a stirring bead and magnetic stirring plate during the electrolysis to aid the flux of silver ions to the electrode surface and to avoid the formation of flocculates that can form in the vicinity of the cathode when the nanoparticle concentration is high.

2.4.1.2 UV-Vis Spectroscopy of PVP-Protected Silver Nanoparticle Solution

The silver nanoparticle solution was placed in a 1 cm diameter quartz cuvette either undiluted or diluted with deionised water. In most cases, the solution required dilution as the absorption intensity was very high. The dilution factor is specified in the relevant result section and figure caption.

For the experiments which monitored the effect of added salts on the stability or aggregation of the PVP-protected silver nanoparticle, the suspension of nanoparticles were diluted 120 times in deionised water. To 2.85 mL of this solution 0.15 mL of either 0.1 mol dm⁻³ AgNO₃ or KNO₃ was added to give a final 3 mL solution containing 5 x 10⁻³ mol dm⁻³ of the added salt. This solution was introduced into 1 cm diameter quartz cuvette and the absorbance monitored over 1 month. All solutions were stored in a sealed vial covered with tinfoil and away from light.

2.4.1.3 Immobilisation of PVP-Protected Silver Nanoparticles onto a Glassy Carbon Electrode for the Electrochemical Detection of Nitrate

A polished 4 mm diameter glassy carbon electrode was polished as outlined in Section 2.2.3. The electrode was then suspended for 12 hours in a PVP-protected silver nanoparticle solution which had been synthesised potentiostatically at an applied potential of -6 V until a charge of 180 C was reached from an aqueous solution containing 0.05 mol dm⁻³ AgNO₃, 0.1 mol dm⁻³ KNO₃ and 423.75 g dm⁻³ PVP. After 12 hours, the electrode was air dried until all solvent had evaporated before being placed in a nitrate-containing solution to test for its ability to perform as an electrochemical sensor.

2.4.1.4 Polyacrylamide-PVP-Protected Silver Nanoparticle Composite

2.4.1.4.1 Polyacrylamide-PVP-Protected Silver Nanoparticle Composite Synthesis

The polyacrylamide-PVP (PAAm-PVP) and the polyacrylamide-PVP-protected silver nanoparticle (PAAm-PVP-Ag-np) composites were prepared by dissolving acrylamide monomer (AAm) and N,N'-methylenebisacrylamide (MBA) in 10 mL of water. The solution was purged for 10 minutes with nitrogen to remove any dissolved oxygen. To this, either 10 mL of a 423.75 g dm⁻³ PVP solution in water, also purged for 10 minutes, was added to make the PAAm-PVP hydrogels or for the PAAm-PVP-Ag-np composites, 10 mL of the PVP-protected silver nanoparticle solution which had been synthesised potentiostatically at an applied potential of -6 V until a charge of 180 C was reached from an aqueous solution containing 0.05 mol dm⁻³ AgNO₃, 0.1 mol dm⁻³ KNO₃ and 423.75 g dm⁻³ PVP. To initiate polymerisation, 300-400 µL of a freshly made 1% ammonium persulfate aqueous solution and 5-10 µL tetramethylethylenediamine (TEMED) were added with vigorous mechanical stirring.

2.4.1.4.2 Polyacrylamide-PVP-Protected Silver Nanoparticle Composite as an Electrode

The hydrogel electrodes were prepared by casting the gel solution around a 1 mm diameter polished platinum wire. This was achieved by suspending the wire in a 6 mm diameter standard household straw 5 cm in length with a plastic plug at one end. The gel solution was poured into the straw where gelation occurred. Once set the plug was removed and the gel slid from the straw easily. The electrodes were suspended in a large beaker of deionised water for 1 day to extract any unreacted reagents.

2.4.1.4.3 Polyacrylamide-PVP-Protected Silver Nanoparticle Composite for Use as a Heterogeneous Catalyst for the Reduction of 4-Nitrophenol

The components of the gels, once combined, were pipetted into a glass vial 5 cm in height and 1 cm in diameter. This served as the mould for the gels to set at room temperature. Typical gelation occurred within 10 minutes but the composites were left in mould for at least 2 hours to allow complete polymerisation. To remove the

gels from the glass vials the bottom of the glass tube was cut with a grinding wheel allowing the gel cylinder to be easily slide out to the tube intact. The gel cylinder was then cut using a sharp razor blade into uniform discs 3 mm in length. The discs once rinsed, were ready for use in subsequent experiments.

4-Nitrophenol and NaBH_4 solutions were freshly made for each experiment and degassed with N_2 for 10 minutes prior to initiating the reduction reaction. The number of discs per volume of solution was kept constant for each run and magnetically stirred at the same RPM as this affected the rate of the reaction. To monitor the rate of the reduction reaction three fully swollen discs were added to a solution containing 3 mL of $1.2 \times 10^{-4} \text{ mol dm}^{-3}$ 4-nitrophenol and 6 mL of 0.1 mol dm^{-3} NaBH_4 , in other words 3 discs in 9 mL of $4 \times 10^{-5} \text{ mol dm}^{-3}$ 4-nitrophenol and $6.7 \times 10^{-2} \text{ mol dm}^{-3}$ NaBH_4 .

2.4.1.5 Biological Preparation for Anti-Bacterial Testing

The potential anti-bacterial activity of the PAAm-PVP and PAAm-PVP-Ag-np composites were tested against five different strains of bacteria, namely (a) *Staphylococcus aureus* (*S. aureus*), (b) methicillin-resistant *Staphylococcus aureus* (MRSA), (c) *Pseudomonas aeruginosa* (ATCC 27853), (d) *Pseudomonas aeruginosa* (ATCC 10145) and (e) *Escherichia coli* (*E.coli*). All anti-bacterial testing was carried out in the Medical Mycology Lab, Department of Biology, Maynooth University under the direction of Dr. Kevin Kavanagh.

2.4.1.5.1 Chemicals for Bacterial Biological Preparations

Chemicals were purchased from commercial sources and were used without further purification. Deionised water was used to prepare all media. The nutrient broth medium containing peptone, yeast extract and nutrient agar were purchased from Scharlau Microbiology and prepared following the manufacturer's instructions in sterilised water (13 g in 1 L of deionised water). *E.coli* was supplied as a clinical isolate by the Clinical Microbiology Laboratory, St. James' Hospital, Dublin, Ireland and were originally isolated from a gastro-intestinal tract infection. *S. aureus* was supplied as a clinical isolate by the Clinical Microbiology Laboratory,

St. James' Hospital, Dublin, Ireland and were originally isolated from a urinary tract infection. MRSA was obtained as a clinical isolate from Microbiologics, North St. Cloud Mn, USA and was originally isolated from a wound infection. *P. aeruginosa* 27853 and 10145 were both obtained from the American Type Culture Collection (ATCC) Marassas, VA, USA.

2.4.1.5.2 Sterilisation

Sterilisation of the microbiological equipment and media was carried out in a Dixons ST2228 autoclave at $121 \pm 2^\circ \text{C}$ and 124 kPa for 20 minutes. All worktops and benches were sterilised by washing with 70 % (v/v) ethanol/water prior to use. Agar plates were prepared in a laminar flow hood and the plates were streaked in an aseptic area around a Bunsen burner.

2.4.1.5.3 Cell Density

Bacterial cell density was recorded at an optical density of 600 nm (OD600) using an Eppendorf BioPhotometer.

2.4.1.5.4 Procedure for Bacterial Biological Preparations

The *in vitro* antimicrobial activity of the PAAm-PVP-Ag-np composite was investigated against both Gram-positive and Gram-negative bacteria. All bacteria were grown on nutrient broth agar plates at $37 \pm 1^\circ \text{C}$ and maintained at $4 \pm 1^\circ \text{C}$ for short term storage. Cultures were routinely sub-cultured every 4-6 weeks. The five different bacteria were grown overnight to the stationary phase in nutrient broth at $37 \pm 1^\circ \text{C}$ and 2000 rpm. The cells were diluted to give an OD600 = 0.05 and streaked onto the agar plates. The plates were incubated for 1 hour at $37 \pm 1^\circ \text{C}$. The hydrogel discs were then placed on the plates and incubated for a further 24 hours at $37 \pm 1^\circ \text{C}$ before the zones of inhibition around the discs were measured.

2.4.1.5.5 Measuring the Zones of Inhibition

To determine the zone of inhibition (ZOI), the diameter of the disc and the diameter of the disc plus the zone itself were measured in mm. Then, using the area of a circle, $A = \pi r^2$, the area of the disc was subtracted from the total area of inhibition to give the area, in mm^2 , of the zone of inhibition ⁽¹¹⁾.

2.4.2 Chapter 4 – Silver Particles Electrochemically Deposited on a Glassy Carbon Electrode for the Electrochemical Detection of Nitrates

2.4.2.1 Electrodeposition of Silver Nanoparticles on a Glassy Carbon Electrode

The silver nanoparticle modified glassy carbon electrode (Ag-np-GC) was formed by immersing a clean GC electrode in an aqueous solution containing $0.001 \text{ mol dm}^{-3} \text{ AgClO}_4$ in $0.1 \text{ mol dm}^{-3} \text{ LiClO}_4$. Firstly, a potentiostatic oxidative pulse of +1 V for 15 mins was applied in order to clean the surface and removed any intercalated silver that may be on the GC surface from previous experiments ⁽¹²⁾. The electrode was then allowed to rest at open circuit potential for one hour. The next step, the electrodeposition step, was varied in duration and magnitude in an attempt to find the ideal experimental conditions to generate uniformly deposited particles with a narrow size distribution and high density surface coverage. Details of these variations will be discussed in the results chapter.

2.4.2.2 Lead Underpotential Deposition at a Bulk Silver and a Silver-Modified Glassy Carbon Electrode

Lead underpotential deposition (UPD) was carried out on a freshly polished 2 mm bulk silver electrode, a 4 mm bare glassy carbon electrode and a 4 mm glassy carbon electrode decorated with silver particles that had been electrochemically deposited as described in Section 2.4.1.1. A Pt wire and a SCE electrode were used as the counter and reference electrode respectively. The lead deposition solution contained either 1 or 10 mmol dm^{-3} of lead(II) chloride in $0.1 \text{ mol dm}^{-3} \text{ HCl}$. Details of scan rate and potential window are outlined in the text and figure captions. The charge associated with the anodic lead stripping peak was calculated by integrating under the curve using the integration function in the CorrView programme. The potential limits were determined, by eye, to be where the current started to increase above the flat background current.

2.4.2.3 Nitrate Detection at a Bulk Silver and a Silver-Modified Glassy Carbon Electrode

CV was primarily used in the analysis of nitrate reduction. In most cases, the modified electrode was first cycled in background electrolyte, $0.1 \text{ mol dm}^{-3} \text{ LiClO}_4$, between -0.2 V and -1.6 V vs. Ag/AgCl for 30 cycles. Where this is not preformed it will be stated in the text. The electrode was then transferred to solutions of various nitrate concentrations (KNO_3 in $0.1 \text{ mol dm}^{-3} \text{ LiClO}_4$) and cycled in the same potential window as the background until a steady state was reached (30 cycles). Any variations in these parameters or solutions will be clearly stated in the text or figure captions. The scan rate used in this study was primarily 50 mV s^{-1} but again was varied to elucidate various kinetic parameters. The contribution from the background charging currents was removed by subtracting the current value in the background scan from the measured current at the peak potential in the nitrate containing solutions. CPA was also employed to access the nitrate limit of detection that could be achieved at the silver-modified GC electrode. The RDV apparatus, as described in Section 2.3.3, was used for this experiment to ensure a constant supply of fresh analyte to the electrode surface and so that a steady state and quick response time could be achieved. Aliquots of $2 \times 10^{-3} \text{ mol dm}^{-3} \text{ KNO}_3$ were added to 25 mL of $0.1 \text{ mol dm}^{-3} \text{ LiClO}_4$ at a rotation speed of 2000 RPM .

2.5 References

1. A.J. Bard, Faulkner L.R., *Electrochemical methods: Fundamentals and Applications*; 2nd ed. ed.; Wiley, 2000.
2. C.M.A. Brett, A.M.O. Brett, *Electrochemistry: Principles, Methods, and Applications*; Oxford University Press, Incorporated, 1993.
3. R. Greef, L.M. Peter, D. Pletcher, J. Robinson, *Instrumental Methods in Electrochemistry*; Horwood Publishing Limited, 1985.
4. C. Brett, A. Brett, *Electroanalysis*; Oxford University Press, 1998; Vol. 64.
5. A.J. Bard, L.R. Faulkner, *Electrochemical methods: fundamentals and applications*; 2nd ed.; Wiley, 2000.
6. M.I. Szykowska In *Encyclopedia of Analytical Science*; Elsevier: 2005.
7. W. Zhou, Z.L. Wang, *Scanning Microscopy for Nanotechnology: Techniques and Applications*; 1st ed.; Springer, 2006.
8. J. Goldstein, D.E. Newbury, D.C. Joy, C.E. Lyman, P. Echlin, E. Lifshin, L. Sawyer, J.R. Michael, *Scanning Electron Microscopy and X-ray Microanalysis*; 3rd ed.; Springer, 2003.
9. N. Kanani, *Electroplating: Basic Principles, Processes and Practice*; Elsevier Science, 2005.
10. B. Yin, H. Ma, S. Wang, S. Chen, "Electrochemical Synthesis of Silver Nanoparticles under Protection of Poly(N-vinylpyrrolidone)", *The Journal of Physical Chemistry B*, **107**, 8898, (2003).
11. S.L. Percival, W. Slone, S. Linton, T. Okel, L. Corum, J.G. Thomas, "The antimicrobial efficacy of a silver alginate dressing against a broad spectrum of clinically relevant wound isolates", *International Wound Journal*, **8**, 237, (2011).
12. A.A. Isse, S. Gottardello, C. Maccato, A. Gennaro, "Silver nanoparticles deposited on glassy carbon. Electrocatalytic activity for reduction of benzyl chloride", *Electrochemistry Communications*, **8**, 1707, (2006).

Chapter 3
**Synthesis and Applications of
PVP-Protected Silver Nanoparticles**

3.1 Introduction

The synthesis of nanoparticles has become one of the most intensely researched topics in chemistry and physics over the last decade. The interest stems from the unique properties that nanoparticles have over their macrosized counterparts. Their small size results in new electrical and optical properties, possibly suitable for a range of electronic and optoelectronic applications ⁽¹⁾. The enhanced properties displayed by nanoparticles have also been explored in the area of sensors and particularly electrochemical sensors ^(2,3). Nanoparticles have been deposited on a wide range of surfaces, from typical electrode materials such as glassy carbon, platinum and gold to modified electrode surfaces such as polymer modified electrodes, metal oxide modified electrodes and self-assembled monolayers. Not only do the nanoparticles give rise to higher surface areas and increased currents but these materials may have catalytic effects on certain redox reactions ⁽⁴⁻⁶⁾. The nanoparticles can be easily electrodeposited on an electrode surface, and they can also be generated as colloidal nanoparticles in solution. Typically, colloidal nanoparticles are synthesised from the metal salts which are chemically reduced using a reducing agent and in the presence of a stabiliser. Electrochemical reduction offers an alternative to reducing agents leading to higher purity, where the applied potential acts as the reducing agent. Also, precise particle size control is possible by adjusting the current density, the applied potential or the concentration of metal salts and protecting agents. The speed of electrochemical synthesis is also an advantage. Large concentrations of uniform sized particles can be generated within minutes without the need for tedious workups.

This chapter is focussed on using electrochemistry to generate colloidal silver nanoparticles. Later the particles are incorporated into a polyacrylamide hydrogel matrix and the possible applications of these materials are investigated. The particles were coated with poly(N-vinylpyrrolidone) (PVP), which acts as a stabiliser, and then incorporated into the polyacrylamide hydrogel. This hydrogel matrix offers a stable and biocompatible support to investigate the potential of these nanoparticles to act as a heterogeneous catalyst for the reduction of

4-nitrophenol to 4-aminophenol. As hydrogels are insoluble in aqueous solutions and yet are highly porous it allows the nanoparticles to come in contact with the 4-nitrophenol molecules. Furthermore, the composite is easily recoverable once the reduction is complete. Because of the biocompatible properties of both polyacrylamide and PVP and also the well-studied activity of silver as an antibacterial agent, the composite material was tested on five strains of bacteria. Finally, the hydrogels were also tested for their ability to act as an electrochemical sensor.

3.2 Experimental

The procedure, materials and equipment used to synthesise the PVP-protected silver nanoparticles and the hydrogel composites are outlined in Chapter 2, Sections 2.2 and 2.4.1.

3.3 Results

3.3.1 PVP and Silver

The method used to synthesis the colloidal silver nanoparticles was previously published by Yin and co-workers ⁽⁷⁾. Here, a novel method to synthesize spherical silver nanoparticles in the aqueous phase is described. The generation of aqueous phase noble metal nanoparticles can be difficult as the metal ions coat the cathode more easily compared to when an organic phase is employed. This method uses PVP as a stabilising agent, also called a protecting agent, for the silver particles as they form. Yin and co-workers found that PVP accelerated the formation of monodispersed silver nanoparticles and lowered the rate of silver deposition on the cathode while allowing for a greater degree of size-control. The structure of PVP is shown in Figure 3.1.

Kim and co-workers ⁽⁸⁾ studied the interaction of various silver salts with PVP and showed, through Raman and IR studies, that silver ions interact with the carbonyl oxygen of the amide group. They also reported the importance the counter anion has on the interaction between PVP and the silver cation.

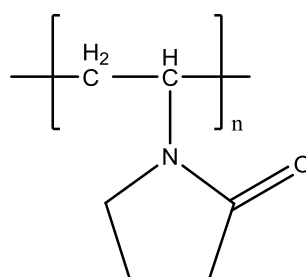


Figure 3.1: Structure of poly(N-vinylpyrrolidone).

A mechanism for PVP protection of silver nanoparticles is outlined in a paper by Zhang and co-workers on the chemical reduction of silver ⁽⁹⁾. Therein, the mechanism of protection was described in three stages. Firstly, the PVP donates lone pairs of electrons to the *sp* hybrid orbitals of silver from an oxygen and nitrogen to form a coordinative complex in solution. Secondly, the enhanced electron density that the silver atom receives from the formation of this complex enhances nucleation, as silver now becomes more readily reduced compared to pure silver ions in water. Finally, the steric hindrance provided by the long alkyl chains of PVP prevents particle agglomeration.

The IR spectrum of both pure PVP and the PVP-protected silver colloids are shown in Figure 3.2. All bands in the spectra occur at the same wavenumber except the C=O stretching absorption. In pure PVP this band occurs at 1663 cm⁻¹ but is red-shifted to 1656 cm⁻¹ in the silver nanoparticle PVP solution. Examples of this shift have been documented in the literature and can be explained by the coordination of silver or other metal ions to the carbonyl oxygen of the amide functionality of PVP ⁽¹⁰⁻¹²⁾. The coordination of silver with the PVP is shown in Figure 3.3. This coordination weakens the C=O bond by drawing electron density from the double bond and therefore shifting the band to a lower frequency.

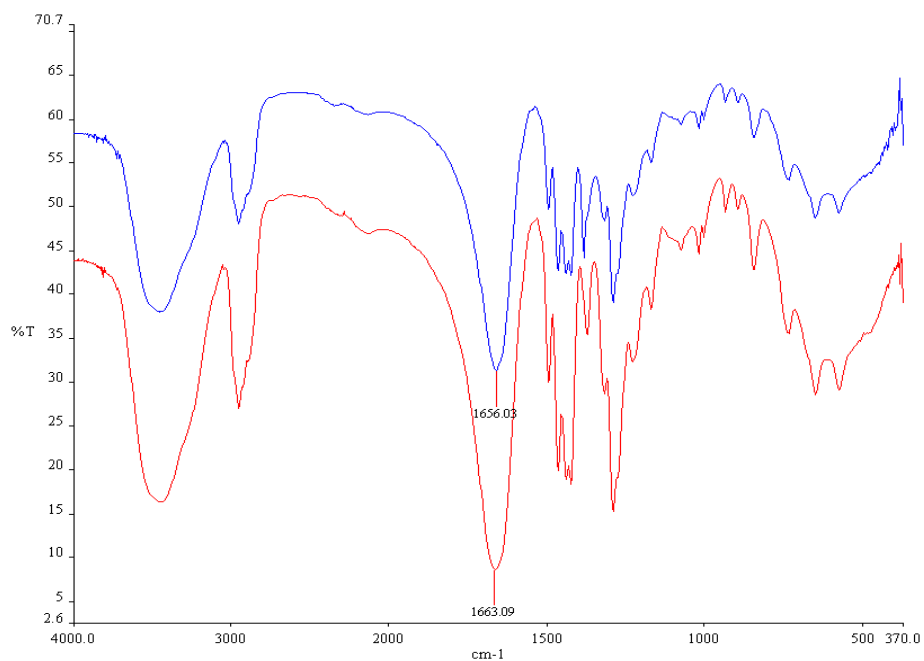


Figure 3.2: FTIR spectra of pure PVP (red trace) and PVP-protected silver colloids (blue trace).

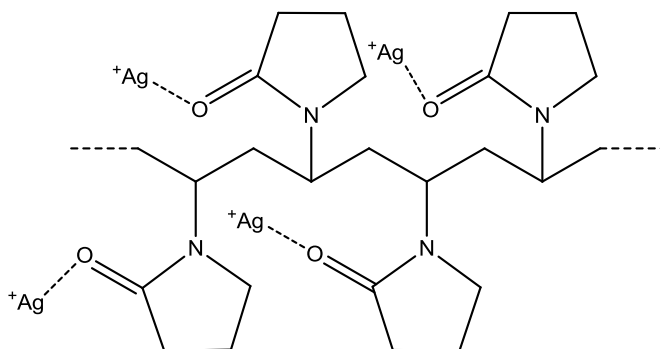


Figure 3.3: Silver ions coordinating to the carbonyl oxygen of PVP polymer chains.

3.3.2 Voltammetric Characterisation of Silver-PVP Solution

The effect of PVP on the electrochemistry of silver ions was investigated. The experimental set up is described in detail in Chapter 2, Section 2.4.1.1. Briefly, a 4 mm platinum disc electrode and a platinum wire were used as the working and counter electrodes, respectively, and a silver wire as a pseudo-reference electrode. The cyclic voltammograms (CVs) of solutions containing $5.0 \times 10^{-3} \text{ mol dm}^{-3} \text{ AgNO}_3$ in $0.1 \text{ mol dm}^{-3} \text{ KNO}_3$, with and without varying amounts of PVP, at a platinum disc electrode were recorded and are shown in Figure 3.4 (cycle 2) and Figure 3.5 (cycle 10). At the beginning of the experiment the voltammograms for all solutions, with and without PVP, have similar profiles as illustrated in Figure 3.4. A peak for the oxidation of Ag to Ag^+ is seen at 0.1 V vs Ag/Ag⁺ and a corresponding peak for the reduction of Ag^+ to Ag is observed at -0.1 V vs Ag/Ag⁺.

Differences begin to become apparent in later cycles, as shown in Figure 3.5. There is a marked difference in the reduction wave between solutions with and without PVP. Electrodeposition of silver occurs more easily on the platinum electrode in solutions containing no PVP as evident by the fact that reduction of the silver ions occurs at a peak potential of -0.10 V vs Ag/Ag⁺, a 33 mV shift with respect to reduction for a PVP-containing solutions, with a peak potential at -0.13 V vs Ag/Ag⁺. Additionally, a much higher oxidation current is observed in the PVP free solution. The peak current for the oxidation of silver varies with the concentration of PVP. Higher peak currents are observed with PVP concentrations of 30 and 40 g dm⁻³. Visually, a layer of silver was seen on the surface of the platinum electrodes. The shift to lower reduction potentials in the presence of PVP is possibly due to the higher viscosity of the solution, which hinders diffusion of the ions to the working electrode, but also by the way the chains of the PVP surround the silver ions further hindering electron transfer, as demonstrated in Scheme 3.2.

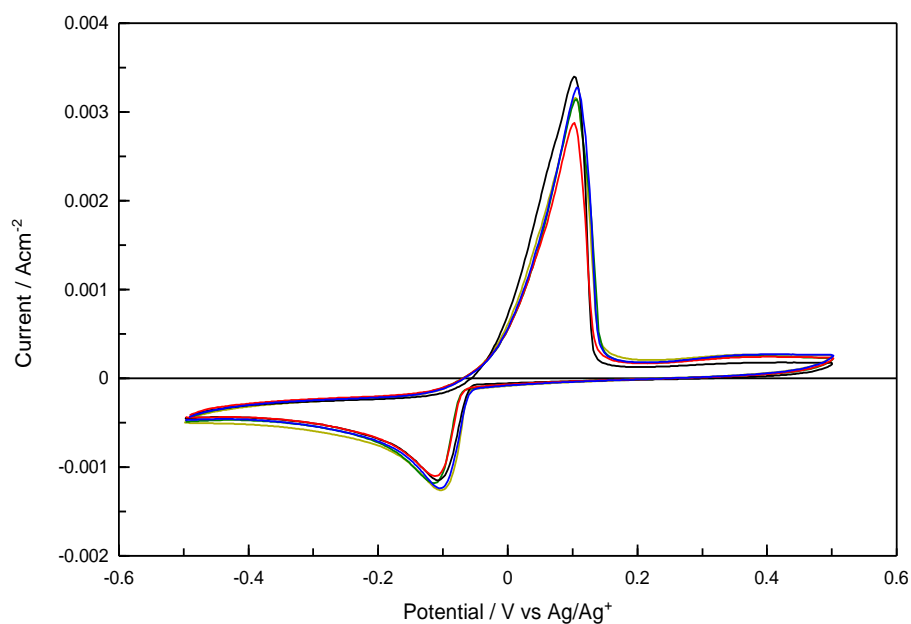


Figure 3.4: Cyclic voltammograms recorded at a scan rate of 20 mV s⁻¹, cycle 2, at a bare Pt electrode in 5.0 x 10⁻³ mol dm⁻³ AgNO₃ in 0.1 mol dm⁻³ KNO₃ with — no PVP, — 15 g dm⁻³ PVP, — 20 g dm⁻³ PVP, — 30 g dm⁻³ PVP, — 40 g dm⁻³ PVP.

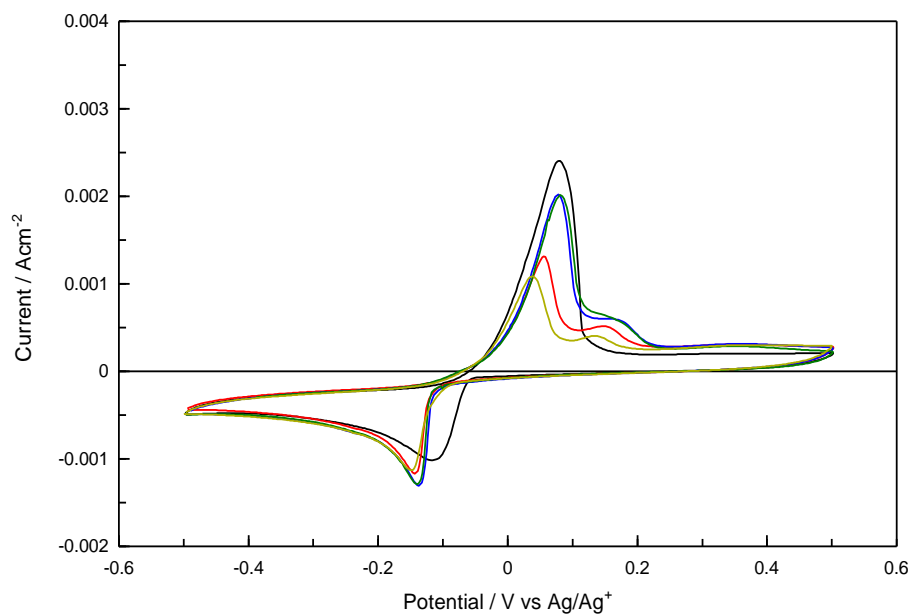
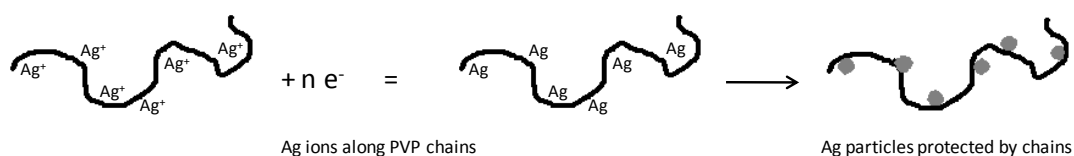


Figure 3.5: Cyclic voltammograms recorded at a scan rate of 20 mV s⁻¹, cycle 10, at a bare Pt electrode in a solution containing 5.0 x 10⁻³ mol dm⁻³ AgNO₃ in 0.1 mol dm⁻³ KNO₃ with — no PVP, — 15 g dm⁻³ PVP, — 20 g dm⁻³ PVP, — 30 g dm⁻³ PVP, — 40 g dm⁻³ PVP.



Scheme 3.2: Schematic diagram demonstrating the interaction between silver and PVP chains.

More notably, upon continuous cycling the oxidation peak of silver at 0.10 V vs Ag/Ag⁺ is dramatically affected by the presences of PVP, Figure 3.5. There is a marked decrease in the magnitude of the current as well as the appearance of a second peak at around 0.15 V vs Ag/Ag⁺ in all PVP-containing solutions. According to Yin and co-workers, the difference in peak oxidation current is attributed to PVP causing silver to be reduced by two different mechanisms ⁽²⁾. The silver is electrodeposited on the platinum electrode surface while in the second mechanism it is reduced as silver nanoparticles protected by PVP. Therefore, upon oxidation, only silver deposited on the electrode surface can be oxidised leading to lower oxidation currents than that observed for PVP-free solutions. In the PVP-free solution, all metallic silver produced during reduction is deposited on the surface and therefore is free to become completely oxidised during the positive sweep, giving rise to a larger oxidation current. Another notable difference is the emergence, with cycle number, of a second oxidation peak at 0.15 V vs Ag/Ag⁺. Figure 3.6 is a CV of PVP in KNO₃ containing no silver, and shows clearly that this second peak is not due to PVP and must be associated with a silver deposit that is more difficult to oxidise. Higher ratios of PVP to silver ion become unfavourable as the solution tends to become very viscous and therefore diffusion of silver ions to and from the surface becomes more difficult. The effect of this is reflected in the oxidation waves in Figure 3.5. Higher ratios of PVP to silver result in higher oxidation currents. Silver reduced in the negative sweep finds it more difficult to diffuse away in the highly viscous solutions to form PVP-protected nanoparticles and instead has a higher probability of depositing on the electrode surface. Different amounts of PVP have little effect on the magnitude of the silver reduction peak, as shown in Figures 3.4 and 3.5.

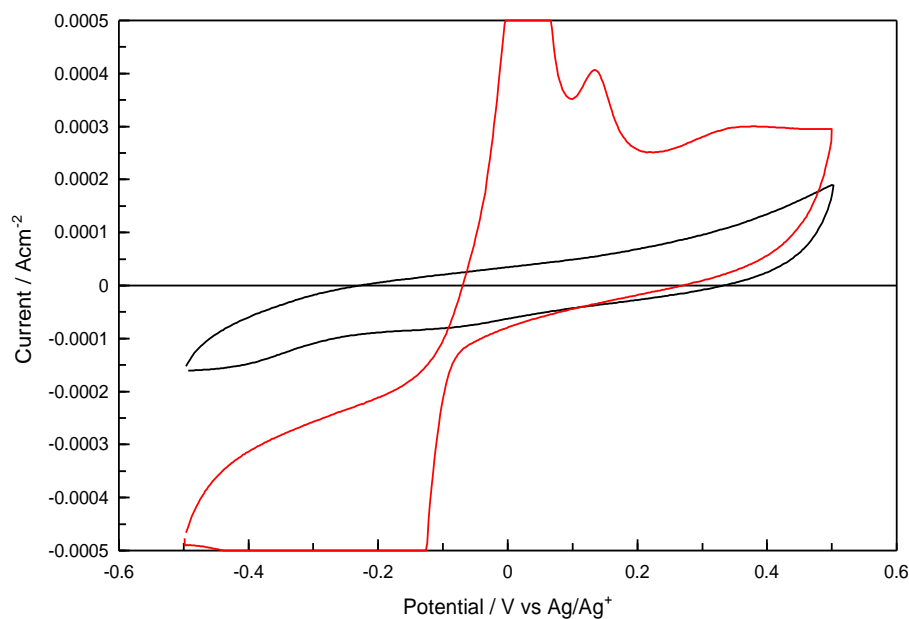


Figure 3.6: Cyclic voltammogram at a bare Pt electrode in a solution containing $0.1 \text{ mol dm}^{-3} \text{ KNO}_3$ and $30 \text{ g dm}^{-3} \text{ PVP}$ — with and — without $5.0 \times 10^{-3} \text{ mol dm}^{-3} \text{ AgNO}_3$. Scan rate of 20 mV s^{-1} .

3.3.3 Electrochemical Synthesis of Silver Nanoparticles

3.3.3.1 Effect of Applied Potential

As outlined in Chapter 2, Section 2.3.1.1, the silver nanoparticles were formed using a three electrode cell containing two $1 \text{ cm} \times 5 \text{ cm}$ platinum sheets which served as the working and counter electrodes and a silver wire as a pseudo-reference electrode. During electrolysis, the solution was constantly stirred to rapidly move newly formed silver clusters away from the vicinity of the cathode. Without stirring, the concentration of nanoparticles at the cathode is very high and the interaction with the PVP chains can lead to the formation of flocculates. Initially, a potentiostatic mode was employed to generate the particles. The applied potential employed by Yin and co-workers⁽⁷⁾ was not mentioned in the paper, so initially experiments were conducted to determine the necessary applied potential needed to generate the nanoparticles. The electrolysis solution contained $5.0 \times 10^{-3} \text{ mol dm}^{-3} \text{ AgNO}_3$ in $0.1 \text{ mol dm}^{-3} \text{ KNO}_3$ with $113 \text{ g dm}^{-3} \text{ PVP}$, giving a PVP to silver ion ratio of 200:1. The applied potential was held for 300 s in each case.

Initially, potentials were chosen close to the reduction peak potential of silver from a PVP solution based on the voltammograms in Figure 3.5. From the voltammograms, reduction begins at around -0.1 V vs Ag/Ag⁺ but the expected stream of a yellow coloured solution from the platinum electrode was not visible even at potentials of -1.0 V vs Ag/Ag⁺. It was only when potentials of -1.5 V vs Ag/Ag⁺ were applied that this stream of yellow particles was observed and the current increased significantly. Figure 3.7 shows a typical current transient for particles generated at a potential of -1.7 V vs Ag/Ag⁺ from a silver-PVP solution over 300 s. Double layer effects are observed in the first few seconds of reduction before the current plateaus and remains reasonably stable. A plot of the applied potential as a function of the current plateau is shown in Figure 3.8. The current remains low until potentials exceeding -1.5 V vs Ag/Ag⁺ are applied after which point the current increases rapidly. The current increase with applied potential and then becomes limited by mass transport effects as the potential is varied from -2.0 V to -4.0 V vs Ag/Ag⁺.

The amount of nanoparticles generated was monitored using UV-Vis spectroscopy. UV-Vis spectroscopy is an effective and easy way to analyse all nanoparticles. Not only can information regarding the concentration of the particles be obtained but it also provides information on the size and size distribution of the particles⁽¹³⁾. In conjunction with monitoring the current generated at each applied potential, the absorption spectrum for the sample was recorded. In some cases, the absorbance was too high and the solutions were diluted. This is indicated in the figure captions.

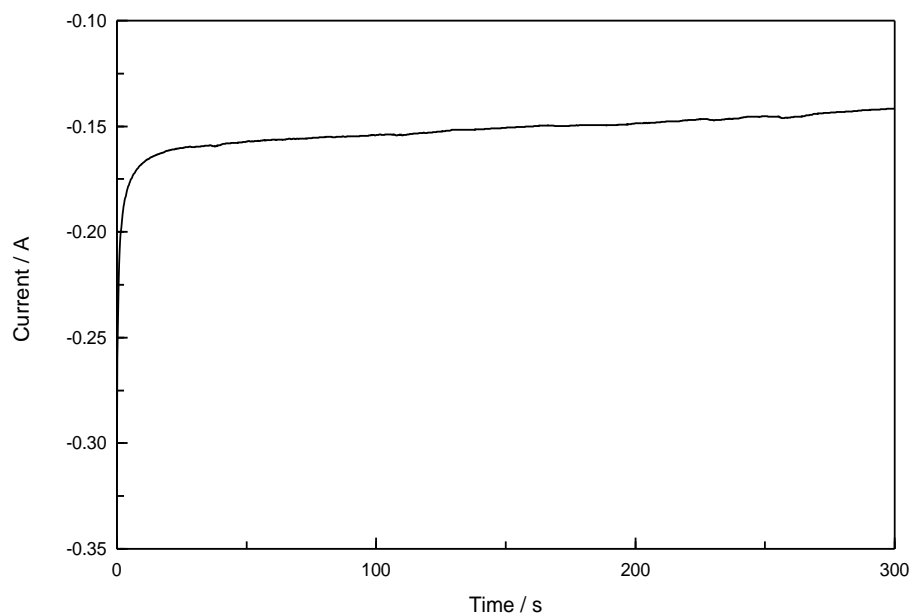


Figure 3.7: Current transients for nanoparticles generated at an applied potential of -1.7 V vs Ag/Ag^+ from a solution of 5.0×10^{-3} mol dm^{-3} AgNO_3 , 0.1 mol dm^{-3} KNO_3 and 113 g dm^{-3} PVP (silver to PVP ratio 200:1).

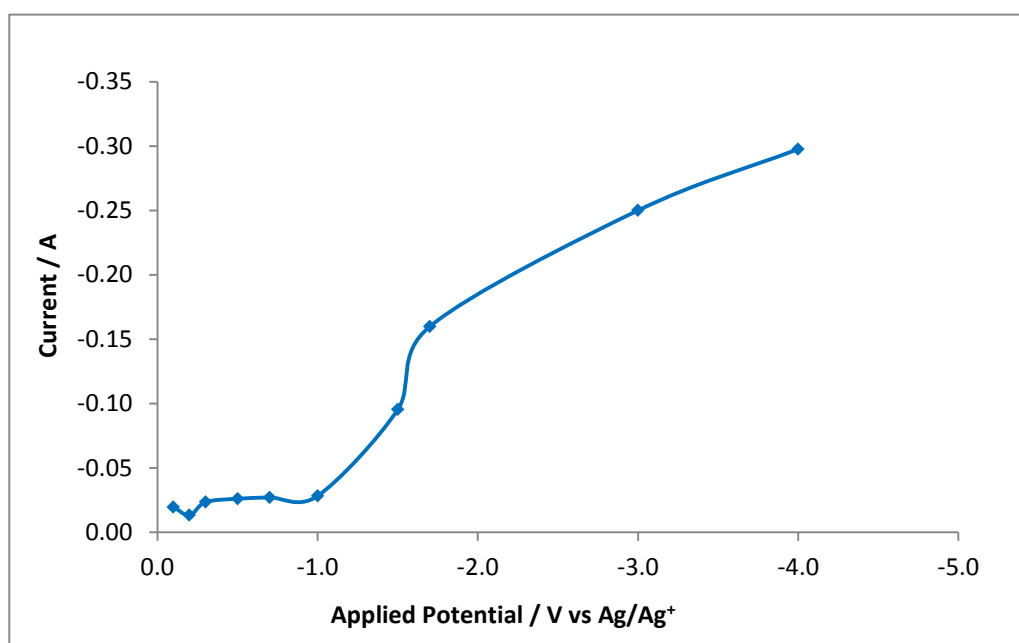


Figure 3.8: Plateau current as a function of applied potential for nanoparticles generated from a solution of 5.0×10^{-3} mol dm^{-3} AgNO_3 , 0.1 mol dm^{-3} KNO_3 and 113 g dm^{-3} PVP (silver to PVP ratio 200:1).

Figure 3.9 shows the absorption spectra of the silver nanoparticle solution (undiluted) generated at applied potentials of -1.6 V to -1.8 V vs Ag/Ag⁺ for 600 s. An absorption band centred on 407 nm is observed and it can be seen that the absorption increases with increasing applied potential. Figure 3.10 is the absorption spectra, 6 times diluted, of particles generated at -4.0 V vs Ag/Ag⁺ for 600 s. Comparing the absorption intensity and taking into account the dilution factor, over 7.5 times more particles are produced at -4.0 V vs Ag/Ag⁺ than at -1.8 V vs Ag/Ag⁺. Clearly, the applied potential is the critical factor in determining the amount of particles formed. Additionally, the band width is narrower for the particles generated at -4.0 V vs Ag/Ag⁺, indicating a smaller size distribution. It is well known that the narrower the peak the more uniform the size distribution of the particles ^(14,15). Larger sized particles give rise to broader peaks and a shift in peak absorbance to longer wavelength, and this can be an indication of particle aggregation if peak broadening is observed over time ⁽¹⁶⁾.

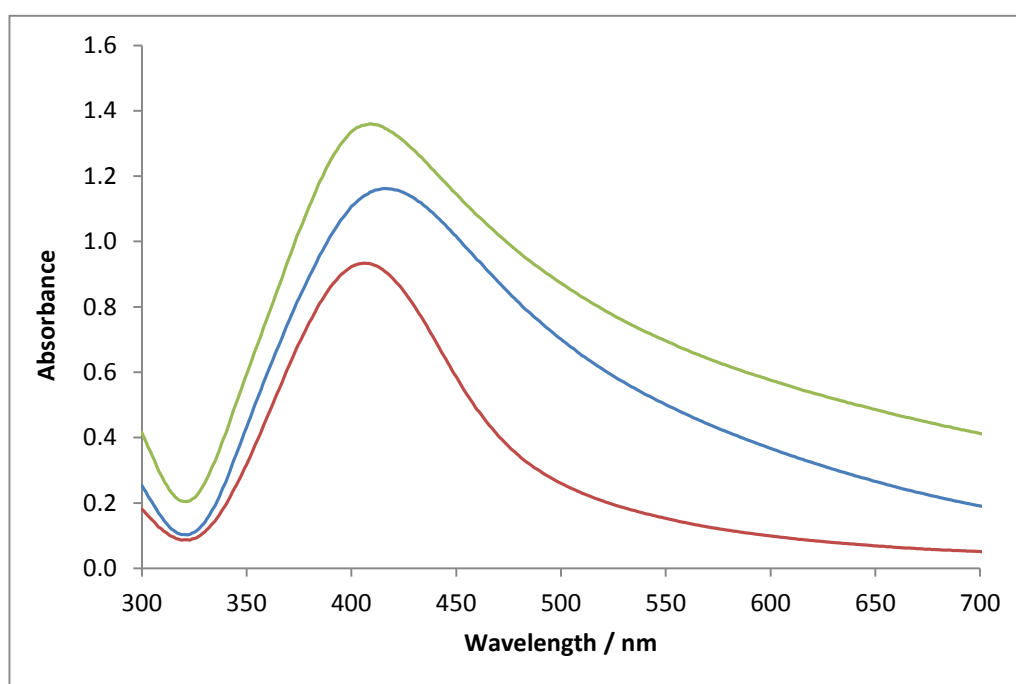


Figure 3.9: UV-Vis spectra of a solution of PVP-protected silver nanoparticles generated from a solution containing $5.0 \times 10^{-3} \text{ mol dm}^{-3} \text{ AgNO}_3$, $0.1 \text{ mol dm}^{-3} \text{ KNO}_3$ and $113 \text{ g dm}^{-3} \text{ PVP}$ (silver to PVP ratio 200:1) after 600 s at different applied potentials, — -1.6 V, — -1.7 V and — -1.8 V vs Ag/Ag⁺.

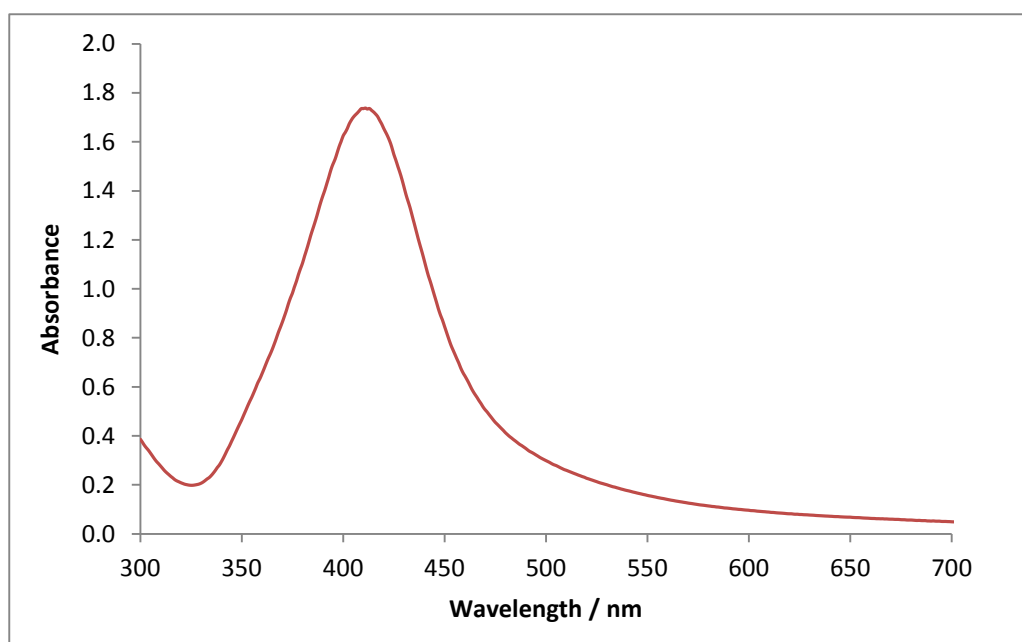


Figure 3.10: UV-Vis spectra of a solution of PVP-protected silver nanoparticles generated from a solution containing $5.0 \times 10^{-3} \text{ mol dm}^{-3} \text{ AgNO}_3$, $0.1 \text{ mol dm}^{-3} \text{ KNO}_3$ and $113 \text{ g dm}^{-3} \text{ PVP}$ (silver to PVP ratio 200:1) after 600 s at $-4.0 \text{ V vs Ag/Ag}^+$. Solution diluted by a factor of 30.

Although at the very high applied potentials of $-4.0 \text{ V vs Ag/Ag}^+$ many more nanoparticles are formed, and reproducibility over fixed pulse durations became an issue. Due to the large amount of hydrogen production at these potentials, coupled with the viscosity of the PVP in solution, bubbling of the solution tended to occur and the current or total amount of charge passed tended to vary between experiments. The experimental approach to generating the particles was explored further by employing other electrochemical techniques. A galvanostatic pulse of -0.3 A , for a fixed amount of time, was investigated as a potentially viable method of reproducibly generating nanoparticle solutions with reasonable success. However, the potential recorded at this fixed current still varied between -5.0 V and $-7.0 \text{ V vs Ag/Ag}^+$ giving rise to different amounts of hydrogen production. A fixed potential approach was revisited in an attempt to control hydrogen production, and reproducibility was achieved by ceasing reduction once a fixed charge had passed rather than limiting reduction to a fixed time. Figure 3.11 is a typical example of the current transient generated by employing such a technique. Reproducibility was achieved by applying $-6.0 \text{ V vs Ag/Ag}^+$ until a total charge of

180 C was reached from a solution comprising $0.05 \text{ mol dm}^{-3} \text{ AgNO}_3$, $0.1 \text{ mol dm}^{-3} \text{ KNO}_3$ and $423.75 \text{ g dm}^{-3} \text{ PVP}$. (As shown in later sections, this corresponds to the optimum solution composition).

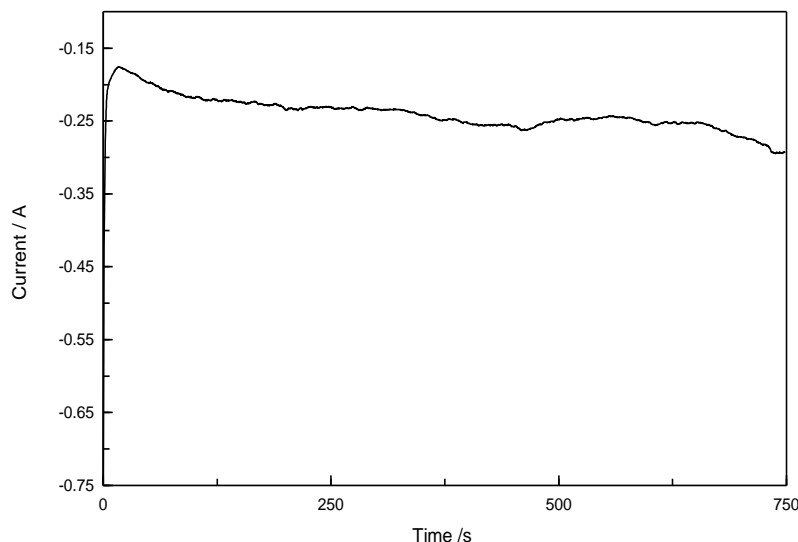


Figure 3.11: Current transients for nanoparticles generated at an applied potential of -6.0 V vs Ag/Ag^+ from a solution containing $0.05 \text{ mol dm}^{-3} \text{ AgNO}_3$, $0.1 \text{ mol dm}^{-3} \text{ KNO}_3$ and $423.75 \text{ g dm}^{-3} \text{ PVP}$ (75:1) until a total charge of 180 C was passed.

3.3.3.2 Effect of Silver Concentration

The effects of varying the silver to PVP ratios were investigated in order to maximise silver nanoparticle formation. These experiments were carried out using a galvanostatic method of -0.3 A for a set amount of time of 600 s. Employing a potentiostatic pulse to a set charge made it difficult to compare experiments as the rates of the reaction changed with the silver concentration. In order to more accurately compare nanoparticle production at different AgNO_3 concentrations reduction was limited to a fixed time. The resulting UV-Vis spectra are presented in Figure 3.12. The maximum absorbance was achieved when the electrolyte solution contained $282.5 \text{ g dm}^{-3} \text{ PVP}$ and $0.05 \text{ mol dm}^{-3} \text{ AgNO}_3$, at a molar ratio of 50:1 PVP:Ag. Beyond this concentration of silver, 0.1 mol dm^{-3} , a molar ratio of 25:1, the absorbance decreases and the band broadens as insufficient PVP is present to protect the newly formed nanoparticles. Lowering the silver concentration to $0.005 \text{ mol dm}^{-3}$ increases the ratio to 500:1 but since less silver is present the absorbance remains low, indicating a lower concentration of silver nanoparticles.

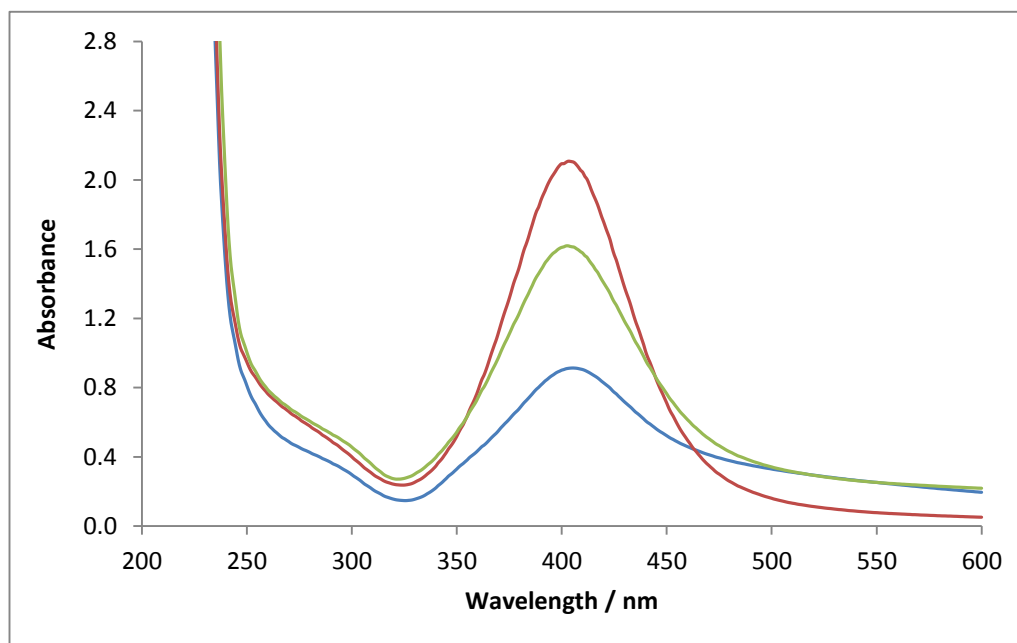


Figure 3.12: UV-Vis absorption spectra of a solution of silver nanoparticles generated at a constant current of -0.3 A for 600 s from a solution of different concentrations of AgNO_3 in 0.1 mol dm^{-3} KNO_3 and 282.5 g dm^{-3} PVP, — $0.005 \text{ mol dm}^{-3}$, — 0.05 mol dm^{-3} and — 0.1 mol dm^{-3} AgNO_3 . Solution diluted by factor of 30.

3.3.3.3 Effect of PVP Concentration

A silver concentration of 0.05 mol dm^{-3} AgNO_3 yielded the highest absorbance as shown in Figure 3.12. This concentration was employed and the PVP concentration was then altered to see if changes in its quantity would further benefit the nanoparticle yield. The same experimental approach was used and the spectra of the resulting solutions are shown in Figure 3.13. A PVP to silver ratio of 75:1 results in the highest absorbance. Increasing the ratio to 100:1 decreases the silver nanoparticle production, which may be due to hindered diffusion of silver ions to the electrode surface as the solution becomes increasingly more viscous.

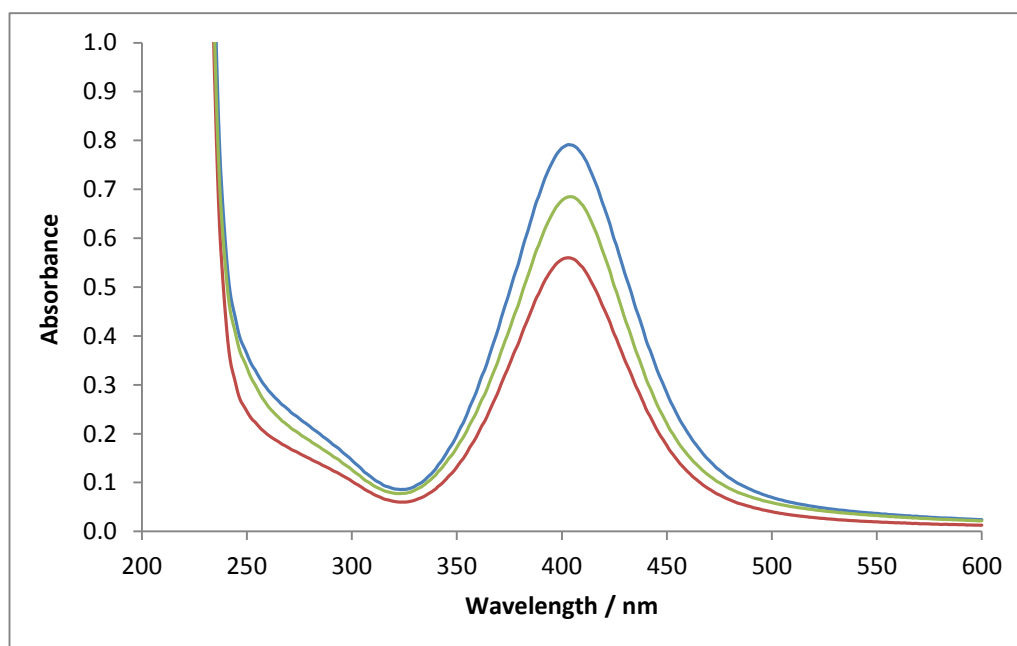


Figure 3.13: UV-Vis absorption spectra of a solution of silver nanoparticles generated at a constant current of -0.3 A for 600 s from a solution of different amounts of PVP in 0.05 mol dm^{-3} AgNO_3 and 0.1 mol dm^{-3} KNO_3 , — 423.75 g dm^{-3} (75:1), — 282.5 g dm^{-3} (50:1) and — 565 g dm^{-3} PVP (100:1). Solution diluted by a factor of 120.

3.3.3.4 Length of Potentiostatic Pulse

Figure 3.14 represents an example of the influence of a potential pulse when it is applied for extended periods of time to a silver solution. Interestingly, more particles are not formed as the electrolysis time is increased. More particles are produced after 1200 s compared to 600 s but beyond this, 2400 s, the absorption spectra show a decrease in intensity coupled with a broadening of the peak. Upon visual inspection agglomerates are visible at the bottom of the electrochemical cell and plating occurs on the glass cell wall. At longer electrolysis times, 6000 s, virtually no nanoparticles are present in the solution as the reduced silver has now almost completely agglomerated and settled out as large particles. Clearly, long periods of applied potential force the nanoparticles to agglomerate. The mechanism by which this occurs can be explained by Ostwald ripening of the nanoparticles ⁽¹⁷⁾.

Ostwald ripening is a phenomenon in which smaller particles in solution dissolve and deposit on larger particles in order to reach a more thermodynamically stable state wherein the surface to area ratio is minimised. It happens because molecules or atoms on the surface of particles are more energetically unstable. Therefore, the unstable surface species often dissolve into the solution shrinking the particles over time and increasing the number of free species in solution. When the solution is supersaturated with these species they will redeposit on larger particles. This gives rise to a higher concentration of larger particles and this is consistent with the broadening of the absorbance peak in Figure 3.14.

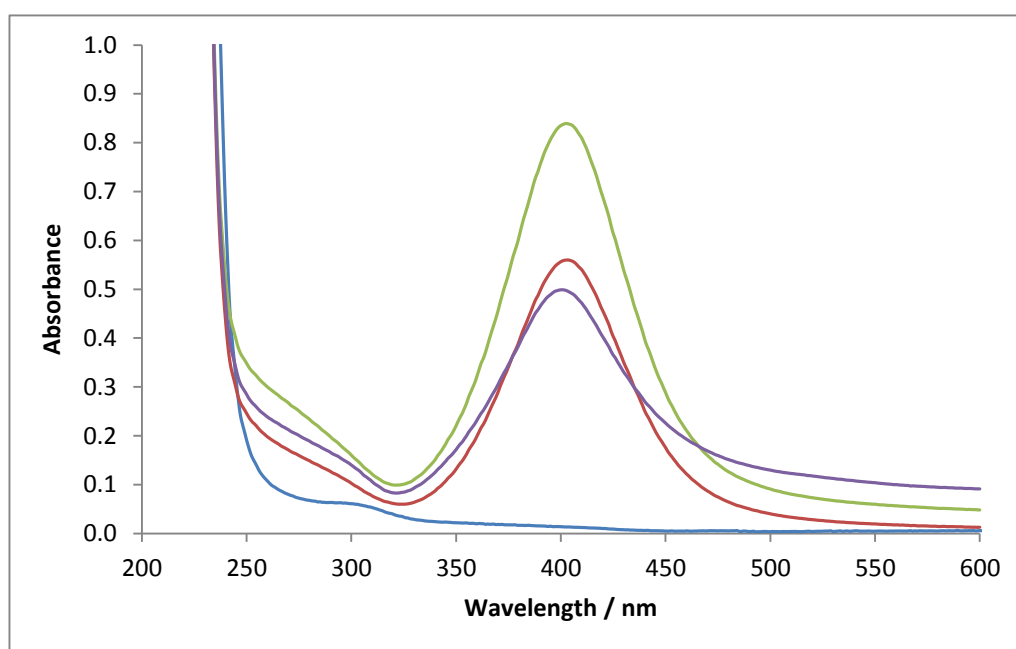


Figure 3.14: UV-Vis absorption spectra of a solution of silver nanoparticles generated at a constant current of -0.3 A from a solution containing 0.05 mol dm^{-3} AgNO_3 , 0.1 mol dm^{-3} KNO_3 and 282.5 g dm^{-3} PVP (50:1) for various pulse durations, —600 s, —1200 s, —2400 s and —6000 s. Solution diluted by a factor of 120.

It is well known that the surface energies of larger particles are lower than those of smaller sizes. When a solution of nanoparticles is continuously heated at high temperatures it drives the dissolution of small nanoparticles to the benefit of larger ones ⁽¹⁸⁾. Electrochemical Ostwald ripening also occurs under open-circuit potential conditions or when energy is put into the system in the form of an

applied potential. Schroder and co-workers discussed how ions are exchanged laterally between the particles via the electrolyte ⁽¹⁹⁾. Their analysis was based on nanocrystalline deposits on a conducting substrate but could equally be applied to colloidal particles as they come in contact with the platinum electrode to undergo reduction. Redmond and co-workers also discussed electrochemical Ostwald ripening of thermally evaporated silver nanoparticles on conducting substrates, and described how the mechanism is driven by the size dependence of the work function and the standard electrode potential ⁽¹⁷⁾. Plieth predicted that small metallic particles will show a negative shift in the standard electrode potential and a decrease in the work function. The difference in the standard electrode potentials causes differences in the equilibrium of Ag^+ ion concentration around each particle ⁽²⁰⁾. The Ag^+ ions move from small to large particles through the water/electrolyte, while electrons travel through the substrate. Due to the greater work function of the larger particles, the smaller particles will have a partial positive charge while the larger particles will have a partial negative charge. Consequently, in background electrolyte there is an electric field drawing positive ions towards the larger particles. Furthermore, due to the standard electrode potential difference, the equilibrium concentration of Ag^+ ions near the larger particles is lower than near the smaller particles. Redmond describes the process in terms of plating and dissolution. An aqueous Ag^+ ion plates out onto the larger nanoparticle by accepting an electron from a neighbouring smaller particle through the conducting substrate. The smaller, and now even more positively charged nanoparticle, re-establishes equilibrium by dissolving Ag^+ into solution. In this way, silver can act as a reaction initiator. They found that adding further amounts of silver nitrate increases the rate of agglomeration.

The formation of large clusters at long deposition times can also be explained using a theory put forward by Socol and co-workers, called the theory of a suspended electrode ⁽²¹⁾. Suspended particles near the cathode collide with the cathode surface and become charged, before moving back into the bulk solution. Socol and co-workers described these charged particles as behaving as part of the cathode and they can facilitate the electrodeposition of silver ions, and as a result the particles become larger. At very long electrolysis times, the ratio of silver

clusters to free silver ions increases and therefore the charge available from the reduction potential has a higher probability of being transferred to already formed silver clusters. Particle growth ceases when all the dissolved silver ions are depleted. Socal describes how a second stage of particle agglomeration now begins but only in the presence of an electric pulse. This agglomeration mechanism is related to the charging of the suspended particles by the electrode. This agglomeration process can take place at the beginning of the reaction but the rate of this reaction is slow when the concentration of free silver ions is high.

3.3.3.5 Optimum Condition for Electrochemical Synthesis of PVP-Protected Silver Nanoparticles

Table 3.1 outlines the final reaction conditions used to synthesise the PVP-protected silver nanoparticles that gave rise to the highest degree of reproducibility. This involved a solution of $0.1 \text{ mol dm}^{-3} \text{ KNO}_3$, $0.05 \text{ mol dm}^{-3} \text{ AgNO}_3$ solution and $423.75 \text{ g dm}^{-3} \text{ PVP}$, to give a ratio of $\text{Ag}^+:\text{PVP}$ of 75:1. An electrochemical pulse of $-6.0 \text{ V vs Ag/Ag}^+$ was applied until a charge of 180 C was reached. The UV-Vis spectra of four separate solutions of PVP-protected silver nanoparticles generated by applying $-6.0 \text{ V vs Ag/Ag}^+$ until a total charge of 180 C was reached from a solution comprising the optimum solution composition is shown in Figure 3.15. The reproducibility is excellent, given the high potentials used to generate the particles. In addition, the bandwidth is narrow (λ_{max} of 405 nm) meaning a small size distribution.

Table 3.1: Optimum Conditions for the electrochemical synthesis of PVP-protected nanoparticles.

AgNO ₃ Concentration / mol dm ⁻³	0.05
KNO ₃ Concentration / mol dm ⁻³	0.1
PVP Concentration / g dm ⁻³	423.75
Electrochemical Pulse	-6.0 V vs Ag/Ag ⁺ for 180 C

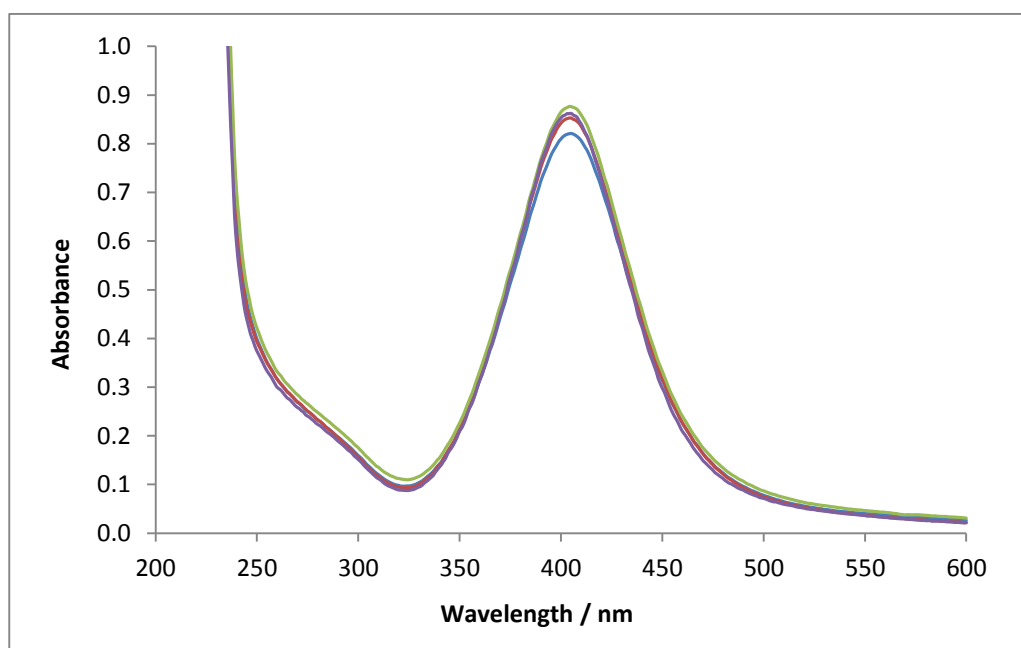


Figure 3.15: UV-Vis spectra of four separate solutions of PVP-protected silver nanoparticles generated by applying -6.0 V vs Ag/Ag^+ until a total charge of 180 C was passed in a solution containing 0.05 mol dm^{-3} AgNO_3 , 0.1 mol dm^{-3} KNO_3 and 423.75 g dm^{-3} PVP (75:1). Solution diluted by factor of 120.

3.3.3.6 Size of PVP-Protected Silver Nanoparticles

UV-Vis spectroscopy is by far one of the most popular characterisation techniques to describe colloidal particles. It is well known that the surface plasmon resonance of nanoparticles is influenced by the size, shape, interparticle interaction, free electron density and surrounding media ⁽¹⁴⁾. More spherical particles shift λ_{max} to lower wavelength ⁽²²⁾ and characteristically a λ_{max} of approximately 400 nm is indicative of spherical particles. For example, Njoki and co-workers found that the λ_{max} shifted 0.7 nm per 1 nm increase in gold nanoparticle size for particles over 25 nm , but found λ_{max} to be almost independent of the particle size for sizes smaller than 25 nm ⁽²³⁾.

In accordance with the quantum size theories, the plasmon resonance bandwidth has been found to increase with decreasing particle size, up to 25 nm diameter, and increase with increasing size for particles over 25 nm ⁽²⁴⁾. For particles less than 25 nm , the bandwidth is inversely proportional to the radius of the particles,

$w \sim 1/R$. This theoretical approach can only be applied when particle size is less than or equal to the mean free path of the electrons. Chakraborty described the relationship between the bandwidth and the radius of the particles using Equation 3.1. ⁽²²⁾

$$w = \frac{(\epsilon_0 + 2n_d^2)cmu_F}{2N_e e^2 R} \quad 3.1$$

In this equation, w is the full width at half maxima (FWHM) of the absorption peak, ϵ_0 is the frequency independent part of ϵ_m , the dielectric constant of the metal (4.9), n_d is the refractive index of the medium, in this case water (1.333), c is the velocity of light ($3.0 \times 10^8 \text{ m s}^{-1}$), m is the mass of an electron, u_F is the electron velocity at the Fermi energy ($1.4 \times 10^6 \text{ m s}^{-1}$), N_e is the number of electrons per unit volume, e is the charge of an electron and R is the particle radius. A value for $N_e e^2/m$ is given as 1.7×10^{31} from data given by Otter ⁽²⁵⁾. The FWHM of the absorption spectra in Figure 3.14 is an average of 72.88 nm and on substituting the respective values into Equation 3.1 this yields a radius, R , value of 2.87 nm and therefore a diameter of 5.73 nm.

3.3.3.7 Stability of PVP-Protected Silver Nanoparticle Solution

As discussed in the Introduction, PVP sterically hinders nanoparticle interactions and thus prevents aggregation. The stability of the particles in solution was monitored over a period of time, using UV-Vis spectroscopy. Figure 3.16 illustrates how the UV-Vis spectra of particles grown at -1.6 V vs Ag/Ag⁺ with a relatively low concentration of AgNO₃, $5.0 \times 10^{-3} \text{ mol dm}^{-3}$, change as a function of time. The absorption drops by 84% of its initial value in the first 24 hours, which signifies a decrease in the number of nanoparticles present in the solution, while the shift in the peak wavelength from 407 nm to 440 nm indicates an increase in particle size, as mentioned earlier ⁽¹³⁾. Since the area under the absorption band is proportional to the total concentration of silver particles, these changes suggest that the nanoparticles are agglomerating. In fact, some agglomerates were seen at the bottom of the sample tubes. This decrease in the absorbance is illustrated more

clearly in Figure 3.17, where the peak absorbance is plotted as a function of time. There is a large decrease in the absorbance from 0.93 to 0.16 over a 24-hour period.

However, particles generated using the optimum conditions, Table 3.1, with a high reduction potential of -6.0 V vs Ag/Ag⁺ and a higher concentration of AgNO₃, appear to be considerably more stable than particles formed at the lower potentials. Figure 3.17 shows the initial UV-Vis spectrum and the spectrum of the same solution a month later, when the particles are generated at -6.0 V vs Ag/Ag⁺. The absorbance has only decreased slightly, and with a minimal change in λ_{max} . A comparison of Figures 3.16 and 3.18 illustrate the significant variation in the stability of the silver nanoparticles.

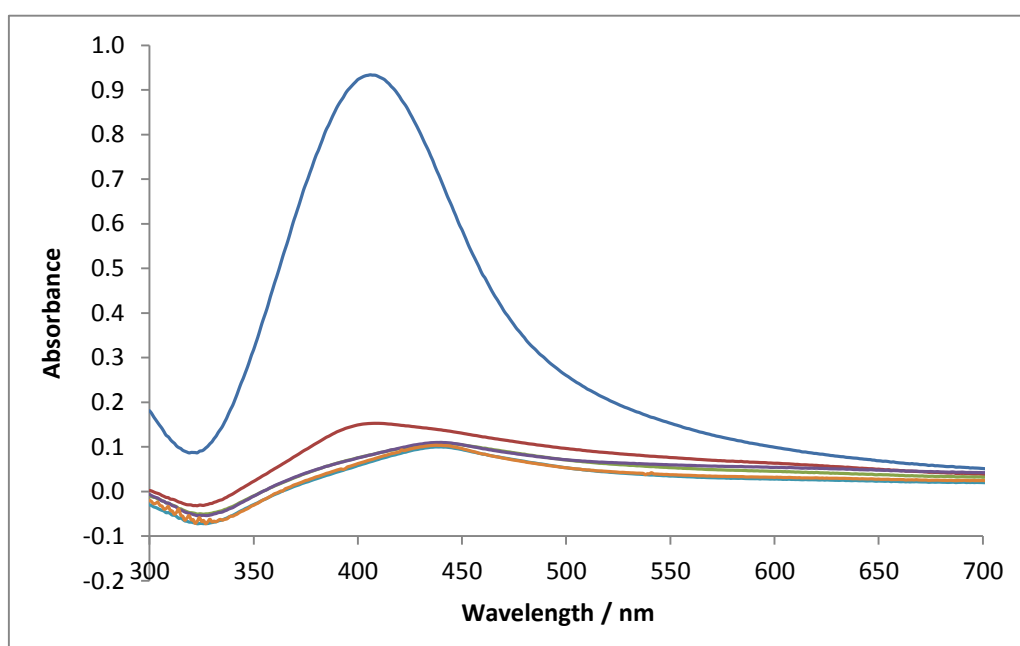


Figure 3.16: UV-Vis spectra of solutions of PVP-protected silver nanoparticles generated from a solution containing 5.0×10^{-3} mol dm⁻³ AgNO₃, 0.1 mol dm⁻³ KNO₃ and 113 g dm⁻³ PVP (silver to PVP ratio 200:1) after 600 s at an applied potential of -1.6 V vs Ag/Ag⁺ over a number of days. — 0, — 1, — 3, — 6, — 9 and — 14 days.

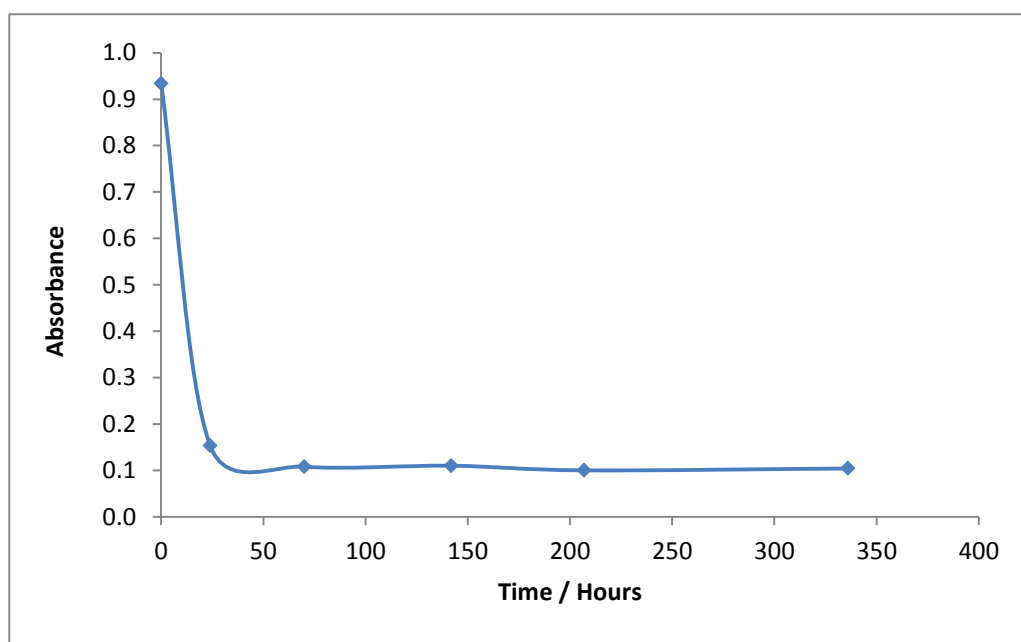


Figure 3.17: Plot of the absorbance at λ_{\max} as a function of time for the UV-Vis spectra shown in Figure 3.16.

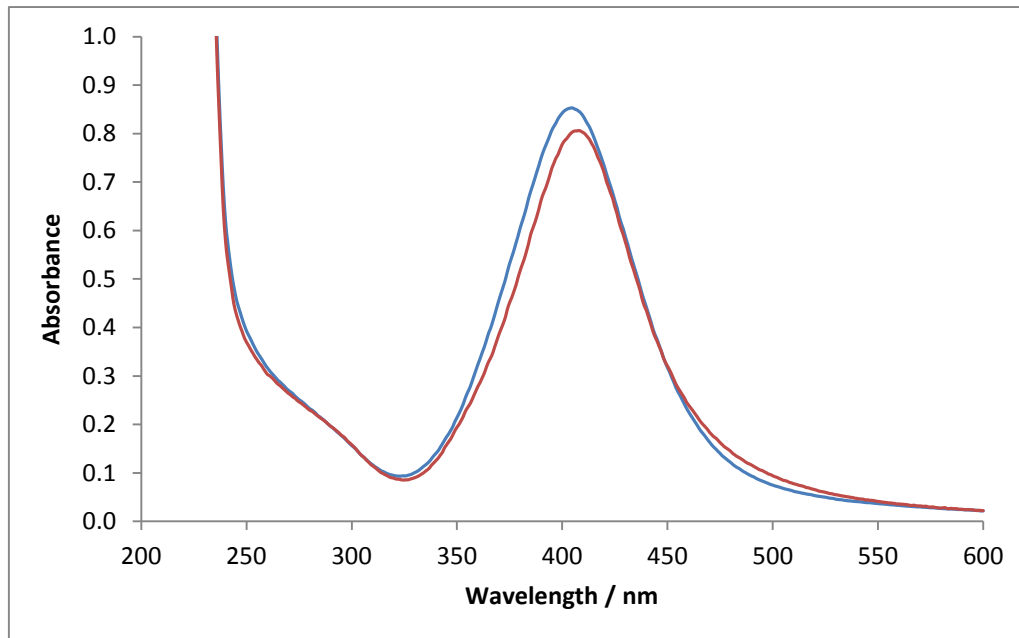


Figure 3.18: UV-Vis spectra of solutions of PVP-protected silver nanoparticle generated by applying -6.0 V vs Ag/Ag^+ until a total charge of 180 C was passed to a solution containing 0.05 mol dm^{-3} AgNO_3 , 0.1 mol dm^{-3} KNO_3 and 423.75 g dm^{-3} PVP (75:1) — initially and — after one month. Solution diluted by a factor of 120.

The nature of the media in which the particles are suspended is continuously acting on the particles, even in the absence of an externally applied potential. Nanoparticles, like any compound in solution, are in a constant state of flux driven to find the lowest energy state. Furthermore, the potentials for smaller particles is negatively shifted compared to larger particles, which sets up an electrical equilibrium where larger particles have a slightly negative charge and smaller particles have a slightly positive charge ⁽¹⁷⁾. For this reason, nanoparticles suspended in a high ionic strength media require the presence of a protecting agent to stabilise the charged particles. The following section examines what effects changes in the surrounding media have on the stability of the nanoparticles in solution.

3.3.3.8 Stability of PVP-Protected Nanoparticles in the Presence of Added Ions

The effect of added electrolytes on the stability of colloidal nanoparticles is reasonably well documented in the literature ⁽²⁶⁻³¹⁾. As outlined in the Introduction, ions, for example borohydride, adsorb on the surface of the particles forming a double layer, creating repulsive forces between the particles and preventing aggregation. Addition of excess ions screen and effectively negate the repulsive charge between the particles in solution.

The reduction of all the silver ions in solution is likely to be incomplete at lower reduction potentials since the UV-Vis absorption intensity is low compared to particles generated at the higher potentials, Figures 3.9 and 3.10. The particles may therefore be more unstable due to larger concentrations of unreduced silver ions. This theory is addressed in the following section where aliquots of 0.1 M AgNO₃ are added to a diluted solution of PVP-protected nanoparticles. To a diluted solution of PVP-protected silver nanoparticles (2.85 mL), generated at -6.0 V vs Ag/Ag⁺ to a total charge of 180 C, an aliquot of 0.1 M AgNO₃ (150 µL) was added to give a final concentration of 5.0 x 10⁻³ M AgNO₃. As a control, the same volume of water was added to another sample of PVP-protected nanoparticles. The UV-Vis absorbance spectrum of each of these samples was monitored over time to see if

the size or stability of the nanoparticles changed. As discussed in the Introduction, changes in the λ_{\max} value and the intensity of the absorption band is indicative of changes in the morphology and concentration of the nanoparticles. The UV-Vis spectra recorded after for the addition of water are shown in Figure 3.19. A small decrease in the absorbance of approximately 11% is seen over a month. Also, there is a small change in the λ_{\max} . This indicates reasonably good stability.

The effect of added silver salt on the previously stable nanoparticles is shown in Figure 3.20. A more significant decrease in the peak absorbance is seen with the addition of AgNO_3 . The peak absorbance decreases by over 64% over a one month period, while the band widens significantly with the emergence of a second peak at 486 nm. Clearly, the addition of AgNO_3 gives rise to changes in the concentration and size of the silver nanoparticles.

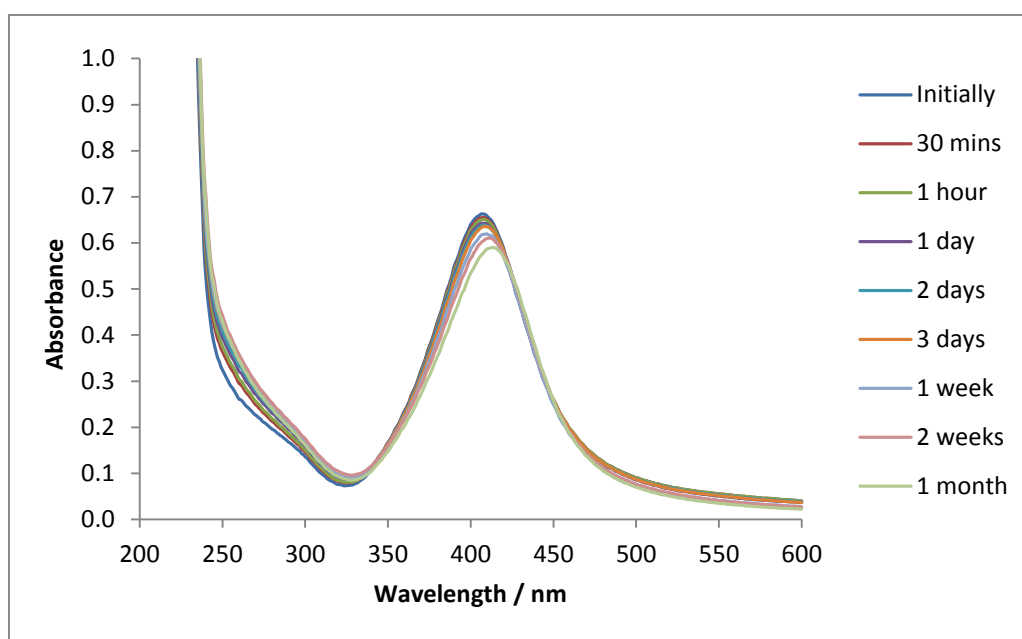


Figure 3.19: UV-Vis spectra recorded over a month after the addition of a water aliquot to a solution of PVP-protected silver nanoparticles generated by applying -6.0 V vs Ag/Ag^+ until a total charge of 180 C was passed in a solution containing $0.05\text{ mol dm}^{-3}\text{ AgNO}_3$, $0.1\text{ mol dm}^{-3}\text{ KNO}_3$ and $423.75\text{ g dm}^{-3}\text{ PVP}$ (75:1).

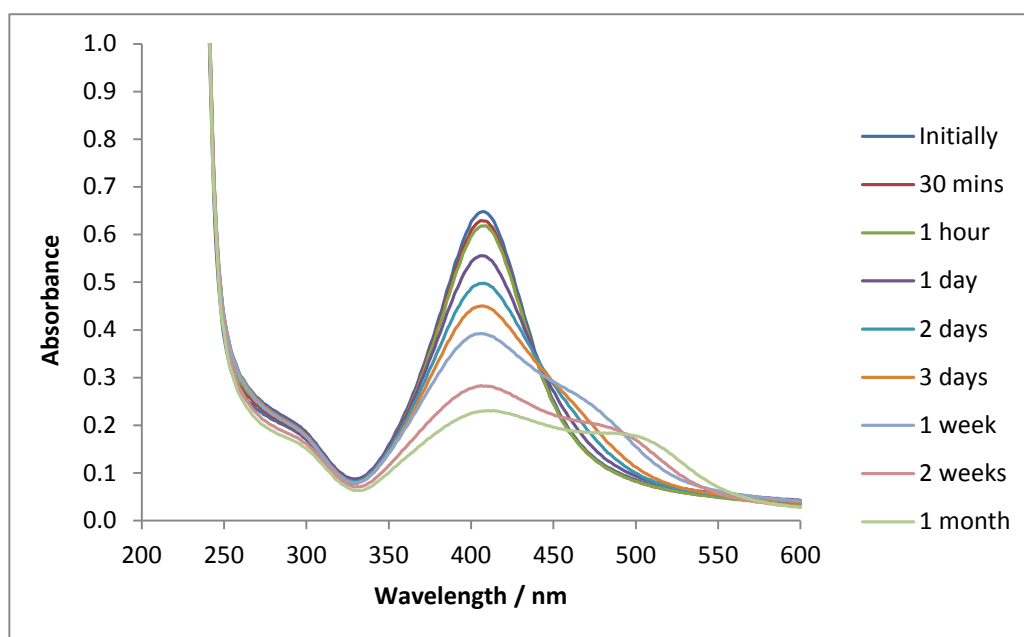


Figure 3.20: UV-Vis spectra recorded over a month after the addition of a AgNO_3 aliquot ($150 \mu\text{L}$ of $0.1 \text{ mol dm}^{-3} \text{AgNO}_3$) to 2.85 mL of the PVP-protected nanoparticles solution) to a solution of PVP-protected silver nanoparticles generated by applying -6.0 V vs Ag/Ag^+ until a total charge of 180 C was passed in a solution containing $0.05 \text{ mol dm}^{-3} \text{AgNO}_3$, $0.1 \text{ mol dm}^{-3} \text{KNO}_3$ and $423.75 \text{ g dm}^{-3} \text{PVP}$ (75:1).

A similar trend in the UV-Vis spectra was observed by Liu and co-workers when metal cations such as Cu^{2+} , Zn^{2+} , Cd^{2+} , Cr^{3+} and Pb^{2+} were added to a silver sol prepared by the reduction of AgNO_3 with NaBH_4 ⁽³²⁾. These workers postulated that the cations entered the diffuse double layer and subsequently neutralised the electrostatic forces that prevent aggregation. It could also be argued that the additional free Ag^+ cations are now available for reduction. PVP is a reducing agent as well as a protecting agent, and although the reduction process is slow at ambient temperature and in the absence of an externally applied potential, reduction of silver can still occur. The lack of energy in the system would favour deposition on the lower energy surface of the already preformed particles, to give larger nanoparticles, which is consistent with the broadening of the absorbance band in Figure 3.20.

It is possible that the nitrate counter anion is the cause of this change in the nanoparticles and not the free Ag^+ cations. Canamares and co-workers looked specifically at the effect of KNO_3 additions to solutions of silver nanoparticles

prepared by the chemical reduction of AgNO_3 using citrate and hydroxylamine ⁽²⁹⁾. They reported a decrease of 0.05 and 0.20 absorbance units for the citrate and hydroxylamine protected particles, respectively. However, no time scale was mentioned, so it is presumed to be an immediate effect. Therefore, the influence of nitrate anions on the stability of the PVP-protected silver nanoparticles was studied. The UV-Vis spectra were recorded over a period of one month on addition of KNO_3 . The UV-Vis spectra recorded as a function of time are shown in Figure 3.21. In this case, the absorbance also decreases by 46% over the month and with a slight shift to a longer wavelength.

For clarity, the changes in the λ_{max} and the intensity of the absorption band for each of the experiments described in this section are summarised in Table 3.2. The addition of KNO_3 and AgNO_3 gives rise to similar changes in the λ_{max} value and the intensity of the absorption band.

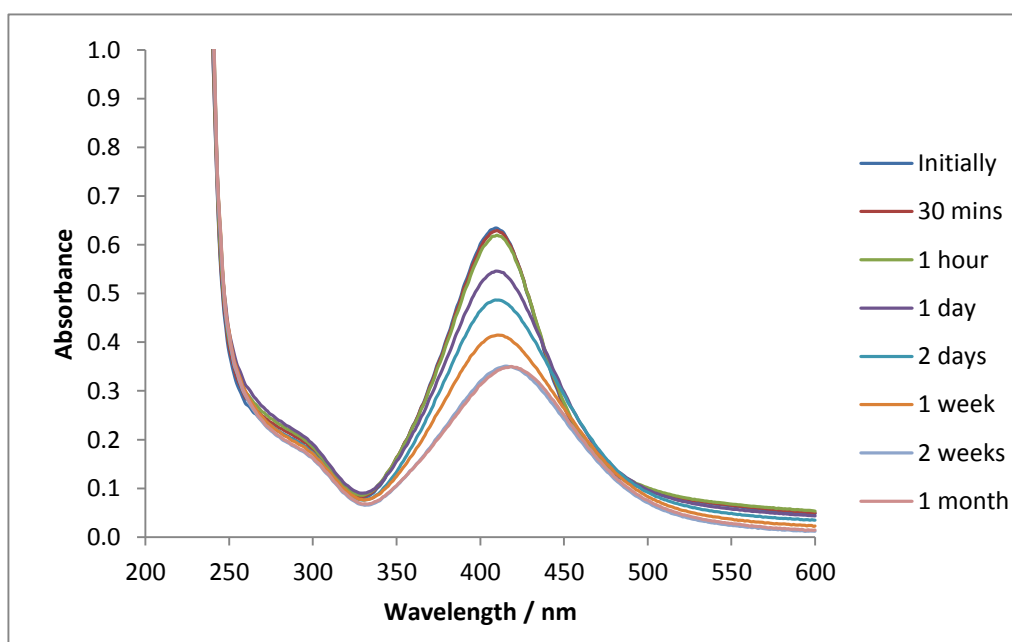


Figure 3.21: UV-Vis spectra recorded over a month after the addition of a KNO_3 aliquot (150 μL of $0.1 \text{ mol dm}^{-3} \text{ KNO}_3$ to 2.85 mL of the PVP-protected nanoparticle solution) to PVP-protected silver nanoparticle generated by applying -6.0 V vs Ag/Ag^+ until a total charge of 180 C was passed in a solution containing $0.05 \text{ mol dm}^{-3} \text{ AgNO}_3$, $0.1 \text{ mol dm}^{-3} \text{ KNO}_3$ and $423.75 \text{ g dm}^{-3} \text{ PVP}$ (75:1).

Table 3.2: Summary of the change in λ_{\max} and the absorbance intensity with the addition of water or salts.

	Added Water	Added AgNO ₃	Added KNO ₃
λ_{\max} change	407 → 414	407 → 414, 486	408 → 418
Abs change	0.663 → 0.590	0.648 → 0.231, 0.183	0.653 → 0.350

Espinoza and co-workers studied the effects of added halides on the stability of nanoparticles⁽³³⁾. Within only a few minutes, the absorbance spectra decreased significantly, which is considerably more rapid than that observed on the addition of AgNO₃ or KNO₃, Figures 3.20 and 3.21. PVP acts as a steric protector for nanoparticles rather than an electrostatic one, and as such, it has been reported as an effective protector against aggregation of nanoparticles⁽³⁰⁾. Although PVP acts sterically to prevent aggregation, the particles are affected by changes in the ionic strength of the solution. Zhang and Zhang⁽²⁷⁾ showed how PVP- and citrate-protected silver nanoparticles both suffered from particle aggregation at high ionic strength, although the citrate protected particles were more susceptible to aggregation.

Greulich and co-workers found that PVP-protected silver nanoparticles agglomerated in different biological media with a high electrolyte content such as phosphate buffered saline⁽³⁴⁾. However, no explanation was given for how the electrolytes disrupt the protecting ability of PVP. Other studies that demonstrate the stability of PVP-protected nanoparticles rarely mention a long term stability study⁽³⁵⁾. From the results obtained in this study, the instability is only observed after 1 day. Therefore, it is possible that this effect was not seen in other studies. While it is understandable why extra salts interfere with the protecting ability of electrostatic protectors like citrate, by disrupting the charged layer around the particles as described above, it is more difficult to understand how they affect the sterically protected PVP nanoparticles. It is generally understood that PVP is a steric capping agent with no charge. Other polymers, such as a branched polyethyleneimine, are electrosteric stabilisers, that is, a polymer whose repeating

unit bears an electrolyte group that dissociates in aqueous solution making the polymer charged ⁽³⁵⁾. The protection mechanism of PVP has been studied and it is understood, by examining IR spectra, that silver interacts with the lone pairs of electrons on the oxygen and the nitrogen on the pyrrolidone rings along the backbone chain ^(9,36). Although the interaction between PVP and silver is not purely electrostatic, PVP does act as an electron-donating polymeric ligand. While PVP-protected particles are known to be stable to high ionic strength media it is still possible that extra ions in solution could affect this interaction.

Some insight may be gained from examining how PVP acts during the generation of the nanoparticles. In general, when PVP is used in the chemical synthesis of silver nanoparticles it is in conjunction with a reductant, such as sodium borohydride, and a silver salt ^(36,37). However, PVP is a mild reducing agent, and heating a solution of PVP and the silver salt is sufficient to generate silver nanoparticles ^(38,39). In fact in this study when PVP was added to the silver nitrate solution heat was generated indicating an exothermic reaction. Washio and co-workers suggested that the reducing power of PVP comes from the hydroxyl end groups of the PVP chains. This functionality is due to the involvement of water and hydrogen peroxide in the synthesis of the PVP polymer ⁽³⁹⁾. Solutions of PVP and silver nitrate were heated in a vial at 60°C for various lengths of time. Washio and co-workers found that by varying the time and the molar ratio of PVP to AgNO₃ different sized particles could be generated. Longer reaction times led to the formation of larger triangular, nanoplates that absorbed higher wavelengths of light in the UV-Vis spectrum. Also, different molecular weight PVP chains were used to see how this affected the shape of the particles. Different molecular weights will have different amounts of hydroxyl end groups when the same molar ratios to silver nitrate are used. In other words, shorter chains will have more hydroxyl groups per weight and this should lead to faster reduction rates. Washio and co-workers explained that faster rates lead to the formation of the thermodynamically favoured shapes and when slowed down the growth changed to kinetic control.

As the silver nanoparticles were not cleaned in this study, the reducing action of PVP may still occur even when the electrochemistry is complete. This can explain the slight red shift in the λ_{max} and the decrease in absorbance for the nanoparticle solution with the added water, Figure 3.19. The emergence of the second peak at 486 nm and a decrease in the absorbance at 407 nm when AgNO_3 is added is indicative of the formation of larger particles either from aggregation of existing particles or newly formed particles from the fresh silver ions. This may occur by a different pathway, i.e., from the chemical reducing power of PVP to give either the thermodynamically or kinetically favoured shapes.

While Greulich and co-workers⁽³⁰⁾ show that PVP particles are susceptible to aggregation by the addition of electrolytes, the nitrate anion may have a more specific effect. Since PVP is a reducing agent it is susceptible to attack by oxidants, such as the nitrate anion. When Hoppe and co-workers studied the synthesis of gold and silver hydrosols, using PVP as the reducing agent, they investigated possible reaction mechanisms for the synthesis⁽³⁸⁾. They postulated that the presence of low amounts of peroxides that remain in the polymer after synthesis could be thermally decomposed and produce extremely reactive radical species that would react with the polymer to form new macro-radicals. This results in PVP degradation in the form of main chain scission, hydrogen atom abstraction or side ring abstraction. They concluded that transition metal salts, such as those of silver and gold, could accelerate this decomposition and as a consequence the metal ions become reduced. They drew on other literature reports that discussed similar observation of metal-catalysed degradation of polymers, including PVP^(40,41). In summary, a possible explanation for the formation of nanoparticles is that the reduction of metals occurs by action of organic radicals formed during the metal-accelerated degradation of PVP. It is possible that nitrate, as an oxidising agent, may act in the same way as peroxide and instead of acting to generate new particles could be actively degrading PVP through main chain scission, hydrogen atom abstraction or side ring abstraction and disrupting the protecting ability of the PVP. To support this argument a solution of the PVP-protected nanoparticles was heated and the absorbance was recorded. The solution was heated at 60 °C over a period of time and the UV-Vis spectra were recorded as shown in Figure

3.22. The plots show a rapid decrease in the absorbance of the particles over time and eventually the absorbance decays to zero. Upon visual inspection the stirrer bead was covered in a layer of silver giving another indication the silver had agglomerated out of solution. Additionally, there is an increase in the absorption bands in the 250 to 350 nm range after 2 hours which has been attributed to the presence of oxidation products of PVP degradation ^(38,40). Therefore, it can be concluded that while heating a silver salt in PVP can generate nanoparticles, according to Hoppe and co-workers further heating leads to degradation of the PVP chains and a total loss of its effectiveness to protect the nanoparticles. The nitrate anion is quite likely acting in a similar manner but at a much slower rate than heating of the solution.

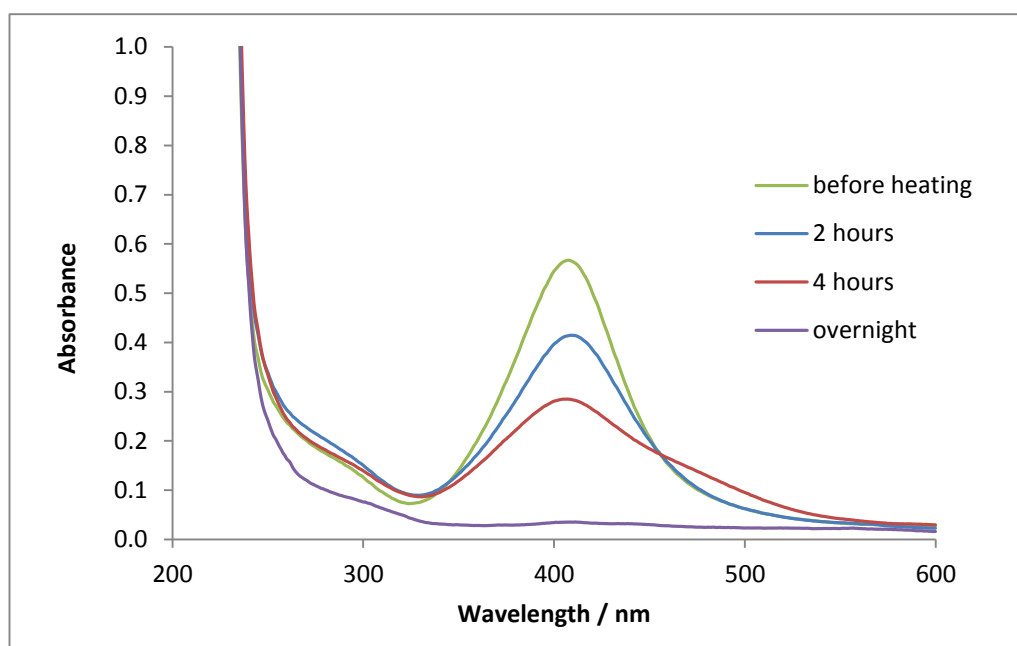


Figure 3.22: UV-Vis absorption spectra of PVP-protected silver nanoparticles heated at 60 °C and monitored overnight.

3.3.4 Immobilisation of the PVP-Protected Nanoparticles onto a Glassy Carbon Electrode for the Electrochemical Detection of Nitrate

In the following sections, the possibility of immobilising the PVP-protected nanoparticles on the surface of a GC electrode was investigated. The potential of the immobilised particles to act as a catalyst for the electrochemical detection of nitrate was then explored. A simple approach, similar to that used by Wang and co-workers, was adopted, which involved immersing a polished GC electrode in the solution of nanoparticles for a period of time ⁽⁴²⁾. Wang and co-workers immersed a GC electrode in a hydrosol of oleate-stabilised silver nanoparticles, which had been synthesised using a NaBH₄ reduction, to electrochemically detect thiocyanate.

A GC electrode was immersed in the solution of silver nanoparticles for 12 hours and then allowed to air dry until all the solvent evaporated. This modified electrode was then placed in a solution containing 0.05 mol dm⁻³ KNO₃ and 0.1 mol dm⁻³ Na₂SO₄ and the voltammograms were recorded at 20 mV s⁻¹. Typical voltammograms are presented in Figure 3.23. Only the forward sweep is shown. Initially, the signal is poor for the nitrate reduction, but as the cycles progress the current increases. Visually, the evaporated layer on the GC electrode is seen to dissolve away as the PVP is a water soluble polymer. However, from the voltammograms in Figure 3.23 it is clear that this outer layer needs to be removed before the particles adhered to the GC electrode can catalyse the reduction reaction. The nitrate reduction currents remain fairly stable from cycles 10 to 30 which suggest that the particles involved in this reduction reaction do adhere well to the GC surface.

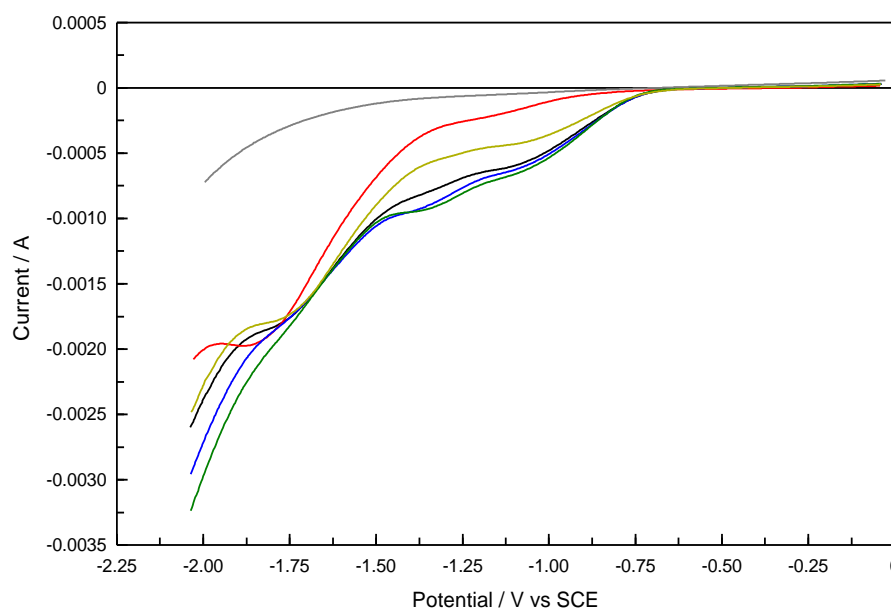


Figure 3.23: Cyclic voltammograms, forward cycle only, recorded at 20 mV s^{-1} in a solution of 0.05 mol dm^{-3} KNO_3 and 0.1 mol dm^{-3} Na_2SO_4 at a glassy carbon electrode which was immersed in a solution of silver nanoparticles for 12 hours, — cycle 2, — cycle 5, — cycle 10, — cycle 20, — cycle 30 and — bare GC.

However, when this process was repeated there was poor reproducibility in the magnitude of the current that was generated for the same concentration of nitrate, as can be seen in Figure 3.24. In this figure, two voltammograms are shown, and it is clear that there is a considerable variation in the nitrate reduction currents. Therefore, an alternative method to immobilise the silver nanoparticles was explored. This involved using hydrogels, and in particular a polyacrylamide gel. The following sections outline the immobilising of the PVP-protected silver nanoparticles in a polyacrylamide hydrogel matrix. This composite was then tested for its ability to perform as an electrochemical sensor.

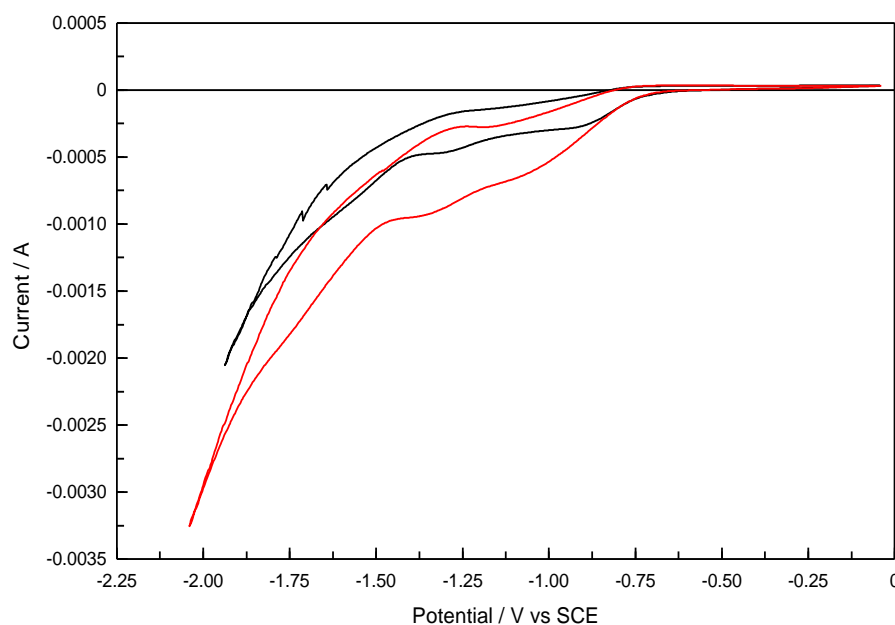
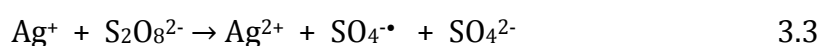


Figure 3.24: Cyclic voltammograms recorded at 20 mV s^{-1} , for two separate electrodes made in the same way, in a solution of $0.05 \text{ mol dm}^{-3} \text{ KNO}_3$ and $0.1 \text{ mol dm}^{-3} \text{ Na}_2\text{SO}_4$ at a glassy carbon electrode which was immersed in a solution of silver nanoparticles for 12 hours.

3.3.5 Synthesis of a Polyacrylamide-PVP-Protected Silver Nanoparticle Composite

The polyacrylamide-PVP (PAAm-PVP) and the polyacrylamide-PVP silver nanoparticle (PAAm-PVP-Ag-np) composites were prepared as outlined in Chapter 2, Section 2.4.1.4.1. Polyacrylamide (PAAm) gels are formed by copolymerisation of acrylamide (AAm) and N,N'-methylenebisacrylamide (MBA) from an aqueous solution. This is a free radical polymerisation initiated by ammonium persulfate (AP) and tetramethylethylenediamine (TEMED). TEMED accelerates the rate of formation of free radicals from AP and acts as a catalyst for the reaction. The persulfate free radicals generate AAm monomer radicals which react with unactivated monomers to begin the polymerisation chain reaction ⁽⁴³⁾. The elongating polymer chains are randomly crosslinked by MBA, resulting in a gel with a characteristic porosity which depends on the polymerisation conditions and monomer concentrations. More detail on the reaction mechanism is given in the Introduction, Chapter 1, Section 1.2.1.

The amounts of initiator and activator, AP and TEMED, were varied for the different gels. Typically, gelation times for standard PAAm gels are 15 to 20 min, however, it was found that the amount of AP and TEMED had to be reduced when silver, in either the in the Ag⁺ oxidation state or as silver nanoparticles, was present in the polymerisation solution. Indeed, like TEMED, silver is known to act as a catalyst for the dissociation of persulfate ⁽⁴⁴⁾. The decomposition of persulfate, as described by Equation 3.2, is slow. Bawn and Margerison proposed the mechanisms in Equation 3.3 and 3.4 to describe how the silver ion can be used to generate radicals from persulfate at a much faster rate ⁽⁴⁵⁾. Similarly, Singh synthesised PAAm in a reaction which was catalysed by silver nitrate ⁽⁴⁶⁾.



As a control, PAAm-PVP hydrogels were also synthesised without silver for comparison with hydrogels containing silver nanoparticles. The amount of each reagent is listed in Table 3.3.

Table 3.3: Reagents for the synthesis of PAAm-PVP and the PAAm-PVP-Ag-np composites. In each case, AAm and MBA were dissolved in 10 mL of deionised water before combining with the PVP solutions. All solutions were purged with N₂ for 10 min prior to polymerisation.

Hydrogel	AAm /g	MBA /g	PVP solution	AP	TEMED/ μL
PAAm-PVP	4.0	0.175	10 mL of 423.75g dm ⁻³ PVP in water	400 μL of a 1% solution	10
PAAm-PVP-Ag-np	4.0	0.175	10 mL of 423.75g dm ⁻³ PVP with Ag-np	300 μL of a 1% solution	5

3.3.6 Application of Polyacrylamide-PVP-Protected Silver Nanoparticle Composite

Once the hydrogel composites were synthesised the possible applications of these materials were explored. In order to investigate if the silver nanoparticles imparted conductivity to an otherwise non-conductive hydrogel material, the electrochemical properties of the materials was studied. The well characterised ferrocyanide/ferricyanide redox couple was used as an electrochemical probe and then the electrochemical detection of nitrates at the composites was investigated, Section 3.3.6.1. In Section 3.3.6.2 the efficiency of PAAm-PVP-Ag-np composites as heterogeneous catalysts for the reduction of 4-nitrophenol is explored. The reduction of 4-nitrophenol to 4-aminophenol with an excess amount of NaBH_4 has often been used as a model reaction to examine the catalytic performance of metal nanoparticles^(47,48). Encapsulation of the nanoparticles in the hydrogel matrix permits a convenient removal of the particles once reduction is complete, but consequently, access to the nanoparticle surface can be hindered. The antibacterial properties of silver have received increased attention recently as bacterial resistance to antibiotics becomes a major health concern. The potential of the PAAm-PVP-Ag-np composite for use as an antibacterial material in, for example, wound dressing was investigated using plate assay experiment on five different strains of bacteria in Section 3.3.6.3.

3.3.6.1 Polyacrylamide-PVP-Protected Silver Nanoparticle composite as an Electrode

The hydrogel silver nanoparticle composite for use as an electrode was prepared as described in Chapter 2, Section 2.4.1.4.2 Firstly, the composites were placed in a solution containing ferrocyanide/ferricyanide to investigate the potential of these hydrogels as suitable electrodes. Figure 3.25 shows the response of the PAAm-PVP-Ag-np composite, the PAAm-PVP composite and a platinum (Pt) wire with no hydrogel cycled in a solution of potassium ferricyanide, $\text{K}_3\text{Fe}(\text{CN})_6$. The redox equations are shown in Equations 3.5 and 3.6, with an oxidation wave observed as the $\text{Fe}(\text{CN})_6^{4-}$ is oxidised and a reduction wave for the conversion of $\text{Fe}(\text{CN})_6^{3-}$ to the $\text{Fe}(\text{CN})_6^{4-}$ species. It is evident from the voltammograms that lower currents and a greater peak separation are observed for the hydrogel composites with and

without the silver. Higher peak currents are observed for the Pt wire. These findings are not surprising as diffusion limitations arise with the hydrogels. Loading the hydrogel composite with metallic silver particles has little effect on the conductivity and the peak currents are somewhat lower than that observed for the composites without the silver particles. It is likely that connections between the particles are disrupted by the hydrogel matrix and that the current response is simply originating from the underlying Pt wire. As the Pt is coated with the hydrogel composite diffusion of the ferrocyanide or ferricyanide ions is slow giving rise to a considerable reduction in the peak currents compared to the uncoated Pt wire.

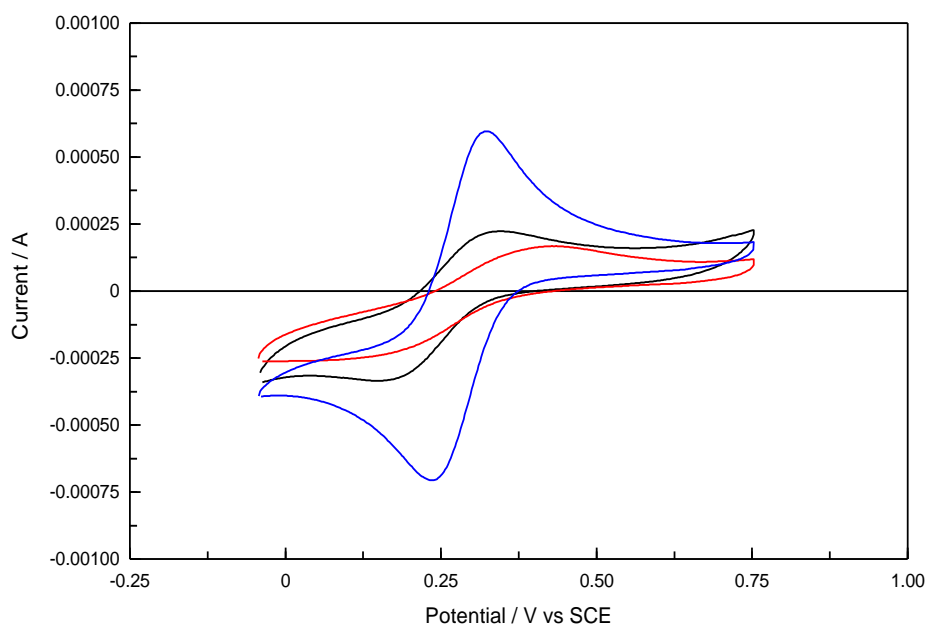
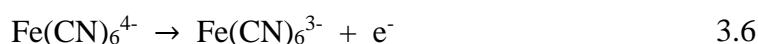
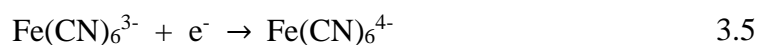


Figure 3.25: Cyclic voltammograms recorded at 20 mV s^{-1} in a solution of $0.01 \text{ mol dm}^{-3} \text{ K}_3\text{Fe(CN)}_6$ and $0.1 \text{ mol dm}^{-3} \text{ Na}_2\text{SO}_4$ at a — PAAm-PVP-Ag-np composite, — PAAm-PVP composite and — 1 mm diameter Pt wire.

Similarly, when the hydrogel-coated electrodes were placed in a solution containing nitrate no improvement in the nitrate reduction signal was observed. Figure 3.26 compares the voltammograms recorded for the PAAm-PVP-Ag-np composite and a Pt wire. It is clear that the magnitude of the current at the Pt wire is superior and continues to increase as the potential is lowered. Much lower nitrate reduction currents are observed with the composite. Reduction of the nitrate begins at -0.70 V vs SCE at the Pt wire and at -0.89 V SCE at the PAAm-PVP-Ag-np composite. It appears that the nanoparticles within the hydrogel matrix are not electrically connected and that any observed faradaic current is simply generated at the underlying Pt wire. Furthermore, the hydrogel matrix only serves to hinder diffusion of any analytes, leading to a lower current response.

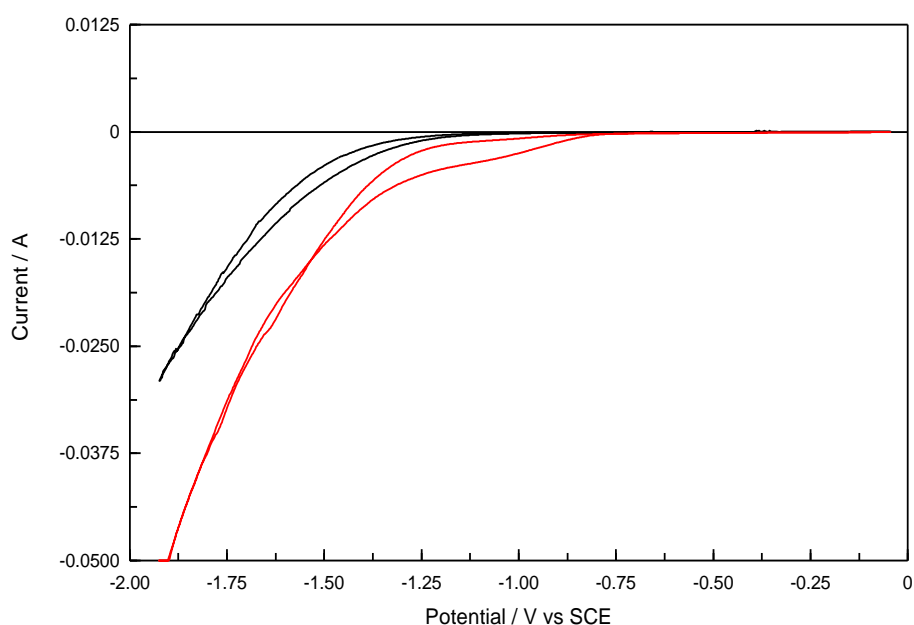


Figure 3.26: Cyclic voltammograms recorded at a scan rate of 20 mV s^{-1} in a solution of $0.05 \text{ mol dm}^{-3} \text{ KNO}_3$ and $0.1 \text{ mol dm}^{-3} \text{ Na}_2\text{SO}_4$ at a — PAAm-PVP-Ag-np composite and — 1 mm diameter Pt wire.

It is clear from these experiments that the PAAm-PVP-Ag-np composite is not suitable for use as an electrochemical sensor. However, many groups report the use of similar materials as catalysts. The catalytic activity of the composite for the reduction of 4-nitrophenol to 4-aminophenol using NaBH_4 was studied and these results are presented and discussed in Section 3.3.6.2.

3.3.6.2 Polyacrylamide-PVP-Protected Silver Nanoparticle Composite for Use as a Heterogeneous Catalyst in the Reduction of 4-Nitrophenol

3.3.6.2.1 General Overview of Heterogeneous Catalysis of 4-Nitrophenol Reduction

As discussed in the Introduction, nanoparticles are often used as catalysts for reactions due to their high surface area and special properties compared to their bulk metal counterparts. The nanoparticles become even more useful when they can be immobilised in a matrix which provides stability as well as an easy method to remove the nanoparticle catalyst once the reaction is complete. The reduction of 4-nitrophenol to 4-aminophenol with an excess amount of NaBH_4 has often been used as a model reaction to examine the catalytic performance of metal nanoparticles. This reaction was first identified by Pradhan and co-workers as a good candidate for the model reaction to quantify and compare the catalytic activity of many types of nanoparticle systems in the literature ⁽⁴⁹⁾. As a model reaction, it offers many advantages. The reaction is well defined, with no by-products formed, the conversion can be monitored easily and quickly using UV-Vis spectroscopy and the reaction is catalysed by free or immobilised nanoparticles in aqueous solution at ambient temperatures. The reducing agent, NaBH_4 , is ineffective at causing this reaction unless provided with some catalyst to remove the kinetic barrier of the reaction to support electron relay for the reaction ⁽⁴⁷⁾.

Hydrogel silver nanoparticle discs were prepared as outlined in Chapter 2 Section 2.4.1.4.3. The performance of the PAAm-PVP-Ag-np composite was evaluated by monitoring changes in the UV-Vis spectrum of 4-nitrophenol over time. Figure 3.27 shows the UV-Vis spectra of 4-nitrophenol dissolved in water with and without added NaBH_4 . In water the λ_{max} for 4-nitrophenol is 318 nm. Immediately, upon the addition of NaBH_4 the peak is red shifted to 401 nm. This is due to the formation of the conjugate base, the 4-nitrophenolate ion, in alkaline condition caused by NaBH_4 ⁽⁴⁸⁾.

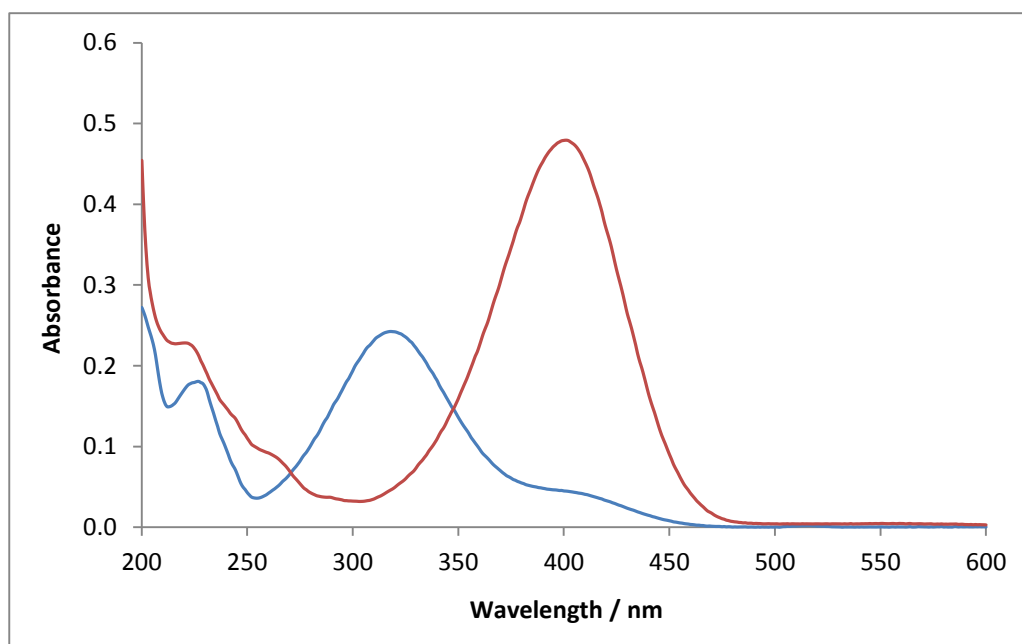
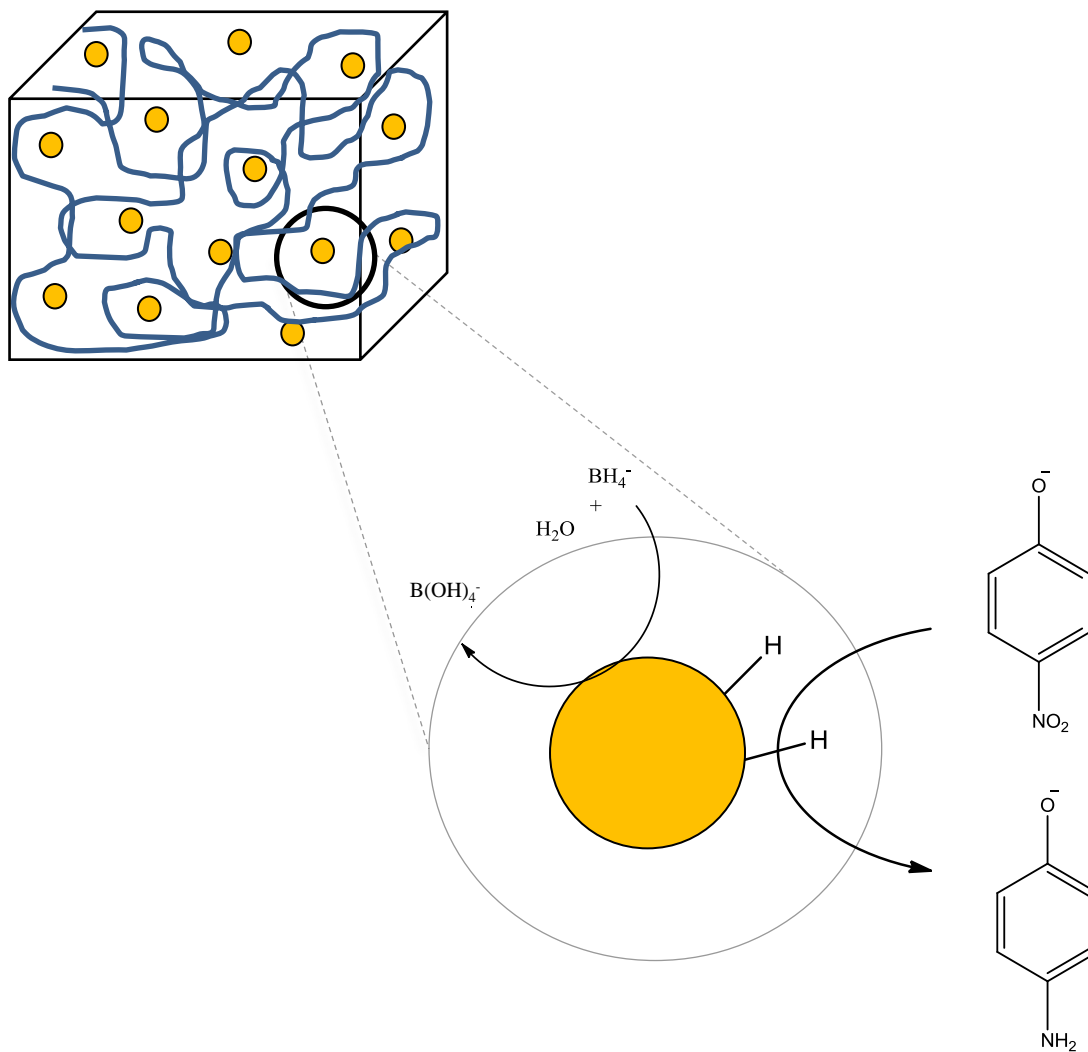
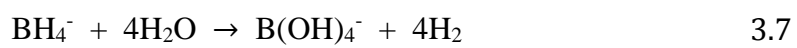


Figure 3.27: UV-Vis spectra of $2.0 \times 10^{-5} \text{ mol dm}^{-3}$ 4-nitrophenol — with and — without $2.0 \times 10^{-2} \text{ mol dm}^{-3}$ NaBH_4 .

Various studies on the catalysed 4-nitrophenol reduction reaction have been carried out ^(48,50). From these studies, it has been deduced that the borohydride ions react with the surface of the nanoparticle and transfer a hydrogen atom to the surface of the particle ⁽⁵¹⁾. The 4-nitrophenol molecule diffuses to the surface and adsorbs to it. This is followed by its reduction by the surface-adsorbed hydrogen atom. The diffusion and adsorption/desorption steps are thought to be reversible and fast, and that it is the reduction step that is the rate-determining step. Once reduction is complete, the product, 4-aminophenol, detaches and the surface is free again to begin the catalytic cycle. The hydrolysis of the borohydride on the metal catalyst has been extensively studied, and although it is not completely understood it is believed that the main product is a tetrahydroxyborate anion, as shown in Equation 3.7 ^(52,53). A schematic representation of the mechanism of the catalysed reduction of 4-nitrophenol to 4-aminophenol at silver nanoparticles is shown in Scheme 3.3.



Scheme 3.3: Mechanistic model of the reduction of 4-nitrophenol by NaBH_4 in the presence of silver nanoparticles (yellow spheres). The particles are contained in a polyacrylamide/PVP matrix.

3.3.6.2.2 4-Nitrophenol Reduction at PAAm-PVP and PAAm-PVP -Ag-np Composites

As reported in the literature, this reduction reaction does not take place without the presence of a catalyst^(47,54). To eliminate any catalytic contribution to the reduction reaction from the matrix, discs of the PAAm-PVP composite containing no silver were placed in a solution of 4-nitrophenol and NaBH₄ and the absorbance was monitored every 8 min over a 30-min period. As shown in Figure 3.28, there is little or no change in the absorbance and this shows that the hydrogel matrix does not have the ability to catalyse the reduction of 4-nitrophenol.

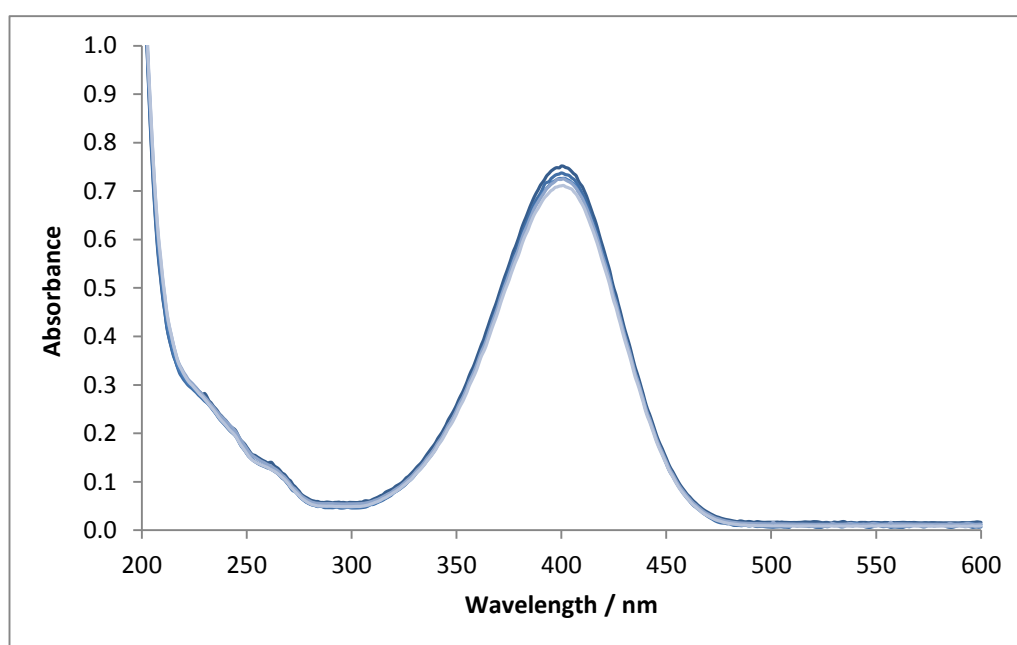


Figure 3.28: UV-Vis spectra of a 9 mL solution containing $4.0 \times 10^{-5} \text{ mol dm}^{-3}$ 4-nitrophenol and $6.7 \times 10^{-2} \text{ mol dm}^{-3}$ NaBH₄ with three PAAm-PVP discs added.

As outlined in the Experimental chapter, the reduction of 4-nitrophenol was studied by immersing three fully swollen PAAm-PVP-Ag-np discs in a solution containing 3 mL of $1.2 \times 10^{-4} \text{ mol dm}^{-3}$ 4-nitrophenol and 6 mL of 0.1 mol dm^{-3} NaBH₄ to give a final solution concentration of $4.0 \times 10^{-5} \text{ mol dm}^{-3}$ 4-nitrophenol and $6.7 \times 10^{-2} \text{ mol dm}^{-3}$ NaBH₄. An initial UV-Vis spectrum of the solution was taken before the discs were added and this is labelled as time zero. The UV-Vis spectra were then recorded as a function of time, and the spectra recorded over a 60 min period are shown in Figure 3.29. A decrease in the absorbance at 400 nm is

observed once the hydrogel discs are added. This decrease coincides with the appearance of a new band at 300 nm. This peak is attributed to the product of the reduction reaction, 4-aminophenol ⁽⁵⁵⁾.

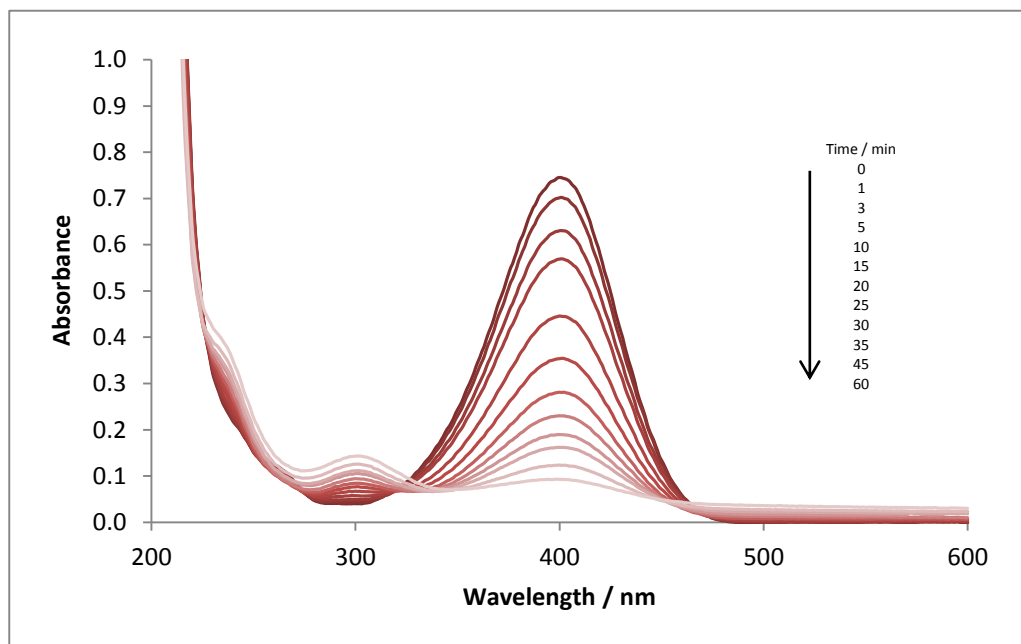


Figure 3.29: UV-Vis spectra of a 9 mL solution containing $4.0 \times 10^{-5} \text{ mol dm}^{-3}$ 4-nitrophenol and $6.7 \times 10^{-2} \text{ mol dm}^{-3}$ NaBH_4 with three PAAm-PVP-Ag-np discs added.

3.3.6.2.3 Rate Constant for the Reduction of 4-Nitrophenol at PAAm-PVP-Ag-np Composite

Once it was established that the composite served as a catalyst for the reduction of 4-nitrophenol, the rate constant for the reaction was ascertained. The reaction conditions used ensured that the concentration of NaBH_4 largely exceeded the concentration of 4-nitrophenol. Therefore, the reaction rates can be assumed to be independent of the NaBH_4 concentration and first-order kinetics with respect to the 4-nitrophenol concentration can be used to evaluate the catalytic rate ^(56,57).

Hence, the apparent rate constant (k_{app}) can be defined using Equation 3.8 where c_t is the concentration of 4-nitrophenol at time t and k_1 is the rate constant normalised to the surface area, S .

$$-\frac{dc_t}{dt} = k_{app}c_t = k_1Sc_t \quad 3.8$$

The absorbance recorded at 400 nm is shown as a function of time in Figure 3.30. Discs of the PAAm-PVP-Ag-np composite were immersed in a continuously stirred solution of $4.0 \times 10^{-5} \text{ mol dm}^{-3}$ 4-nitrophenol with $6.7 \times 10^{-2} \text{ mol dm}^{-3}$ NaBH_4 and the absorbance was recorded as a function of time. The experiments were repeated five times and the average absorbance is plotted in Figure 3.30. It is clear that the absorbance decays indicating the reduction of 4-nitrophenol. The absorbance decreases to values of approximately 0.06 after 3600 s, corresponding to the near complete reduction of the 4-nitrophenol solution. A linear correlation between the logarithm of the absorbance (absorbance at λ_{max} of 400 nm for the 4-nitrophenolate ion) and time was obtained and a typical plot is shown in Figure 3.31. This linear relationship is consistent with first-order kinetics. Using the slope of the linear graph in Figure 3.31 a rate constant of $7.4 \times 10^{-4} \text{ s}^{-1}$ was obtained.

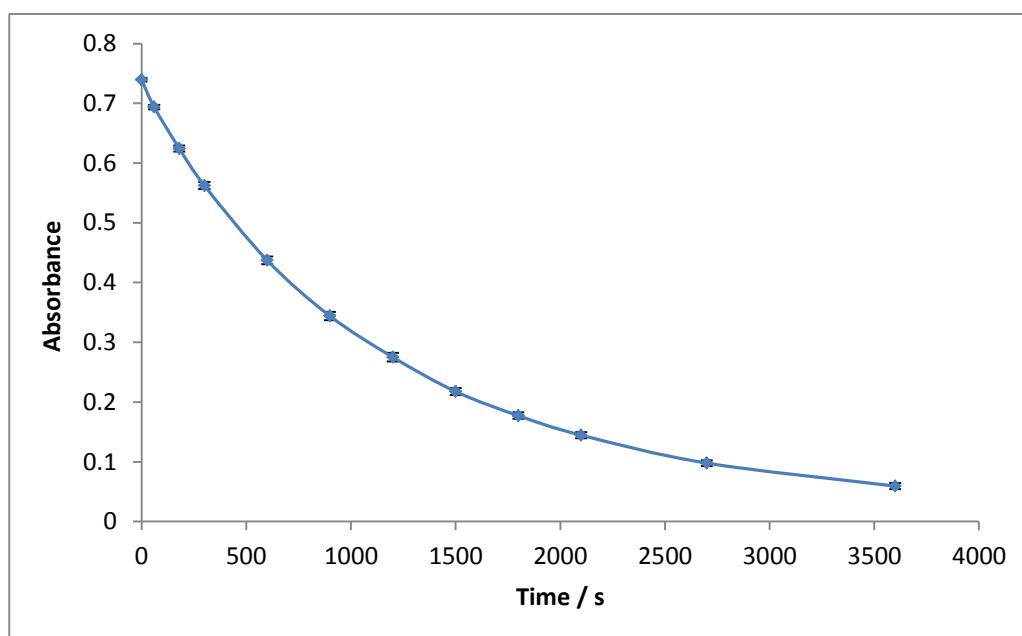


Figure 3.30: Plot of the absorbance at λ_{max} as a function of time for the catalytic reduction of 4-nitrophenol ($n=5$) in a 9 mL aqueous solution containing $4.0 \times 10^{-5} \text{ mol dm}^{-3}$ 4-nitrophenol and $6.7 \times 10^{-2} \text{ mol dm}^{-3}$ NaBH_4 with three PAAm-PVP-Ag-np discs added.

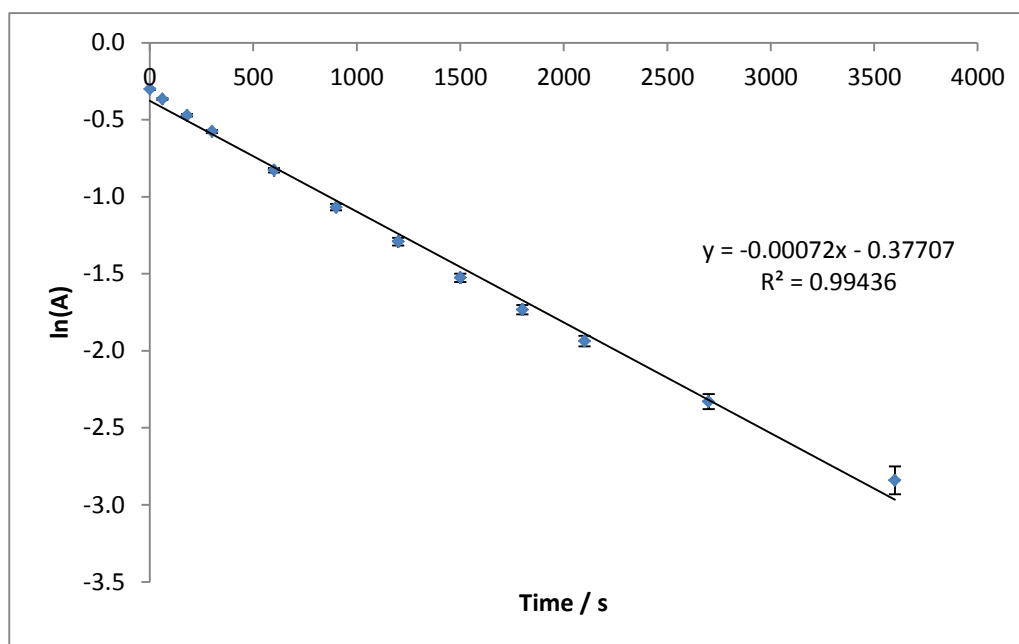


Figure 3.31: Plot of the logarithm of absorbance at λ_{\max} as a function of time for the catalytic reduction of 4-nitrophenol ($n=5$) in a 9 mL aqueous solution containing $4.0 \times 10^{-5} \text{ mol dm}^{-3}$ 4-nitrophenol and $6.7 \times 10^{-2} \text{ mol dm}^{-3}$ NaBH_4 with three PAAm-PVP-Ag-np discs added.

Comparing rate constants for different nanoparticle systems is often attempted in the literature ^(51,58). Many reports show how the rate is very often dependent on the amount of catalyst or the surface area ^(56,59). Others have shown that the surface area is less important and that the nature of the material or its crystallinity governs the catalytic activity ^(57,60). Since the reduction of 4-nitrophenol involves adsorption of the molecules prior to reduction, attempts were made to calculate the rate constant per unit surface area. A few different techniques have been employed to ascertain the surface area of nanoparticles. Ballauff and co-workers used a combination of thermogravimetric analysis and transmission electron microscopy to calculate the theoretical specific surface area ^(48,56,61). These calculations involve many assumptions and estimations including choosing the density of bulk silver as a substitute for the density of the silver nanoparticles. Alternatively, Zhang and co-workers used BET to determine the surface area of silver nanodendrites ⁽⁵⁷⁾. Others simply express the rate constant normalised to the silver concentration used in the synthesis of the nanoparticles in order to compare

to other literature values ⁽⁵¹⁾. The usefulness of these comparisons is questionable since many assumptions are made in the calculations and many other factors come into play once the nanoparticles are immobilised on a surface or in a matrix such as a hydrogel. Diffusion of the reactants and products through the matrix now becomes important in the evaluation of the rate constant. Since the hydrogel nanoparticle composite is a very porous material and has swelling properties, the surface area is very difficult to determine and, additionally, is related to the bulk material rather than the active catalytic surface only.

In this study, the rate of the reaction was monitored as a function of the number of discs used. This is probably a more useful expression of the catalytic activity of the composite and the data may be used to show if the rate of the reaction is indeed dependent on the surface area. Different numbers of discs, ranging from one to six, were immersed in the 4-nitrophenol solution and the absorbance of the solution was measured and the data were fitted to first-order kinetics to obtain the rate constant. Figure 3.32 shows how the rate constant changes with different numbers of discs. It shows that the rate changes linearly with disc number, indicating that the rate is dependent on the surface area. From the slope of the graph, the rate constant per disc for this set of reaction conditions can be expressed as $2.3 \times 10^{-4} \text{ s}^{-1}$ per disc. While this is difficult to compare to other literature values for the reasons mentioned above, the time for the complete reduction of the 4-nitrophenol with the conditions used in this study is comparable to other studies in the literature. Similar studies were reported by Lu and co-workers on a composite hydrogel made from a poly(vinyl alcohol) matrix containing silver nanoparticles ⁽⁶²⁾. Similarly, the hydrogels were cut into discs of a diameter of 1 cm and a length of 5 mm. When the reaction conditions in the present experiment were scaled to closely match the conditions used by Lu and co-workers the rates are very comparable. Lu and co-workers reported a rate constant of $7.0 \times 10^{-4} \text{ s}^{-1}$ for one disc in a solution containing $1.0 \times 10^{-4} \text{ mol dm}^{-3}$ 4-nitrophenol, while in this study the rate constant was calculated as $2.3 \times 10^{-4} \text{ s}^{-1}$ for a solution containing $4.0 \times 10^{-5} \text{ mol dm}^{-3}$ 4-nitrophenol. Literature reports quoting the time required to complete the reduction can vary from 10 min to 60 min. The PAAm-PVP-Ag-np

composite falls within this time range and so is deemed to be an adequate heterogeneous material for this reduction reaction.

Faster reduction rates may be obtained if the surface area of the catalyst is increased and this is possible by making the discs smaller. While the PAAM-PVP-Ag-np composite may not be the fastest catalyst for this reaction it does offer advantages over other materials described in the literature. The use of silver nanoparticles embedded in a matrix or on a solid support facilitates catalyst retrieval. Catalysts in the form of powders are easily lost during filtration or magnetic separation and washing. Efficient retrieval and recycling of the catalyst may be more important than speed of reaction from a cost perspective. Another important parameter is the reusability of the catalyst. In the next section, the performance of the hydrogel nanoparticle composite is studied as a function of the number of repeated uses, i.e., the reusability of the catalyst.

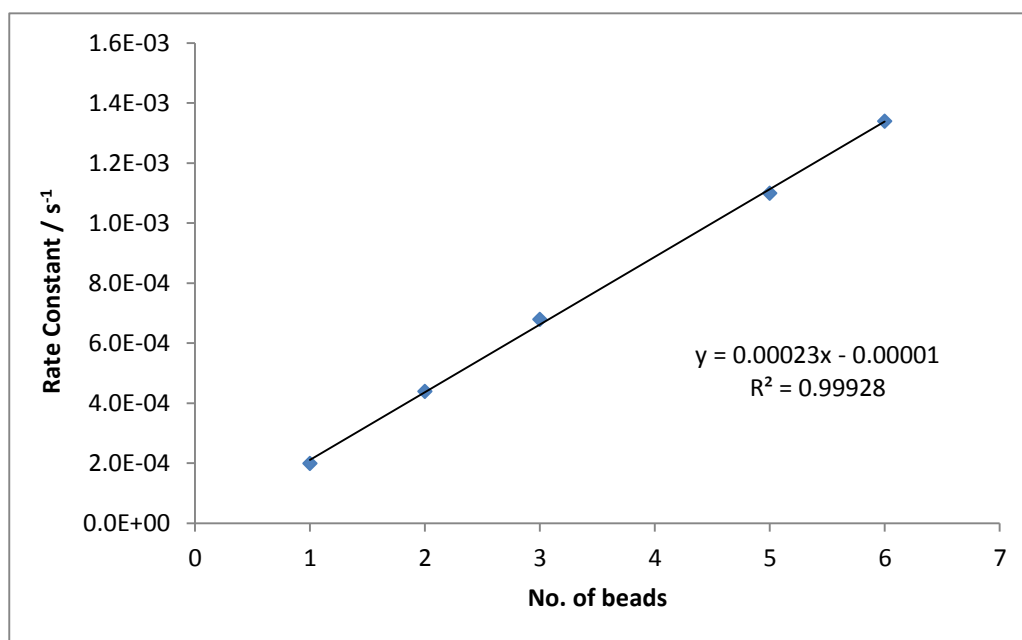


Figure 3.32: Plot of the rate constant as a function of time for the catalytic reduction of a 4-nitrophenol solution with different numbers of PAAM-PVP-Ag-np discs. Solution is a 9 mL aqueous solution containing $4.0 \times 10^{-5} \text{ mol dm}^{-3}$ 4-nitrophenol and $6.7 \times 10^{-2} \text{ mol dm}^{-3}$ NaBH₄.

3.3.6.2.4 Reusability of the PAAm-PVP-Ag-np Composite as a Catalyst

The repeated use of the same catalyst sample or the recycling of the catalyst is often investigated in the literature and the outcomes are varied. Narayanan and El-Sayed discussed how the surface atoms of a nanoparticle may be so active that the size and shape of nanoparticle could change over the course of the catalytic reaction and affect their recycling potential ⁽⁶³⁾. Many authors report excellent reproducibility ⁽⁶⁴⁾ and others show a rapid decline in the performance over successive runs, as reflected in a decrease in the rate constant ⁽⁶⁵⁾. The performance of the PAAm-PVP-Ag-np composite was studied by exposing three discs to a solution containing $4.0 \times 10^{-5} \text{ mol dm}^{-3}$ 4-nitrophenol and $6.7 \times 10^{-2} \text{ mol dm}^{-3}$ NaBH₄. The reduction of 4-nitrophenol was monitored over a period of 60 min and then the discs were exposed to a fresh solution of 4-nitrophenol. This was repeated five times and the results are shown in Figure 3.33. Clearly, the same batch of discs can be used five times with little change in their effectiveness as catalysts for the reduction reaction, as indicated by the small error bars. A plot of the logarithm of the absorbance as a function of time is shown in Figure 3.34. Excellent linearity is maintained upon repeated uses. The rate constants were calculated for each use and these are presented in Figure 3.35. Only a small decrease in the rate constant is observed with successive runs. This decrease in rate can be explained by an accumulation of 4-aminophenol within the discs. Diffusion of the 4-nitrophenol from the matrix is not sufficient to remove the molecule and this could potentially block the way for 4-nitrophenol molecules to come close enough to the surface of the nanoparticles for the reduction reaction. It is possible that more washing may be required to remove the entire 4-aminophenol product effectively. Indeed, it was found that when the discs were washed for 1 day (run 5, Figure 3.36), as opposed to 20 min, the slope returned closer to the original value, indicating a near constant rate constant value. The rate constant was only 8% lower compared to the first use of the discs.

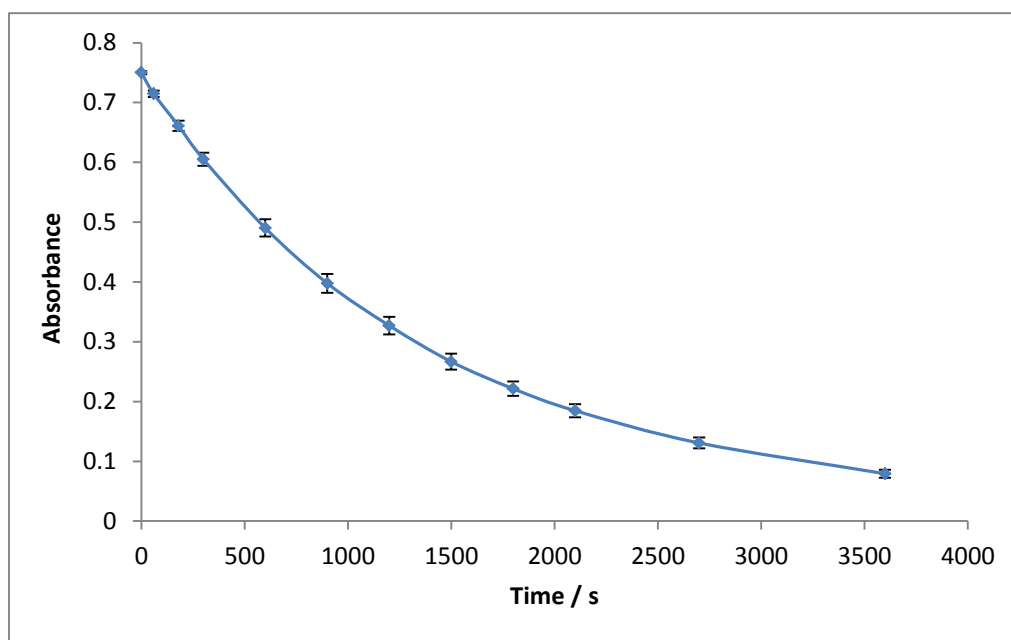


Figure 3.33: Plot of the absorbance at λ_{\max} as a function of time for the catalytic reduction of 4-nitrophenol using the same set of discs 5 times. Solution is a 9 mL aqueous solution containing $4.0 \times 10^{-5} \text{ mol dm}^{-3}$ 4-nitrophenol and $6.7 \times 10^{-2} \text{ mol dm}^{-3}$ NaBH_4 with three PAAm-PVP-Ag-np discs added.

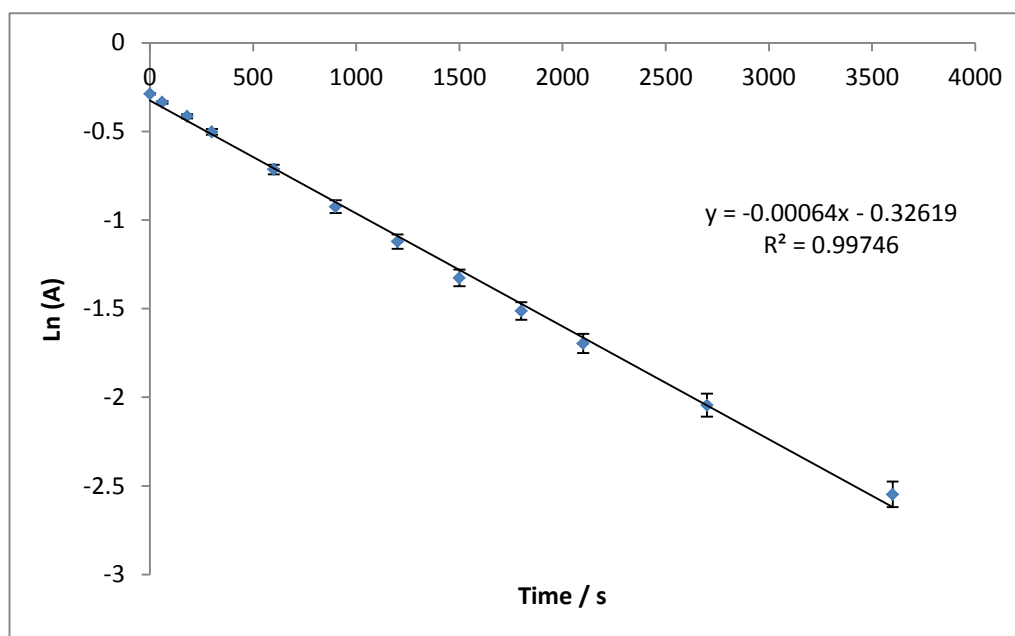


Figure 3.34: Plot of logarithm of the absorbance at λ_{\max} as a function of time for the catalytic reduction of 4-nitrophenol using the same set of discs 5 times. Solution is a 9 mL aqueous solution containing $4.0 \times 10^{-5} \text{ mol dm}^{-3}$ 4-nitrophenol and $6.7 \times 10^{-2} \text{ mol dm}^{-3}$ NaBH_4 with three PAAm-PVP-Ag-np discs added.

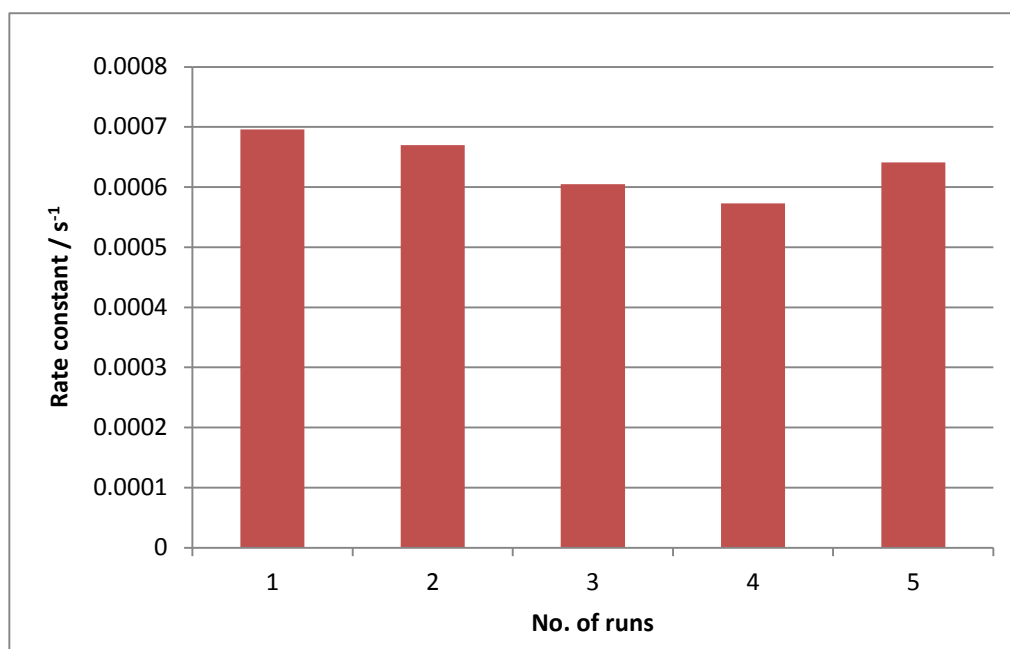


Figure 3.35: Rate constant values for the catalytic reduction of 4-nitrophenol using the same set of discs 5 times. Solution is a 9 mL aqueous solution containing $4.0 \times 10^{-5} \text{ mol dm}^{-3}$ 4-nitrophenol and $6.7 \times 10^{-2} \text{ mol dm}^{-3}$ NaBH_4 with three PAAm-PVP-Ag-np discs added.

There are mixed reports in the literature about the reusability of silver nanoparticle-based catalysts. Some report excellent reproducibility and conclude that the catalysts can be reused many times with little or no decrease in the rate, whereas for other materials the performance decreases with consecutive runs⁽⁵¹⁾. While the rate constant obtained in this work may not be as fast as some of the reported systems in the literature, these hydrogel composites offer other benefits including simple synthesis, easy removal from the reaction media and good reusability.

3.3.6.2.5 Reduction of 4-Nitrophenol at Rehydrated PAAm-PVP-Ag-np Composite Discs

From a practical point of view, the storage of the discs in a dried form is more useful. In this section, results are presented and discussed on the performance of the PAAm-PVP-Ag-np composite discs to catalyse the 4-nitrophenol reduction reaction once dried and subsequently rehydrated. In this study, five sets of discs were dried and then rehydrated and the catalytic activity of these discs was compared to freshly prepared discs. The absorbance at 400 nm was monitored as a function of time and the logarithm of the absorbance is shown plotted as a function of time in Figure 3.36 for the fresh and rehydrated discs. Excellent linearity is obtained for both the rehydrated and freshly prepared discs. Furthermore, the slopes are very similar and this shows that it is possible to store the dehydrated discs for long periods of time with the discs remaining effective catalysts for the reduction of 4-nitrophenol.

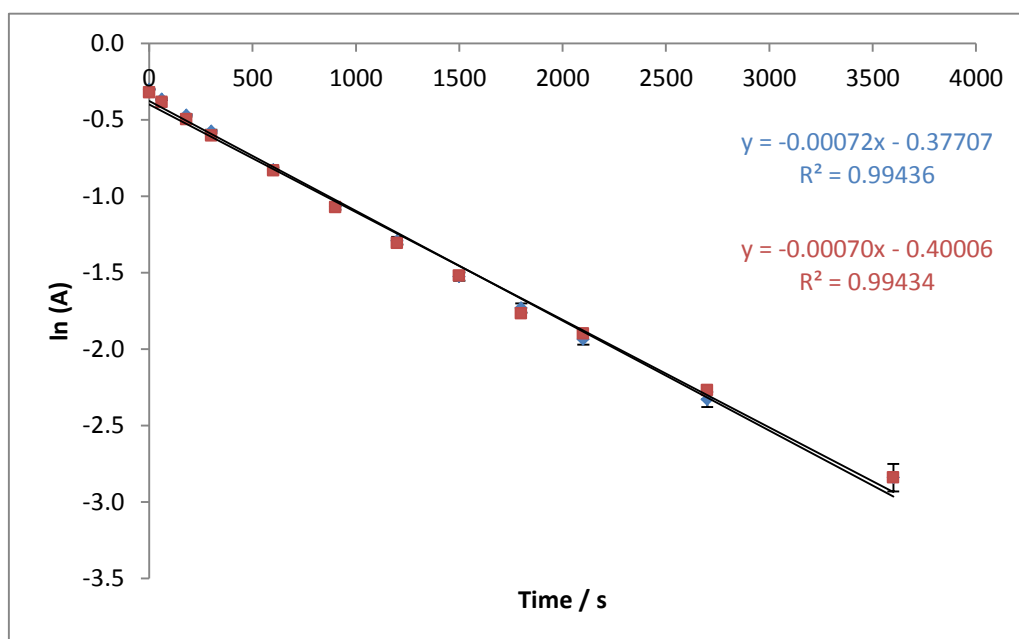


Figure 3.36: Plot of logarithm of absorbance at λ_{\max} as a function of time for the catalytic reduction of 4-nitrophenol. Blue trace is freshly prepared discs and red trace is rehydrated discs. Solution is a 9 mL aqueous solution containing $4.0 \times 10^{-5} \text{ mol dm}^{-3}$ 4-nitrophenol and $6.7 \times 10^{-2} \text{ mol dm}^{-3}$ NaBH_4 with three PAAm-PVP-Ag-np discs added.

3.3.6.3 Anti-Bacterial Activity of Polyacrylamide-PVP-Protected Silver Nanoparticle Composite

3.3.6.3.1 Introduction

Bacteria are simple unicellular organisms which can be divided into two main classes based on differences in the structure of their cell wall. These are Gram-positive and Gram-negative bacteria. The names originate from a staining technique developed by Hans Christian Gram which can differentiate between the two types of cell wall. Cells with a thick cell wall containing up to forty layers of peptidoglycan stain dark purple when exposed to the primary dye, crystal violet, and are referred to as gram-positive bacteria. Gram-negative bacteria, with walls consisting of only a few layers of peptidoglycan, stain pink as they retain the counter staining dye called safranin. In general, Gram-negative bacteria are more pathogenic than gram-positive bacteria. This is due to a number of factors. Gram-negative bacteria have an additional outer layer coated with hydrophilic lipopolysaccharides which prevent many lipophilic antibiotics from entering the cell. Additionally, many antibiotics act to interrupt mechanisms which form crosslinks in the cell wall and are therefore more effective on Gram-positive bacteria. Here, silver has a distinct advantage over traditional antibiotics in the fight against Gram-negative bacteria such as *E. coli*. The hydrophilic nature of silver ions means they can effectively enter Gram-negative bacteria through the outer membrane pores. However, it also means that entry into Gram-positive bacteria is more difficult due to the presence of the thick hydrophobic peptidoglycan layer and lack of membrane pores ⁽⁶⁶⁾.

There is a constant demand for new, cost effective antimicrobial agents as the emergence of multi-drug resistant bacterial strains is a constant threat to public health. Silver-based materials have shown great promise as they exhibit broad-spectrum antibacterial activity ⁽⁶⁷⁾. Silver immobilised in polymers is of particular interest as it offers a means to deliver slow release biocidal activity over long periods ⁽⁶⁸⁾. In addition, it offers a chemically stable environment for the silver compound and the polymers are relatively low in cost.

In this study, plate assays were used to assess whether the PAAm-PVP-Ag-np composite exhibited any antibacterial activity. All the materials tested were evaluated against five different strains of bacteria. Gram-positive bacteria, *S. aureus* and MRSA, and Gram-negative bacteria, *P. aeruginosa* (ATCC 27853), *P. aeruginosa* (ATCC 10145) and *E.coli* were the five strains used in this study. The experimental procedure used to carry out the plate assay is described in Chapter 2, Section 2.4.1.5. Four hydrogels were tested in the plate assay study and descriptions of the hydrogel composition are outlined in Table 3.4. As a control, PAAm-PVP gels containing no silver were tested alongside gels containing silver. PAAm hydrogels containing two different amounts of PVP-protected silver nanoparticles were tested as well as a PAAm-PVP gel that contained non-reduced silver as AgNO₃. Figure 3.37 shows a typical plate assay. Each material was tested five times, n = 5.

Table 3.4: Composition of hydrogels used in the antibacterial study.

Hydrogel	AAm/g	MBA/g	PVP solution	AP	TEMED/ μL
PAAm-PVP	4.0	0.175	10 mL of 423.75 g dm^{-3} PVP in water	400 μL of a 1% solution	10
PAAm-PVP-Ag-np-10mL	4.0	0.175	10 mL of 423.75 g dm^{-3} PVP with silver-np	300 μL of a 1% solution	5
PAAm-PVP-Ag-np-5mL	4.0	0.175	5 mL of 423.75 g dm^{-3} PVP with silver-np and 5 mL of 423.75 g dm^{-3} PVP in water	300 μL of a 1% solution	5
PAAm-PVP-Ag-ions	4.0	0.175	10 mL of 423.75 g dm^{-3} PVP in $50 \times 10^{-3} \text{ mol dm}^{-3}$ AgNO_3	300 μL of a 1% solution	5

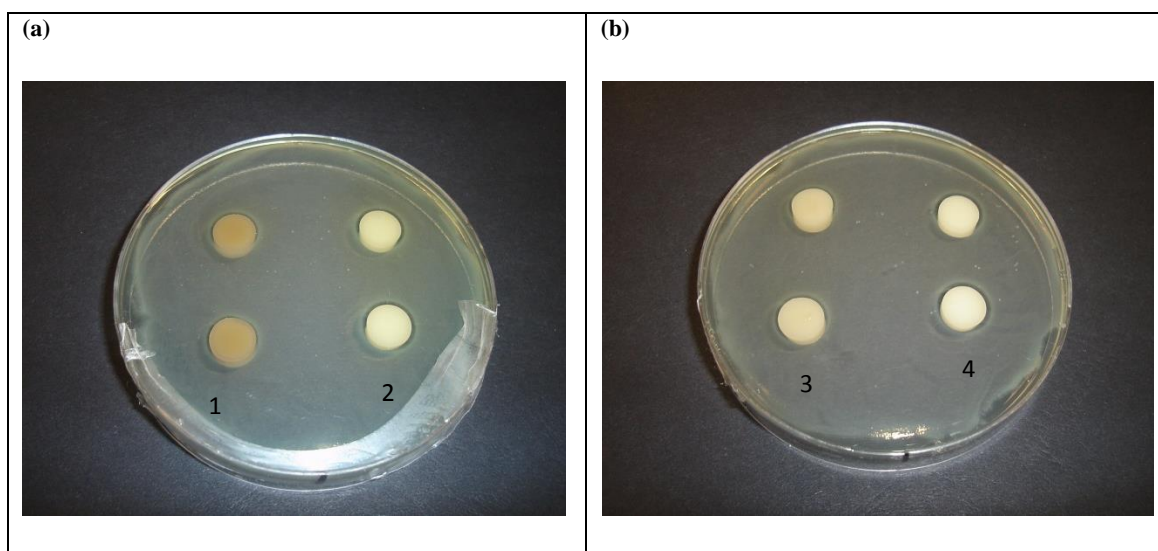


Figure 3.37: Photograph of a typical *P. aeruginosa* (ATCC 10145) plate assay for (1) PAAm-PVP-Ag-np-10 mL, (2) PAAm-PVP-Ag⁺-ions discs, (3) PAAm-PVP-Ag-np-5 mL and (4) PAAm-PVP-Ag⁺-ions discs.

3.3.6.3.1 Plate Assay on *S. aureus*

S. aureus is a Gram-positive bacterium. The colonies of these Gram-positive bacteria grow in a cluster of yellow-white spheres, as shown in Figure 3.38. This species is non-motile and non-spore forming and can undergo respiration in the presence of air and change to fermentation in its absence. *S. aureus* is the most common strain of the *Staphylococci* bacteria. In general, it only results in disease when the bacteria penetrate the bodies protective mechanisms where there is skin damage. Common infections caused by *S. aureus* are bacteraemia, endocarditis and pneumonia.

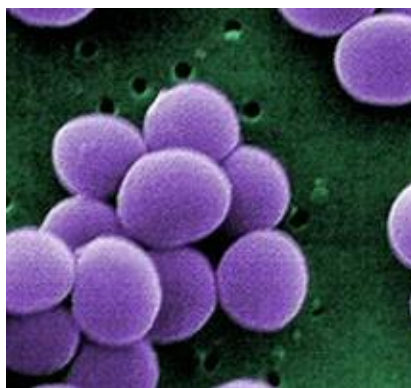


Figure 3.38: Electron micrograph of artificially stained *S. aureus*.⁽⁶⁹⁾

The anti-bacterial results for the different hydrogel composites are collated in Figure 3.39 and Table 3.5. The composite containing no silver has only a minor degree of inhibition against *S. aureus*. The largest zone of inhibition (ZOI) was observed for the composite containing AgNO_3 where the silver was not reduced. Hydrogel composites containing silver nanoparticles, where silver is maintained in the zero oxidation state, display a smaller zone than that observed for composites containing the silver ion, Ag^+ . This indicates that silver in the zero oxidation state, Ag , is not as effective at inhibiting the growth of *S. aureus* as the Ag^+ ion. This substantiates what has already been discussed in the Introduction chapter, where metallic silver is known to be inert to both human and bacterial cells and that it is the silver (I) ion, Ag^+ , which has the capability to bind to cell surface receptors and interrupt cell metabolism. The protective environment afforded by the hydrogel composite to the silver nanoparticles may slow down the release of silver ions to

the surrounding area. While in the short term it may appear that the electrochemical reduction of silver is an unnecessary step to inhibit bacterial growth, the nanoparticles-hydrogel composites could be viewed as a means of achieving long term antibacterial action.

Table 3.5: Results for the plate assay on *S. aureus* for the different hydrogel composites. ZOIs were recorded after 24 hours incubation at $37 \pm 1^\circ \text{C}$.

Hydrogel	Zone of Inhibition (mm^2)	Description
PAAm-PVP	1.6 ± 0.5	Zone of inhibition
PAAm-PVP-Ag-np-10 mL	10.7 ± 0.8	Zone of inhibition
PAAm-PVP-Ag-np-5 mL	5.8 ± 0.9	Zone of inhibition
PAAm-PVP-Ag-ions	18.1 ± 1.8	Zone of inhibition

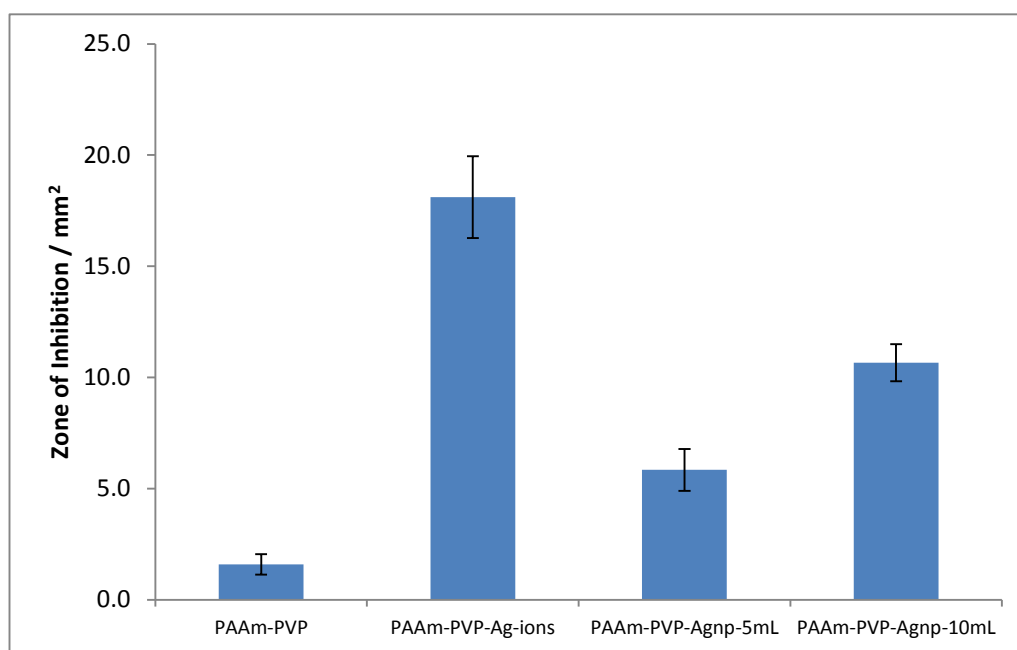


Figure 3.39: ZOI for the growth of *S. aureus* measured for the plate assay. ZOIs were recorded after 24 hours incubation at $37 \pm 1^\circ \text{C}$.

3.3.6.3.2 Plate Assay on Methicillin-Resistant *S. aureus* (MRSA)

MRSA is any strain of *S. aureus* that has developed a resistance to β -lactam antibiotics and, like *S. aureus*, is a Gram-positive, facultative, anaerobic, coccus bacterium, Figure 3.40. This resistance makes an infection by MRSA particularly difficult to treat and the increasing incidence of infections in hospitals means MRSA is now considered a global health concern.

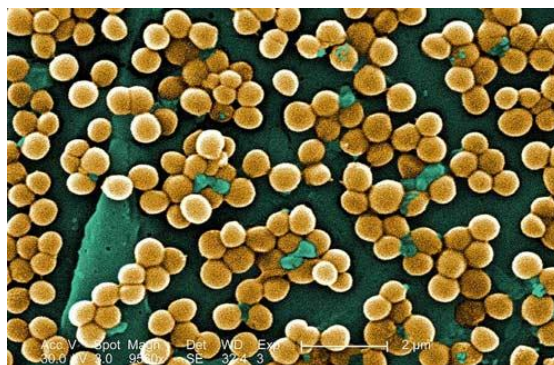


Figure 3.40: Electron micrograph of artificially stained methicillin-resistant *S. aureus* ⁽⁷⁰⁾.

The results for the different hydrogel composites are compared in Figure 3.41 and Table 3.6. A similar trend to that observed for *S. aureus* is seen for the plate assays against MRSA, although the overall ZOIs are somewhat smaller. Again, minimal inhibition is observed for the hydrogels containing no silver, and silver in the +1 oxidation state, Ag^+ , is the most effective at inhibiting growth of MRSA around the disc. It is surprising that there is not a more significant difference between the hydrogels with different amounts of PVP-protected nanoparticles. Composites containing 5 mL of PVP-protected Ag nanoparticles have zones of approximately 6.4 mm^2 in diameter whereas zones of about 7.9 mm^2 are observed for hydrogels containing 10 mL.

Table 3.6: Results for the plate assay on MRSA for the different hydrogel composites. ZOIs were recorded after 24 hours incubation at $37 \pm 1^\circ \text{C}$.

Hydrogel	Zone of Inhibition (mm^2)	Description
PAAm-PVP	2.8 ± 0.6	Zone of inhibition
PAAm-PVP-Ag-np-10mL	7.9 ± 0.7	Zone of inhibition
PAAm-PVP-Ag-np-5mL	6.4 ± 0.5	Zone of inhibition
PAAm-PVP-Ag-ions	12.0 ± 1.0	Zone of inhibition

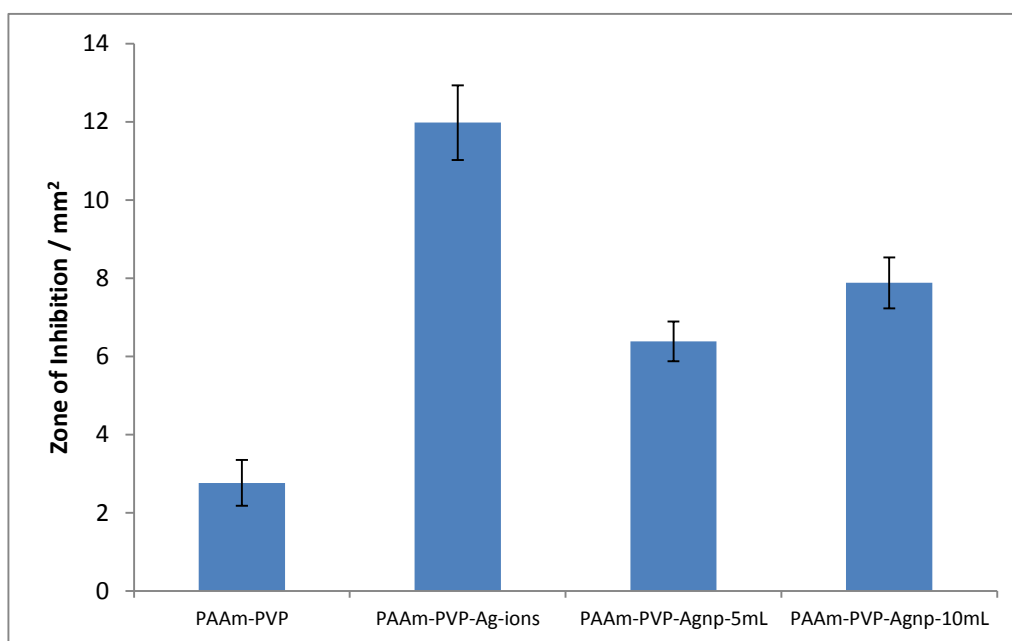


Figure 3.41: ZOI for the growth of MRSA measured for the plate assay. ZOIs were recorded after 24 hours incubation at $37 \pm 1^\circ \text{C}$.

3.3.6.3.3 Plate Assay on *Escherichia coli* (*E. coli*)

E. coli are a Gram-negative, rod shaped bacteria, typically 2.0 μm in length, as shown in Figure 3.42. These bacteria have the ability to grow hair-like structures called flagella which confer mobility to the bacteria and allow it to attach to human cells. Most *E. coli* strains are harmless and are part of the normal flora of the lower intestine and are in fact beneficial. It is only when these bacteria move outside of the intestine that infection can set in. For example, bladder and kidney infections are as a result of bacteria moving to the urinary tract. The pathogenic *E. coli* strains found on contaminated foods produce toxins that can result in symptoms including diarrhoea and intestinal inflammation.



Figure 3.42: Electron micrograph of artificially stained *Escherichia coli* ⁽⁷¹⁾.

The results for the different hydrogel composites are collated in Figure 3.43 and Table 3.7. It was expected that the results of the plate assays for *E. coli* would support other studies which show Gram-negative bacteria to be more susceptible to the effect of silver than Gram-positive strains such as *S. aureus*. However, as the data in Table 3.7 and Figure 3.43 show, these results are quite similar to those recorded for the MRSA bacteria. This is consistent with the findings of Ma and co-workers, where chitosan-nylon-6 membranes impregnated with silver(I) show no difference in the bacteriostatic effect against both *E. coli* and *S. aureus*. Again, Ag^+ has the largest inhibitory effect on *E. coli* growth and the size of the ZOI does not increase significantly upon doubling the concentration of silver nanoparticles within the composite.

Table 3.7: Results for the plate assay on *E. coli* for the different hydrogel composites. ZOIs were recorded after 24 hours incubation at $37 \pm 1^\circ \text{C}$.

Hydrogel	Zone of Inhibition (mm^2)	Description
PAAm-PVP	0.4 ± 0.2	Zone of inhibition
PAAm-PVP-Ag-np-10 mL	5.4 ± 1.3	Zone of inhibition
PAAm-PVP-Ag-np-5 mL	4.0 ± 0.9	Zone of inhibition
PAAm-PVP-Ag-ions	13.0 ± 1.8	Zone of inhibition

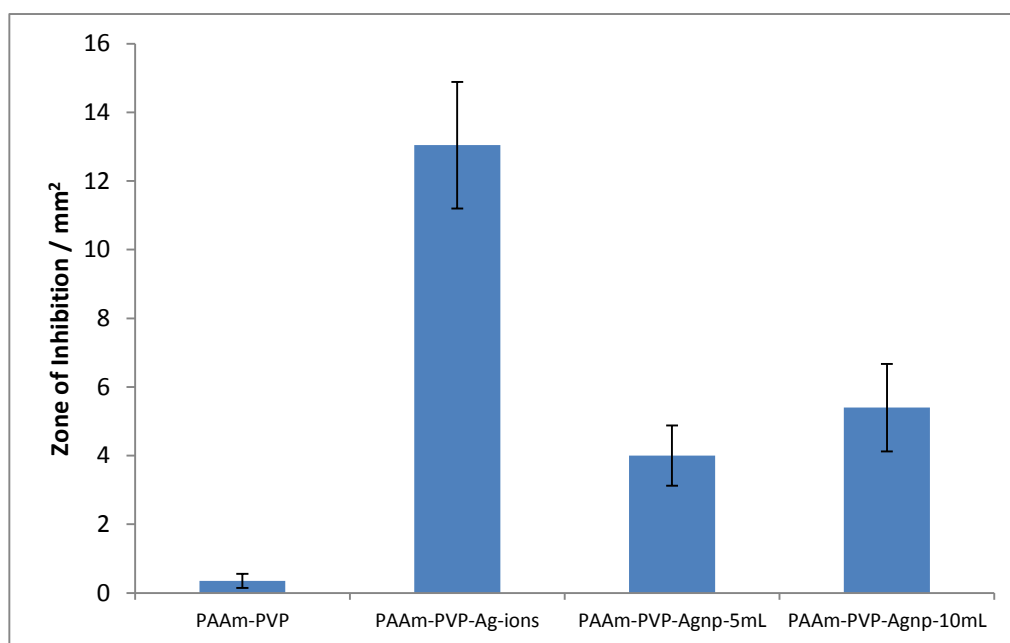


Figure 3.43: ZOI for the growth of *E. coli* measured for the plate assay. ZOIs were recorded after 24 hours incubation at $37 \pm 1^\circ \text{C}$.

3.3.6.3.4 Plate Assay on *Pseudomonas aeruginosa* (27853 and 10145)

P. aeruginosa is also a Gram-negative, rod shaped bacterium measuring 1.5 to 3 μm in length, as shown in Figure 3.44. Although it is classified as an aerobic organism, it can survive in environments with little or no oxygen. Often found in water and soil, it achieves mobility through a flagellum or attaches to surfaces as a biofilm. It is a resilient species which can survive in a wide variety of physical conditions including very high temperatures and where the availability of nutrition is low. It displays a high tolerance to antiseptics, heavy metals and high salt concentrations. Like *S. aureus* and *E. coli*, it is an opportunistic bacterium and only poses a potential health risk if the barrier to infection is broken or if the immune system is compromised. Cystic fibrosis patients are at particular risk since *P. aeruginosa* typically infects the pulmonary tract but can also infect the urinary tract and the blood system.



Figure 3.44: Electron micrograph of artificially stained *P. aeruginosa*.⁽⁷²⁾

Plate assays on two strains of *P. aeruginosa* were performed to test the bactericidal effect of the hydrogel composites. The plate assay results for the different hydrogel composites on the 27853 strain of *P. aeruginosa* are collated in Figure 3.45 and Table 3.8 while in Figure 3.46 and Table 3.9 the measured zones found for the plate assays on strain 10145 are shown.

There are very clear differences in the measured ZOI for the two strains of *P. aeruginosa*. In the case of *P. aeruginosa* 27853, a measurable ZOI (5 mm²) was only visible for hydrogel composites containing silver in the +1 oxidation state. This is the smallest recorded zone for composites containing non-reduced silver of all the bacteria tested. Contrastingly, the largest recorded zones in this study were found on the *P. aeruginosa* 10145 plate assays. These were again seen for hydrogels containing Ag⁺. Increasing the concentration of silver nanoparticles did not proportionally increase the size of the inhibition zones.

Table 3.8: Results for the plate assay on *P. aeruginosa* (ATCC 27853) for the different hydrogel composites. ZOIs were recorded after 24 hours incubation at 37 ± 1° C.

Hydrogel	Zone of Inhibition (mm ²)	Description
PAAm-PVP	-	Direct inhibition
PAAm-PVP-Ag-np-10 mL	-	Direct inhibition
PAAm-PVP-Ag-np-5 mL	-	Direct inhibition
PAAm-PVP-Ag-ions	5.1 ± 0.4	Zone of inhibition

Table 3.9: Results for the plate assay on *P. aeruginosa* (ATCC 10145) for the different hydrogel composites.

Hydrogel	Zone of Inhibition (mm ²)	Description
PAAm-PVP	-	Direct inhibition
PAAm-PVP-Ag-np-10 mL	19.1 ± 0.5	Zone of inhibition
PAAm-PVP-Ag-np-5 mL	17.5 ± 0.3	Zone of inhibition
PAAm-PVP-Ag-ions	32.4 ± 1.0	Zone of inhibition

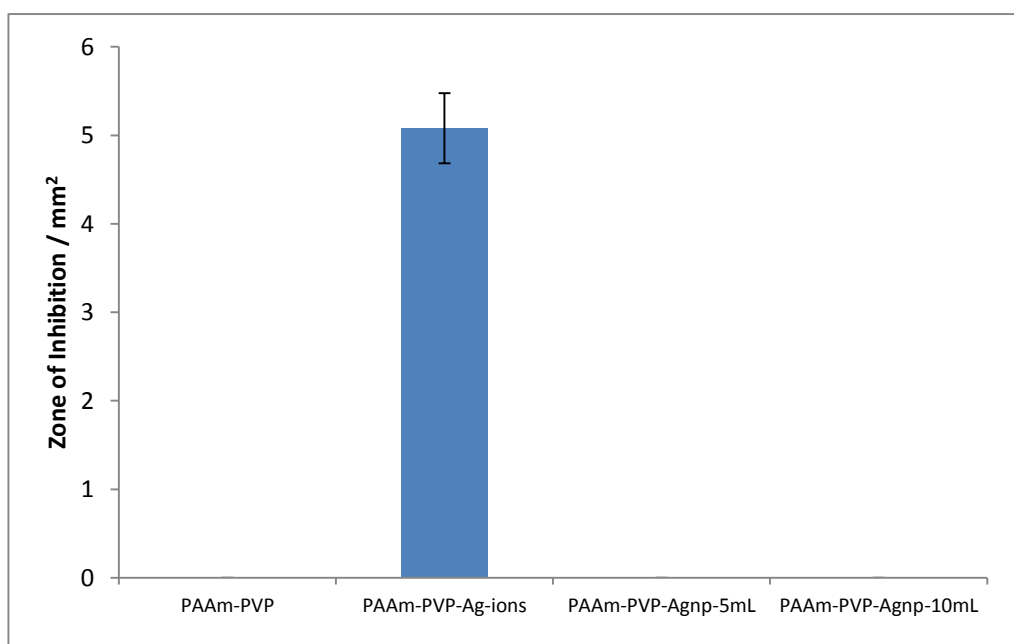


Figure 3.45: ZOI for the growth of *P. aeruginosa* (ATCC 27853) measured for the plate assay. ZOIs were recorded after 24 hours incubation at $37 \pm 1^\circ \text{C}$.

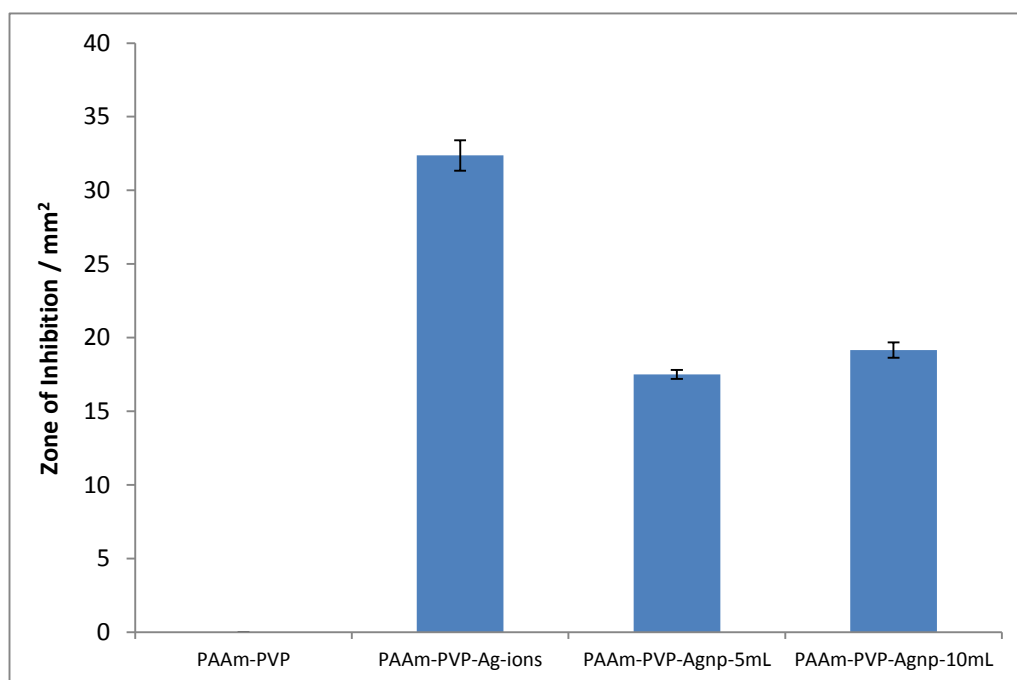


Figure 3.46: ZOI for the growth of *P. aeruginosa* (ATCC 10145) measured for the plate assay. ZOIs were recorded after 24 hours incubation at $37 \pm 1^\circ \text{C}$.

3.3.7 Characterisation of the Polyacrylamide-PVP-Protected Silver Nanoparticle Composite

3.3.7.1 Physical Appearance of Polyacrylamide-PVP-Protected Silver Nanoparticle Composite

The swollen and dried forms of the hydrogel composite discs are shown in Figure 3.47. The gel discs double in diameter, from 0.5 cm in the dried state to 1.0 cm in the fully swollen state. This illustrates the extent to which these gels absorb water and expand. The colour changes from dark brown to yellow upon uptake of water. The texture is also completely different between the two states. In the dried state, the composite is extremely hard and difficult to crush in a pestle and mortar, whereas in the swollen state the composite is gel-like and spongy and is easily cut with a knife.

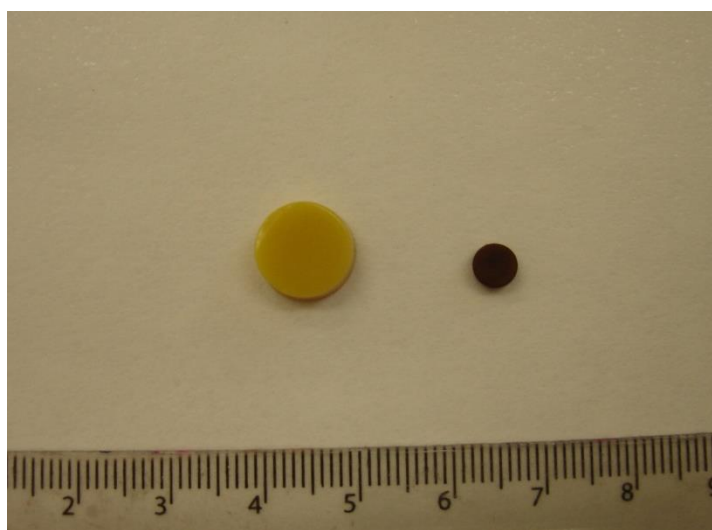


Figure 3.47: Photograph of the fully swollen (left hand side) and the fully dried (right hand side) PAAm-PVP-Ag-np discs.

3.3.7.2 SEM and EDX Analysis of the Polyacrylamide-PVP-Protected Silver Nanoparticle Composite

The surface morphology of the dried PAAm-PVP-protected silver nanoparticles was studied using SEM. The composites were dried and the SEM micrographs are shown in Figure 3.48 at two different magnifications. The surfaces show an almost cauliflower morphology, which is more evident at the higher magnification. The corresponding EDX spectrum is shown in Figure 3.49. This confirms the presence of silver and although its abundance is quite low this is not surprising considering the higher amount of polymer. The carbon and oxygen signals arise from the PAAm-PVP polymer and as these dried discs were sputter coated with a thin layer of gold, a gold signal is also evident.

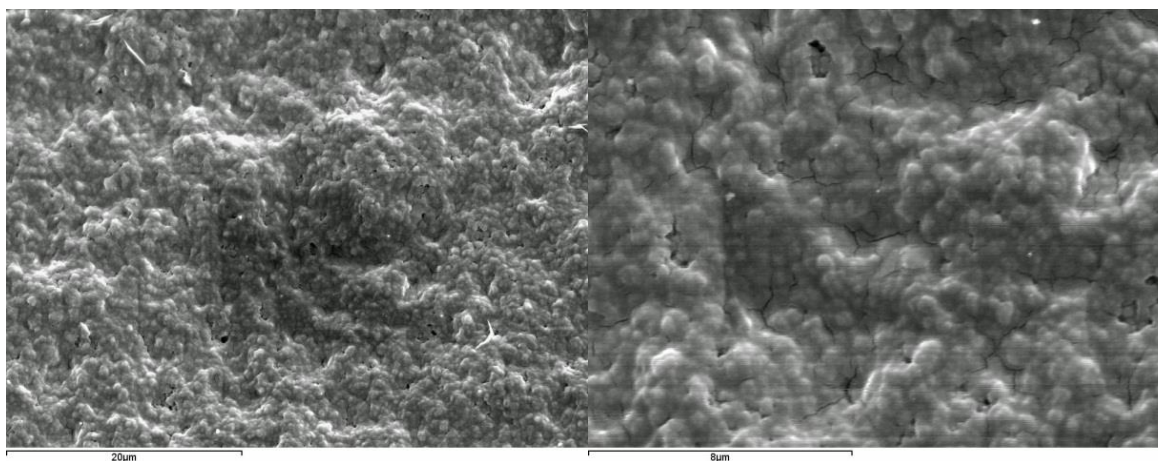


Figure 3.48: SEM micrograph of the surface of the dried PAAm-PVP-Ag-np discs at two different magnifications.

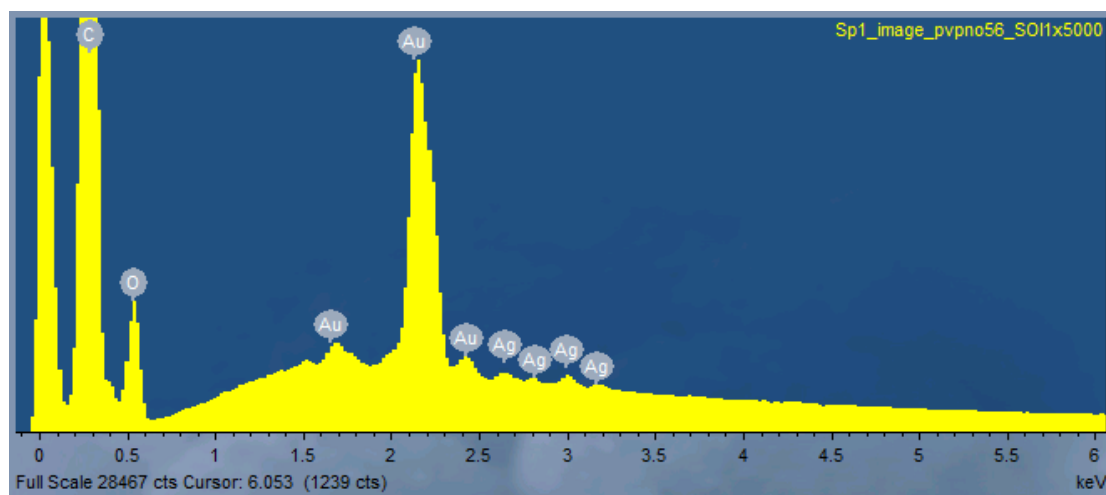


Figure 3.49: EDX spectrum of a fully dried PAAm-PVP-Ag-np disc.

3.3.7.3 Leaching of Silver Nanoparticles from the Hydrogel Matrix

Leaching of nanoparticles from the hydrogel matrix was monitored by placing one disc in 10 mL of water and monitoring the UV-Vis spectra over the course of a month. The absorption band at 425 nm is due to silver nanoparticles. Figure 3.50 illustrates the very slow release of particles from the hydrogel matrix. There is no evidence of leaching after one day immersion and after 4 weeks the absorbance only reached 0.085. This is low considering leaching was monitored into a very small volume, 10 mL.

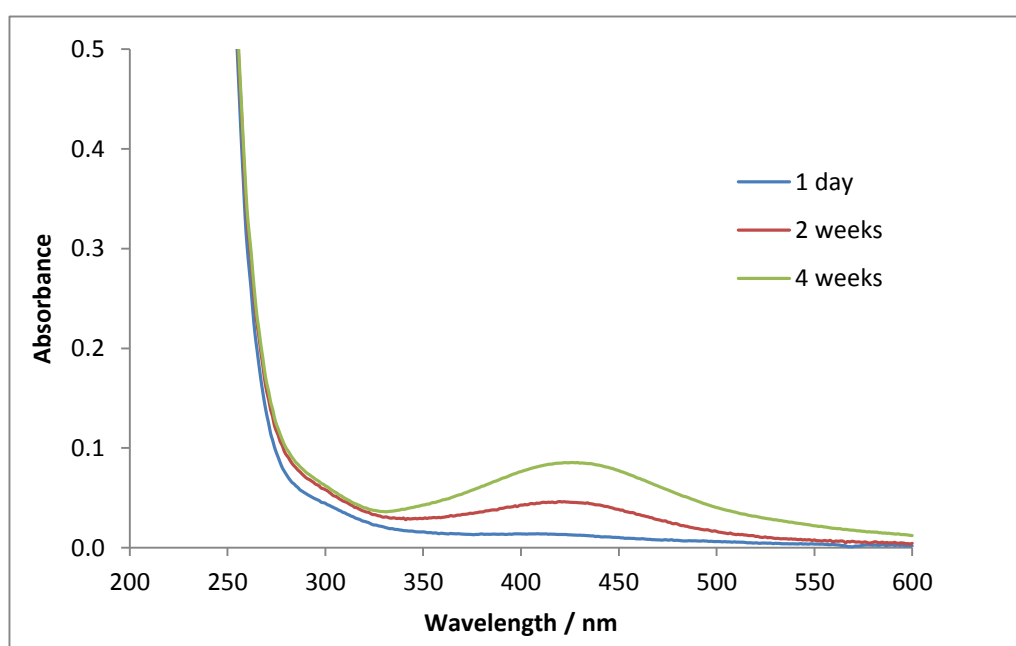


Figure 3.50: The UV-Vis spectra over a month monitoring leaching of silver nanoparticles from one PAAm-PVP-Ag-np disc into 10 mL of H₂O.

3.4 Summary of Results

In this chapter, the synthesis and applications of PVP-protected silver nanoparticles were described and discussed. The effect of PVP on the electrochemistry of the silver ions was first investigated. On addition of PVP to the silver-containing solution, the reduction of the silver ion was inhibited. This was attributed to an increase in the viscosity of the solution, which hinders diffusion of the silver ions to the electrode surface. Furthermore, the PVP chains surround the silver ions, making the electron-transfer step difficult.

The silver nanoparticles were synthesised in a solution containing AgNO_3 , KNO_3 and PVP. The optimum concentrations were 0.05 mol dm^{-3} AgNO_3 , 0.1 mol dm^{-3} KNO_3 , 423.75 g dm^{-3} PVP with an electrochemical pulse of -6.0 V vs Ag^+/Ag . The concentration of silver nanoparticles was monitored using UV-Vis spectroscopy. The silver particles generated at low potentials (from -1.6 V to -1.8 V vs Ag^+/Ag) gave rise to a low concentration of silver particles. Increasing the potential to values of -4.0 V and -6.0 V vs Ag/Ag^+ resulted in a significant increase in the concentration of the nanoparticles. The AgNO_3 and PVP concentrations were varied. At high AgNO_3 concentrations (0.1 mol dm^{-3}), low absorbance values were obtained and a broader absorption band was observed, as insufficient PVP was present to protect the newly formed nanoparticles. A silver ion to PVP ratio of 75:1 gave the highest absorbance, while increasing the PVP concentrations gave rise to a decrease in the silver nanoparticle production due to the viscous nature of the solution at high PVP concentrations. Increasing the period of the potential pulse gave rise to an increase in the concentration of the silver nanoparticles for pulse periods lower than 1200 s. At longer times, agglomeration of the silver nanoparticles was observed. This was explained in terms of an Ostwald ripening phenomenon in which smaller particles dissolve in solution and the silver ions were then deposited on larger particles in order to reach a more thermodynamically stable state. The diameter of the silver nanoparticles generated using the optimum conditions was calculated to be as 5.73 nm by relating the radius of the nanoparticles with the bandwidth of the absorbance band. These nanoparticles showed very good stability and there was only a slight

change in the absorbance band on monitoring the absorbance of the nanoparticles over a 30 day period. However, the addition of AgNO_3 and KNO_3 gave rise to significant changes in the absorbance band. The intensity of the band decreased by 64% and a wider band with an emerging second peak at 486 nm was observed. This was attributed to the additional cations, which enter the diffuse double layer and neutralise the electrostatic forces that prevent aggregation. The additional free Ag^+ ions may be reduced in the presence of PVP which acts as a reducing agent in addition to a protecting agent. Furthermore, the nitrate anion is a potential oxidant and this may lead to the degradation of the PVP chains and the loss of its effectiveness to protect the nanoparticles.

The PVP-protected nanoparticles were immobilised onto a GC electrode and used in the electrochemical detection of nitrates. Poor reproducibility was observed. The silver nanoparticles were then immobilised in a polyacrylamide hydrogel and employed in the electrochemical detection of nitrates and for the reduction of 4-nitrophenol. The presence of the silver was confirmed using energy dispersive X-Ray analysis (EDX). Using the ferrocyanide/ferricyanide electrochemical probe, low peak currents and high peak separations were observed for the polyacrylamide-PVP-protected silver nanoparticles. These findings were explained in terms of diffusion limitations within the hydrogel. Similarly, the composite showed poor detection of nitrates, indicating that the polyacrylamide-PVP-protected silver nanoparticles are not suitable for use as an electrochemical sensor. The polyacrylamide-PVP-protected silver nanoparticles composite was then investigated as a catalyst for the reduction of 4-nitrophenol. The rate of the catalytic reaction was studied using UV-Vis spectroscopy by monitoring the 4-nitrophenol absorbance at 400 nm. In the presence of NaBH_4 , the 4-nitrophenol was nearly completely reduced within a 60 min period. The reduction reaction was modelled using first-order kinetics and a rate constant of $7.4 \times 10^{-4} \text{ s}^{-1}$ was obtained. The rate of the reduction reaction was further improved by increasing the number of hydrogel discs, giving a higher surface area for the reduction of the 4-nitrophenol. The reusability of the composite was excellent showing similar rate constants for five repeated reactions. Furthermore, the activity of the composites was maintained on dehydrating and rehydrating. The surface morphology of the

dehydrated composite was rough with cauliflower-like structures. A smooth gel was obtained upon rehydration.

The anti-bacterial activity of the polyacrylamide-PVP-protected silver nanoparticles was tested using *Staphylococcus aureus*, *MRSA*, *Escherichia coli* and *P. aeruginosa*. Plate assays were performed on two strains of *P. aeruginosa* (ATCC 27853 and ATCC 10145). The hydrogel was loaded with two different volumes of the silver nanoparticles and a solution of AgNO_3 to give Ag^+ ions. The greatest zones of inhibition were observed for the composites containing the Ag^+ ions. The smallest zone of inhibition was observed with the *P. aeruginosa* (ATCC 27853). In contrast, the largest recorded zones were found with the *P. aeruginosa* 10145 plate assays, with the zones of inhibition reaching values of 19.1 mm² for the polyacrylamide-PVP-protected silver nanoparticles with 10 mL of particles; 17.5 mm² for the polyacrylamide-PVP-protected silver nanoparticles with 5 mL of particles; and 32.4 mm² for the polyacrylamide PVP composite with incorporated Ag^+ ions.

3.5 References

1. J. Wilcoxon, "Optical Absorption Properties of Dispersed Gold and Silver Alloy Nanoparticles", *Journal of Physical Chemistry B*, **113**, 2647, (2009).
2. F.W. Campbell, R.G. Compton, "The use of nanoparticles in electroanalysis: an updated review", *Analytical and Bioanalytical Chemistry*, **396**, 241, (2010).
3. A.O. Simm, S. Ward-Jones, C.E. Banks, R.G. Compton, "Novel methods for the production of silver microelectrode-arrays: Their characterisation by atomic force microscopy and application to the electro-reduction of halothane", *Analytical Sciences*, **21**, 667, (2005).
4. V. Bansal, V. Li, A.P. O'mullane, S.K. Bhargava, "Shape dependent electrocatalytic behaviour of silver nanoparticles", *CrystEngComm*, **12**, 4280, (2010).
5. A.A. Isse, S. Gottardello, C. Maccato, A. Gennaro, "Silver nanoparticles deposited on glassy carbon. Electrocatalytic activity for reduction of benzyl chloride", *Electrochemistry Communications*, **8**, 1707, (2006).
6. J.N. Tiwari, F.-M. Pan, T.-M. Chen, R.N. Tiwari, K.-L. Lin, "Electrocatalytic activity of Pt nanoparticles electrodeposited on amorphous carbon-coated silicon nanocones", *Journal of Power Sources*, **195**, 729, (2010).
7. B. Yin, H. Ma, S. Wang, S. Chen, "Electrochemical Synthesis of Silver Nanoparticles under Protection of Poly(N-vinylpyrrolidone)", *The Journal of Physical Chemistry B*, **107**, 8898, (2003).
8. J.H. Kim, C.K. Kim, J. Won, Y.S. Kang, "Role of anions for the reduction behavior of silver ions in polymer/silver salt complex membranes", *Journal of Membrane Science*, **250**, 207, (2005).
9. Z. Zhang, B. Zhao, L. Hu, "PVP Protective Mechanism of Ultrafine Silver Powder Synthesized by Chemical Reduction Processes", *Journal of Solid State Chemistry*, **121**, 105, (1996).
10. S.H. Joo, J.H. Kim, S.W. Kang, J. Jang, Y.S. Kang, "Propylene sorption and coordinative interactions for poly(N-vinyl pyrrolidone-co-vinyl acetate)/silver salt complex membranes", *Journal of Polymer Science Part B: Polymer Physics*, **45**, 2263, (2007).
11. W.-X. Tu, X.-B. Zuo, H.-F. Liu, "Study on the Interaction between Polyvinylpyrrolidone and Platinum Metals During the Formation of the Colloidal metal Nanoparticles.", *Chinese Journal of Polymer Science*, **26**, 23, (2008).
12. A. Slistan-Grijalva, R. Herrera-Urbina, J.F. Rivas-Silva, M. Ávalos-Borja, F.F. Castellón-Barraza, A. Posada-Amarillas, "Synthesis of silver nanoparticles in a polyvinylpyrrolidone (PVP) paste, and their optical properties in a film and in ethylene glycol", *Materials Research Bulletin*, **43**, 90, (2008).
13. D.D. Evanoff, G. Chumanov, "Synthesis and optical properties of silver nanoparticles and arrays", *Chemphyschem*, **6**, 1221, (2005).
14. S.K. Ghosh, T. Pal, "Interparticle coupling effect on the surface plasmon resonance of gold nanoparticles: From theory to applications", *Chemical Reviews*, **107**, 4797, (2007).
15. M. Murawska, A. Skrzypczak, M. Kozak, "Structure and Morphology of Gold Nanoparticles in Solution Studied by TEM, SAXS and UV-Vis", *Acta Physica Polonica A*, **121**, 888, (2012).
16. R. Desai, V. Mankad, S.K. Gupta, P.K. Jha, "Size Distribution of Silver Nanoparticles: UV-Visible Spectroscopic Assessment", *Nanoscience and Nanotechnology Letters*, **4**, 30, (2012).
17. P.L. Redmond, A.J. Hallock, L.E. Brus, "Electrochemical Ostwald Ripening of Colloidal Ag Particles on Conductive Substrates", *Nano Letters*, **5**, 131, (2004).

18. Y. Sun, Y. Yin, B.T. Mayers, T. Herricks, Y. Xia, "Uniform Silver Nanowires Synthesis by Reducing AgNO₃ with Ethylene Glycol in the Presence of Seeds and Poly(Vinyl Pyrrolidone)", *Chemistry of Materials*, **14**, 4736, (2002).
19. A. Schröder, J. Fleig, D. Gryaznov, J. Maier, W. Sitte, "Quantitative Model of Electrochemical Ostwald Ripening and Its Application to the Time-Dependent Electrode Potential of Nanocrystalline Metals", *The Journal of Physical Chemistry B*, **110**, 12274, (2006).
20. W.J. Plieth, "Electrochemical properties of small clusters of metal atoms and their role in the surface enhanced Raman scattering", *The Journal of Physical Chemistry*, **86**, 3166, (1982).
21. Y. Socol, O. Abramson, A. Gedanken, Y. Meshorer, L. Berenstein, A. Zaban, "Suspensive electrode formation in pulsed sonoelectrochemical synthesis of silver nanoparticles", *Langmuir*, **18**, 4736, (2002).
22. P. Chakraborty, "Metal nanoclusters in glasses as non-linear photonic materials", *Journal of Materials Science*, **33**, 2235, (1998).
23. P.N. Njoki, I.I.S. Lim, D. Mott, H.-Y. Park, B. Khan, S. Mishra, R. Sujakumar, J. Luo, C.-J. Zhong, "Size correlation of optical and spectroscopic properties for gold nanoparticles", *Journal of Physical Chemistry C*, **111**, 14664, (2007).
24. S. Link, M.A. El-Sayed, "Size and Temperature Dependence of the Plasmon Absorption of Colloidal Gold Nanoparticles", *The Journal of Physical Chemistry B*, **103**, 4212, (1999).
25. M. Otter, *Z. Phys.*, **161**, 163, (1961).
26. B. Xu, "Adsorption behavior of metal cations on gold nanoparticle surfaces studied by isothermal titration microcalorimetry", *J. Chin. Chem. Soc. (Taipei, Taiwan)*, **57**, 309, (2010).
27. H. Zhang, C. Zhang, "Transport of silver nanoparticles capped with different stabilizers in water saturated porous media", *J. Mater. Environ. Sci.*, **5**, 231, (2014).
28. D.L. Van Hyning, W.G. Klemperer, C.F. Zukoski, "Characterization of Colloidal Stability during Precipitation Reactions", *Langmuir*, **17**, 3120, (2001).
29. M.V. Cañamares, J.V. Garcia-Ramos, J.D. Gómez-Varga, C. Domingo, S. Sanchez-Cortes, "Comparative Study of the Morphology, Aggregation, Adherence to Glass, and Surface-Enhanced Raman Scattering Activity of Silver Nanoparticles Prepared by Chemical Reduction of Ag⁺ Using Citrate and Hydroxylamine", *Langmuir*, **21**, 8546, (2005).
30. M. Tejamaya, I. Römer, R.C. Merrifield, J.R. Lead, "Stability of Citrate, PVP, and PEG Coated Silver Nanoparticles in Ecotoxicology Media", *Environmental Science & Technology*, **46**, 7011, (2012).
31. X. Li, J.J. Lenhart, H.W. Walker, "Dissolution-Accompanied Aggregation Kinetics of Silver Nanoparticles", *Langmuir*, **26**, 16690, (2010).
32. Y. Liu, C.-Y. Liu, L.-B. Chen, Z.-Y. Zhang, "Adsorption of cations onto the surfaces of silver nanoparticles", *Journal of Colloid and Interface Science*, **257**, 188, (2003).
33. M.G. Espinoza, M.L. Hinks, A.M. Mendoza, D.P. Pullman, K.I. Peterson, "Kinetics of Halide-Induced Decomposition and Aggregation of Silver Nanoparticles", *The Journal of Physical Chemistry C*, **116**, 8305, (2012).
34. C. Greulich, S. Kittler, M. Eppele, G. Muhr, M. Köller, "Studies on the biocompatibility and the interaction of silver nanoparticles with human mesenchymal stem cells (hMSCs)", *Langenbeck's Archives of Surgery*, **394**, 495, (2009).
35. A.M.E. Badawy, T.P. Luxton, R.G. Silva, K.G. Scheckel, M.T. Suidan, T.M. Tolaymat, "Impact of Environmental Conditions (pH, Ionic Strength, and Electrolyte Type) on the Surface Charge and Aggregation of Silver Nanoparticles Suspensions", *Environmental Science & Technology*, **44**, 1260, (2010).

36. H. Wang, X. Qiao, J. Chen, X. Wang, S. Ding, "Mechanisms of PVP in the preparation of silver nanoparticles", *Materials Chemistry and Physics*, **94**, 449, (2005).
37. A.M. Brito-Silva, L.A. Gomez, C.B. De Araujo, A. Galembek, "Laser Ablated Silver Nanoparticles with Nearly the Same Size in Different Carrier Media", *Journal of Nanomaterials*, (2010).
38. C.E. Hoppe, M. Lazzari, I. Pardiñas-Blanco, M.A. López-Quintela, "One-Step Synthesis of Gold and Silver Hydrosols Using Poly(N-vinyl-2-pyrrolidone) as a Reducing Agent", *Langmuir*, **22**, 7027, (2006).
39. I. Washio, Y. Xiong, Y. Yin, Y. Xia, "Reduction by the End Groups of Poly(vinyl pyrrolidone): A New and Versatile Route to the Kinetically Controlled Synthesis of Ag Triangular Nanoplates", *Advanced Materials*, **18**, 1745, (2006).
40. H. Kaczmarek, A. Kamińska, M. Świątek, J.F. Rabek, "Photo-oxidative degradation of some water-soluble polymers in the presence of accelerating agents", *Die Angewandte Makromolekulare Chemie*, **261-262**, 109, (1998).
41. K. Mallick, M.J. Witcomb, M.S. Scurrall, "Polymer stabilized silver nanoparticles: A photochemical synthesis route", *Journal of Materials Science*, **39**, 4459, (2004).
42. G.-F. Wang, M.-G. Li, Y.-C. Gao, B. Fang, "Amperometric sensor used for determination of thiocyanate with a silver nanoparticles modified electrode", *Sensors*, **4**, 147, (2004).
43. B.D. Hames, D. Rickwood, Editors, *Gel Electrophoresis of Proteins. A Practical Approach*; 3rd edition ed.; IRL Press, 1998.
44. D.A. House, "Kinetics and Mechanism of Oxidations by Peroxydisulfate", *Chemical Reviews*, **62**, 185, (1962).
45. C.E.H. Bawn, D. Margerison, "Molecular dissociation processes in solution. Part 4.-The rate of decomposition of persulphate ion and its catalysis by metal ions", *Transactions of the Faraday Society*, **51**, 925, (1955).
46. A. Singh, "Synthesis and applications of polyacrylamide gels catalyzed by silver nitrate", *Journal of Applied Polymer Science*, **119**, 1084, (2011).
47. H. Wu, Z. Liu, X. Wang, B. Zhao, J. Zhang, C. Li, "Preparation of hollow capsule-stabilized gold nanoparticles through the encapsulation of the dendrimer", *Journal of Colloid and Interface Science*, **302**, 142, (2006).
48. S. Wunder, F. Polzer, Y. Lu, Y. Mei, M. Ballauff, "Kinetic Analysis of Catalytic Reduction of 4-Nitrophenol by Metallic Nanoparticles Immobilized in Spherical Polyelectrolyte Brushes", *The Journal of Physical Chemistry C*, **114**, 8814, (2010).
49. N. Pradhan, A. Pal, T. Pal, "Silver nanoparticle catalyzed reduction of aromatic nitro compounds", *Colloids and Surfaces a-Physicochemical and Engineering Aspects*, **196**, 247, (2002).
50. B.H. Liu, Z.P. Li, "A review: Hydrogen generation from borohydride hydrolysis reaction", *Journal of Power Sources*, **187**, 527, (2009).
51. H. Zhang, X. Li, G. Chen, "Ionic liquid-facilitated synthesis and catalytic activity of highly dispersed Ag nanoclusters supported on TiO₂", *Journal of Materials Chemistry*, **19**, 8223, (2009).
52. C.M. Kaufman, B. Sen, "Hydrogen Generation by Hydrolysis of Sodium Tetrahydroborate - Effects of Acids and Transition-metals and their Salts", *Journal of the Chemical Society-Dalton Transactions*, 307, (1985).
53. G. Guella, C. Zanchetta, B. Patton, A. Miotello, "New Insights on the Mechanism of Palladium-Catalyzed Hydrolysis of Sodium Borohydride from ¹¹B NMR Measurements", *The Journal of Physical Chemistry B*, **110**, 17024, (2006).
54. H. Zhao, F.-J. Yin, X.-Y. Xu, Z. Tong, J.-W. Zheng, G. Zhao, "A Novel Catalyst SiO₂@NiO for Reduction of 4-NP", *Synthesis and Reactivity in Inorganic, Metal-Organic, and Nano-Metal Chemistry*, **37**, 15, (2007).

55. K. Kuroda, T. Ishida, M. Haruta, "Reduction of 4-nitrophenol to 4-aminophenol over Au nanoparticles deposited on PMMA", *Journal of Molecular Catalysis A: Chemical*, **298**, 7, (2009).
56. Y. Lu, Y. Mei, M. Ballauff, M. Drechsler, "Thermosensitive Core–Shell Particles as Carrier Systems for Metallic Nanoparticles", *The Journal of Physical Chemistry B*, **110**, 3930, (2006).
57. W. Zhang, F. Tan, W. Wang, X. Qiu, X. Qiao, J. Chen, "Facile, template-free synthesis of silver nanodendrites with high catalytic activity for the reduction of p-nitrophenol", *Journal of Hazardous Materials*, **217–218**, 36, (2012).
58. M.H. Rashid, T.K. Mandal, "Synthesis and Catalytic Application of Nanostructured Silver Dendrites", *The Journal of Physical Chemistry C*, **111**, 16750, (2007).
59. S. Panigrahi, S. Basu, S. Praharaj, S. Pande, S. Jana, A. Pal, S.K. Ghosh, T. Pal, "Synthesis and Size-Selective Catalysis by Supported Gold Nanoparticles: Study on Heterogeneous and Homogeneous Catalytic Process", *The Journal of Physical Chemistry C*, **111**, 4596, (2007).
60. K. Esumi, R. Isono, T. Yoshimura, "Preparation of PAMAM– and PPI–Metal (Silver, Platinum, and Palladium) Nanocomposites and Their Catalytic Activities for Reduction of 4-Nitrophenol", *Langmuir*, **20**, 237, (2004).
61. Y. Lu, Y. Mei, M. Schrinner, M. Ballauff, M.W. Möller, J. Breu, "In Situ Formation of Ag Nanoparticles in Spherical Polyacrylic Acid Brushes by UV Irradiation", *The Journal of Physical Chemistry C*, **111**, 7676, (2007).
62. Y. Lu, P. Spyra, Y. Mei, M. Ballauff, A. Pich, "Composite Hydrogels: Robust Carriers for Catalytic Nanoparticles", *Macromolecular Chemistry and Physics*, **208**, 254, (2007).
63. R. Narayanan, M.A. El-Sayed, "Catalysis with transition metal nanoparticles in colloidal solution: Nanoparticle shape dependence and stability", *Journal of Physical Chemistry B*, **109**, 12663, (2005).
64. Z. Zhang, C. Shao, Y. Sun, J. Mu, M. Zhang, P. Zhang, Z. Guo, P. Liang, C. Wang, Y. Liu, "Tubular nanocomposite catalysts based on size-controlled and highly dispersed silver nanoparticles assembled on electrospun silica nanotubes for catalytic reduction of 4-nitrophenol", *J. Mater. Chem.*, **22**, 1387, (2012).
65. S. Jana, S.K. Ghosh, S. Nath, S. Pande, S. Praharaj, S. Panigrahi, S. Basu, T. Endo, T. Pal, "Synthesis of silver nanoshell-coated cationic polystyrene beads: A solid phase catalyst for the reduction of 4-nitrophenol", *Appl. Catal., A*, **313**, 41, (2006).
66. Q.L. Feng, J. Wu, G.Q. Chen, F.Z. Cui, T.N. Kim, J.O. Kim, "A mechanistic study of the antibacterial effect of silver ions on Escherichia coli and Staphylococcus aureus", *Journal of Biomedical Materials Research*, **52**, 662, (2000).
67. C. Marambio-Jones, E.M.V. Hoek, "A review of the antibacterial effects of silver nanomaterials and potential implications for human health and the environment", *Journal of Nanoparticle Research*, **12**, 1531, (2010).
68. B.-H. Jun, J.-W. Byun, J. Kim, H. Kang, H.-J. Park, J. Yoon, Y.-S. Lee, "Facile method of preparing silver-embedded polymer beads and their antibacterial effect", *Journal of Materials Science*, **45**, 3106, (2010).
69. http://www.ox.ac.uk/media/news_stories/2012/120306.html.
70. <http://www.hospitalmanagement.net/features/feature68910/feature68910-2.html>.
71. <http://melpor.hubpages.com/hub/Understanding-the-E-Coli-Bacteria#>.
72. <http://ausubellab.mgh.harvard.edu/cgi-bin/pa14/home.cgi>.

Chapter 4
**Silver-Modified Glassy Carbon
Electrode for the Electrochemical
Detection of Nitrate**

4.1 Introduction

This chapter discusses the preparation of silver nanoclusters deposited on a glassy carbon (GC) electrode and investigates the potential of this probe as an electrochemical sensor for nitrates. In Chapter 3, the potential for colloidal silver particles to sense nitrates was explored, however, it was found that although dispersing the particles on a GC electrode did result in an observed current for the reduction of nitrate, its magnitude was erratic and resulted in unacceptable errors in terms of reproducibility. Therefore, it was decided to look at techniques that directly deposit metallic particles onto bare substrates in the hope that this would result in a sensor capable of monitoring nitrates with a greater degree of reproducibility.

The most reported technique in the literature to deposit metallic particles on an electrode surface is a potentiostatic pulse method, where parameters such as overpotential, time and concentration are varied ⁽¹⁻⁵⁾. There are many benefits associated with direct electrochemical deposition on a conducting surface but, equally, several challenges are faced. Namely, it is often much more difficult to control the size and uniformity of the electrodeposited particles when compared to other techniques such as chemical and laser synthesis that generated colloidal or powder forms of metal particles ⁽⁶⁾. This work aims to investigate the features that influence the electrodeposition process and consequently how the electrochemical detection of nitrate is affected. GC was chosen as the substrate so as any current generated for the reduction of nitrate could be attributed to the deposited particles and not to the underlying electrode material, since GC has been shown to have no catalytic ability to reduce nitrates ⁽⁷⁾. The concept of electrochemical deposition of silver on GC is not a new one and the literature offers a variety of ways by which metallic particles can be electrodeposited ^(1,5,8-10). In this study, different techniques to deposit silver particles on GC are explored and the resulting relationship between the size and surface area of these silver particles and the reduction of nitrate are investigated. The sensitivity of this modified electrode at detecting low levels of nitrate is explored, how the surface area of silver on GC can be accurately determined and the kinetics and mechanism of nitrate reduction at

this modified electrode are examined. Differences between silver deposited in this manner and a bulk crystalline silver electrode, in terms of the nitrate reduction electrochemistry, is also discussed.

4.2 Experimental

The instrumentation, apparatus and software employed are described in Section 2.2. The experimental parameters are outline in Chapter 2 Section 2.4.2.

4.3 Results and Discussion

4.3.1 Electrodeposition of Silver on Glassy Carbon

While electrochemistry is an extremely versatile and powerful tool to deposit virtually any metal from an ionic solution onto a conductive surface at a precise coverage, the ability to disperse the metal in a dimensionally uniform way is still a major challenge faced by electrochemists. In the following sections, different methods of depositing particles by varying the magnitude and duration of the pulse are presented. The influence of these parameters on the morphology of the particles and, importantly, the ability of these particles to electrochemically detect nitrate are then discussed.

4.3.1.1 Double Pulse Method

The potentiostatic double pulse method was introduced by Sheludko and co-workers ⁽¹¹⁾ as a means of controlling particle size. A schematic representation of the potentiostatic double pulse method is shown in Figure 4.1. It works on the principle of separating the nucleation and growth modes into two separate steps. The first step is to apply a short pulse of very high overpotential (E_1 for a time t_1) to instantaneously seed all available sites. The second pulse, of much lower overpotential, causes these sites to grow but avoids the formation of new sites (E_2 for a time t_2). In this way, progressive nucleation, which leads to polydispersity of particle size, is avoided.

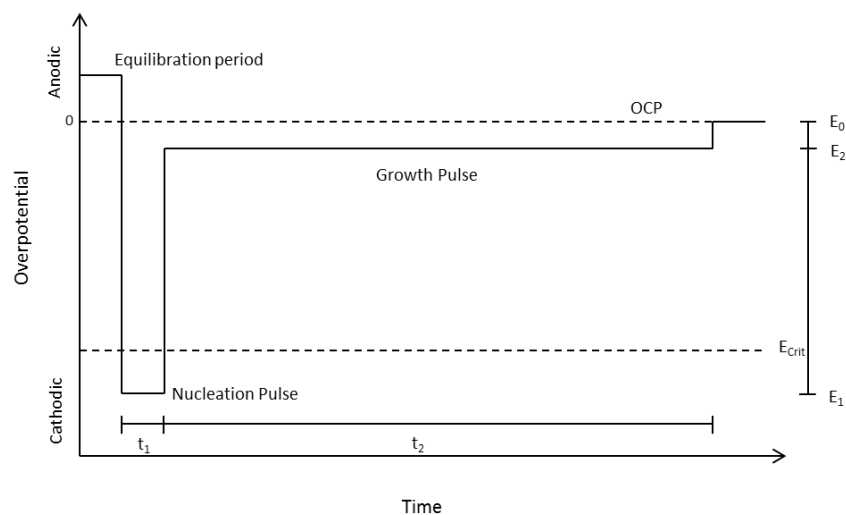


Figure 4.1: Schematic representation of the potentiostatic double pulse method.

Penner also utilized this method and discussed in detail why progressive nucleation leads to polydispersity of particle size by introducing the idea of diffusion zone coupling ^(12,13). He noticed that particles that were close in proximity to each other tended to be smaller than particles that were more isolated. Around each growing nucleus the supply of metal ions in the electrolyte is different from the bulk solution as the ions are deposited as metal on the electrode surface. This creates a depletion layer around the metal particle. These depletion layers extend as the ions are used up and the concentration is lowered. If the depletion zones of two nearby nuclei overlap, the rate of growth of these nuclei will be lower compared to nuclei that grow in relative isolation because the nuclei grown in isolation will have a larger share of metal ions surrounding it. This overlap of depletion layer is referred to as diffusion zone coupling.

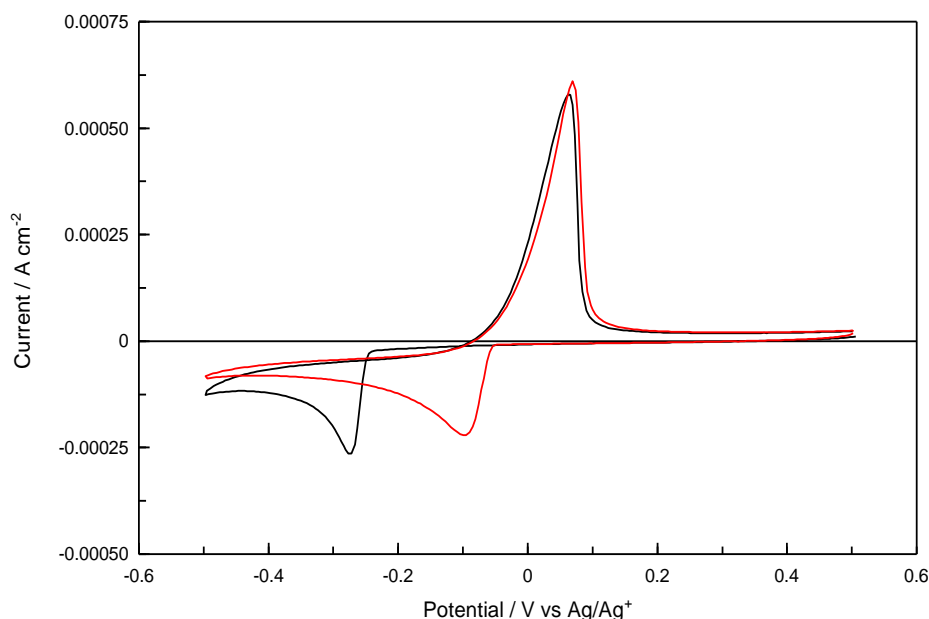


Figure 4.2: Cyclic voltammogram of $1 \times 10^{-3} \text{ mol dm}^{-3} \text{ AgClO}_4$ in $0.1 \text{ mol dm}^{-3} \text{ LiClO}_4$ at a GC electrode at a scan rate of 20 mV s^{-1} . Black trace is cycle 1 and red trace is cycle 2.

In practice the two potential pulses, E_1 and E_2 , are determined by examining the CV of silver deposition and subsequent stripping from the surface of a GC electrode, Figure 4.2. The first and second scans of the CV are shown and the cathodic and anodic waves for the deposition and stripping of silver are clearly visible. The reduction wave for the second scan is positively shifted with respect to the first scan. If the nucleation overpotential, μ_{dep} , is defined as the difference between the potential corresponding to the foot of the reduction wave and the equilibrium potential, i.e., $E = 0.0 \text{ V vs Ag|Ag}^+$, the μ_{dep} for the first and second scans are -236 and -48 mV , respectively. This indicates a considerable difference in the deposition of silver from the first to the second cycle. Similar behaviour for metal deposition and stripping at carbon-based electrodes has been reported ^(14,15) and this has been explained by only partial stripping of silver in the first anodic wave. The presence of this residual silver, which is intercalated in the carbon matrix, facilitates the deposition of silver in the second and subsequent cycles. In fact, the same behaviour was observed in Chapter 3 of this work when cycling a Pt electrode in a solution containing $5.0 \times 10^{-3} \text{ mol dm}^{-3} \text{ AgNO}_3$ with $0.1 \text{ mol dm}^{-3} \text{ KNO}_3$ when examining the effect of the presence of PVP on the redox properties of silver.

Upon inspection of the CV in Figure 4.2 it was established that a growth pulse of $-0.06\text{ V vs Ag/Ag}^+$ was suitable since it was sufficiently reductive to allow deposition of silver on already formed silver particles but anodic enough that, in theory, no new nucleation sites should be formed. To demonstrate this, the deposition of silver was performed with no nucleation pulse and only a growth pulse of $-0.06\text{ V vs Ag/Ag}^+$ for 50 s. Figure 4.3 shows the SEM micrograph of this electrode and it is evident that only a small quantity of silver, the bright spots in Figure 4.3, is deposited under these conditions.

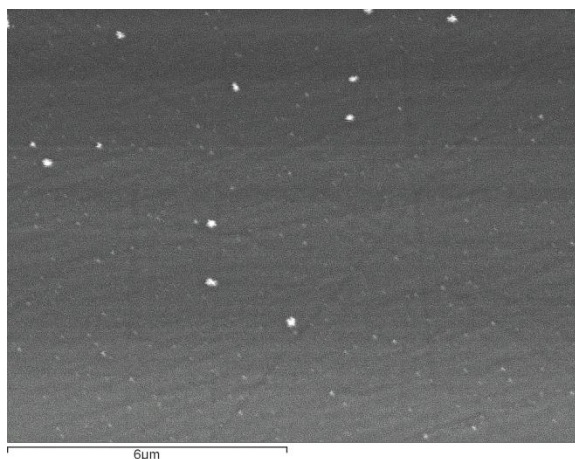


Figure 4.3: SEM images for silver deposited at -0.06 V for 50 s on a GC electrode from a solution of $1.0 \times 10^{-3}\text{ mol dm}^{-3}\text{ AgClO}_4$ in $0.1\text{ mol dm}^{-3}\text{ LiClO}_4$.

The effect of the magnitude of the nucleation pulse on the morphology of the silver deposits was then investigated while the growth pulse of $-0.06\text{ V vs Ag/Ag}^+$ was kept constant and held for 50 sec. An oxidation pulse of 1.0 V was applied for 15 min prior to the deposition pulse as part of electrode preparation and cleaning. This was done to ensure complete removal of any intercalated silver that may persist on the electrode surface. Isse and co-workers found that a pulse of 0.5 V vs Ag/Ag^+ applied for 15 min was sufficient to remove any silver⁽⁵⁾. As well as visual inspection of the silver deposits by employing SEM, the main objective, the electrochemical detection of nitrate, was used as a benchmark for the effectiveness or lack thereof with which the electrodeposits detected nitrates, with the greatest sensitivity being the desirable outcome. Figure 4.4 shows a series of SEM micrographs along with a histogram generated using the ImageJ program and a table of percentage size distributions of the silver deposits generated using the

double pulse technique on a GC electrode from a solution of $1.0 \times 10^{-3} \text{ mol dm}^{-3}$ AgClO_4 in 0.1 mol dm^{-3} LiClO_4 . Details on the generation of the histograms through ImageJ and Microsoft Excel are outlined in Chapter 2, Section 2.3.7. The overpotential of the first nucleation pulse, E_1 , was varied and held for 1 s (t_1). The growth pulse, E_2 , was kept constant for each nucleation pulse at a potential of -0.06 V for 50 s (t_2).

For each E_1 , the size distribution of particles is less than ideal but some trends can be identified. The lower the potential of E_1 the fewer total amount of particles are deposited. This is unsurprising as a greater number of sites are generated when the energy barrier to nucleation is overcome by a higher overpotential⁽¹⁶⁾. Apart from less particles nucleated at lower E_1 overpotentials (-0.25 V, Figure 4.4(a)), the particles are also larger. An overpotential of -0.06 V vs Ag/Ag⁺ is not energetic enough to nucleate fresh sites on the GC so all silver ions in the diffusional layer deposit on the already formed silver metal from the E_1 pulse, resulting in a higher number of particles that have diameters greater than 200 nm.

As E_1 is increased to more reductive potentials more nucleation sites are formed, but polydispersity becomes apparent. Even though the growth pulse, E_2 , is not low enough to nucleate fresh sites, according to the CV's in Figure 4.2, it is still not clear whether within the already formed sites there are sites where silver deposition will be more favourable to give rise to polydispersity. It is well documented that nucleation of any metal will preferentially occur at low energy defected sites and edges⁽¹⁷⁾. However, it is unclear and rarely discussed whether, within the array of sites formed during the nucleation pulse, there are sites of variable energy where silver may also prefer to grow, i.e., all silver deposited in the nucleation pulse may not be equivalent.

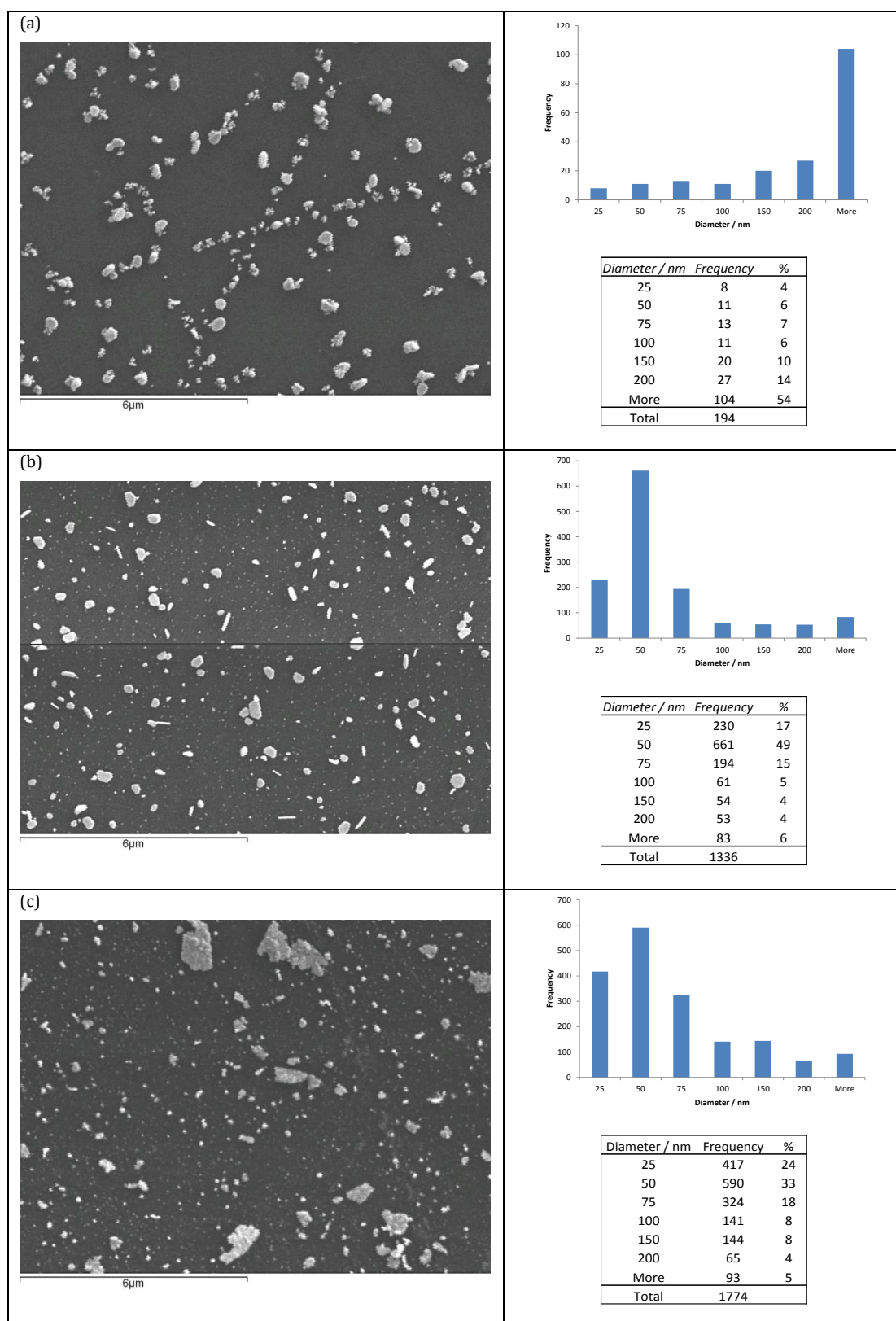


Figure 4.4: SEM images and size distribution histogram and tables for silver particles deposited on GC by the double pulse method. E_1 varied (a) -0.25 (b) -0.50 and (c) -1.00 V vs Ag/Ag^+ for 1 s. E_2 constant -0.06 V for 50 s.

It has been shown is that not all particles that are nucleated go on to form mature particles. Liu and Penner stated that the probability of whether a nucleated particle survives and grows to maturity depends largely on the growth pulses, overpotential and time. Particles subjected to longer pulse durations become larger as they grow but the density decreases showing that many of the clusters are not stable. Even at large growth potentials, only 1 in 10 of the 1 nm clusters initially deposited matured into particles of 10 nm or more, and at lower growth overpotentials the survival rate is even lower, just 1 in 1000 ⁽¹²⁾.

The influence of increasing the duration of the E_2 pulse at $-0.06\text{ V vs Ag/Ag}^+$ is shown in Figure 4.5. In this case, E_2 was increased from 50 s to 100 s. It is clear from these data that the number density of particles decreases with longer growth times. The number of particles for the 50 s deposition period is approximately 1336, while at 100 s, the number decreases to approximately 806. Furthermore, the number of larger particles increases while the percentage of smaller particles slightly decreases as the pulse period is increased from 50 to 100 s. Liu and Penner also found that particles that did not mature also didn't persist on the surface. Although a mechanism for the disappearance of smaller particles is not understood, a possible explanation put forward by Sandmann and co-workers is that a larger particle has the capacity to draw a disproportionate fraction of the metal ion electrolyte towards it at the expense of the smaller particles, extending its diffusion zone until it overlaps with the smaller particles ⁽¹⁸⁾⁽¹⁸⁾. This lack of electrolyte destabilises smaller particles, causing them to dissolve and redeposit on the larger particles in an Ostwald ripening type fashion.

These data were compared with the results obtained after the nucleation pulse, but before the application of a growth pulse. In this case, the silver was deposited at $-0.50\text{ V vs Ag/Ag}^+$, E_1 , for 1 s and the corresponding micrograph and histogram are shown in Figure 4.6. It can be seen that the number density is higher in the absence of the growth pulse and the application of the growth pulse leads to a reduction in the number of particles, with a more significant reduction at 100 s.

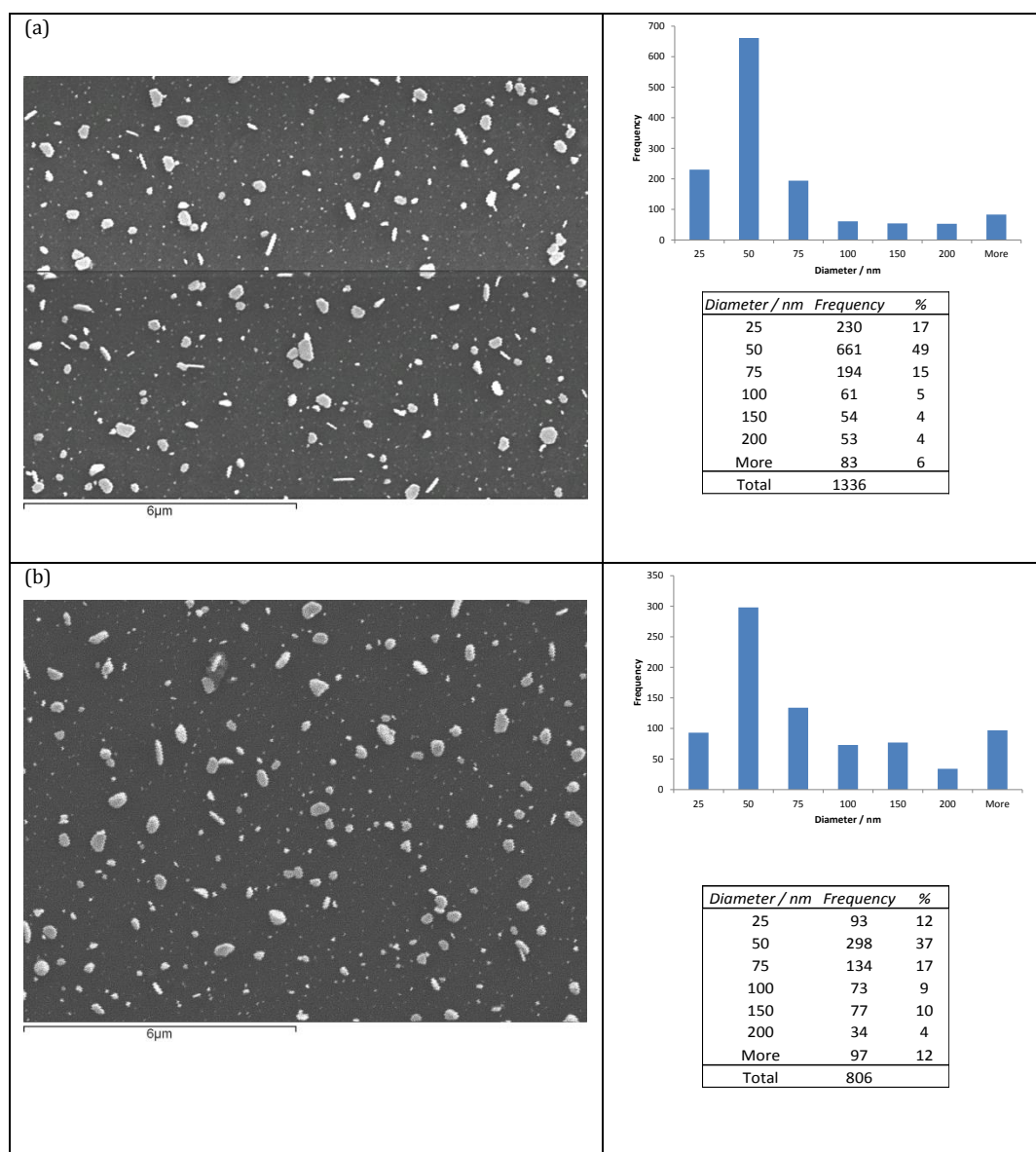


Figure 4.5: SEM images and size distribution histogram and tables for silver particles deposited on GC by the double pulse method. E_1 , t_1 and E_2 constant, -0.50 V, 1 s and -0.06 V vs Ag/Ag^+ respectively. t_2 varied (a) 50 s and (b) 100 s.

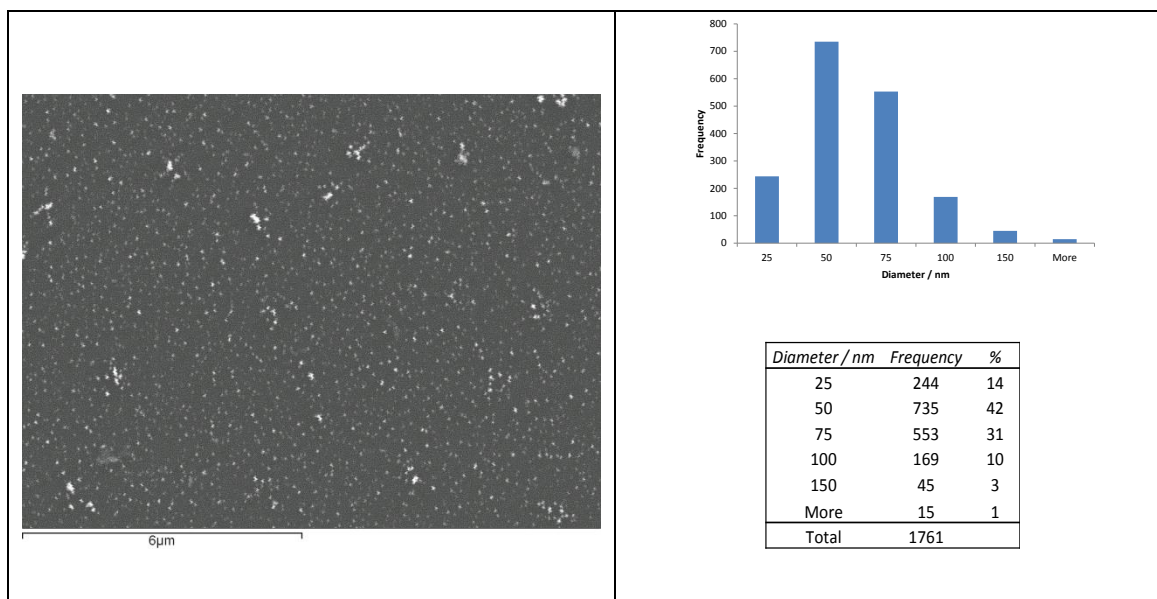


Figure 4.6: SEM images and size distribution histogram and tables for silver particles deposited on GC when only an E_1 pulse is applied for t_1 of 1 s.

The electrochemical detection of nitrates at the silver particles deposited on the GC electrode was studied in a solution of $5.0 \times 10^{-3} \text{ mol dm}^{-3} \text{ KNO}_3$ and $0.1 \text{ mol dm}^{-3} \text{ LiClO}_4$. The CV's were recorded at 50 mV s^{-1} and the potential was scanned from 0.0 V to -1.40 V vs SCE. Figure 4.7 shows the first example in this work of the current response of silver particles deposited on GC corresponding to the SEM micrographs in Figure 4.4 to a solution containing nitrate. Figure 4.8 shows the response of the particles formed for different t_2 values from Figure 4.5. A peak current is observed at approximately -0.90 V vs SCE, which is typically ascribed to the reduction of nitrate to nitrite. The onset of the nitrate reduction begins at approximately -0.60 V vs SCE and this continues until potentials in the vicinity of -1.20 V vs SCE are reached. At lower potentials, the water reduction reaction occurs rapidly, beginning at potentials negative to -1.25 V vs SCE. There is also a reduction current response at -0.38 V vs SCE, which is found in the CV of the background electrolyte, $0.1 \text{ mol dm}^{-3} \text{ LiClO}_4$, Figure 4.9. This is shown more clearly in the inset. This peak may be related to the reduction of surface oxides on the silver electrode.

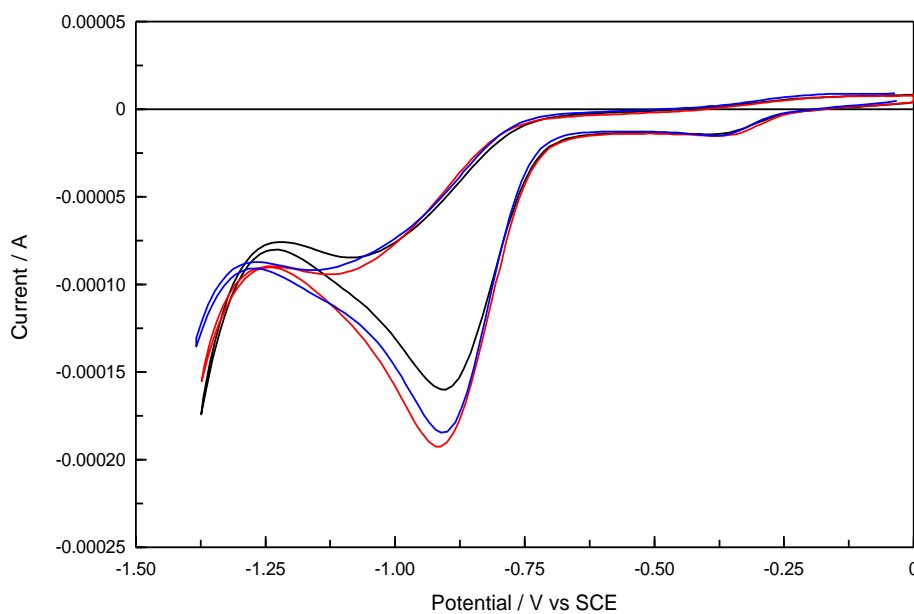


Figure 4.7: Cyclic voltammograms at a scan rate 50 mVs⁻¹ in a solution of 5.0×10^{-3} mol dm⁻³ KNO₃ and 0.1 mol dm⁻³ LiClO₄ at a GC electrode with silver particles deposited by the double pulse method. E₁ varied -0.25 V —, -0.50 V —, -1.00 V — for 1 s. E₂ constant -0.06 V vs Ag/Ag⁺ for 50 s.

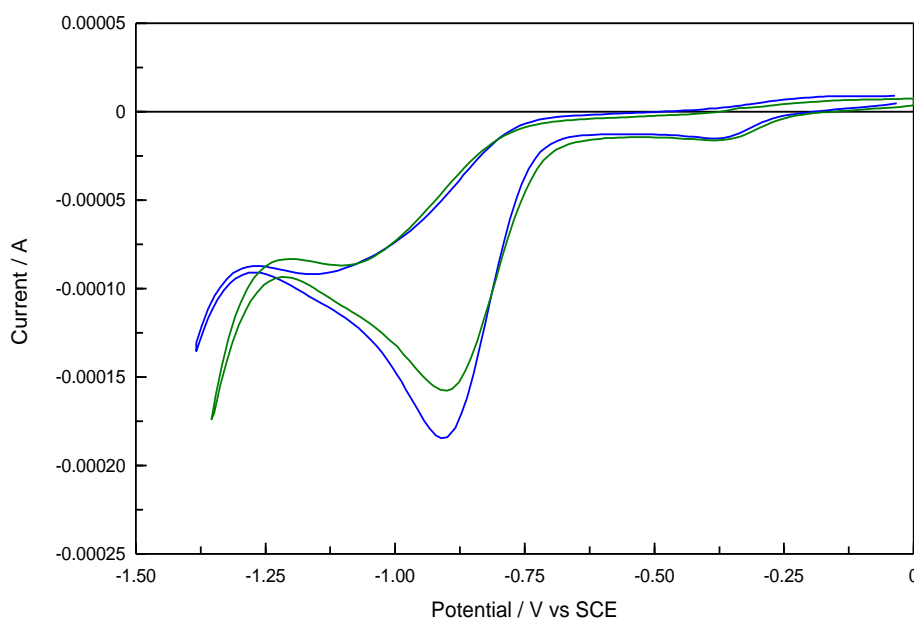


Figure 4.8: Cyclic voltammograms at a scan rate 50 mVs⁻¹ in a solution of 5.0×10^{-3} mol dm⁻³ KNO₃ and 0.1 mol dm⁻³ LiClO₄ at a GC electrode with silver particles deposited by the double pulse method. t₂ varied 50 s — and 100 s —. All other parameters the same for both traces, E₁ -0.50 V, E₂ -0.06 V and t₁ for 1 s.

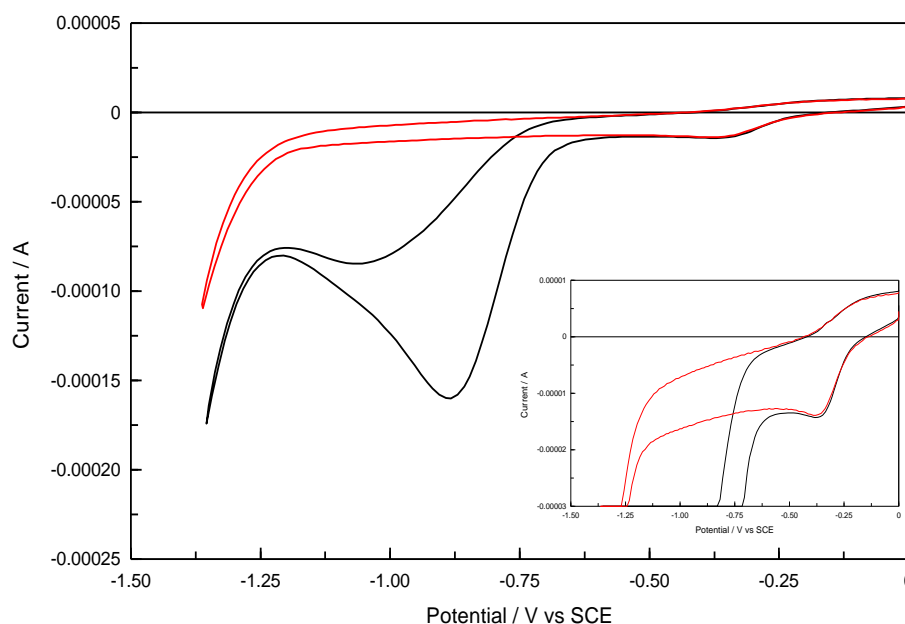


Figure 4.9: Cyclic voltammograms at a GC electrode with silver particles deposited by the double pulse method. E_1 varied -0.25 V vs Ag/Ag^+ for 1 s and E_2 constant -0.06 V vs Ag/Ag^+ for 50 s. — in a solution of 5.0×10^{-3} mol dm^{-3} KNO_3 and 0.1 mol dm^{-3} LiClO_4 and — background electrolyte 0.1 mol dm^{-3} LiClO_4 only. Scan rate 50 mVs^{-1} . Inset: Close-up of silver oxide reduction.

The influence of the value of E_1 on the detection of nitrates at the silver particles is evident in Figure 4.7, where the silver was deposited with E_2 at -0.06 V vs Ag/Ag^+ for 50 s and E_1 at -0.25 V, -0.50 V and -1.00 V vs Ag/Ag^+ for 1 s. The profile of the nitrate peak is very similar for each value of E_1 , except that the magnitude of the current depends on the value of E_1 , with slightly larger peak currents as E_1 is varied from -0.25 V to -1.00 V vs Ag/Ag^+ . This may be connected to a higher density of silver particles as E_1 is varied to -1.00 V vs Ag/Ag^+ , as shown in Figure 4.4. It is also evident from Figure 4.8 that the peak current for the reduction of the nitrate depends on the duration of the t_2 pulse. The peak current is higher for the silver particles deposited with a t_2 value of 50 s, while the longer t_2 period of 100 s gives rise to a lower peak current. This is consistent with the SEM micrographs presented in Figure 4.5, where the longer deposition time gives a lower density of the particles.

Figure 4.10 shows the response of a bare GC electrode to a solution with and without nitrate and illustrates that GC does not have the ability to reduce nitrate unless potentials of over -1.75 V vs SCE are applied, and even then the current magnitude is low for such a high concentration of nitrate ⁽⁷⁾. It is clear from a comparison of the data in Figures 4.7, 4.8, 4.9 and 4.10 that the GC substrate supporting the silver particles does not contribute to the reduction of nitrate. A more detailed analysis of the CV profile is discussed later in Section 4.3.8.

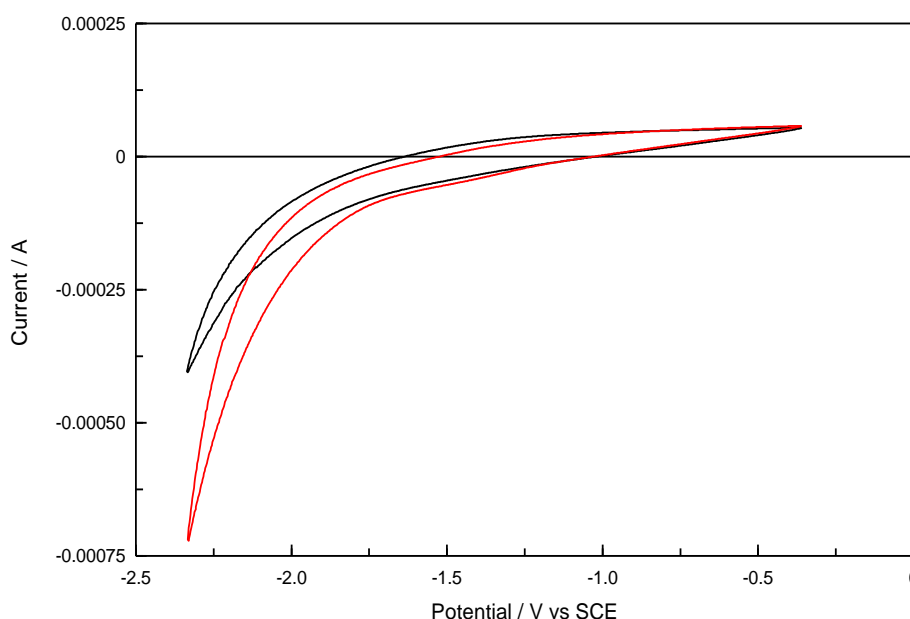


Figure 4.10: Cyclic voltammograms at a bare GC electrode in a solution of $0.1 \text{ mol dm}^{-3} \text{ LiClO}_4$ — with and — without of $0.05 \text{ mol dm}^{-3} \text{ KNO}_3$. Scan rate 50 mV s^{-1} .

In order to determine if the detection of nitrate was connected with variations in the amount of silver at the GC electrodes, stripping voltammograms were recorded for the silver-modified electrodes formed at -0.25 V, -0.50 V and -1.00 V vs Ag/Ag^+ . Representative stripping voltammograms are shown in Figure 4.11. Stripping the silver from the GC surface reveals that the amount of silver on the electrodes is similar. This is in good agreement with the charge data, shown in Figure 4.12, where the charge recorded during the deposition is similar, as the duration of the growth pulse is the same for each electrode. This shows that the growth pulse dictates the amount of silver deposited.

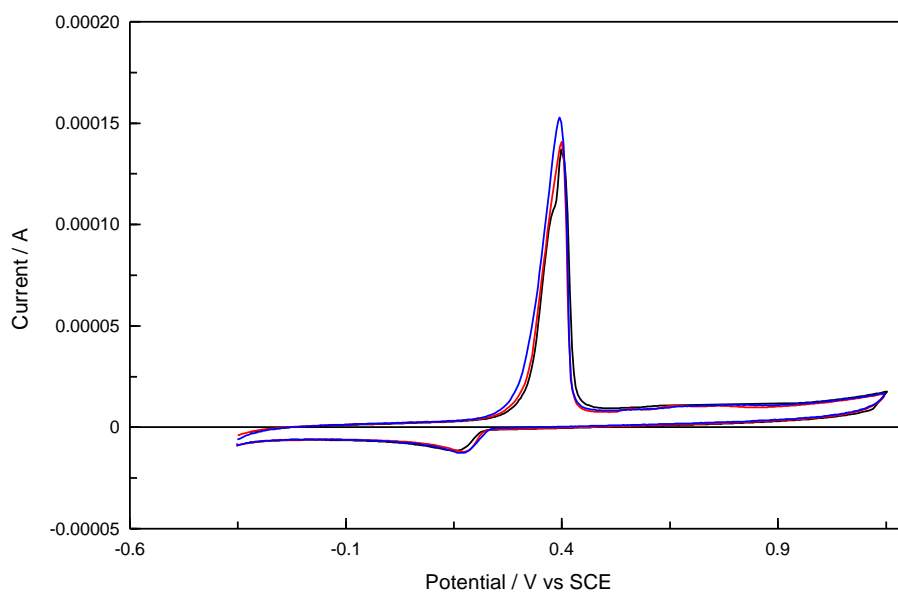


Figure 4.11: Stripping voltammograms in $0.1 \text{ mol dm}^{-3} \text{ LiClO}_4$ of GC electrode with silver particles deposited by the double pulse method. E_1 varied -0.25 V —, -0.50 V —, -1.00 V vs Ag/Ag^+ — for 1 s. E_2 constant at -0.06 V vs Ag/Ag^+ for 50 s.

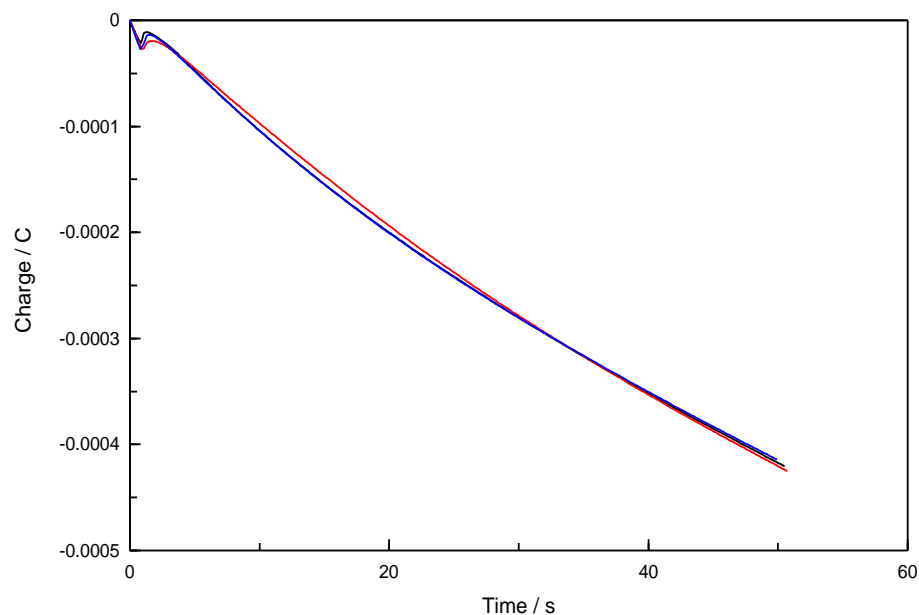


Figure 4.12: Charge-time transients for silver particles deposited on a GC electrode by the double pulse method. E_1 varied -0.25 V —, -0.50 V —, -1.00 V vs Ag/Ag^+ — for 1 s. E_2 constant at -0.06 V vs Ag/Ag^+ for 50 s.

It is clear from the voltammograms shown in Figure 4.8 that a longer growth pulse of 100 s does not enhance, but actually diminishes, the magnitude of the nitrate reduction current. The corresponding stripping voltammogram is shown in Figure 4.13, where it is evident that a greater amount of silver is deposited at the longer 100 s period. Clearly, the higher amount of silver deposited at the GC electrode does not give rise to better detection of nitrates. It appears that the number or density of the silver particles is important in the detection of the nitrates rather than the overall amount of silver. The higher peak currents observed for the silver particles deposited with E_1 at -1.00 V vs Ag/Ag⁺ for 1 s, Figure 4.7, may be connected to the higher number of particles, as shown in Figure 4.4, while a higher number of silver particles are also obtained at E_2 for 50 s compared to E_2 for 100 s, as shown in the SEM micrographs in Figure 4.5. Having a higher percentage of smaller particles may be conducive to better nitrate detection rather than larger quantities of silver.

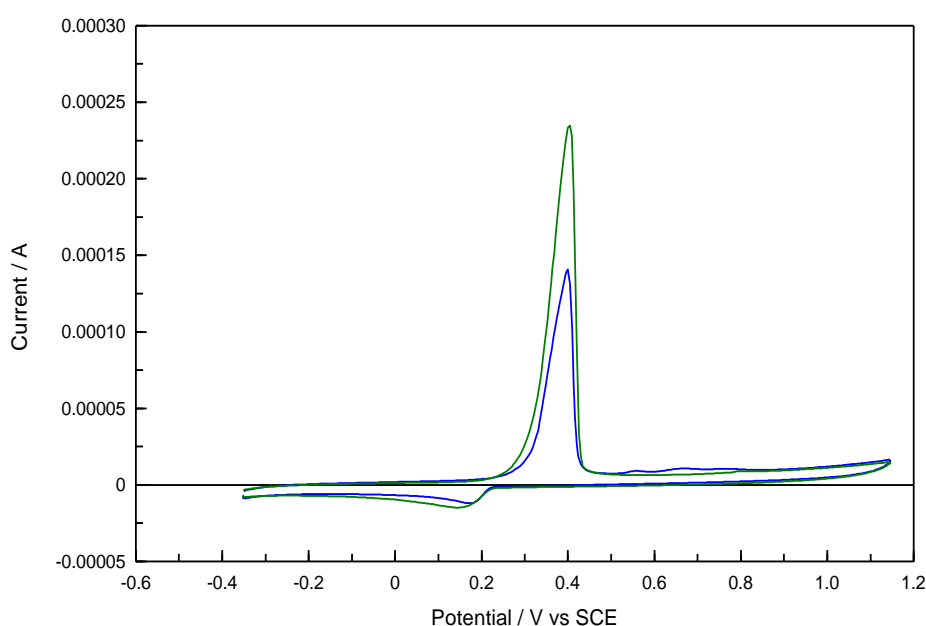


Figure 4.13: Stripping voltammograms in 0.1 mol dm⁻³ LiClO₄ of GC electrode with silver particles deposited by the double pulse method. t_2 varied 50 s — and 100 s — . All other parameters the same for both traces, E_1 -0.50 V, E_2 -0.06 V and t_1 1 s.

To test this theory the silver-modified GC electrode from Figure 4.6, which had only undergone an E_1 pulse of -0.50 V vs Ag/Ag^+ for 1 s and no growth pulse, was placed in a nitrate solution. The electrochemical response to the nitrate is shown as the red trace in Figure 4.14. Despite having small particles of high density, the nitrate reduction peak did not have as large a nitrate current when compared to particles subjected to a growth pulse (blue trace). When the stripping voltammogram is examined, Figure 4.15, it is clear that the quantity of silver was not sufficient to generate a good signal despite the presence of small sized particles.

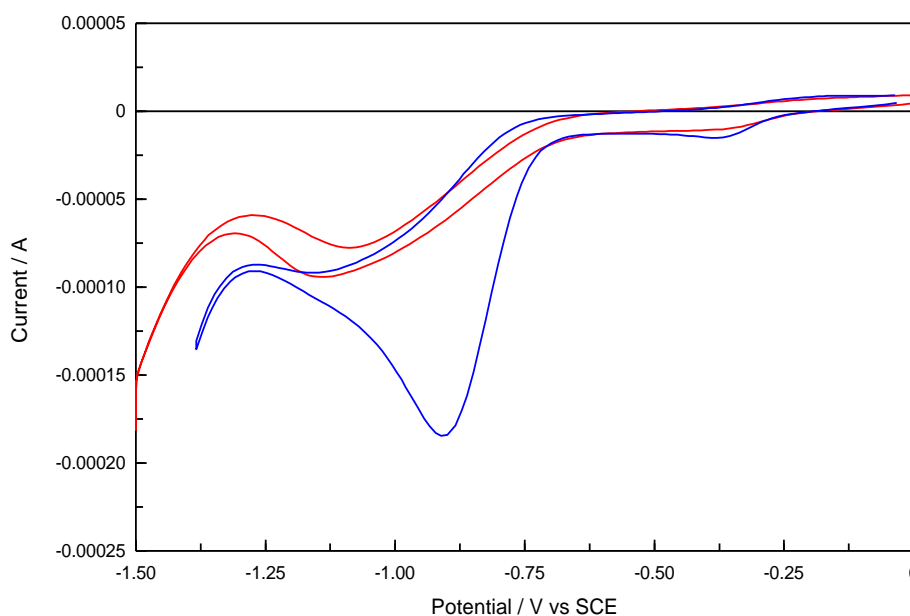


Figure 4.14: Cyclic voltammograms at a scan rate 50 mVs^{-1} in a solution of $5.0 \times 10^{-3} \text{ mol dm}^{-3} \text{ KNO}_3$ and $0.1 \text{ mol dm}^{-3} \text{ LiClO}_4$ at a GC electrode with silver particles deposited by the double pulse method. E_1 , t_1 , E_2 and t_2 are -0.50 V, 1 s, -0.06 V and 50 s respectively for — and an E_1 and t_1 pulse only of -0.50 V 1 s for — (no growth pulse).

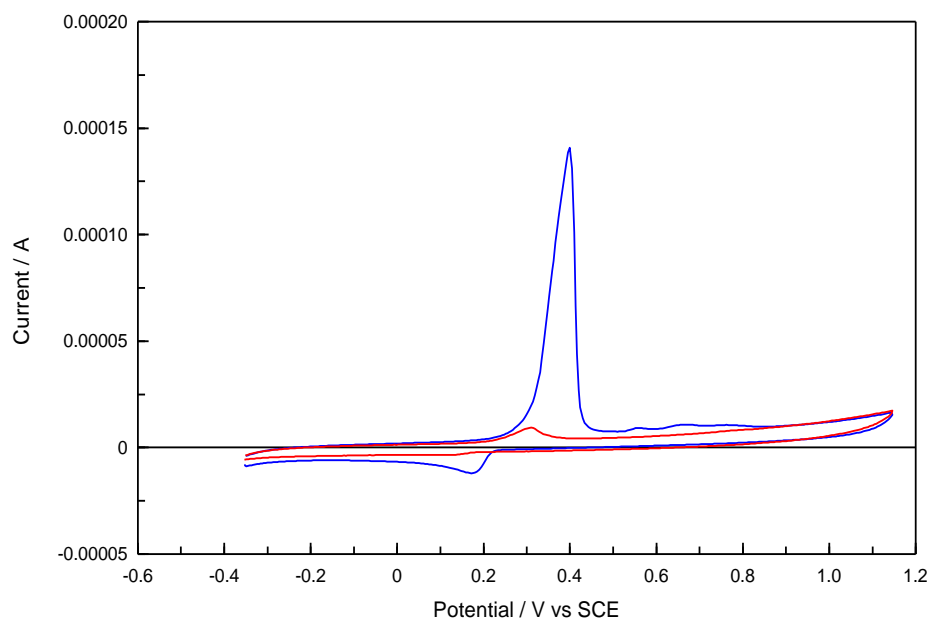


Figure 4.15: Stripping voltammograms at a scan rate of 20 mV s^{-1} in $0.1 \text{ mol dm}^{-3} \text{ LiClO}_4$ of GC electrode with silver particles deposited by the double pulse method. E_1 , t_1 , E_2 and t_2 are -0.50 V , 1 s , -0.06 V and 50 s respectively for — and an E_1 and t_1 pulse only of -0.50 V 1 s for — (no growth pulse).

Although the double pulse method did result in a well-defined nitrate reduction peak, the particles had a wide distribution of sizes, which was an undesired outcome. It is possible, as mentioned previously, that all particles formed during the nucleation pulse are not necessarily equal and some sites still remain more favourable to silver deposition. The next section continues to explore the ways in which the homogeneity of particle sizes can be achieved by using a single pulse.

4.3.1.2 Single Pulse Method

The single pulse method involves the application of one pulse at high overpotential for extended periods. In this way, surface energies may be negated as the potential is so reductive that silver should nucleate at all sites and now diffusion of silver ions become the limiting factor of deposition.

In the single pulse method, potentials of -0.25 V , -0.50 V , -0.75 V and -1.0 V vs Ag/Ag^+ were applied to the GC electrode in the silver-containing solution. A cleaning pulse of 1.0 V vs SCE applied for 15 mins was also used. However, before the potential was applied, the electrode was immersed under open-circuit conditions, in the silver-containing solution for a period of time. The particles

deposited more evenly and the reproducibility was considerably improved with this immersion period. At the open-circuit potential (OCP) there is enough energy to seed silver at suitable sites, and once an external potential is applied silver ions in the solution will preferentially deposit at these sites. On application of the deposition potential, silver may be nucleated at fresh GC sites, but the seeding gives rise to more stable nucleation sites and the growth of these already established sites is more likely than the formation of new ones.

The OCP plot of the GC electrode in the silver-containing solution is shown in Figure 4.16. After the cleaning pulse of 1.0 V was applied, the potential decays towards lower values. After about an hour, potentials of approximately -0.05 V Ag/Ag^+ are recorded and these are sufficient to deposit silver from the solution. The presence of deposited silver was confirmed using stripping voltammograms. A typical voltammogram is shown in Figure 4.17. The stripping peak at 0.20 V vs SCE shows that indeed a very small amount of silver was deposited under open-circuit conditions on the GC electrode. As there was clear evidence for the deposition of silver on immersion of the GC electrode, this step was incorporated after the oxidative cleaning step at 1.0 V of 15 min. The GC electrode was immersed in the silver-containing solution at OCP for 60 min and then the reduction potentials were applied.

The current and charge transients for the single deposition pulse at potentials of -0.25 V, -0.50 V, -0.75 V and -1.00 V vs Ag/Ag^+ for 50 s are shown in Figure 4.18. A reduction current is obtained on application of the potential and this current decays as the deposition period is increased. The charge increases with the deposition period with near linear responses for periods from 20 to 50 s. Higher currents and charges are obtained on deposition at -1.00 V vs Ag/Ag^+ , indicating a higher rate of silver deposition. There is a three-fold decrease in the charge on varying the deposition potential from -1.00 V to -0.25 V vs Ag/Ag^+ .

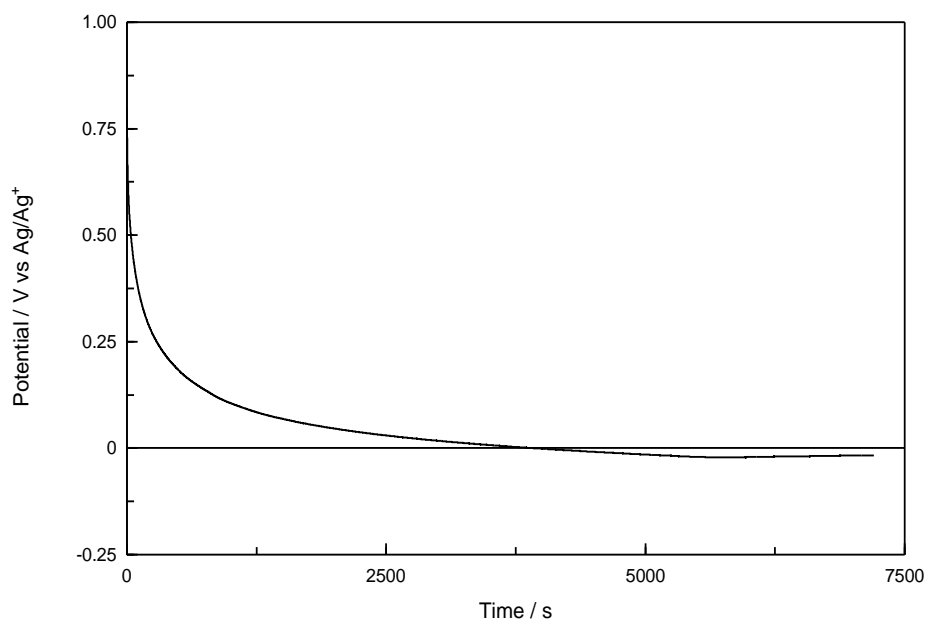


Figure 4.16: Open circuit potential transient for a GC electrode immersed in a solution of $1 \times 10^{-3} \text{ mol dm}^{-3}$ AgClO_4 in 0.1 mol dm^{-3} LiClO_4 .

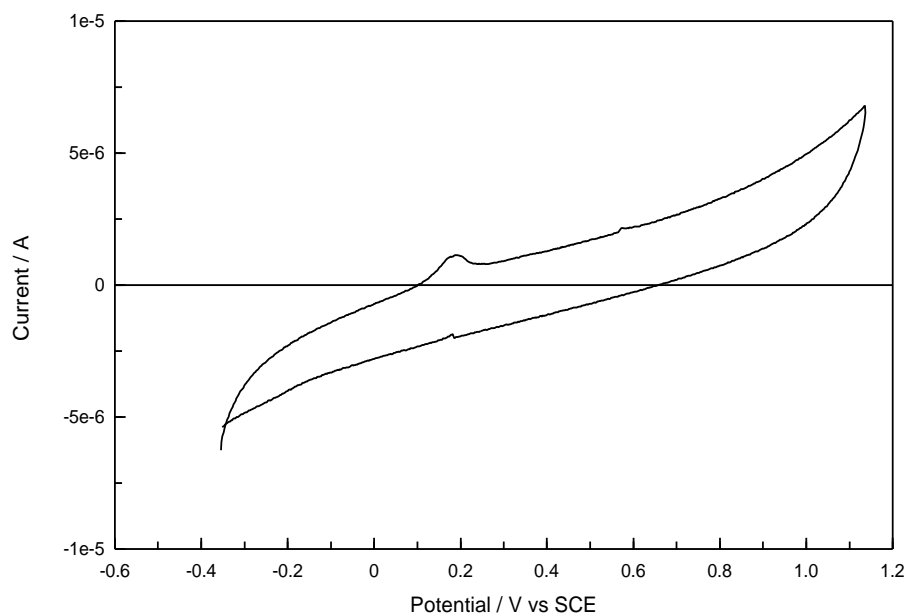


Figure 4.17: Stripping voltammograms at a scan rate of 20 mV s^{-1} in 0.1 mol dm^{-3} LiClO_4 of GC electrode that has been immersed in a solution of $1.0 \times 10^{-3} \text{ mol dm}^{-3}$ AgClO_4 in 0.1 mol dm^{-3} LiClO_4 at OCP for 1 h.

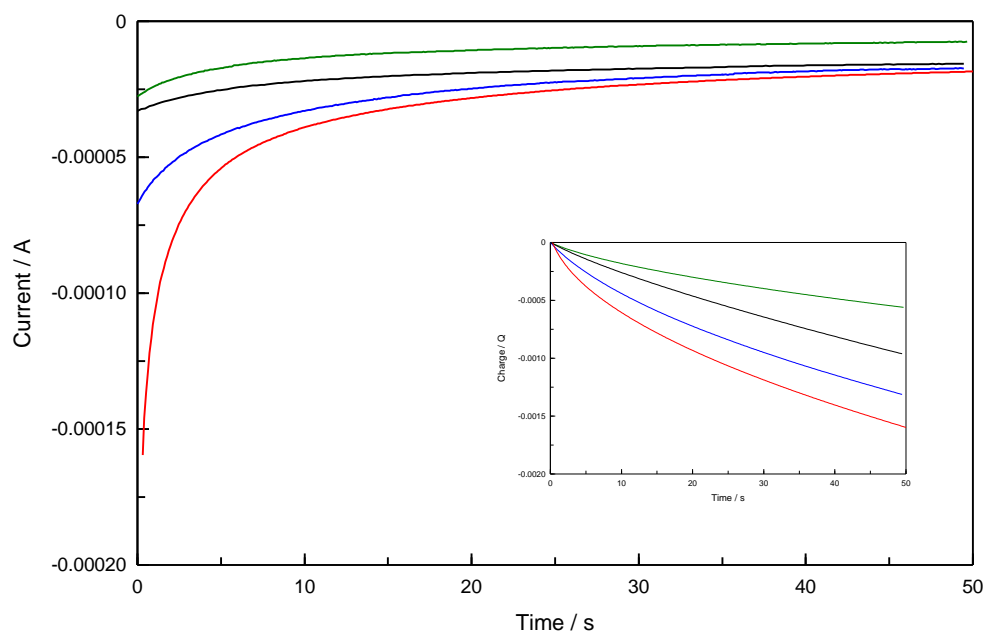


Figure 4.18: Current and charge (insert) transients for silver particles deposited on a GC electrode by single pulse method. Potential set at -0.25 V —, -0.50 V —, -0.75 V — and -1.00 V vs Ag/Ag^+ — for 50 s.

Figure 4.19 (a) shows the SEM micrograph of the resulting GC surface when a potential of -0.50 V vs Ag/Ag^+ is applied for 50 s in the silver-containing solution. The morphology of the deposited silver on the surface is very different when this method is employed compared to that obtained using the double pulse method, Figure 4.19 (b). There is a higher density of silver particles deposited on the surface as the potential is reductive enough to allow nucleation to occur during the entire pulse (progressive nucleation). Furthermore, fewer large particles are evident on the surface, with most of the particles adopting sizes of 100 nm in diameter or less. Indeed, 94% of the particles have diameters equal to or below 100 nm, compared to 85% for the double pulse method.

The SEM micrographs obtained for the deposition of silver at -1.00 V , -0.75 V and -0.50 V vs Ag/Ag^+ applied for 50 s are presented in Figure 4.20. While the number of particles is little changed at the deposition potentials, the particles generated at -0.50 V vs Ag/Ag^+ have the narrowest size distribution and a lower number of particles have diameters greater than 75 nm.

If the potential is maintained at -0.25 V vs Ag/Ag^+ the morphology is completely different, as shown in Figure 4.21. Flower-like deposits are seen, varying from 1 to 2 μm in size and there is no evidence of any smaller silver deposits on the surface. As can be seen from the CV in Figure 4.2, the overpotential for silver reduction on a clean GC electrode is -0.236 V, which is close to the reduction potential used in Figure 4.21. Under these conditions, where the deposition potential is close to the onset of silver deposition, the silver ions will preferentially deposit on the most stable sites rather than nucleate on new sites, giving rise to a few large deposits.

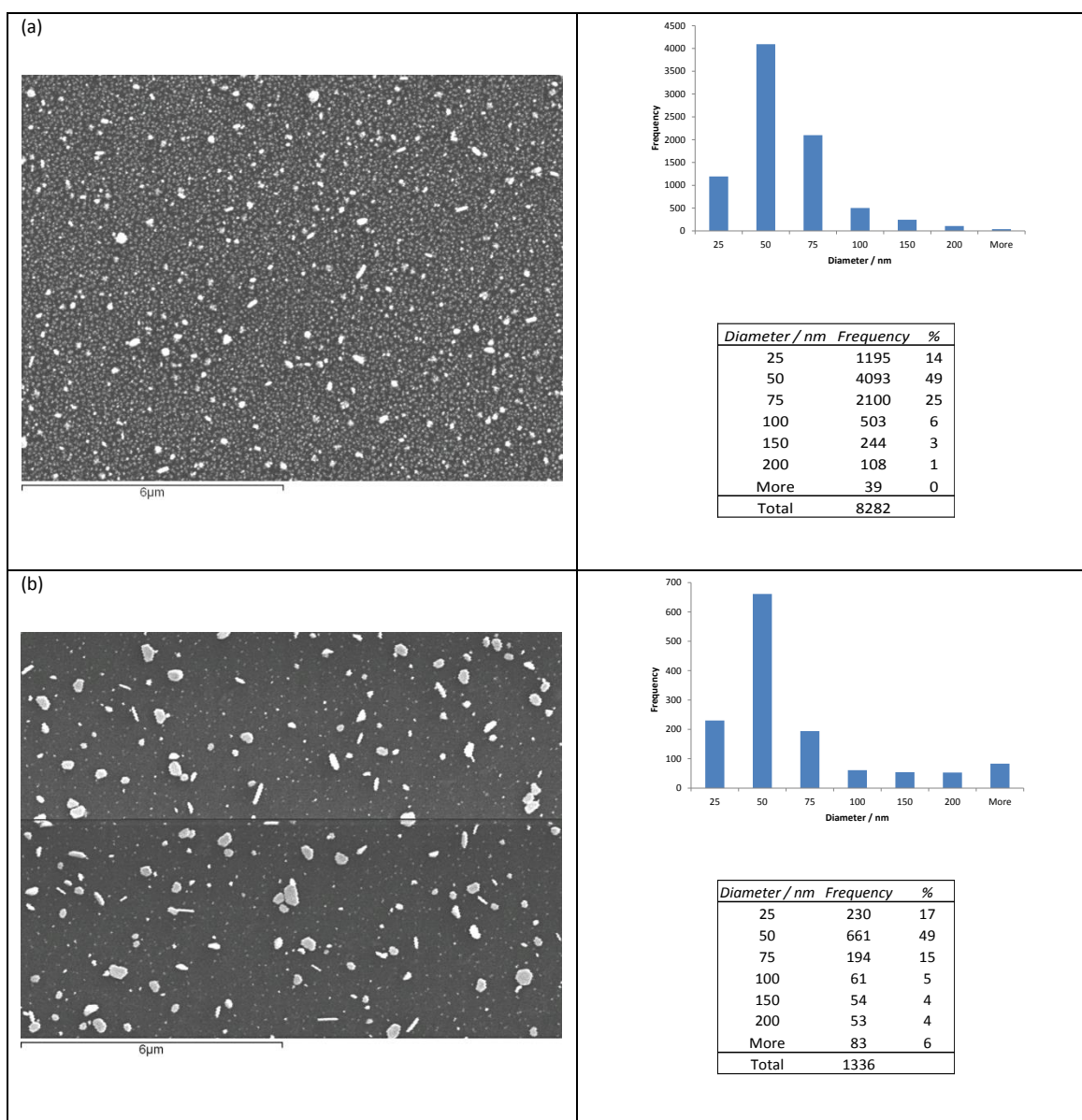


Figure 4.19: SEM micrographs, size distribution histograms and tables for silver particles deposited on GC by (a) the single pulse method using an applied potential of -0.50 V vs Ag/Ag^+ for 50 s, (b) double pulse method $E_1 = -0.50$ V vs Ag/Ag^+ , $t_1 = 1$ s, $E_2 = -0.06$ V vs Ag/Ag^+ and $t_2 = 50$ s.

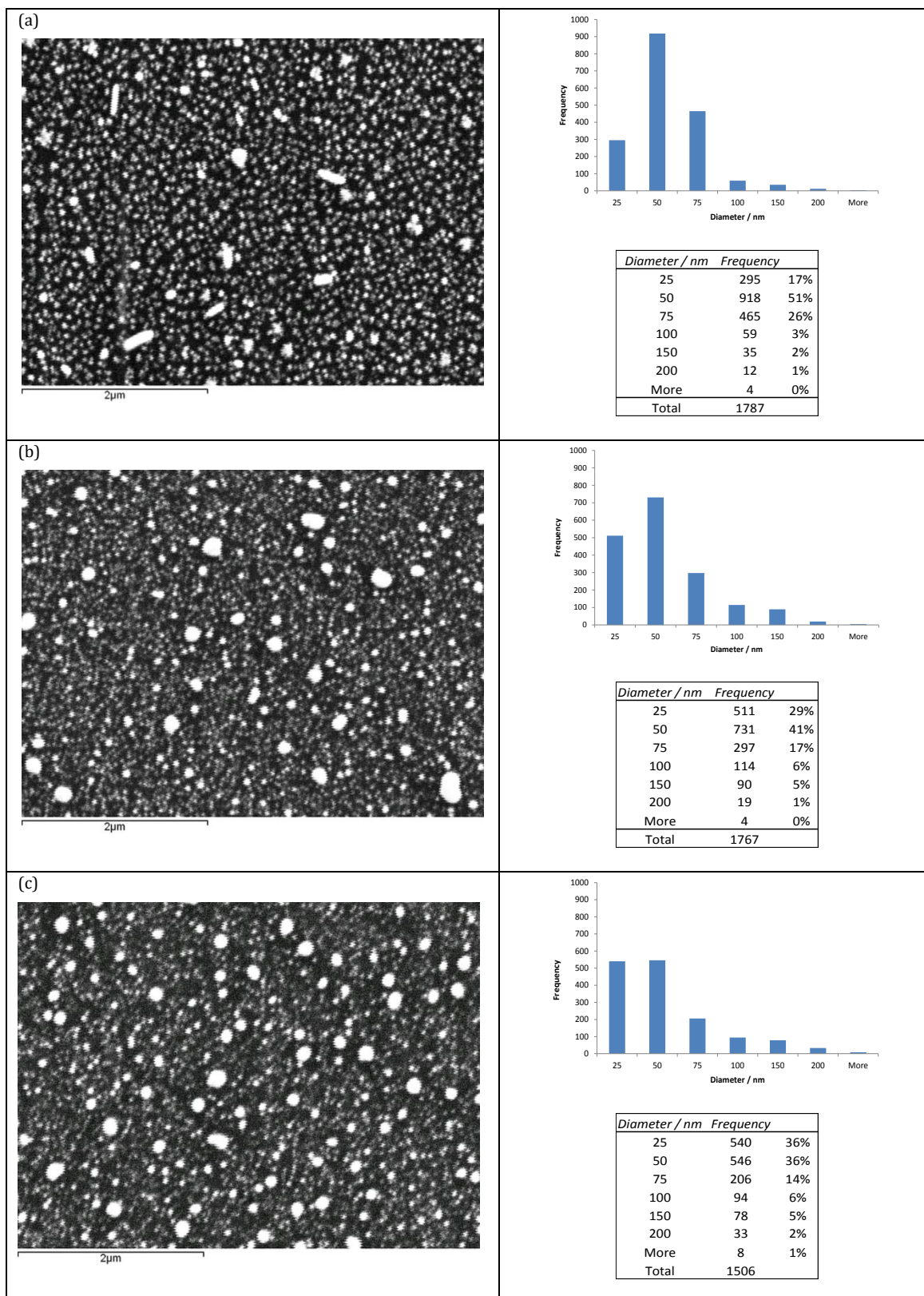


Figure 4.20: SEM micrographs, size distribution histograms and tables for silver particles deposited on GC by the single pulse method. (a) -0.50 V (b) -0.75 V and (c) -1.00 V vs Ag/Ag⁺ for 50 s.

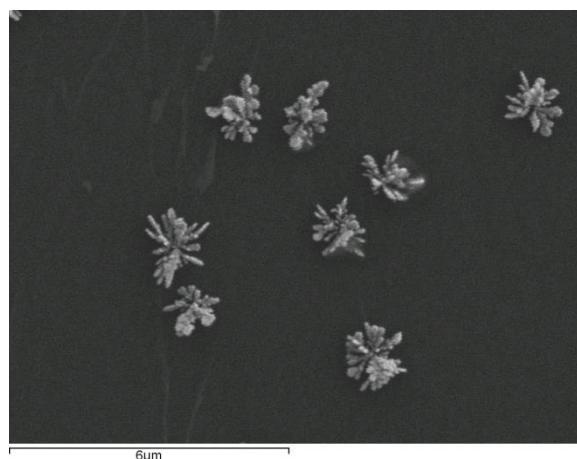


Figure 4.21: SEM image for silver particles deposited on GC by the single pulse method using an applied potential of $-0.25\text{ V vs Ag/Ag}^+$ for 50 s.

The electrochemical detection of nitrates at these silver particles was studied in a solution of $5.0 \times 10^{-3}\text{ mol dm}^{-3}\text{ KNO}_3$ and $0.1\text{ mol dm}^{-3}\text{ LiClO}_4$ and compared with the data obtained using the double pulse method. Figure 4.22 shows the response of the silver-modified GC electrode generated by various single pulses and also an electrode generated by a double pulse for comparison to a nitrate containing solution. It is clear that the voltammograms are similar for the single and double pulse deposition at $-0.50\text{ V vs Ag/Ag}^+$. There is little difference in the peak currents and the peak potentials, suggesting that the morphology of the silver deposited on the surface has little influence on the catalytic ability of silver to reduce nitrate. However, the flower-like deposits obtained at $-0.25\text{ V vs Ag/Ag}^+$ give a very low peak current, at approximately $68\text{ }\mu\text{A}$, and this is probably connected to the low number of deposits.

The corresponding stripping voltammograms, presented in Figure 4.23, although not an accurate measure of the amount of silver deposited on the surface, do give an indication of the quantity of silver. The stripping peaks are similar for the single and double pulse methods at -0.50 V vs Ag/Ag⁺, however, the quantity of silver deposited is much lower at -0.25 V vs Ag/Ag⁺, which is reflected in the lower nitrate reduction current, Figure 4.22. The stripping peak is also slightly lower for the silver deposited at -1.00 V vs Ag/Ag⁺, which may be as a consequence of competitive reactions occurring at the surface at this high overpotential (water reduction reaction).

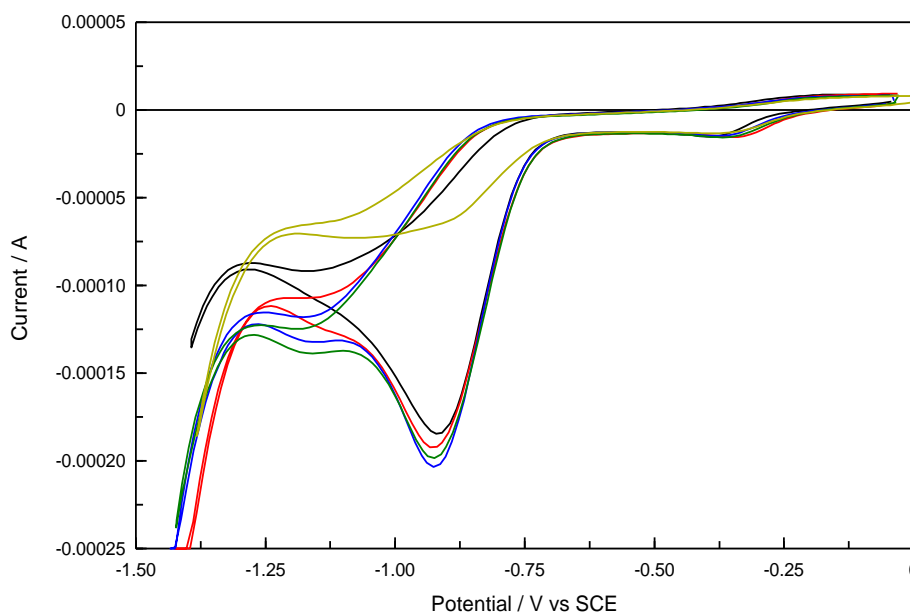


Figure 4.22: Cyclic voltammograms at a scan rate 50 mVs^{-1} in a solution of $5.0 \times 10^{-3} \text{ mol dm}^{-3} \text{ KNO}_3$ and $0.1 \text{ mol dm}^{-3} \text{ LiClO}_4$ at a GC electrode with silver particles deposited by the — double pulse method E_1 at -0.50 V vs Ag/Ag⁺, t_1 at 1s, E_2 at -0.06 V vs Ag/Ag⁺ and t_2 at 50 s, — single pulse at -0.25 V vs Ag/Ag⁺ for 50 s, — single pulse at -0.50 V vs Ag/Ag⁺ for 50 s, — single pulse at -0.75 V vs Ag/Ag⁺ for 50 s and — -1.00 V vs Ag/Ag⁺ for 50 s.

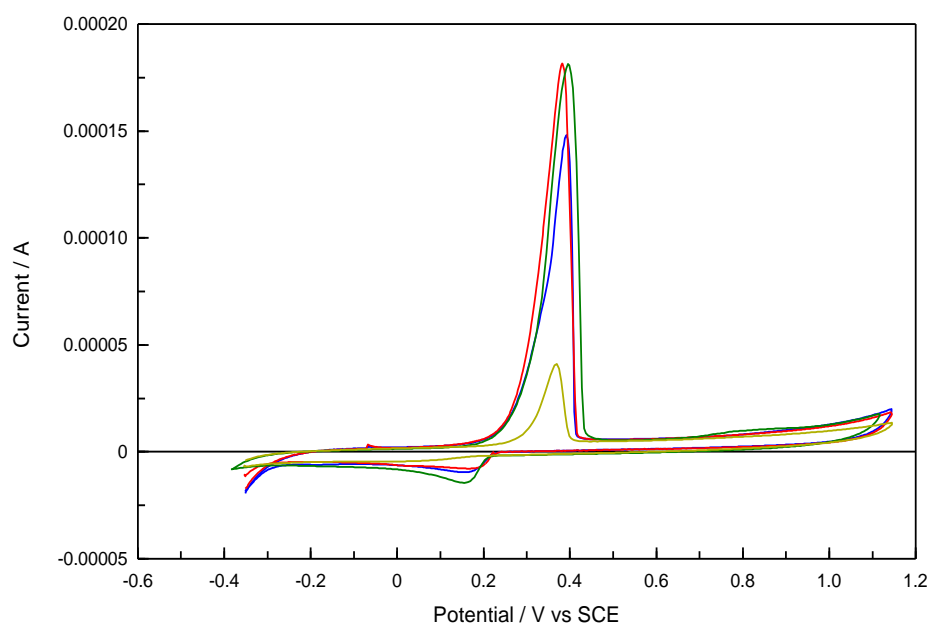


Figure 4.23: Stripping voltammogram at a scan rate 50 mVs^{-1} in a solution of $0.1 \text{ mol dm}^{-3} \text{ LiClO}_4$ at a GC electrode with silver particles deposited by — single pulse -0.25 V for 50 s , — single pulse -0.50 V 50 s , — single pulse -0.75 V 50 s and — -1.00 V for 50 s .

Because of the more homogenous deposition of silver particles, in conjunction with a higher nitrate reduction current, much of the rest of this chapter will investigate the nitrate reduction reaction at a GC electrode modified with silver using a single pulse of -0.50 V vs Ag/Ag^+ of 50 s . However, modelling of the nanoparticle growth is first examined. The current transients recorded during deposition were examined to determine if any insight into the mechanism of silver deposition on the GC surface could be obtained. The current transients were analysed by fitting the data to the commonly employed Scharifker and Hills models.

4.3.2 Modelling of Nanoparticle Growth

It is well known that the shape of the current transients during the first few seconds can give an insight into the mechanism by which a metal is deposited. The study of the nucleation and growth of electrodeposits has been extensively studied, both experimentally and theoretically, by many groups ^(2,19-23). A commonly referred to model for the potentiostatic current-time transient with diffusion controlled growth of two and three dimensional nucleation is the Scharifker and Hills model ⁽²³⁾. The model outlines two scenarios that were described earlier in Section 4.3.1.1, one for instantaneous nucleation, where all nuclei are formed during the initial electrodeposition pulse at the same time, and the other for progressive nucleation, where new nuclei sites are formed throughout the entire period of growth. Proceeding nucleation is a growth phase, and this can occur by two different mechanisms. Two-dimensional (2D) growth proceeds via adatoms attaching to the edge of existing nuclei and eventually coalescing to form a complete layer on the electrode. Nucleation can then occur on this first layer, where the process can be repeated indefinitely. Three-dimensional (3D) growth occurs when adatoms attach to nuclei at any point, resulting in upward and lateral growth at similar rates.

Combining these processes of instantaneous and progressive nucleation and 2D and 3D growth yield the following four equations which describe the early stages of deposition and growth.

Progressive nucleation and 2D growth (PN2D)

$$\frac{I}{I_{max}} = \left(\frac{t}{t_{max}}\right)^2 \exp\left\{-\frac{2}{3}\left(\frac{t^3 - t_{max}^3}{t_{max}^3}\right)\right\} \quad 4.1$$

Instantaneous nucleation and 2D growth (IN2D)

$$\frac{I}{I_{max}} = \left(\frac{t}{t_{max}}\right) \exp\left\{-\frac{1}{2}\left(\frac{t^2 - t_{max}^2}{t_{max}^2}\right)\right\} \quad 4.2$$

Progressive nucleation and 3D growth (PN3D)

$$\left(\frac{I}{I_{max}}\right)^2 = \frac{1.2254}{\left(\frac{t}{t_{max}}\right)} \left\{1 - \exp\left[-2.3367\left(\frac{t}{t_{max}}\right)^2\right]\right\}^2 \quad 4.3$$

Instantaneous nucleation and 3D growth (IN3D)

$$\left(\frac{I}{I_{max}}\right)^2 = \frac{1.9542}{\left(\frac{t}{t_{max}}\right)} \left\{1 - \exp\left[-1.2564\left(\frac{t}{t_{max}}\right)^2\right]\right\}^2 \quad 4.4$$

In Figure 4.24, the current-time transients for the single pulse deposition during the early stages of growth are presented, and exhibit the typical shape for a nucleation process with 3D growth of nuclei under diffusion control. It should be noted that the reduction current is presented as a positive current in this figure.

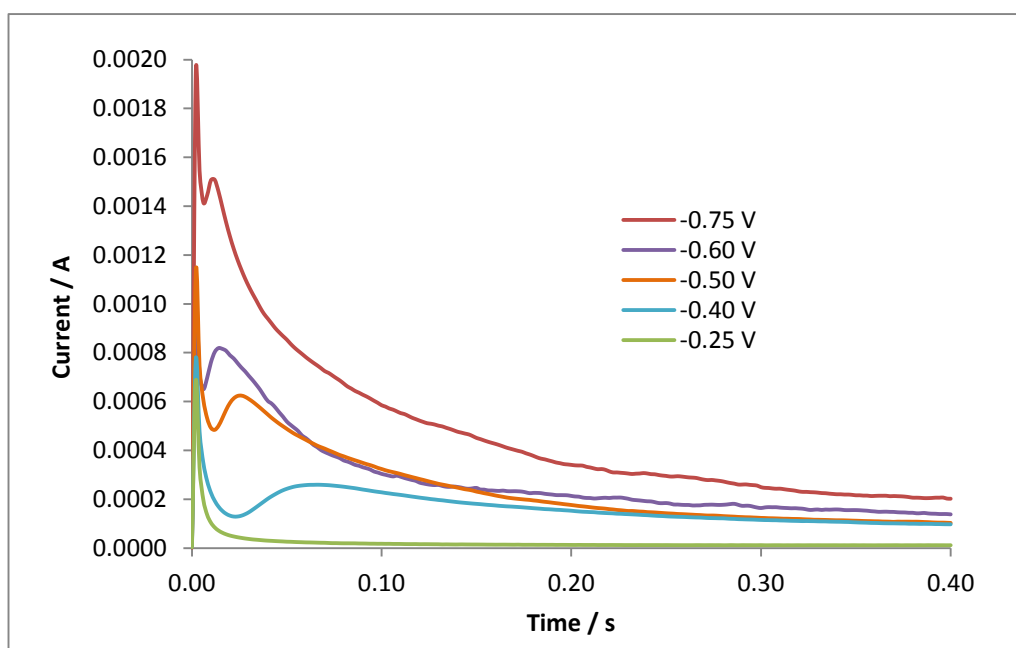


Figure 4.24: Current transients for silver deposition on a GC electrode from a solution of $1.0 \times 10^{-3} \text{ mol dm}^{-3}$ AgClO_4 in 0.1 mol dm^{-3} LiClO_4 at various applied potentials.

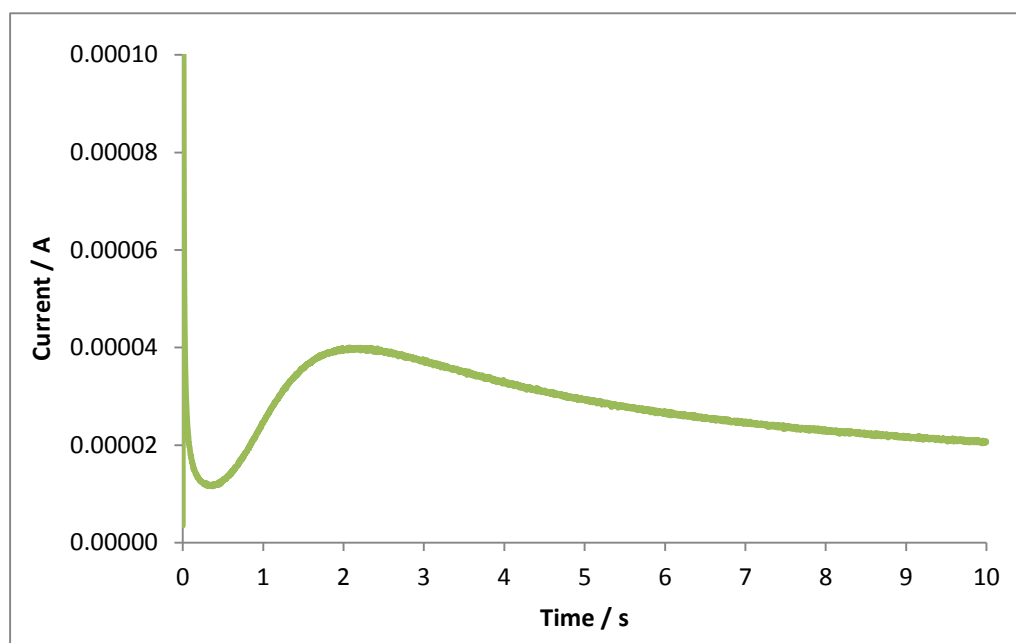


Figure 4.25: Current transients for silver deposition on a GC electrode from a solution of $1.0 \times 10^{-3} \text{ mol dm}^{-3}$ AgClO_4 in 0.1 mol dm^{-3} LiClO_4 at $-0.25 \text{ V vs Ag}/\text{Ag}^+$.

Initially, there is a decreasing current corresponding to the charging of the double layer. This is followed by a rising current as the energy barrier to nucleation is overcome; nuclei expand which provide additional sites for further reduction of silver to occur and therefore more current to flow. Up to this point, the process is kinetically controlled. A maximum current, I_{\max} , is reached at time, t_{\max} , when the diffusion zones around the nuclei begin to overlap. The process now comes under diffusion control and nucleation exclusion zones develop around the nuclei. This is seen experimentally as a drop in the current. The shape of the current-time transients is similar for each of the applied potentials, except at -0.25 V vs Ag/Ag⁺ where the current decays to low values during the first few seconds. However, the magnitude of the I_{\max} and the time, t_{\max} , at which it occurs are altered with a shift to longer t_{\max} and lower I_{\max} as the potential is lowered. This is in agreement with previous studies ⁽²³⁾. In Figure 4.25, the current-time transient recorded at -0.25 V vs Ag/Ag⁺ is shown over a longer period, and the current maxima is now reached at much later times (2.178 s) compared to the other potentials ⁽²³⁾. The current at I_{\max} is also considerably lower. This is consistent with the morphology of the particles deposited at this potential, Figure 4.21, which are very different to the particles deposited at the other potentials.

A comparison between the experimental data and a theoretical plot derived from the appropriate equations, Equations 4.1 to 4.4, is shown in Figures 4.26, 4.27 and 4.28 for the applied potentials of -0.75 , -0.50 and -0.25 V vs Ag|Ag⁺, respectively. The data are presented as non-dimensional plots of (I/I_{\max}) or $(I/I_{\max})^2$ for 2D and 3D growth, respectively, as a function of t/t_{\max} . It is clear from the plots that the experimental data resembles the modelled PN3D model. However, the trend is towards instantaneous nucleation up to t/t_{\max} of 1 as the potential is increased to higher reduction potentials. This is unsurprising as a greater number of sites are generated when the energy barrier to nucleation is overcome by higher overpotentials ⁽⁸⁾. However, progressive nucleation is not the ideal behaviour as it can lead to increased polydispersity.

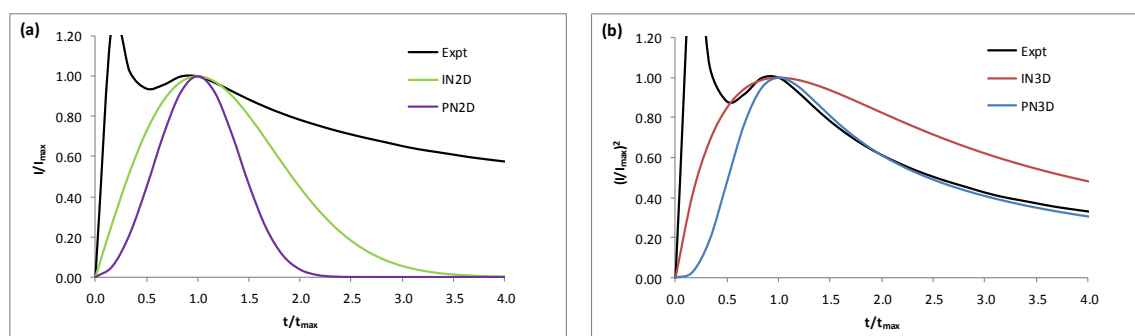


Figure 4.26: Dimensionless theoretical and experimental plots for silver deposited at -0.75 V vs Ag/Ag⁺ for (a) 2-D and (b) 3-D instantaneous and progressive nucleation.

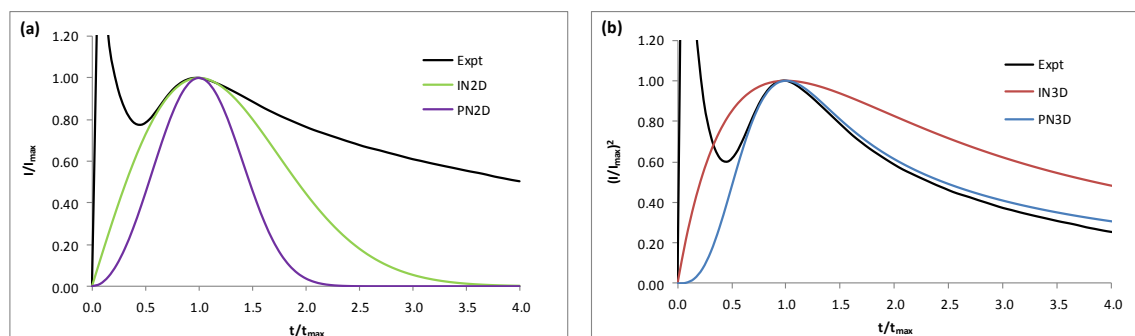


Figure 4.27: Dimensionless theoretical and experimental plots for silver deposited at -0.5 V vs Ag/Ag⁺ for (a) 2-D and (b) 3-D instantaneous and progressive nucleation.

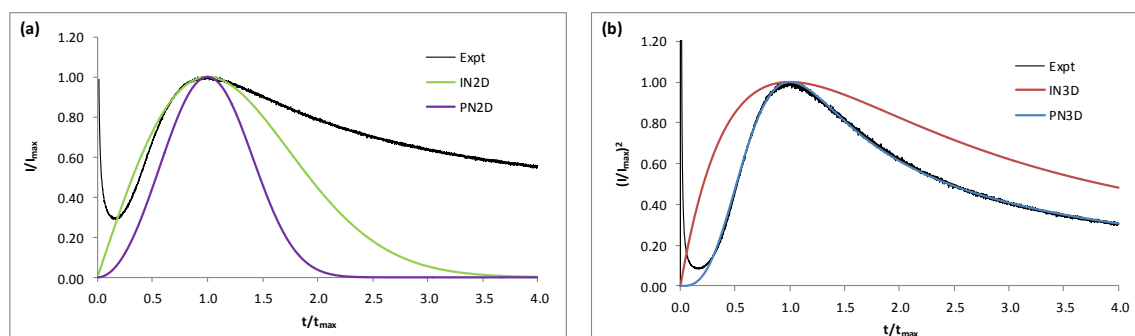


Figure 4.28: Dimensionless theoretical and experimental plots for silver deposited at -0.25 V vs Ag/Ag⁺ for (a) 2-D and (b) 3-D instantaneous and progressive nucleation.

Because of the more homogenous deposition of silver in conjunction with a strong nitrate reduction current, particles grown using a single deposition pulse of -0.50 V vs Ag/Ag^+ were the focus of the rest of this chapter in terms of maximising the nitrate current and determination of the associated kinetic terms. Figure 4.29 examines the nitrate current and how it is affected when the length of the -0.50 V vs Ag/Ag^+ pulse is varied. The peak current obtained for the 25 s pulse period is considerably lower and this may be connected to the amount of silver deposited. The highest peak currents are obtained for pulse periods of 50 s and 75 s and extending the duration of the pulse to 75 s, does little to enhance the signal. It appears that a single pulse of 50 s at a potential of -0.50 V leads to the optimal nitrate signal. As with most sensors, it is preferential to express the signal as a current density. This makes comparisons to other sensors more sensible and reveals a truer understanding of the sensors catalytic ability. To achieve this, the surface area must be known.

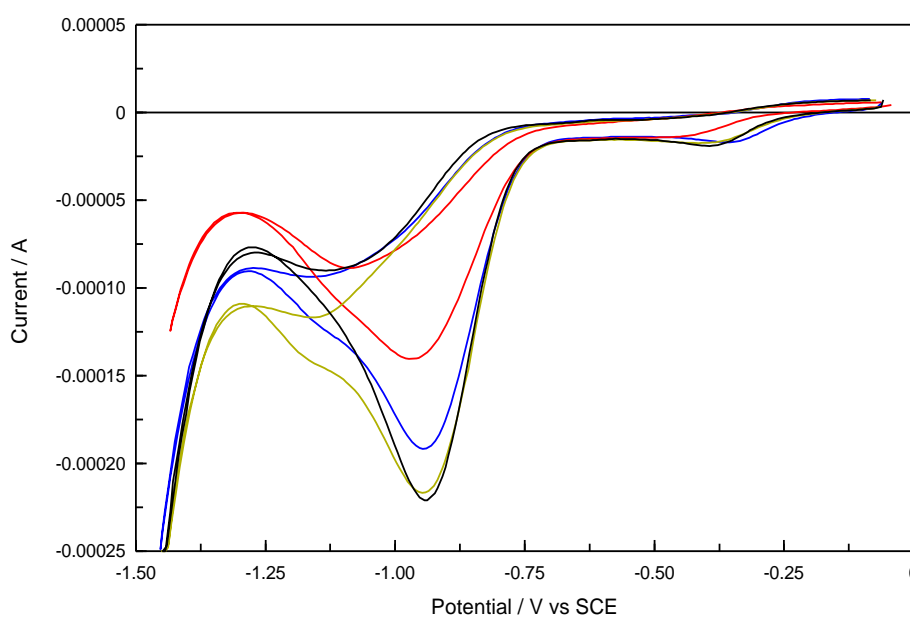


Figure 4.29: Cyclic voltammograms at a scan rate 50 mV s^{-1} in a solution of $5.0 \times 10^{-3}\text{ mol dm}^{-3}\text{ KNO}_3$ and $0.1\text{ mol dm}^{-3}\text{ LiClO}_4$ at a GC electrode with silver particles deposited by the single pulse method of -0.50 V vs Ag/Ag^+ for — 25 s, — 50 s, — 75 s and — 100 s.

While SEM is important in order to show the morphology of the deposit it does not allow for an accurate way to determine the surface area. There is some evidence, particularly in Figure 4.29, that the amount of silver on the electrode is not directly proportional to the magnitude of the nitrate signal. For example, a 75 s or 100 s period of deposition at -0.50 V vs Ag/Ag⁺ does not give rise to an increase in the nitrate reduction current compared to a period of 50 s, Figure 4.29. It was thought that increased deposition time would lead to higher surface area and hence more sites for nitrate adsorption and subsequent reduction to occur. To understand why this appeared not to be the case, more accurate data on the actual surface area obtained at different deposition times were required. In this next section, some electrochemical means of determining the surface area and how it can be related to the nitrate signal are presented and discussed.

4.3.3 Size and Surface Area of the Electrodeposited Nanoparticles

4.3.3.1 Introduction

When studying electrochemical processes at an electrode, knowledge of the real surface area of the electrode is vital as many reaction rates and important relationships studied in electrochemistry, such as the Levich and Randles-Sevcik relationships, are defined per unit area of the interface ⁽²⁴⁾. Comparisons between experimental data for different materials and/or from different laboratories are essentially meaningless without normalisation to unit real surface area. Geometric surface area, except at liquid electrodes, often grossly underestimates the actual surface area by not accounting for microscopic surface roughness. The roughness factor, i.e., the ratio between the real and geometric area of the electrode, is far more accurate for evaluating basic parameters such as the current density. Yet there are plenty of examples across the literature with regard to sensors where geometric area is used to normalize current and this can lead to inconsistency when comparing the sensitivities of materials ⁽²⁵⁻²⁷⁾. In particular, the large surface area of nanoparticles is often quoted as one of the major advantages of these materials so accurate quantification of the real surface area is important to assess if their size contributes to their catalytic behaviour. Accurate knowledge of the real surface area allows comparisons to be made between electrodeposited particles

and bulk electrodes of the same material. A comprehensive discussion on real area determination is given by Trasatti and Petrii ⁽²⁸⁾. They scrutinised various *in-situ* and *ex-situ* methods and approaches used to determine real surface area and the suitability to the specific experimental situation. Cyclic voltammetry featured in a number of different ways in the review and two of them were utilized in this report to elucidate the real surface area.

Firstly, the charge involved in the reduction of surface oxides generated during consecutive potential cycling can be used to determine surface areas. The sweep begins at the same potential but the anodic inversion potential is incrementally increased. A plot of the inversion potential and reduction charge of the oxide results in multiple linear regions associated with different numbers of electrons transferred. The first linear region is attributed to the reduction of the first metal hydroxide monolayer. The inversion potential at which this region loses linearity and the charge increases exponentially corresponds to metal dissolution. The charge associated with this inversion potential can be related to the electroactive surface area ^(29,30).

The other method utilized in this report also involved cyclic voltammetry. It is an extremely useful and convenient technique to determine the active surface of the electrode. The underpotential deposition (UPD) of lead is one of the most studied methods to determine the surface area of silver. The process is well known to be highly sensitive to the surface structure of the electrode. In general, the Pb UPD stripping peak is not observed at a bare GC electrode ^(8,31,32), which makes the technique ideal for selectively determining the area of the deposited silver. Indeed, this was observed in the present study, where there was no evidence of UPD Pb stripping currents on a bare GC electrode.

The phenomenon of UPD refers to the deposition of a monolayer or sub-monolayer of metal on a foreign substrate at potentials more positive than that predicted by the Nernst equation for bulk deposition ⁽³³⁻³⁵⁾. This occurs because the depositing atoms have a higher affinity for the substrate than they do for each other. Using the ratio of the charge associated with the anodic dissolution of a monolayer of the foreign metal atoms and a literature known charge density for a monolayer of

deposition of that metal, allows the surface area to be evaluated, as shown in Equation 4.5 ⁽³⁶⁾.

$$A = \frac{Q_{upd} - Q_{dl}}{q_m} \quad 4.5$$

In this equation, Q_{upd} corresponds to the charge of the UPD stripping peak, Q_{dl} is the charge of the double layer capacitance and q_m is the charge of a complete monolayer of metal. Streltsov and co-workers estimated that the theoretical charge associated with a monolayer of Pb is $302 \mu\text{C cm}^{-2}$ ⁽³⁷⁾. This is assuming that the surface atomic density of closely packed Pb atoms, of 0.175 nm in radius, is $9.4 \times 10^{14} \text{ cm}^{-2}$ and two electrons are needed to discharge a Pb atom. This, however, is lower than that observed experimentally, which is typically $380 \pm 40 \mu\text{C cm}^{-2}$. To arrive at this charge density Streltsov used AFM and computer analysis to determine the roughness factor. Across the literature, many groups arrived at similar values ⁽³⁷⁻⁴³⁾. In general, the comparison is made with the charge associated with a monolayer of the adatoms on a substrate whose surface area can be calculated by another means, such as the reduction of surface oxides of gold or by comparison to a homogeneous, atomically flat single-crystal electrode⁽⁴³⁾.

The discrepancy between the theoretical and estimated experimental observations can be explained. Staitkov and co-workers have shown that the interaction between Pb and substrates, such as Ag and Au, results in the formation of a compressed 2D hexagonal close packed (hcp) Pb monolayer ^(44,45). The charge density corresponding to this highly compressed layer exceeds that of an uncompressed layer. Additionally, the ionic radius may be more appropriate to use since the nature of the bond with silver is essentially ionic/covalent. Also, the sizes of silver and Pb atoms are different, therefore, a commensurate layer of Pb on silver cannot be formed⁽⁴⁶⁾. This technique suffers from other limitations, in particular corrections for background charging are arbitrary and it can be difficult to identify the end points of the UPD oxidation peak leading to further error. In this work, every attempt was made to be consistent in choosing the potential limits of the oxidation wave. A monolayer can be formed using constant potential amperometry or cyclic voltammetry ^(39,42). There is only one set of UPD peaks for

Pb on silver, compared to two sets observed on gold. They are also considerably sharper and more defined ⁽⁴⁷⁾. The characteristic shape of the CV is strongly dependent on the composition of the solution, with the presence of halides giving rise to sharp and well defined peaks⁽⁴⁶⁾.

Preparing a monolayer or sub-monolayers of Pb on an electrode can be achieved in a number of different ways. Hupp and co-workers used a rotating silver disc electrode held at a constant potential rotating at 600 RPM and immersed in a solution containing μM concentrations of Pb^{+2} ⁽⁴⁸⁾. The electrode potential was set so that it was negative with respect to the UPD peak but positive with respect to bulk deposition. The time required to reach a full monolayer was reached when longer deposition times no longer increased the size of the UPD anodic stripping peak. Hupp and co-workers, by controlling deposition times, used this technique to deposit percentages of monolayer to see how underpotentially deposited Pb affected the capacitance at the interface. When only full monolayers are required, as is the case in this study, cyclic voltammetry in a mM Pb^{+2} solution is sufficient to reach full coverage ^(9,38,42). The procedure to form a monolayer is outlined in Chapter 2, Section 2.4.2.2.

For metals that show a well-defined double layer potential region where no faradaic process occurs in a CV, the pseudo-capacitance from the slope of a plot of the change in capacitance current as a function of scan rate, Equation 4.6, can be used to determine the real surface area ⁽⁴⁹⁾.

$$C = \frac{\Delta i}{\Delta E/t} \quad 4.6$$

The real surface area (A_s) can be ascertained by comparison of C to a known value of the capacity per unit area (C_s), determined from an independent experiment using an electrode with a defined surface area (e.g., $16 \mu\text{F cm}^{-2}$ for mercury ⁽⁵⁰⁾ and $25 \mu\text{F cm}^{-2}$ for silver ⁽⁵¹⁾), Equation 4.7.

$$A_s = C/C_s \quad 4.7$$

4.3.3.2 Pb Underpotential Deposition on a Bulk Silver Electrode

As described in the Introduction, UPD refers to the process where a monolayer is formed on a foreign metal substrate at potentials more positive than the Nernst equilibrium potential. UPD is one of the most used methods to determine the surface area of silver and the following sections utilise the technique to determine the real surface area of the deposited particles and of a bulk silver electrode so that accurate comparisons can be made between the systems.

The response of a bulk silver electrode, when cycled in a solution containing lead(II) chloride, is shown in Figure 4.30. Two sets of redox peaks are observed. The first set of peaks corresponds to the UPD of Pb at silver. The peak potentials for the reduction and oxidation are approximately -0.41 V and -0.39 V vs SCE, respectively, and this corresponds to a reversible process. Scanning further in the negative direction reveals another set of peaks corresponding to bulk or multilayered deposition of Pb at -0.53 V and -0.48 V vs SCE for reduction and oxidation, respectively. Although the overall charge for stripping of the UPD monolayer is similar if the electrode is scanned into the region of bulk deposition for the first cycle, successive cycling presents challenges as the larger redox peaks for the multilayers of Pb shift the UPD stripping peak. This makes it more difficult to identify the potential limits under which to measure the charge and subtract the background currents. Surface roughening of the electrode also occurs when the electrode is cycled into the bulk Pb redox window. For this reason, all Pb UPD experiments were carried out in a potential window where bulk deposition was avoided.

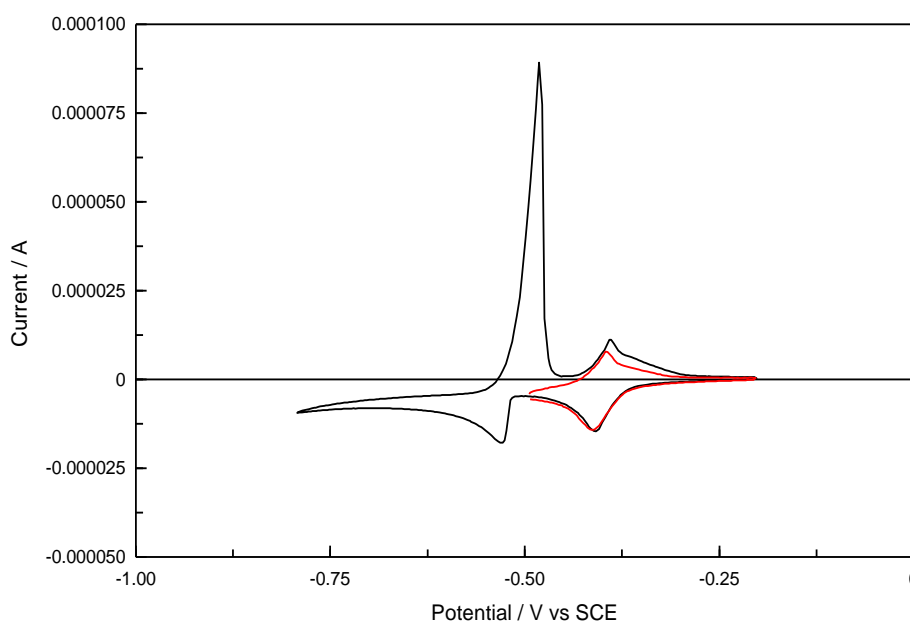


Figure 4.30: Cyclic voltammograms recorded at 20 mV s^{-1} at a silver electrode in $1.0 \times 10^{-3} \text{ mol dm}^{-3} \text{ PbCl}_2$ and $0.1 \text{ mol dm}^{-3} \text{ HCl}$ between -0.20 V and -0.80 V vs SCE -0.20 V — and -0.50 V vs SCE —.

4.3.3.2.1 Surface Roughening

One of the limitations of this technique is its destructive nature. Depositing Pb atoms and subsequently stripping them may cause surface reconstruction of silver atoms^(30,52). The voltammograms of multiple cycling of a bulk silver electrode in a Pb solution are shown in Figure 4.31 and Figure 4.32. In Figure 4.31, the negative sweep is reversed at -0.50 V vs SCE before bulk Pb deposition occurs, whereas in Figure 4.32 the potential is scanned into the bulk region to -0.80 V vs SCE. Figure 4.33 illustrates how scanning into the bulk deposition region has affected the anodic stripping charge of the UPD peak. After 10 cycles, up to -0.80 V vs SCE, the surface has roughened by 15%, as the charge has become larger, while cycling to -0.50 V vs SCE, as shown in Figure 4.31, very little change in the charge over cycle number is observed with less than 6% variation from the initial cycle. This indicates that little surface roughening occurs if the bulk deposition region is avoided.

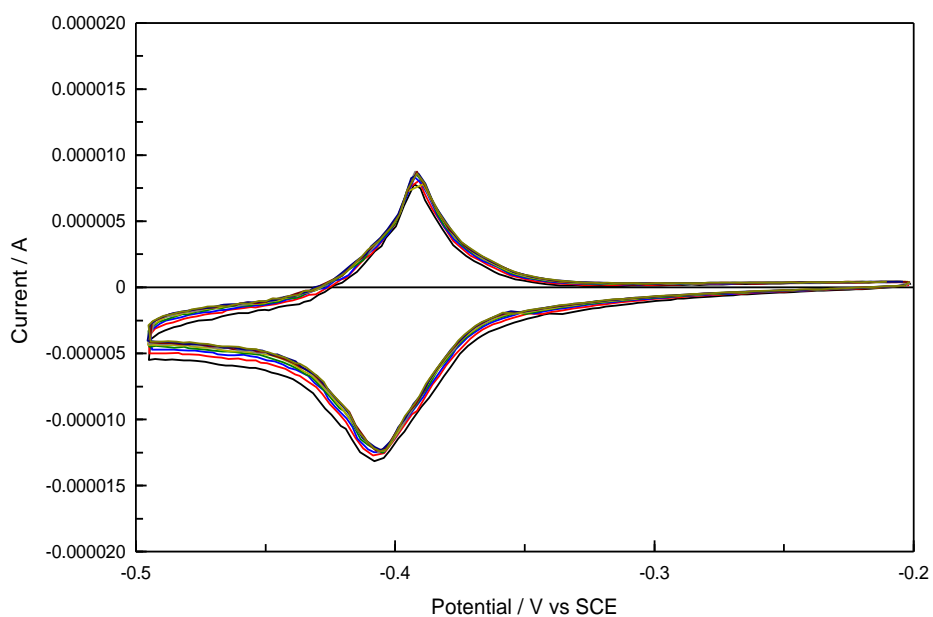


Figure 4.31: Cyclic voltammograms at a bulk silver electrode from -0.20 V to -0.50 V vs SCE in $10.0 \times 10^{-3} \text{ mol dm}^{-3} \text{ PbCl}_2$ and $0.1 \text{ mol dm}^{-3} \text{ HCl}$. Cycle 1 to 10 at a scan rate of 20 mV s^{-1} .

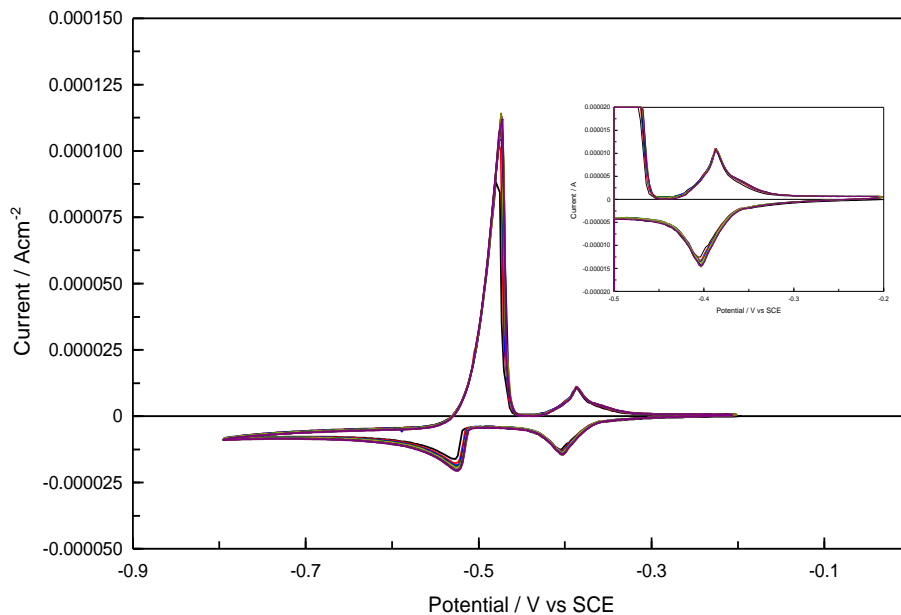


Figure 4.32: Cyclic voltammograms at a bulk silver electrode from -0.20 V to 0.80 V vs SCE in $10.0 \times 10^{-3} \text{ mol dm}^{-3} \text{ PbCl}_2$ and $0.1 \text{ mol dm}^{-3} \text{ HCl}$. Cycle 1 to 10 at a scan rate of 20 mV s^{-1} . Inset: Close-up of Pb UPD peaks.

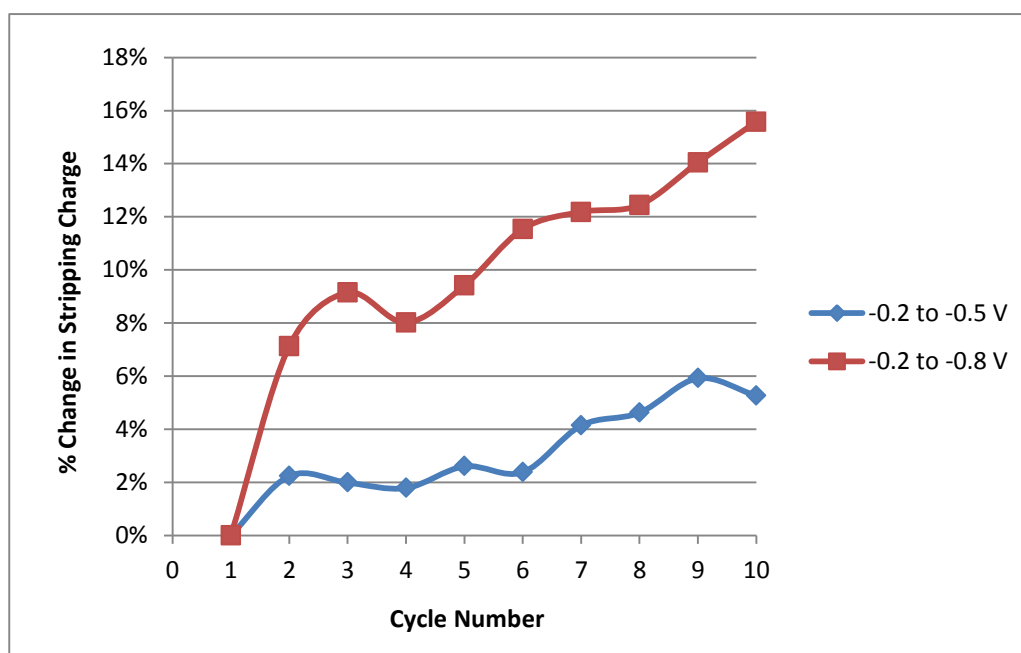


Figure 4.33: Anodic stripping charge % change from cycles 1 to 10 for two different potential windows corresponding to CVs in Figure 4.31 and 4.32.

Another feature of the profile of the CV is the presence of a side peak at -0.38 V vs SCE, as indicated by the arrow in Figure 4.34. It can be seen more clearly when the sweep rate is slow. The cycle shown in Figure 4.34 was recorded at 10 mV s^{-1} . It occurs at the same potential as the anodic stripping, at -0.38 V vs SCE, and, therefore, is indicative of an absorption process. If not, then it certainly points to two processes taking place simultaneously. Jovic and Jovic found a similar cathodic side peak during the UPD of Cd on Cu ⁽⁵³⁾.

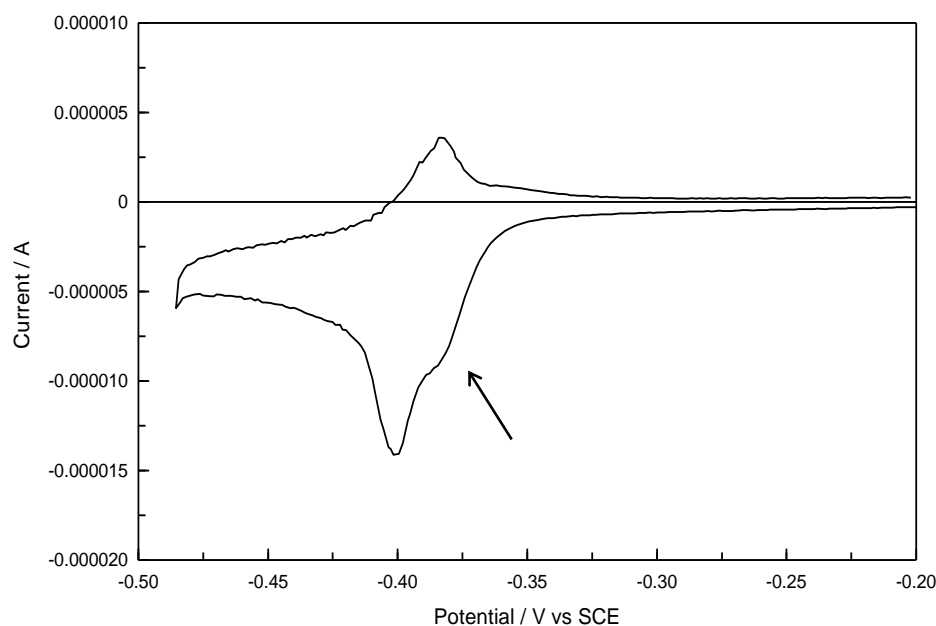


Figure 4.34: Cyclic voltammograms at a bulk silver electrode in $10.0 \times 10^{-3} \text{ mol dm}^{-3} \text{ PbCl}_2$ and $0.1 \text{ mol dm}^{-3} \text{ HCl}$. Scan rate set at 10 mV s^{-1} .

4.3.3.2.2 Effect of Pb Concentration

In order to confirm complete monolayer coverage the bulk silver electrode was cycled in two solutions containing different concentration of Pb^{2+} . Figure 4.35 shows the voltammograms recorded in $1.0 \times 10^{-3} \text{ mol dm}^{-3}$ and $10.0 \times 10^{-3} \text{ mol dm}^{-3} \text{ PbCl}_2$ in aqueous $0.1 \text{ mol dm}^{-3} \text{ HCl}$ solution at a bulk silver electrode. The charge associated with the UPD anodic stripping peak for 1.0 and $10.0 \times 10^{-3} \text{ mol dm}^{-3} \text{ Pb}^{2+}$ solution is closely matched with values of 2.22×10^{-5} and $2.16 \times 10^{-5} \text{ C}$, respectively. This shows that potential scans in Pb^{2+} concentration above $1.0 \times 10^{-3} \text{ mol dm}^{-3}$ are sufficient to form a full monolayer. Indeed, Bonfil and co-workers found that cycling in a $0.5 \times 10^{-3} \text{ mol dm}^{-3} \text{ Pb}^{2+}$ solution produced close to full monolayer coverage⁽⁴⁷⁾. However, all further experiments were carried out using $10.0 \times 10^{-3} \text{ mol dm}^{-3} \text{ PbCl}_2$ in $0.1 \text{ mol dm}^{-3} \text{ HCl}$.

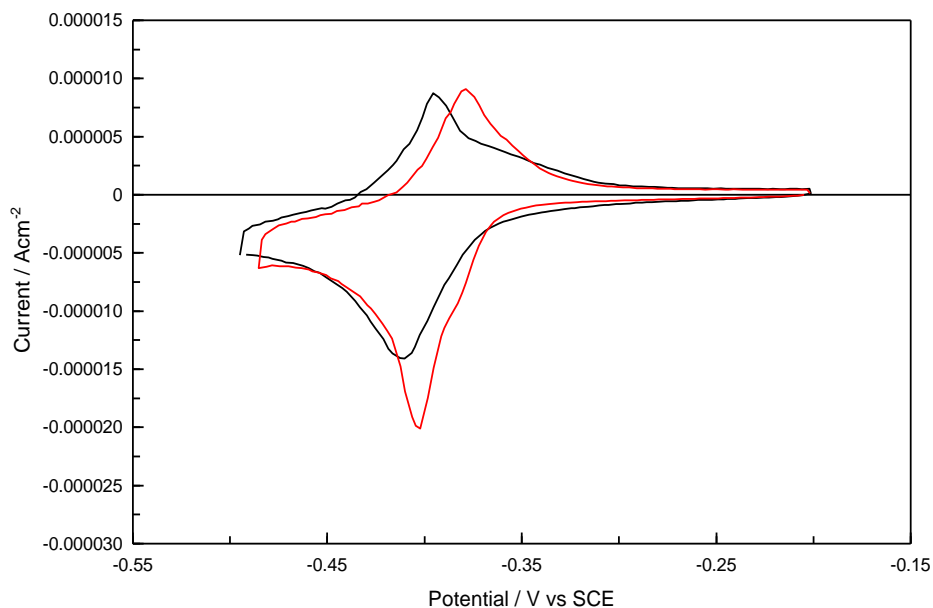


Figure 4.35: Cyclic voltammograms at a bulk silver electrode in — $1.0 \times 10^{-3} \text{ mol dm}^{-3}$ and — $10.0 \times 10^{-3} \text{ mol dm}^{-3} \text{ PbCl}_2$ with $0.1 \text{ mol dm}^{-3} \text{ HCl}$ as background electrolyte. Scan rate of 20 mV s^{-1} .

It is evident from Figure 4.35 that there is a shift to more positive peak potentials with increasing Pb^{+2} concentration for both the anodic and cathodic peaks which is consistent with Nernstian behaviour. This was also found to be the case in a study by Ragoisha and co-workers.⁽⁴⁰⁾ The shift is 17 mV/decade for the anodic peak and 9 mV/decade for the cathodic peak. The height and charge associated with the oxidation and reduction waves are also not equal. There is little discussion on this in the literature. Osipovich and Poznyak observed a greater charge passed on the cathodic deposition scan for Cd on a Te electrode compared to the subsequent anodic stripping scan. This was explained by the fact that only Cd atoms on the CdTe surface are dissolved, while deeper ones are not oxidized in the potential region under investigation⁽⁵⁴⁾. Chloride adsorption could also be playing a role. Jovic and co-workers discussed how chloride adatoms on silver are not desorbed when Cd is underpotentially deposited, but rather are replaced by Cd atoms and displaced on top of the layer of Cd⁽⁵⁵⁾. This chloride displacement contributes an additional cathodic charge of 74 to $149 \mu\text{C cm}^{-2}$. This same process may be occurring between Pb and silver, as evident in Figure 4.35.

4.3.3.2.3 Effect of Potential Window

To ensure that a full monolayer of Pb was deposited within the potential window of the cyclic voltammogram, the reduction limit was varied while the oxidation limit was fixed. Typical CV's are shown in Figure 4.36, where the potential was cycled to -0.47 V, -0.48 V, -0.49 V, -0.50 V and -0.51 V vs SCE. As can be seen from the CV's, there is very little difference in the cycles as the window is extended in the negative direction. However, interference from the current related to the anodic stripping of bulk deposited Pb makes it difficult to identify the potential limits with which to measure the charge related to the UPD stripping current. For this reason, the chosen reduction limit was set at -0.49 V vs SCE, the maximum potential beyond which bulk deposition occurred. In this way, sufficient time was given to allow full surface coverage of a monolayer of Pb to be deposited but avoided the deposition of subsequent layers. Bonfil and co-workers also scanned a silver electrode in a Pb^{+2} containing solution to different negative potential limits and observed similar results ⁽⁴⁷⁾.

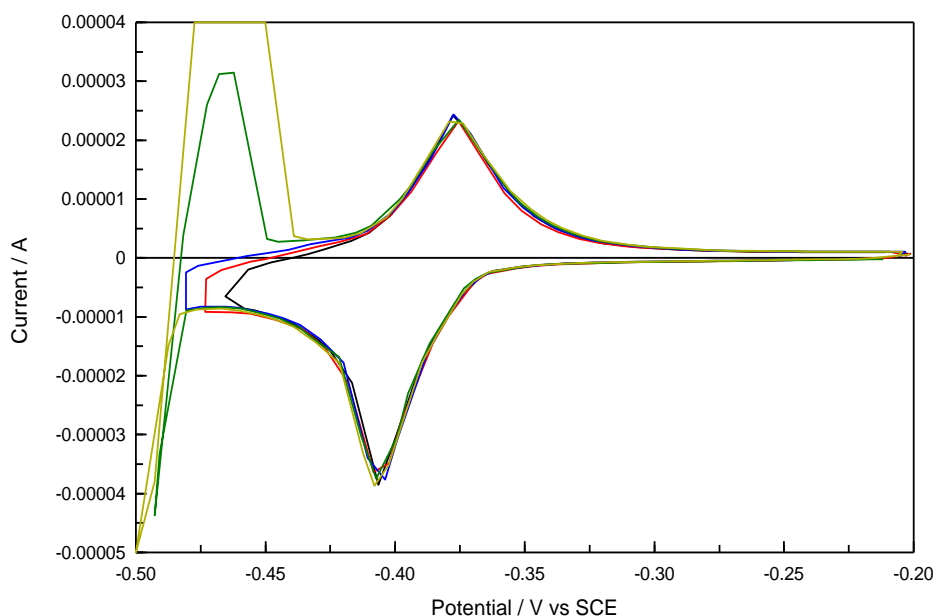


Figure 4.36: Cyclic voltammograms at a bulk silver electrode in $10.0 \times 10^{-3} \text{ mol dm}^{-3} \text{ PbCl}_2$ and $0.1 \text{ mol dm}^{-3} \text{ HCl}$. Negative potential limit varied from -0.47 V, -0.48 V, -0.49 V, -0.50 V and -0.51 V vs SCE. Positive potential limit was constant at -0.20 V vs SCE in all cases. Scan rate of 50 mV s^{-1} .

4.3.3.2.4 Effect of Scan Rate on Stripping Charge

Using the optimum potential window identified in Section 4.3.3.2.3 a number of different scan rates were investigated. The scan rate was varied from 10 to 100 mV s^{-1} and the corresponding CV's are shown in Figure 4.37. The charge associated with the anodic stripping peak at each scan rate is presented in Table 4.1. The consistency observed for the anodic charge with respect to scan rate is an indication that indeed the monolayer is complete ⁽³⁰⁾. The anodic charge remains essentially constant at 20.5 μC . Also, the peak potential does not change with scan rate and occurs at -0.38 V vs SCE. A plot of the logarithm of the scan rate as a function of the logarithm of the peak current is shown in Figure 4.38. The plot is linear with a slope of 0.95, up to 100 mV s^{-1} , indicating an adsorption-controlled process.

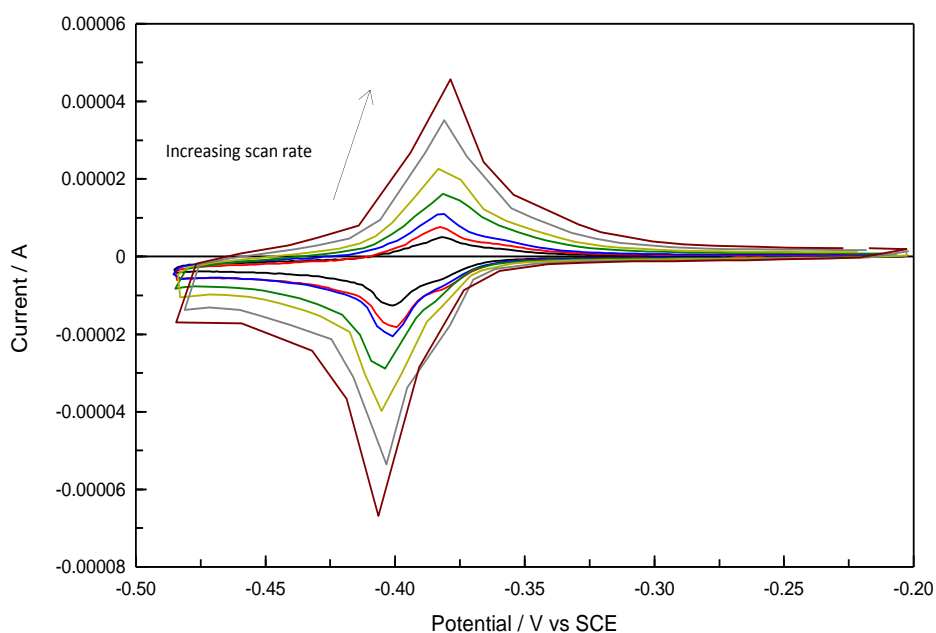


Figure 4.37: Cyclic voltammograms at a bulk silver electrode in $10.0 \times 10^{-3} \text{ mol dm}^{-3} \text{ PbCl}_2$ and $0.1 \text{ mol dm}^{-3} \text{ HCl}$. Scan rate set at 10, 15, 20, 35, 50, 75 and 100 mV s^{-1} .

Table 4.1: Anodic stripping charge associated with a monolayer of Pb on a bulk silver electrode at various scan rates.

Scan Rate / mV s^{-1}	Stripping Charge / μC
10	20.49
15	20.66
20	20.50
35	20.69
50	20.74
75	20.40
100	20.63

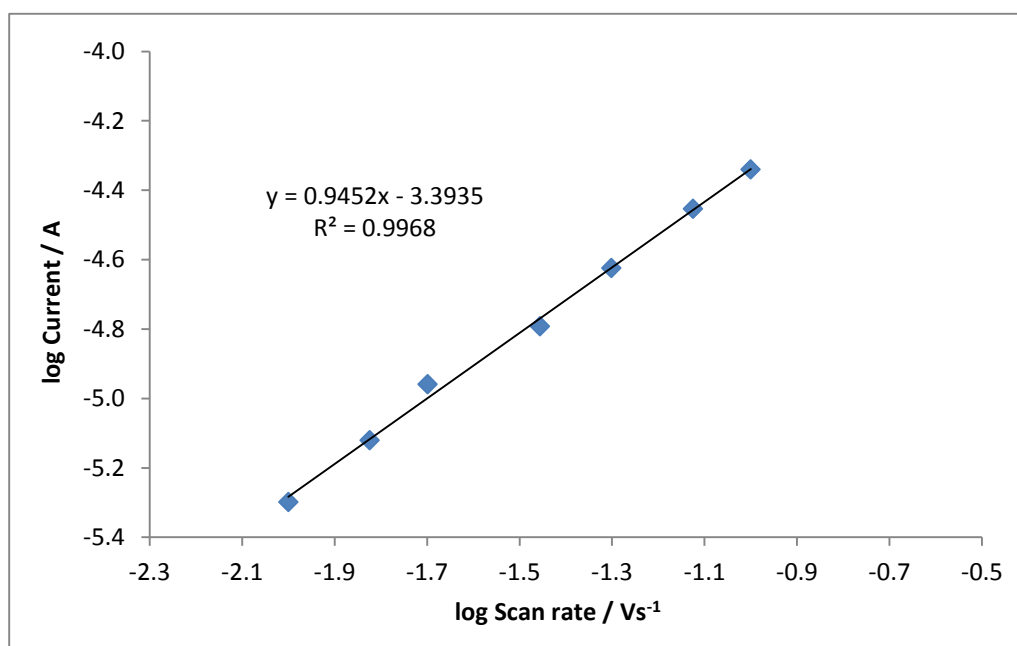


Figure 4.38: Plot of the logarithm of anodic stripping charge against the logarithm of scan rate at a bulk silver electrode in $10.0 \times 10^{-3} \text{ mol dm}^{-3} \text{ PbCl}_2$ and $0.1 \text{ mol dm}^{-3} \text{ HCl}$. Voltammograms cycled from -0.20 V to -0.49 V vs SCE.

4.3.3.2.5 Real Surface Area as Determined by Pb UPD of Bulk Silver Electrode

Once the optimum conditions for Pb UPD were established, namely by cycling a silver electrode, 0.2 cm in diameter, between -0.20 and -0.49 V vs SCE at a scan rate of 20 mV s⁻¹ in a solution of 10.0 × 10⁻³ mol dm⁻³ PbCl₂ and 0.1 mol dm⁻³ HCl, an average value for the anodic stripping charge was obtained by repeating the experiment to give an average value with n = 6. The average value for the charge, after background subtraction, was found to be 20.65 μC with a standard error of ± 2%. To transform this value into an expression of real surface area, Equation 4.5, as described in Section 4.3.3.1, was utilized. In this equation, Q_{upd} is the total charge under the UPD anodic stripping peak, Q_{dl} is the charge contributed by the background double layer capacitance current and q_m is the charge for a complete monolayer of Pb as taken from various literature sources. This estimated value of the anodic charge spent on the oxidation of a monolayer of Pb adatoms is typically 380 ± 40 μC cm⁻² (37-43). Applying Equation 4.5, the real surface area for a 2 mm bulk silver electrode becomes 0.0543 cm². Expressing this value as a fraction of the geometric surface area (0.0314 cm²), yields a value of 1.73 for the roughness factor. This highlights how inaccurate geometric surface area can be.

4.3.3.3 Pb Underpotential Deposition on a Silver-Modified Glassy Carbon Electrode

The same principle of Pb UPD at a bulk silver electrode, as mentioned above, was then applied to the silver particles on the GC electrode. This technique is often used in the literature to determine the surface coverage of metallic particles on GC and specifically silver on GC (3,8,9,31,42,56-58). While bulk deposition of Pb occurs at GC, the UPD of Pb does not occur, making this an attractive method to determine the surface area of silver particles on the GC substrates (3,8,31).

4.3.3.3.1 Comparison of Pb UPD at Bare Glassy Carbon Electrode and Silver-Modified Glassy Carbon Electrode

The electrochemical response of a 4 mm GC electrode to a 0.1 mol dm⁻³ HCl solution, with and without 10.0 x 10⁻³ mol dm⁻³ PbCl₂, is shown in Figure 4.39. While a reduction peak is apparent at -0.41 V vs SCE, no anodic stripping peak is observed. During the reverse cycle, the currents are similar in the presence and absence of the PbCl₂ indicating no evidence for the anodic stripping of Pb. However, the voltammogram is very different when silver particles are deposited on the GC electrode as depicted in Figure 4.40. In this figure voltammograms recorded for the GC and silver-modified GC electrode are presented. The reduction peak is shifted positively and is much larger for the silver-modified GC electrode, but more significantly, an anodic stripping current is now present. Again, the anodic peak is centred at -0.38 V vs SCE, which is similar to that obtained with the bulk silver electrode. The charge under this anodic peak can be used, in conjunction with Equation 4.5, to determine a value for the surface area.

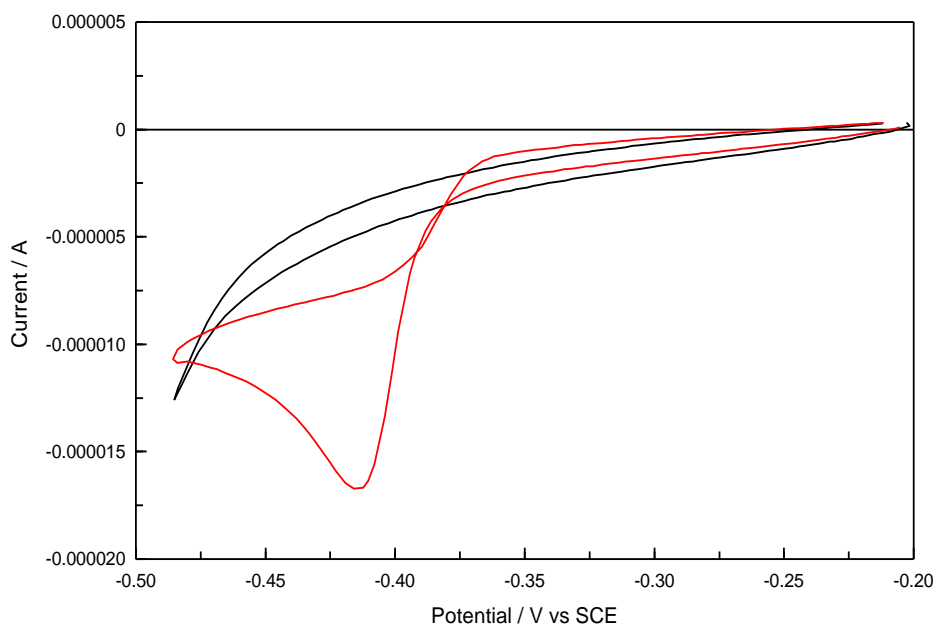


Figure 4.39: Cyclic voltammograms at a bare GC electrode in 0.1 mol dm⁻³ HCl — with and — without 10.0 x 10⁻³ mol dm⁻³ PbCl₂. Scan rate 20 mV s⁻¹.

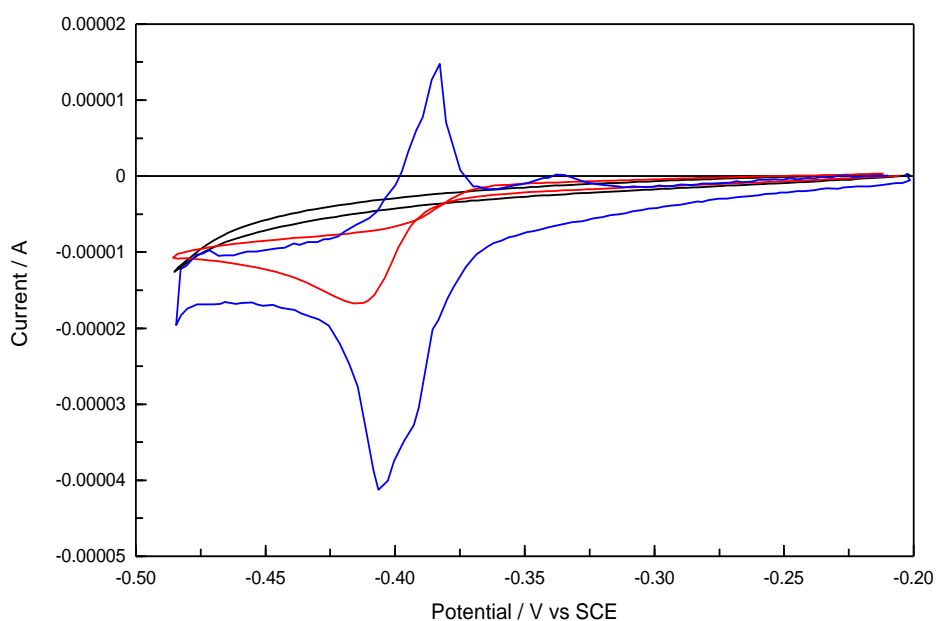


Figure 4.40: Cyclic voltammograms at a bare GC electrode in $0.1 \text{ mol dm}^{-3} \text{ HCl}$ — with and — without $10.0 \times 10^{-3} \text{ mol dm}^{-3} \text{ PbCl}_2$ and — GC electrode with silver particles deposited at -0.50 V for 50 s . Scan rate of 20 mV s^{-1} .

4.3.3.3.2 Comparison of Pb UPD at a Bulk Silver and a Silver-Modified Glassy Carbon Electrode

The profile of Pb UPD at both a bulk silver electrode and a silver-modified electrode are displayed in Figure 4.41. The reduction waves at both electrodes are very similar in profile although the magnitudes differ. However, the major differences can be seen in the oxidation wave. While the peak potentials are similar at -0.38 V vs SCE, the shape of the peaks are very different. The peak for the bulk silver electrode is much broader than the distinctly narrow Pb UPD anodic peak at the silver-modified electrode. This narrower Pb UPD anodic peak observed at the silver-modified GC electrode is indicative of surface sites on the silver of similar energy. The bulk electrode has many different sites where the Pb atom can bind with a different energy and so can be removed at different potentials.

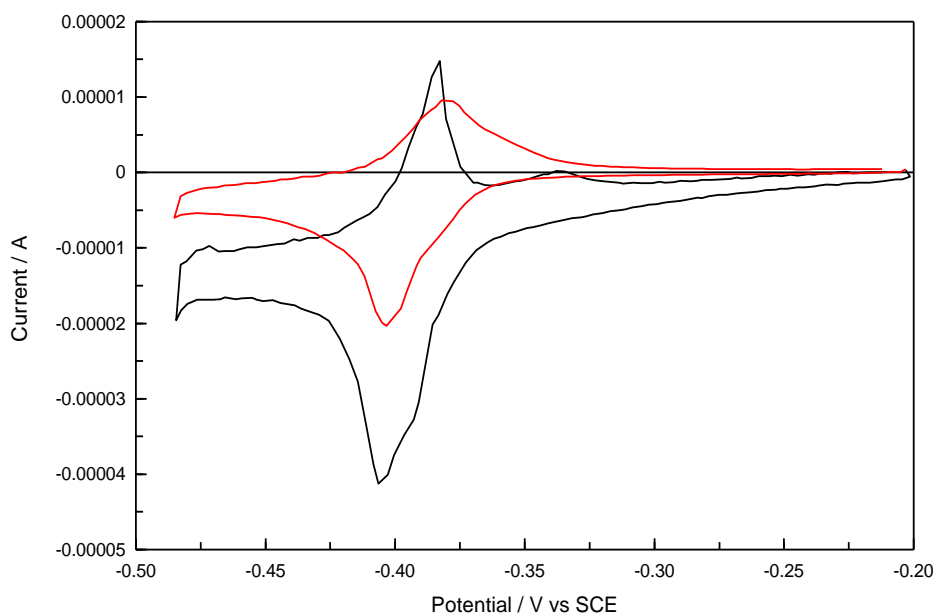


Figure 4.41: Cyclic voltammograms at — silver-modified GC electrode (particles deposited at -0.50 V vs Ag/Ag^+ for 50 s) and — a bulk silver electrode from -0.20 to -0.50 V in 10.0×10^{-3} mol dm^{-3} PbCl_2 and 0.1 mol dm^{-3} HCl at a scan rate 20 mV s^{-1} .

4.3.3.3 Surface Roughening

As in section 4.3.3.2.1, the effect of repeated cycling on the amount of charge under the Pb UPD anodic stripping peak was examined. As detailed earlier, the silver-modified GC electrode was cycled between -0.20 and -0.50 V vs SCE in 0.1 mol dm^{-3} HCl with 10.0×10^{-3} mol dm^{-3} PbCl_2 . Representative cycles are shown in Figure 4.42 and it is evident that the voltammograms are similar for cycles 1 to 10. The percentage change in the stripping charge was computed and this is shown plotted as a function of the cycle number in Figure 4.43. While the surface of a bulk silver electrode becomes slightly rougher with cycling, as suggested by the increasing charge with cycle number, Figure 4.33, the charge at the silver-modified GC electrode becomes slightly smaller and stabilises from cycle 7, at around 3.5% as shown in Figure 4.43. This indicates that small amounts of loosely bound particles are removed during the repetitive cycling. This decrease, however, is small and within experimental error and does not detract from the validity of this technique.

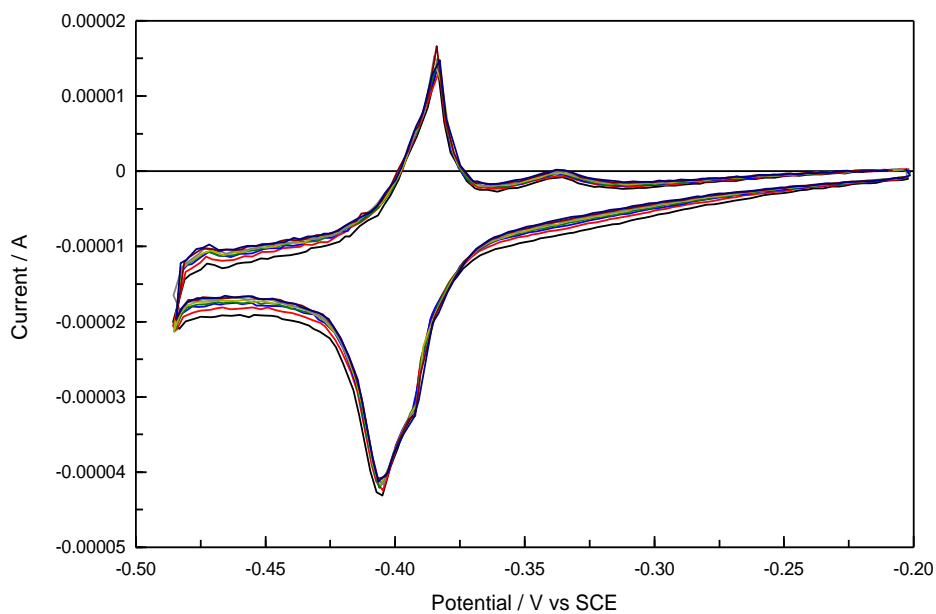


Figure 4.42: Cyclic voltammograms at silver-modified GC electrode (particles deposited at -0.50 V vs Ag/Ag⁺ for 50 s) from -0.20 V to -0.50 V in $10.0 \times 10^{-3} \text{ mol dm}^{-3} \text{ PbCl}_2$ and $0.1 \text{ mol dm}^{-3} \text{ HCl}$. Cycle 1 to 10 recorded at a scan rate of 20 mV s^{-1} .

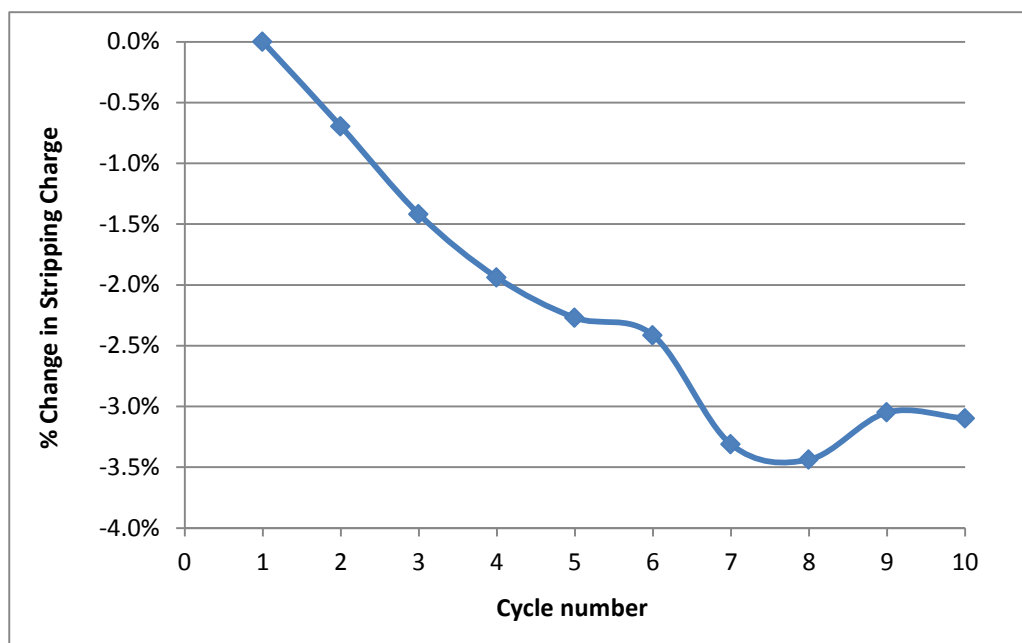


Figure 4.43: Anodic stripping charge % change from cycles 1 to 10, cycled at a scan rate of 20 mV s^{-1} in $10.0 \times 10^{-3} \text{ mol dm}^{-3} \text{ PbCl}_2$ and $0.1 \text{ mol dm}^{-3} \text{ HCl}$ for a silver-modified GC electrode (particles deposited at -0.50 V vs Ag/Ag⁺ for 50 s).

4.3.3.3.4 Effect of Potential Window on UPD of Pb on a Silver-Modified Glassy Carbon Electrode

The effect of the potential window on the measured charge under the anodic stripping peak at a silver particle modified GC electrode was determined in the same manner as the bulk silver electrode, Section 4.3.3.2.3. The oxidation potential limit was fixed at -0.20 V vs SCE and the reduction potential limit was varied from -0.47 V to -0.51 V vs SCE. The resulting voltammograms and charge plot are presented in Figures 4.44 and 4.45, respectively. As with the bulk silver electrode, there is very little difference between the magnitudes of the peak currents with different reduction potential limits. However, the charges decrease as the potential limit is lowered to -0.50 V vs SCE, Figure 4.45. This difference in charge is mainly due to the difficulty in accurately subtracting the background currents caused by the bulk Pb stripping current as the potential limit becomes more negative. There is a more significant decrease in the total charge of the UPD stripping peak compared to the bulk electrode when scanned into the bulk deposition region as illustrated in Figure 4.45. This may be due to the destructive nature of stripping layers of Pb from the silver particles which may remove some of the silver, as mentioned in Section 4.3.3.2.1.

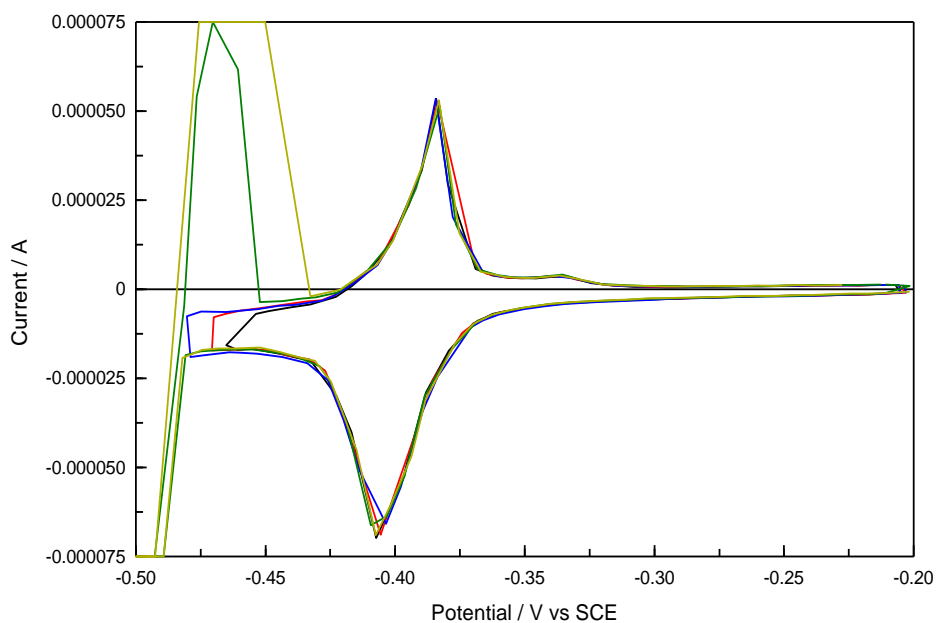


Figure 4.44: Cyclic voltammograms at a silver-modified GC electrode (silver deposited at -0.50 V vs Ag/Ag^+ for 50 s) in $10.0 \times 10^{-3} \text{ mol dm}^{-3} \text{ PbCl}_2$ and $0.1 \text{ mol dm}^{-3} \text{ HCl}$. Negative potential limit varied from -0.47 , -0.48 , -0.49 , -0.50 and -0.51 V vs SCE. Positive potential limit was constant at -0.20 V vs SCE in all cases. Scan rate of 50 mV s^{-1} .

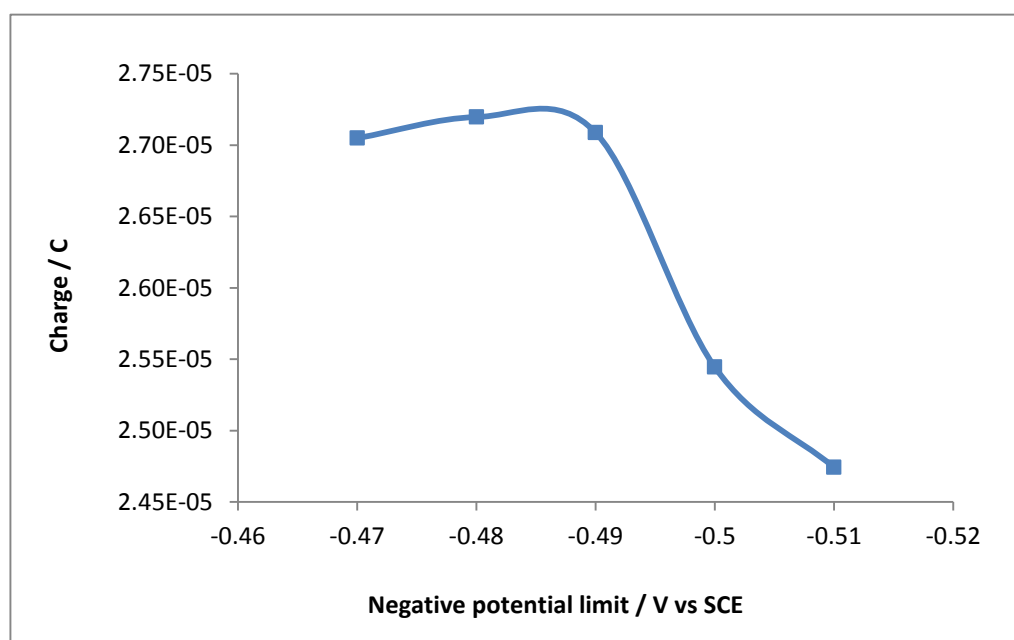


Figure 4.45: Effect of negative potential limit on the integrated charge of the UPD anodic stripping charge corresponding to the CVs in Figure 4.44.

4.3.3.3.5 Effect of Scan Rate on the UPD of Pb on Silver-Modified Glassy Carbon Electrode

As with the bulk silver electrode in Section 4.3.3.2.4, the effect of scan rate was investigated at the silver-modified GC electrode. The scan rate was varied from 10 to 100 mV s^{-1} and the resulting voltammograms are shown in Figure 4.46. The charge associated with the anodic stripping of a monolayer of Pb on the GC electrode modified with silver particles that were deposited at $-0.50 \text{ V vs Ag/Ag}^+$ for 50 s at various scan rates are outlined in Table 4.2. The charge remains relatively constant and independent of the scan rate, at $26 \mu\text{C}$. Again, the consistency of the charge indicates that a full monolayer was successfully deposited. Also, the peak potential does not change with the scan rate and remains constant at -0.38 V vs SCE . A plot of the logarithm of the peak current as a function of the logarithm of the scan rate is shown in Figure 4.47. A linear plot was obtained with a R^2 value of 0.97, indicating good linearity. The slope of the plot was calculated as 1.04, which is close to 1.0, indicating an adsorption-controlled process.

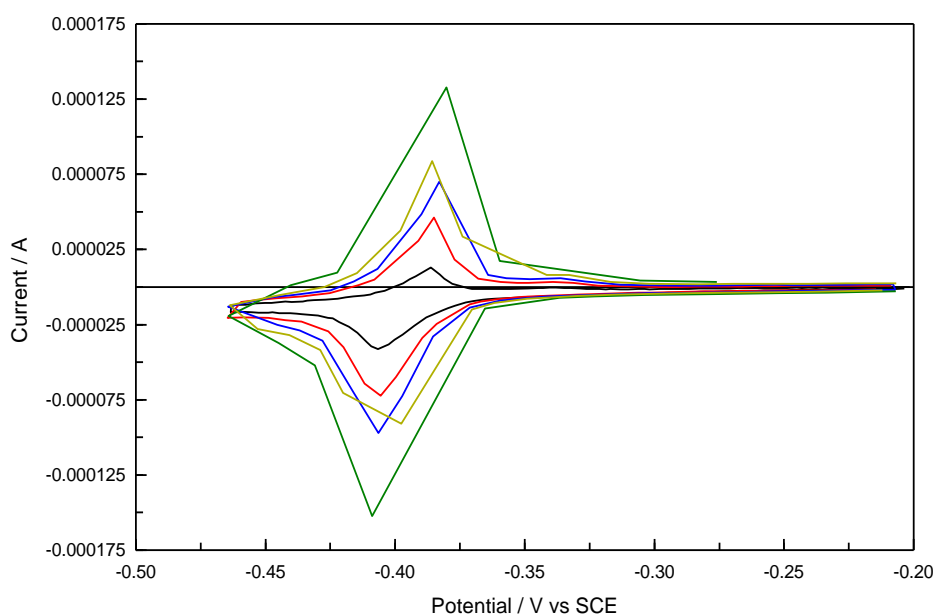


Figure 4.46: Cyclic voltammograms at a silver-modified GC electrode (silver deposited at $-0.50 \text{ V vs Ag/Ag}^+$ for 50 s) in $10.0 \times 10^{-3} \text{ mol dm}^{-3} \text{ PbCl}_2$ and $0.1 \text{ mol dm}^{-3} \text{ HCl}$. Scan rate set at 10, 15, 20, 35, 50, 75 and 100 mV s^{-1} .

Table 4.2: Anodic stripping charge associated with a monolayer of Pb on silver-modified GC electrode (silver deposited at -0.50 V vs Ag/Ag⁺ for 50 s) at various scan rates.

Scan Rate / mV s ⁻¹	UPD Stripping Charge / μC
20	26.79
50	26.87
75	26.73
100	26.42
150	26.31

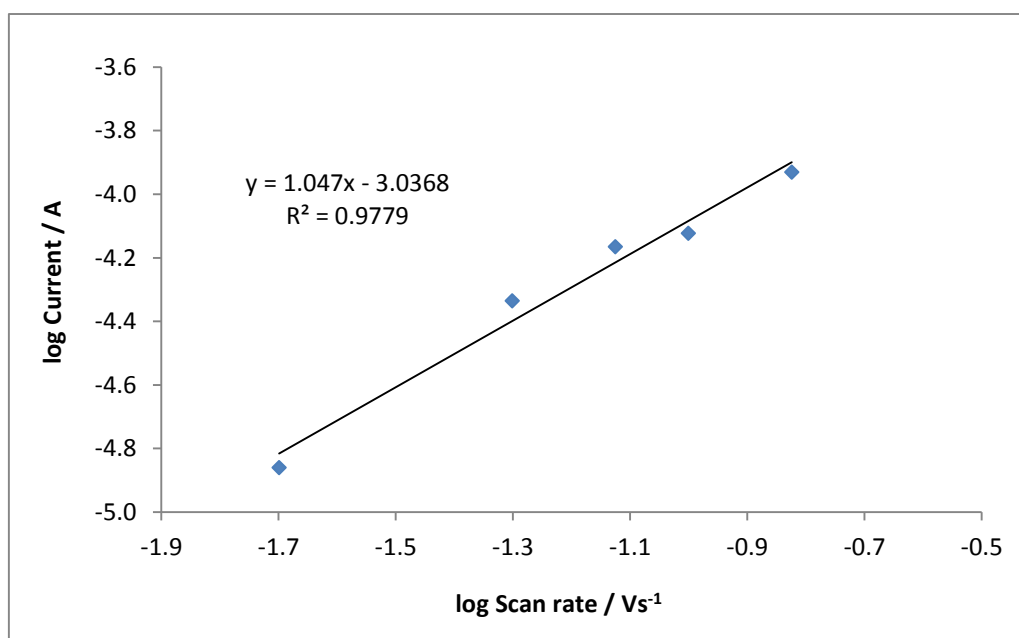


Figure 4.47: Plot of the logarithm of anodic stripping charge as a function of the logarithm of scan rate at a silver-modified GC electrode (silver deposited at -0.50 V vs Ag/Ag⁺ for 50 s) in $10.0 \times 10^{-3} \text{ mol dm}^{-3} \text{ PbCl}_2$ and $0.1 \text{ mol dm}^{-3} \text{ HCl}$. Voltammograms cycled from -0.20 V to -0.47 V vs SCE.

4.3.3.3.6 Real Surface Area as Determined by Pb UPD at a Silver-Modified Glassy Carbon Electrode

The optimum conditions for Pb underpotential deposition were as follows: a solution of $10.0 \times 10^{-3} \text{ mol dm}^{-3}$ PbCl_2 and 0.1 mol dm^{-3} HCl and cycling the electrode between -0.20 V and -0.49 V vs SCE at a scan rate of 20 mV s^{-1} . These conditions were used to obtain the surface area of the silver particles on the GC electrode. The charges for the various silver particles formed at different deposition times in the silver-containing solution were measured and used with Equation 4.5 to generate quantitative surface area values. Again, an average value for the anodic stripping charge was obtained by repeating the experiments to give an n value of 6. The silver-modified GC electrodes were prepared by depositing silver at -0.50 V vs Ag/Ag^+ for 25, 50, 75 and 100 s and then cycled in the Pb^{+2} -containing solution. The resulting voltammograms are presented in Figure 4.48. It can be seen at the lowest deposition time of 25 s, that the Pb deposition at the bare GC dominates the reduction wave. The anodic peak is small, with a charge that is considerably lower than the reduction peak. The peak current and the charge of the anodic Pb UPD peak increases as the particles are deposited for longer times from the silver-containing solution. The highest peak currents are obtained with a deposition period of 100 s from the silver-containing solution. The results are tabulated in Table 4.3 and the trend is illustrated more clearly in Figure 4.49, where the calculated surface area is plotted as a function of the deposition time in the silver-containing solution. There is a near linear increase in the surface area as the deposition period is increased. The highest surface area of 0.10 cm^2 was obtained when the silver was deposited at -0.50 V vs Ag/Ag^+ for 100 s. Indeed, the surface area of this silver-modified GC electrode is higher than the bulk silver electrode, Table 4.3. The surface areas following 75 and 50 s were calculated as 0.0873 and 0.0692 cm^2 , respectively, which are somewhat higher than the surface area of the bulk silver electrode.

As shown in Figures 4.19 and 4.20, a more homogenous deposition of silver is obtained at -0.50 V vs Ag/Ag^+ for 50 s. Furthermore, this silver-modified GC electrode gives rise to the best detection of nitrate, Figure 4.22. Although the surface area is higher for the 75 and 100 s deposition times, the lower surface area of 0.0692 cm^2 with a more homogenous deposition of the silver gives the best detection of nitrate.

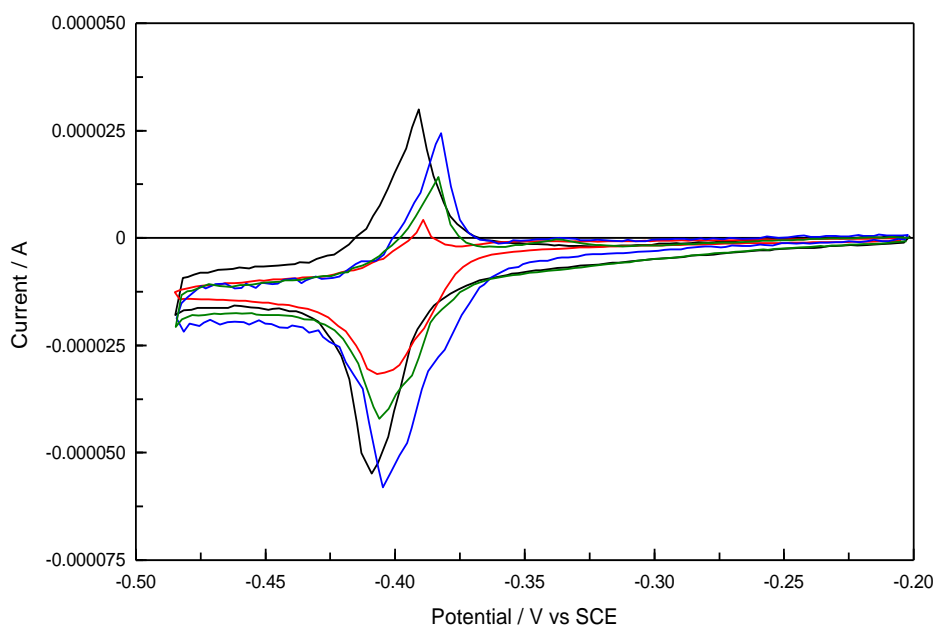


Figure 4.48: Cyclic voltammograms of a silver-modified GC electrode (silver deposited at -0.50 V vs Ag/Ag^+). Silver deposited for different times, — 25 s, — 50 s, — 75 s and — 100s, in 10.0×10^{-3} mol dm^{-3} PbCl_2 and 0.1 mol dm^{-3} HCl . Scan rate of 20 mV s^{-1} .

Table 4.3: Anodic stripping charge associated with a monolayer of Pb on a silver-modified GC electrode (silver deposited at -0.50 V vs Ag/Ag^+). Silver deposited for various times.

Deposition time / s	UPD Stripping Charge / μC	Surface Area / cm^2
25	12.95	0.0341
50	26.28	0.0692
75	33.18	0.0873
100	39.66	0.1044
Bulk	20.65	0.0543

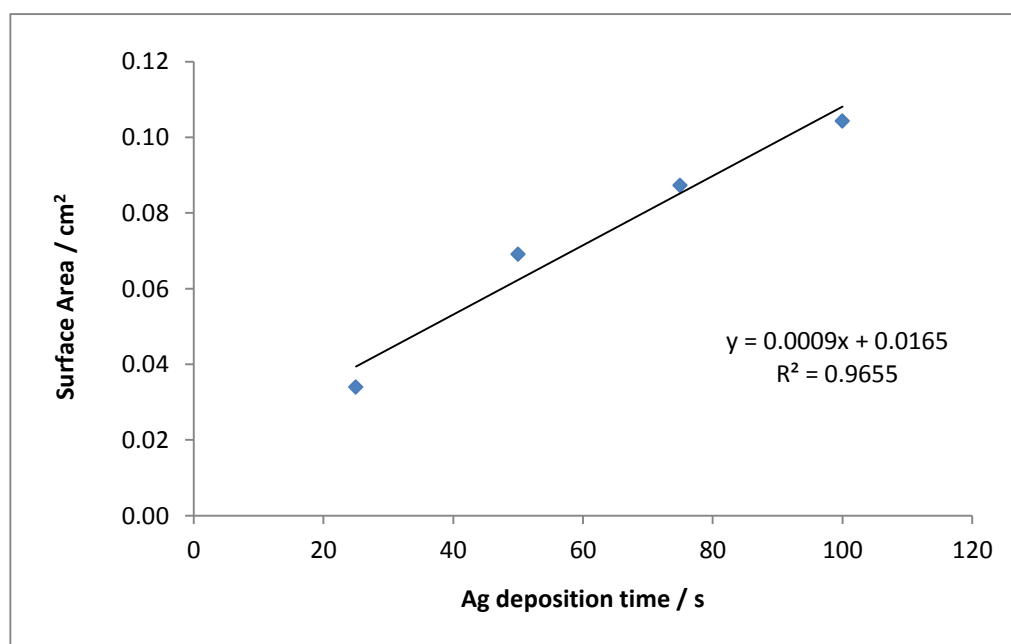


Figure 4.49: Plot of surface area of a silver-modified GC electrode (silver deposited at -0.50 V vs Ag/Ag^+) as a function of silver deposition time.

4.3.3.4 Surface Area by Reduction of Surface Oxides using Cyclic Voltammetry

As was briefly introduced in Section 4.3.3.1, another technique to determine the real surface area of a metal is to measure the charge associated with the reduction of the surface oxides which are generated in the forward scan of the metal. The sweep begins at the same potential but the anodic inversion potential is incrementally increased. Multiple linear regions are obtained when the inversion potential and reduction charge are plotted. The first linear region is attributed to the reduction of the metal hydroxide monolayer. The inversion potential at which this region loses linearity and the charge increases exponentially corresponds to metal dissolution. The charge associated with this inversion potential can be related to the electroactive surface area ^(29,30). This technique is commonly applied to gold and gold particles but can also be applied to silver ^(3,59). This technique was used here as a comparison and to corroborate the surface area values determined by the Pb UPD technique as listed in Table 4.3.

The CV's for a bulk silver electrode cycled in $0.1 \text{ mol dm}^{-3} \text{ LiClO}_4$ to different anodic inversion potentials is shown in Figure 4.50. The reduction peak at approximately 0.35 V vs SCE corresponds to the reduction of the silver oxides and this peak becomes larger as the inversion potential is increased. The charge was obtained by integration of the charge of the cathodic branch by considering a straight line from -0.10 to 0.10 V as the baseline for the reduction of the silver oxides at the bulk silver electrode. These charges were plotted as a function of inversion potential and these data are presented in Figure 4.51. The two linear regions can be seen clearly and the inversion potential at which the first region loses its linearity is approximately 375 mV . The reduction charge associated with this inversion potential is $1.14 \times 10^{-5} \text{ C}$. According to Tang and Furtak⁽⁶⁰⁾, a complete monolayer of either AgOH or Ag_2O consumes approximately 2.10 C m^{-2} . Therefore, the real surface area of this 2 mm silver electrode is 0.0542 cm^2 , which agrees extremely well with the surface area calculated by the UPD of Pb for the same electrode (0.0543 cm^2 , Table 4.3).

Figure 4.52 shows the CV's for the reduction of silver oxides formed at different anodic inversion potentials for silver particles deposited on a GC electrode at $-0.50 \text{ V vs Ag/Ag}^+$ for 50 s . Again, the silver oxide reduction peak is evident, but at a slightly lower potential of 0.28 V vs SCE . As the window is extended, the oxide peak initially increases until a maximum peak current is obtained. However, beyond this point the current decreases as the silver begins to dissolve and diffuse away from the surface and into the bulk solution. Again, two linear regions are evident, as shown in Figure 4.53. The point of inflection, which represents the formation of a complete monolayer, occurs at approximately 340 mV and with a reduction charge of $1.53 \times 10^{-5} \text{ C}$, yielding a calculated real surface area of 0.0729 cm^2 . This value is quite close to the calculated surface area as determined by Pb UPD (0.0692 cm^2 , Table 4.3).

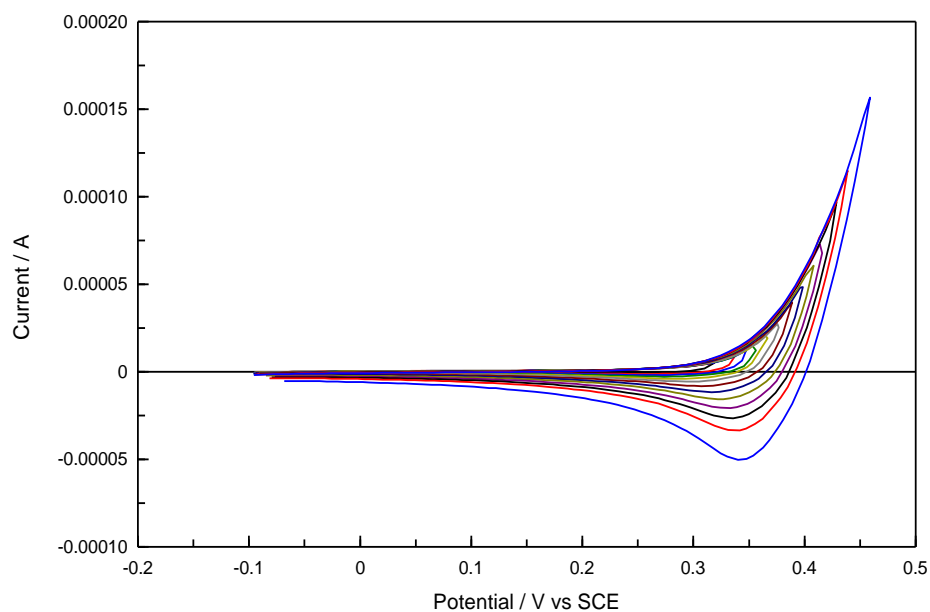


Figure 4.50: Cyclic voltammograms for a polished bulk silver electrode cycled in a solution of 0.1 mol dm^{-3} LiClO_4 at a scan rate of 50 mV s^{-1} to different anodic inversion potentials.

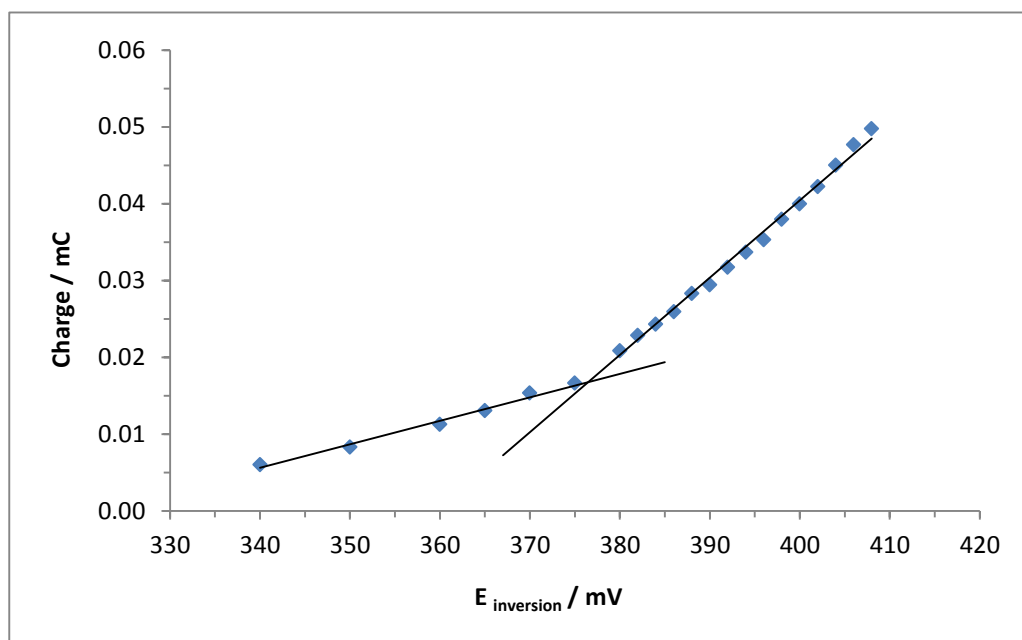


Figure 4.51: Reduction charge of the silver oxides formed in the anodic scan as a function of inversion potential from the CV in Figure 4.50.

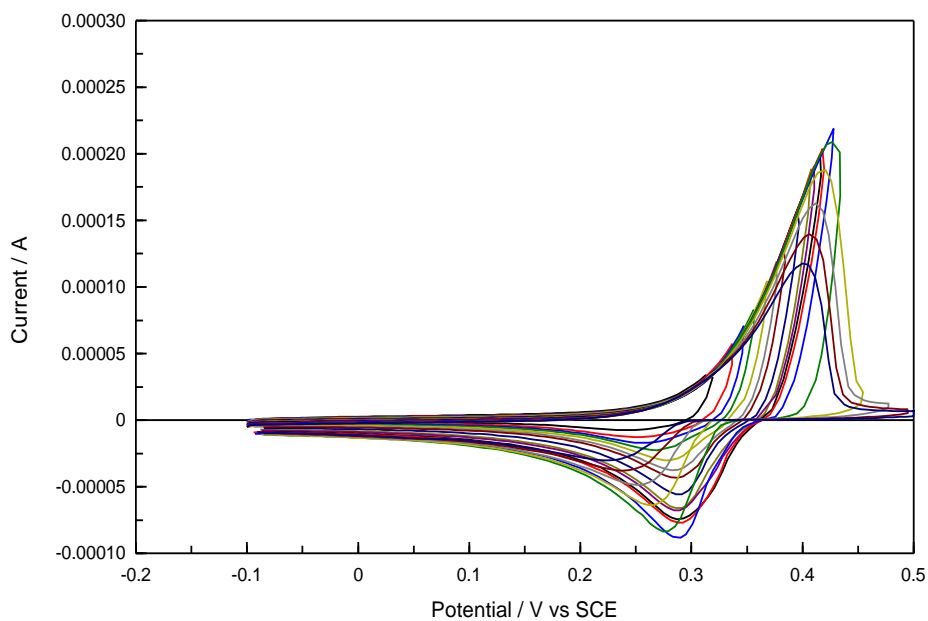


Figure 4.52: Cyclic voltammograms for a silver-modified GC electrode (silver deposited at -0.50 V vs Ag/Ag^+ for 50 s), cycled in a solution of 0.1 mol dm^{-3} LiClO_4 at a scan rate of 50 mV s^{-1} to different anodic inversion potentials.

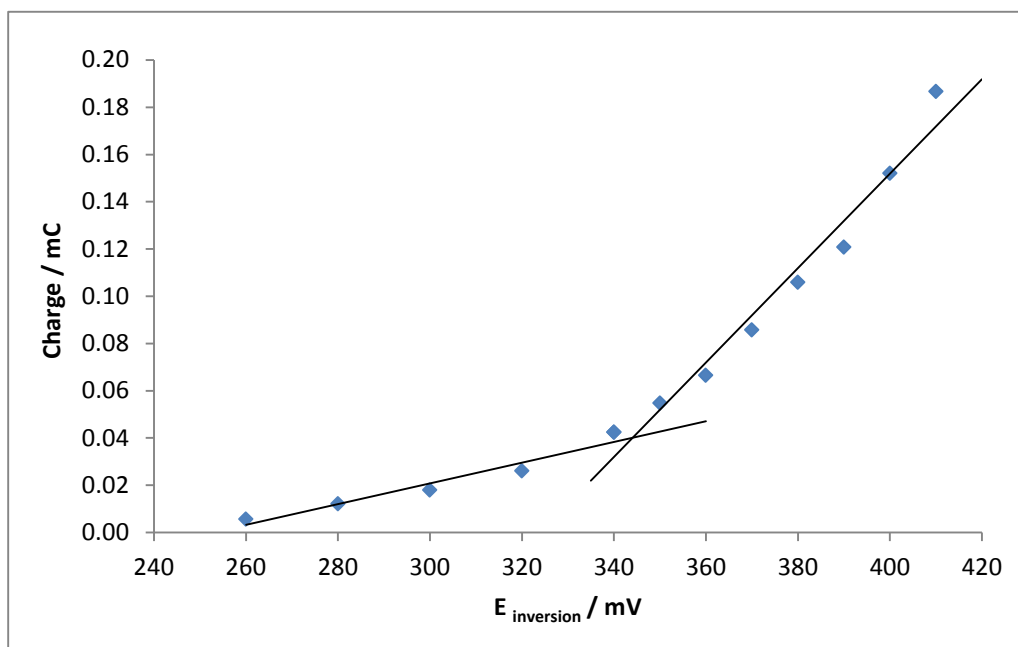


Figure 4.53: Reduction charge of the silver oxides formed in the anodic scan as a function of inversion potential from the CV in Figure 4.52.

4.3.3.5 Size of the Electrodeposited Nanoparticles as Determined by SEM and ImageJ

The sizes of the electrodeposited nanoparticles were measured using the image analysis tool, ImageJ, as described in Chapter 2, Section 2.3.7. The histograms generated using ImageJ give information on the size distribution of the silver deposits but also generate data on the percentage area covered with silver. In order to check the accuracy of the ImageJ data and indeed how it compares to the other methods outlined above to determine the surface area, the average percentage area, as given by ImageJ, for six random sites on a silver-modified GC electrode were analysed. The particles were deposited by applying $-0.50\text{ V vs Ag/Ag}^+$ for 50 s. Data are presented in Table 4.4, where the count, total area of the image, total area occupied by the particles, average area of a particle and percentage area occupied, are shown for the six random sites selected. The average percentage area was calculated as $18.49 \pm 1.61\%$. The SEM images and hence ImageJ view only the topography of the particles, and therefore the particles are viewed as 2D circles rather than being hemispherical in shape. It is reasonable to assume that the surface area is given as $2\pi r^2$ rather than πr^2 , giving a percentage area coverage of $36.98 \pm 3.22\%$. The GC electrode used for these experiments was 5 mm in diameter and therefore has a geometric surface area of 0.1963 cm^2 . Therefore, an average percentage area of $18.49 \pm 1.61\%$ yields the silver particle coverage of $0.0725 \pm 0.006\text{ cm}^2$. This compares very well with the surface area measurements generated by Pb UPD, which was 0.0692 cm^2 , and the reduction of surface oxide which gave an area of 0.0729 cm^2 .

Based on all the data collected to ascertain the surface area, values of 0.0543 cm^2 and 0.0692 cm^2 for the bulk silver electrode and the silver-modified GC electrode, respectively, were used to normalise the currents recorded in all background electrolytes and in the nitrate-containing solutions.

Table 4.4: Area and count data as determined from Image J analysis of six random sites on a silver-modified GC electrode (silver deposited at -0.50 V vs Ag/Ag⁺ for 50 s).

Slice	Count	Total area of image / nm ²	Total area occupied by particles / nm ²	Average area per particle / nm ²	% of surface occupied by particles
deposit_60_SOI1x10000	8282	1.157 x10 ⁸	2.119 x 10 ⁷	2558	18.31
deposit_60_SOI2x10000	8660	1.157 x10 ⁸	1.985 x 10 ⁷	2291	17.15
deposit_60_SOI3x10000	8213	1.157 x10 ⁸	1.892 x 10 ⁷	2303	16.35
deposit_60_SOI2x25000	1908	1.844 x 10 ⁷	3.319 x 10 ⁶	1739	18.05
deposit_60_SOI3x25000	1626	1.844 x 10 ⁷	3.872 x 10 ⁶	2381	20.99
deposit_60_SOI4x25000	1828	1.844 x 10 ⁷	3.712 x 10 ⁶	2030	20.14
				Average	18.49 ± 1.61

4.3.4 Nitrate Calibration Curves

In order to obtain detailed information on the sensitivity of the sensor, cyclic voltammetry and constant potential amperometry experiments were carried out using the optimum conditions for the formation of the silver particles on a GC electrode. As outlined earlier, this involved the deposition of silver at -0.50 V vs Ag/Ag⁺ for 50 s. Also, calibration curves were performed at a bulk silver electrode as a comparison to investigate any differences in the sensitivity of the bulk silver electrode and the silver-modified GC electrode and to determine if the silver-modified electrode exhibited any catalytic ability.

4.3.4.1 Nitrate Detection at a Silver-Modified Glassy Carbon Electrode by Cyclic Voltammetry

The sensitivity of the silver-modified GC electrode was investigated using cyclic voltammetry. Figure 4.54 shows how the nitrate reduction peak becomes less defined as the concentration of nitrate is lowered. The calibration curve obtained on plotting the current at -1.10 V vs SCE as a function of the nitrate concentration is shown in Figure 4.55. A linear curve is obtained over the entire concentration range, giving a regression equation $I_{pc} = -0.53121C_{NO_3^-}$ and a correlation coefficient of 0.997. The lowest concentration of KNO_3 that could be detected at the silver-modified GC electrode using this technique was 2.0×10^{-5} mol dm^{-3} .

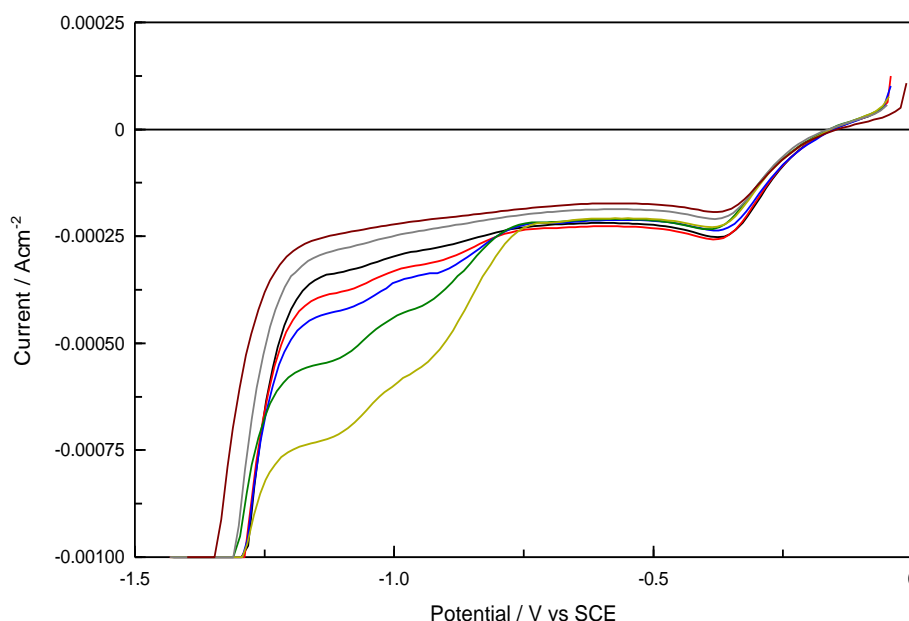


Figure 4.54: Cyclic voltammograms at a scan rate of 50 mV s^{-1} in a solution of $0.1 \text{ mol dm}^{-3} \text{ LiClO}_4$ with — no KNO_3 , — 2.0×10^{-5} , — 4.0×10^{-5} , — 8.0×10^{-5} , — 1.6×10^{-4} , — 3.2×10^{-4} and — $6.4 \times 10^{-4} \text{ mol dm}^{-3} KNO_3$ at a silver-modified GC electrode (silver deposited at $-0.50 \text{ V vs Ag/Ag}^+$ for 50 s).

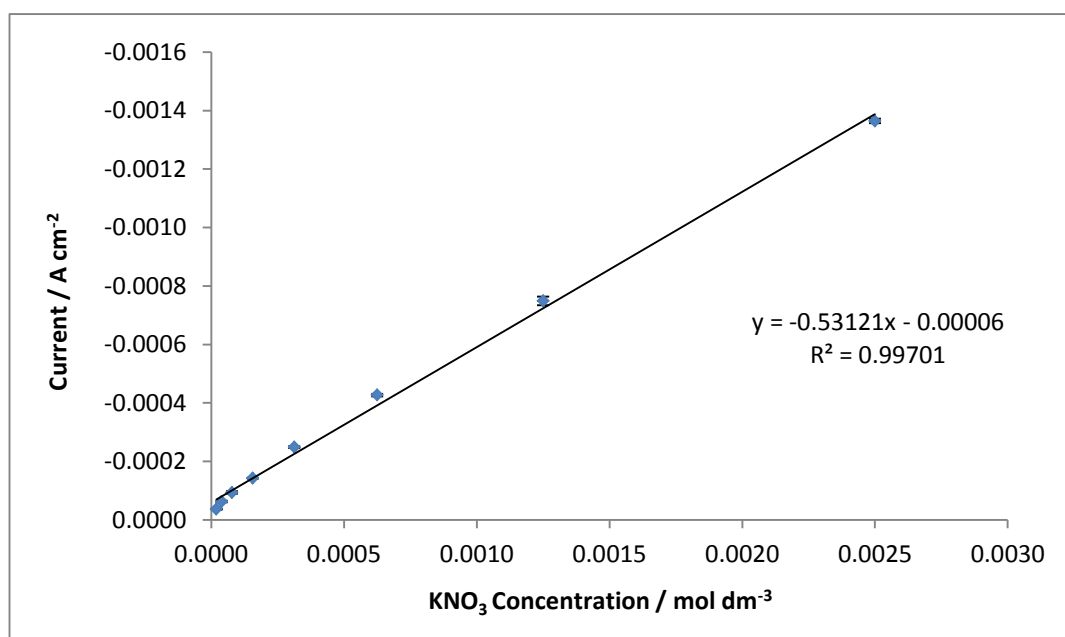


Figure 4.55: The peak reduction currents for nitrate reduction at the silver-modified GC electrode (silver deposited at -0.50 V vs Ag/Ag⁺ for 50 s) as a function of KNO₃ concentration. A background electrolyte of 0.1 mol dm⁻³ LiClO₄ was used for all solutions and CVs were recorded at 50 mV s⁻¹.

The peak potential becomes less defined as the concentration of nitrate is lowered so a calibration curve was also generated by plotting the total reduction charge minus the background charge, as determined from integrating between the potential limits where nitrate reduction occurs, as a function of the concentration of KNO₃. The potential limits for the reduction of each of the nitrate concentrations are shown in Table 4.5 and the resulting calibration curve is shown in Figure 4.56. The regression equation $C = -4.2412C_{\text{NO}_3^-}$ was obtained with a correlation coefficient of 0.999, indicating excellent linearity. The groundwater limits under the Nitrate Directive (91/676/EEC) are set at 50 mg/l NO₃⁻, which is equivalent to 8.0×10^{-4} mol dm⁻³ NO₃⁻. While the silver-modified GC electrode can sense within the limits set by this directive by employing CV, a much more sensitive technique, constant potential amperometry, was employed in the Section 4.3.4.3 to determine if lower detection limits could be reached.

Table 4.5: Oxidative and reductive potential limits of the nitrate reduction wave for each concentration of KNO_3 at the silver-modified GC electrode. A background electrolyte of $0.1 \text{ mol dm}^{-3} \text{ LiClO}_4$ was used for all solutions and CVs were recorded at 50 mV s^{-1} .

Conc. of KNO_3 / mol dm^{-3}	Reductive potential limit / V vs SCE	Oxidative potential limit / V vs SCE
2.50×10^{-3}	-1.31	-0.63
1.25×10^{-3}	-1.27	-0.67
6.25×10^{-4}	-1.23	-0.73
3.13×10^{-4}	-1.21	-0.74
1.56×10^{-4}	-1.19	-0.74
7.81×10^{-5}	-1.18	-0.74
3.91×10^{-5}	-1.17	-0.73
1.95×10^{-5}	-1.16	-0.73

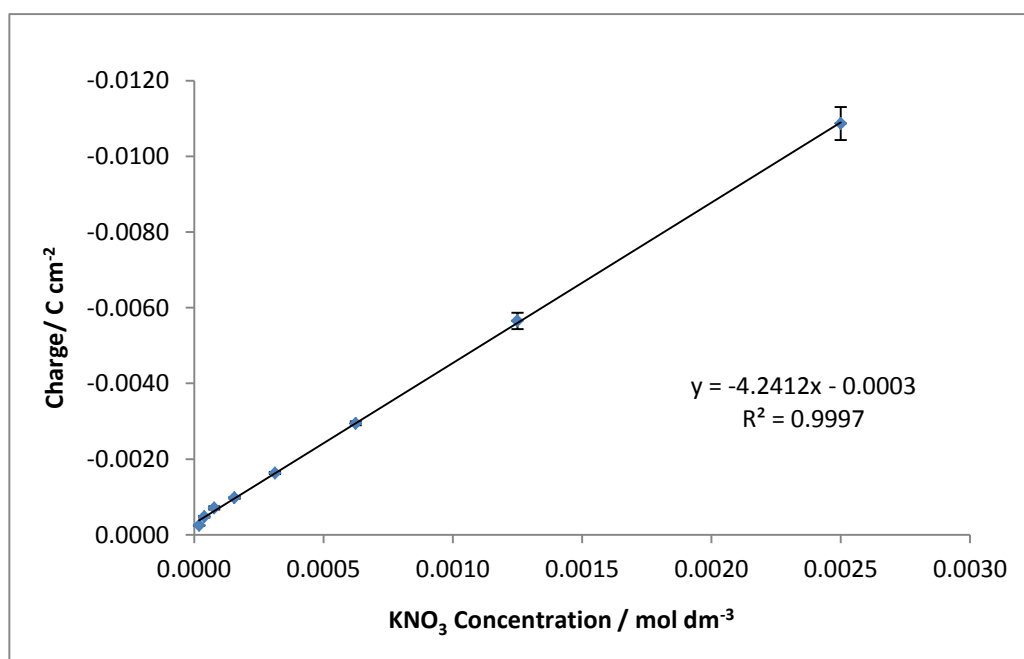


Figure 4.56: Plot of reduction charge against KNO_3 concentration at the silver-modified GC electrode (silver deposited at $-0.50 \text{ V vs Ag/Ag}^+$ for 50 s). A background electrolyte of $0.1 \text{ mol dm}^{-3} \text{ LiClO}_4$ was used for all solutions and CVs were recorded at 50 mV s^{-1} .

4.3.4.2 Nitrate Detection at a Bulk Silver Electrode by Cyclic Voltammetry

To draw a comparison between the sensitivity of silver-modified GC electrode and a bulk crystalline electrode to the nitrate reduction reaction, nitrate calibration curves at a 2 mm silver disc electrode were also generated. Firstly, Figure 4.57 shows a comparison of the bulk silver electrode to the silver-modified GC electrode, normalised to the surface areas, in the same concentration of nitrate ($5.0 \times 10^{-3} \text{ mol dm}^{-3} \text{ KNO}_3$). The profile of the peak and the potential of the peak current are the same at approximately -0.91 V vs SCE for both electrodes, but the magnitude of the normalised peak current is 5.2 times larger for the silver-modified GC electrode. This shows that the silver-modified GC electrode is significantly more sensitive to the nitrate reduction than bulk silver.

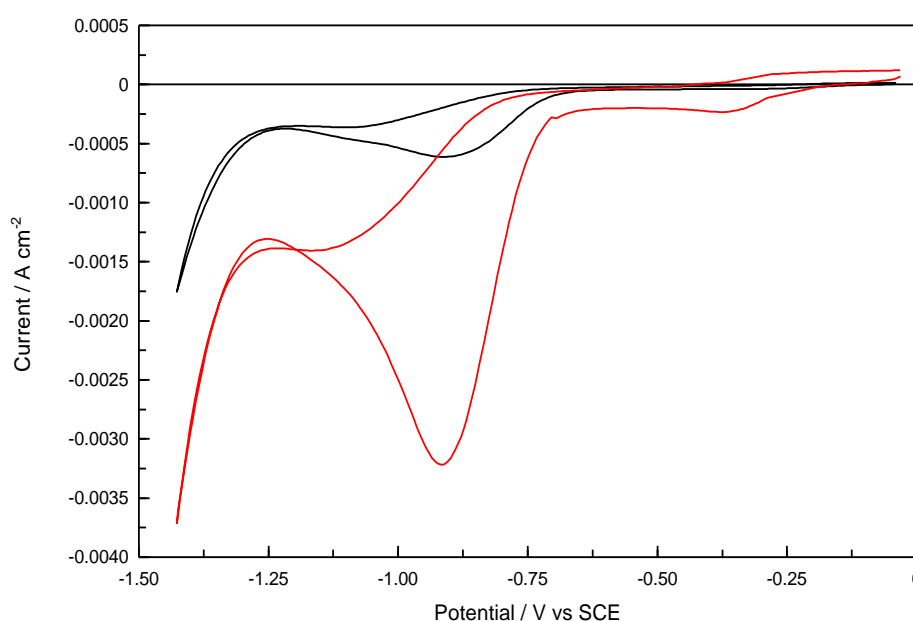


Figure 4.57: Cyclic voltammograms at a scan rate 50 mV s^{-1} in a solution of $5.0 \times 10^{-3} \text{ mol dm}^{-3} \text{ KNO}_3$ and $0.1 \text{ mol dm}^{-3} \text{ LiClO}_4$ at — a silver-modified GC electrode (silver deposited at -0.50 V vs Ag/Ag^+ for 50 s) and — at a bulk silver electrode.

The performance of the bulk silver electrode was also examined over a range of concentrations. The calibration curve of current at -1.10 V vs SCE plotted as a function of the nitrate concentration is shown in Figure 4.58. The linear regression equation was obtained as, $I_{pc} = -0.1094C_{NO_3^-}$ with a correlation coefficient of 0.9923, and a limit of detection of 3.9×10^{-5} mol dm $^{-3}$ was obtained. A limit of detection of 2.0×10^{-5} mol dm $^{-3}$ and a 5 times larger slope value of -0.5312 A mol $^{-1}$ dm 3 shows that the silver-modified GC electrode is more sensitive to the presence of nitrate than bulk crystalline silver. The integrated reduction charge of the CV was also plotted as a function of the nitrate concentration at the bulk silver electrode. The potential limits listed in Table 4.6 become broader as the concentration of nitrate is increased. When the total charge, minus the background charge, beneath the CV was used to generate the calibration curve, Figure 4.59, the linear regression equation $C = -0.7855C_{NO_3^-}$ with a correlation coefficient of 0.9982, was obtained.

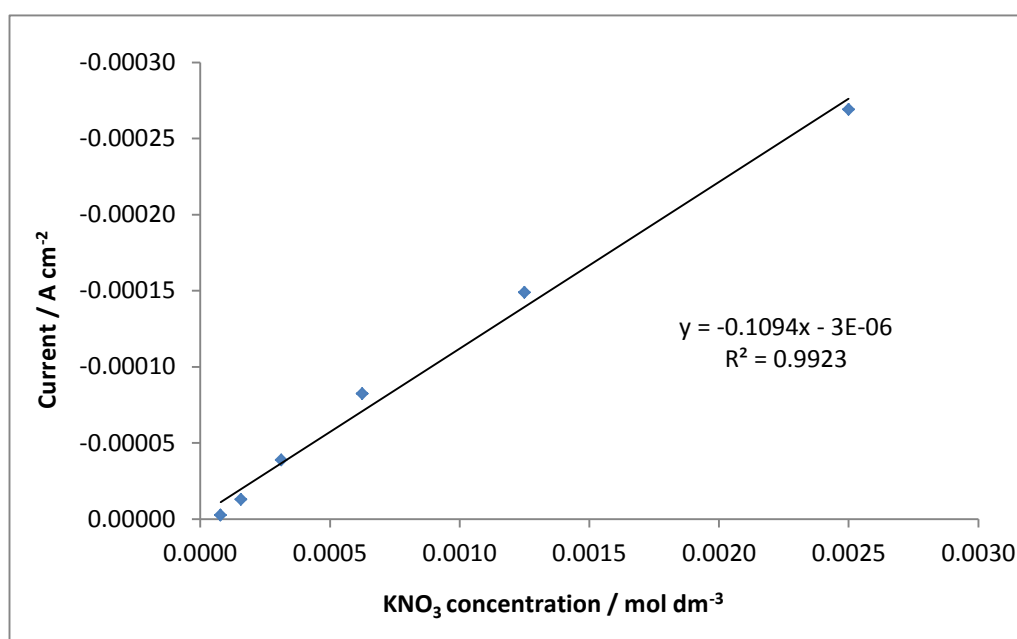


Figure 4.58: The peak reduction currents for nitrate reduction at a bulk silver electrode as a function of KNO₃ concentration. A background electrolyte of 0.1 mol dm $^{-3}$ LiClO₄ was used for all solutions and the scan rate was 50 mV s $^{-1}$.

Table 4.6: Oxidative and reductive potential limits of the nitrate reduction wave for each concentration of KNO_3 at the bulk silver electrode. A background electrolyte of 0.1 mol dm^{-3} LiClO_4 was used for all solutions and CVs were carried out at a 50 mV s^{-1} scan rate.

Conc. of KNO_3 / mol dm^{-3}	Reductive potential limit / V vs. SCE	Oxidative potential limit / V vs. SCE
2.50×10^{-3}	-1.19	-0.69
1.25×10^{-3}	-1.17	-0.71
6.25×10^{-4}	-1.16	-0.74
3.13×10^{-4}	-1.15	-0.74
1.56×10^{-4}	-1.14	-0.76
7.81×10^{-5}	-1.07	-0.77
3.91×10^{-5}	-1.00	-0.78

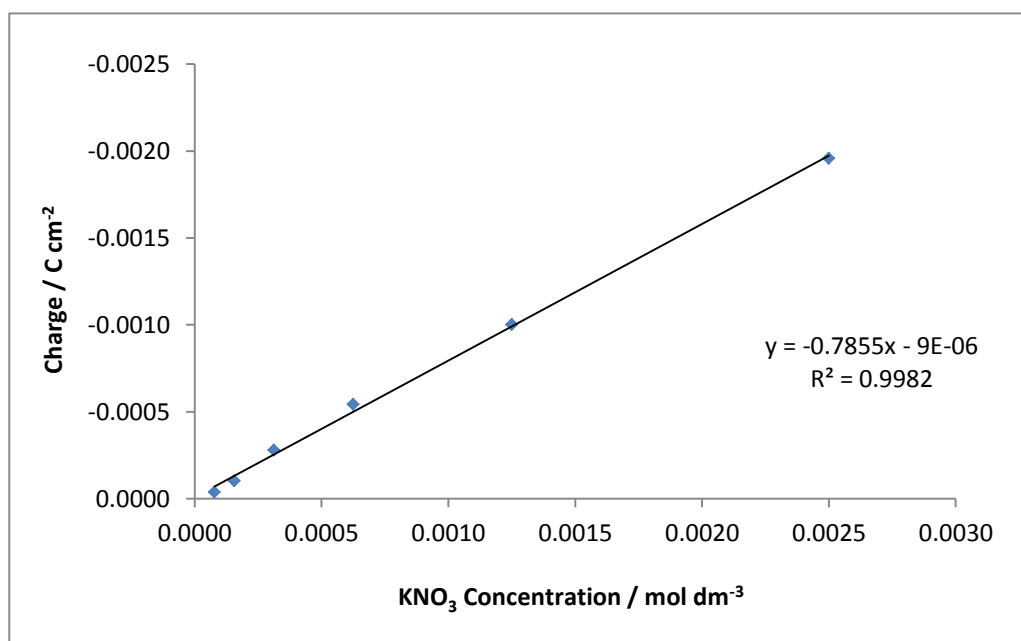


Figure 4.59: Plot of reduction charge against KNO_3 concentration at a bulk silver electrode. A background electrolyte of 0.1 mol dm^{-3} LiClO_4 was used for all solutions and CVs were carried out at a 50 mV s^{-1} scan rate.

4.3.4.3 Nitrate Detection at a Silver-Modified Glassy Carbon Electrode by Constant Potential Amperometry

A typical plot of the current response at a silver-modified GC electrode under a constant rotation of 2000 rpm and at an applied potential of -1.20 V vs SCE to aliquot additions of nitrate to a background electrolyte solution of 0.1 mol dm⁻³ LiClO₄ is shown in Figure 4.60. The response time was reasonably quick, within 3 s. The relationship between the measured current and the concentration of nitrate is shown in Figure 4.61. Over a wide concentration range the plot appears to be slightly curved but with a clear linear region at lower concentrations with a correlation coefficient of 0.9903. Using the linear calibration curve at the lower concentrations, the limit of detection was found to be 9.8 x 10⁻⁶ mol dm⁻³ KNO₃. This was obtained using the expression in Equation 4.8, where C_m is the detection limit, S_b is the standard deviation of the blank response and m is the slope of the linear calibration curve ⁽⁶¹⁾.

$$C_m = \frac{3S_b}{m} \quad 4.8$$

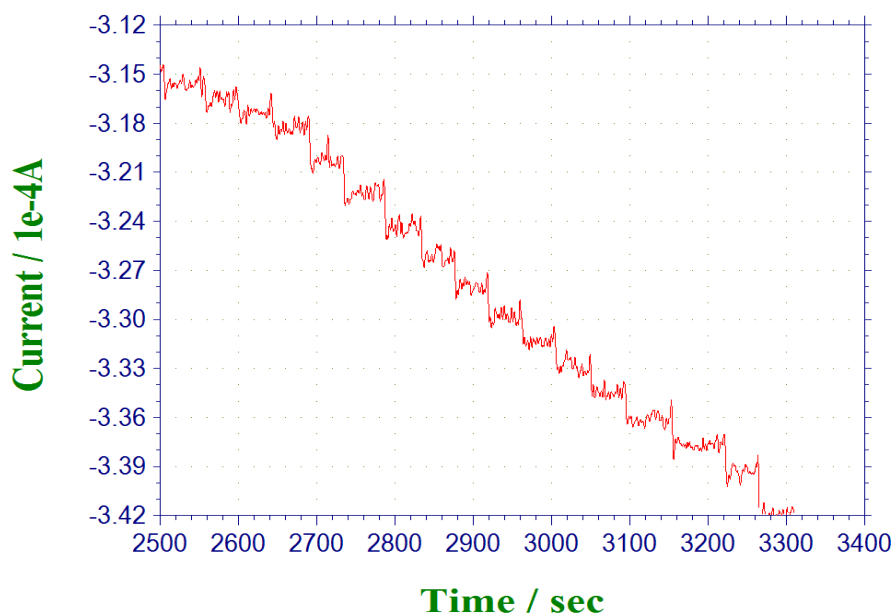


Figure 4.60: Constant potential amperometry, recorded at -1.20 V vs SCE for silver-modified GC electrode (silver deposited at -0.50 V vs Ag/Ag⁺ for 50 s) as a function of time with successive additions of aliquots of 2 x 10⁻³ mol dm⁻³ KNO₃ to 25 mL of 0.1 mol dm⁻³ LiClO₄.

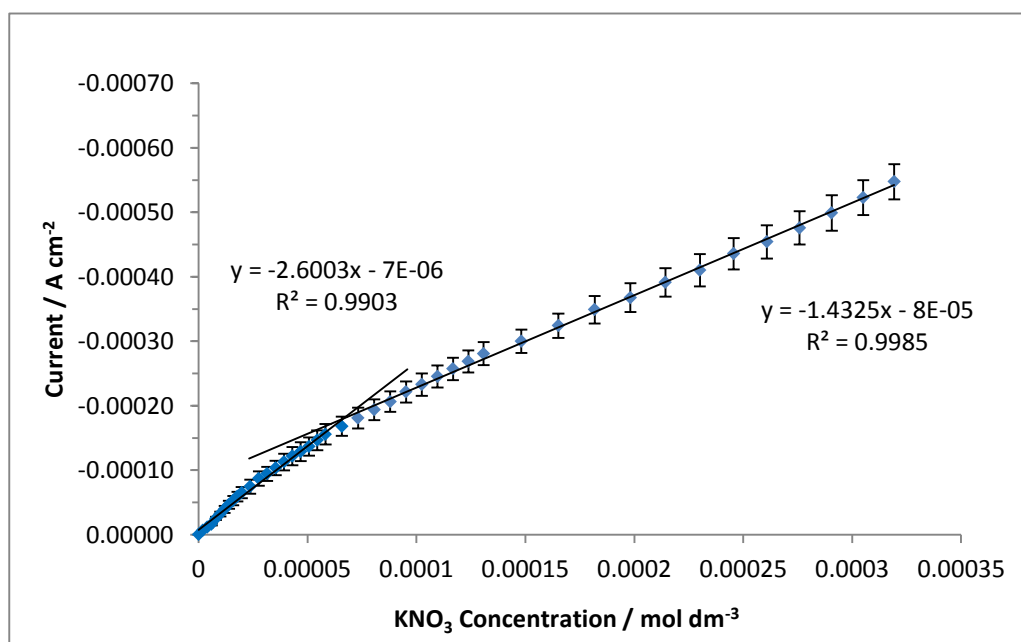


Figure 4.61: Steady-state currents from constant potential amperometry plotted as a function of KNO₃ concentration recorded at a silver-modified GC electrode (silver deposited at -0.50 V vs Ag/Ag⁺ for 50 s).

It is clear from a comparison of the amperometry and voltammetry data that the sensitivity of the sensor is increased 10-fold using constant potential amperometry. The limit of detection falls well below the maximum concentration levels as set out by the EPA for groundwater limits under the Nitrate Directive (91/676/EEC) of 50 mg/l NO₃⁻ or 8.0 x 10⁻⁴ mol dm⁻³ NO₃⁻. The detection of nitrates is extensive and a review by Moorcroft, Davis and Compton offers a summary of the progress made in utilising different techniques to accurately determine nitrate at low concentrations ⁽⁶²⁾. Examples of some of these techniques are given in Table 4.7 along with the limit of detection. As shown in Table 4.7, the detection limit observed in this study compares well with several studies.

Table 4.7: Limit of detection for techniques used in the determination of nitrate concentrations.

Technique	Material	Detection limit / mol dm ⁻³	Reference
Amperometry	Silver-modified GC electrode	1.0 x 10 ⁻⁵	This work
Potential-step chronocoulometry	Silver disc electrode	1.7 x 10 ⁻⁶	(26)
Cyclic voltammetry	Copper modified electrode	1.0 x 10 ⁻⁵	(63)
Enzyme bio-electrode	Nitrate reductase in poly(vinyl alcohol)	4.1 x 10 ⁻⁶	(64)
UV-Vis spectroscopy	Griess reagent	5.0 x 10 ⁻⁷	(65)
Chromatography	HPLC	3.7 x 10 ⁻⁷	(66)
Ion-selective membrane	Sulfonated poly(ether ether ketone)	5.0 x 10 ⁻⁵	(67)
IR	-	1.0 x 10 ⁻⁴	(68)
Gas chromatography	-	1.0 x 10 ⁻⁵	(69)

4.3.5 Influence of pH on Nitrate Reduction Peak

The products of the nitrate reduction reaction, the rate of the reduction reaction and the mechanism all depend on a number of parameters and one of these is the initial pH of electrolyte solution. There are multiple examples of the study of nitrate reduction in both acidic (70,71) and alkaline media (72-74) as well as neutral media (75,76), mostly driven by the need to electrochemically remove nitrates from different types of waste products. Nitrate reduction is frequently carried out in alkaline solution to ensure good separation of the nitrate peak from the hydrogen evolution reaction (26).

The influence of the solution pH on the nitrate reduction current was next evaluated and the results are presented in this section. The pH of a solution containing 5.0 x 10⁻³ mol dm⁻³ KNO₃ and 0.1 mol dm⁻³ LiClO₄ was adjusted using

0.5 mol dm⁻³ H₂SO₄ and 0.5 mol dm⁻³ NaOH, to give pH values ranging from 2.0 to 12.0. The CV's recorded in the various solutions are presented in Figure 4.62 and a plot of the peak current as a function of pH is shown in Figure 4.63. There are small changes in the magnitude of the peak current from pH 4.0 to 12.0 with a tendency to lower currents for more alkaline solutions. At pH 2.0, the peak changes dramatically with a shift to lower reduction potentials and an increase in the peak current. This is in agreement with groups such as De and co-workers where little change was seen between the various pH values but a significant change was seen at extremely low pH⁽⁷⁵⁾. Wang and co-workers found that the rate of the nitrate reduction decreased slightly with an increase of solution pH and suggested that at different pH values different adsorbed species cover the active metal surface. At the lower pH of around 5.0, adsorbed H⁺ species on the surface necessary for nitrate reduction are present, but as the pH is increased hydroxide ions occupy active sites and hinder nitrate adsorption⁽⁷⁷⁾.

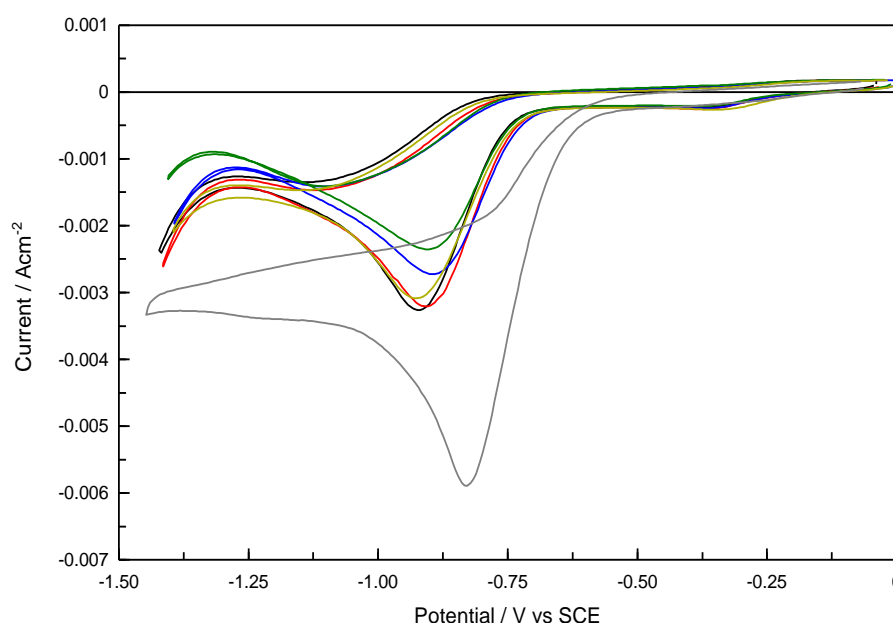


Figure 4.62: Cyclic voltammograms at a scan rate of 50 mV s⁻¹ in a solution of 5.0 x 10⁻³ mol dm⁻³ KNO₃ and 0.1 mol dm⁻³ LiClO₄ at various pH values at a silver-modified GC electrode (silver deposited at -0.50 V vs Ag/Ag⁺ for 50 s) — pH 2.0, — pH 4.0, — pH 8.0, — pH 10.0, — pH 12.0 and — and unadjusted pH.

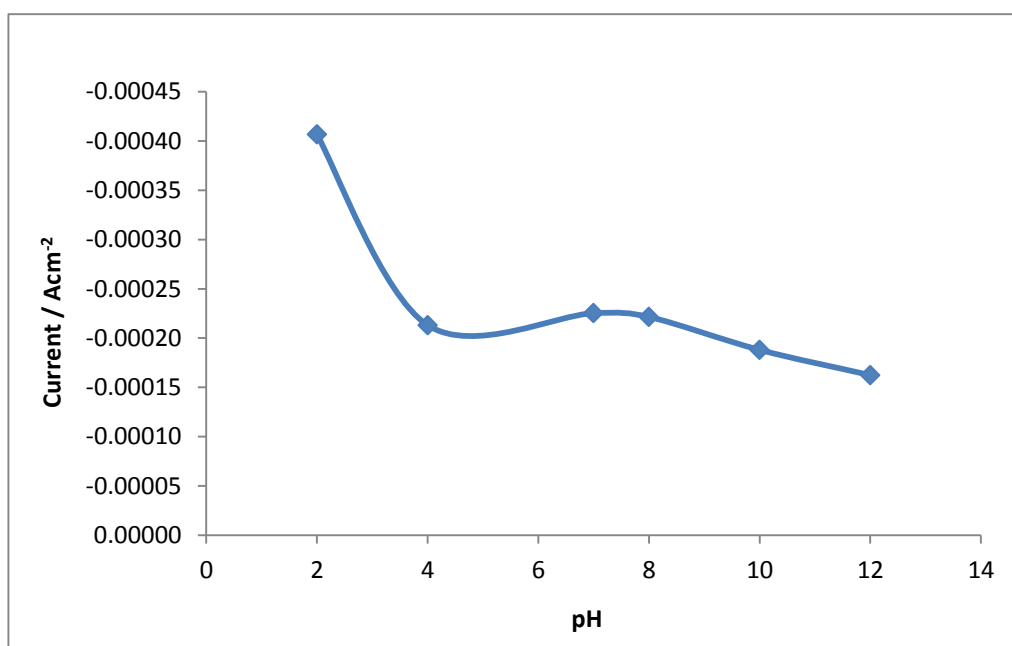


Figure 4.63: Plot of peak current as a function of pH for the cyclic voltammograms in Figure 4.62.

4.3.6 Effect of Electrolyte on Nitrate Reduction Peak

The reduction of nitrate to nitrite is preceded by an adsorption step where the nitrate anion adsorbs to the electrode surface. The reaction rate is therefore highly dependent on the surface coverage of nitrate, and competitive adsorption from competing anions in the supporting electrolyte can influence this process ⁽⁷⁸⁾. The effect of different electrolytes on the nitrate reduction peak at the silver-modified GC electrode was investigated. A range of different commonly used salts were chosen and the effect on the peak current and potential is presented in Table 4.8 with the corresponding voltammograms shown in Figures 4.64a and 4.65b (CV shown in two plots for clarity). It is evident that the nature of the supporting electrolyte has a significant effect on the profile of the nitrate reduction peak, illustrating further the complexity of the nitrate reduction mechanism.

The two alkaline solutions, NaOH and Na₂CO₃, exhibit the lowest nitrate current and at the most negative overpotentials, with substantial broadening of the peak. This is in good agreement with the data presented in Section 4.3.5 where, at the high pH values, hydroxide ions may be hindering nitrate access to the surface ⁽⁷⁷⁾. The silver-modified GC electrode in the hydroxide solution may be a poor catalyst

for nitrate reduction and this is supported by the fact that the nitrate signal improves with longer cycling in a reductive potential window where these hydroxides are less likely to be present.

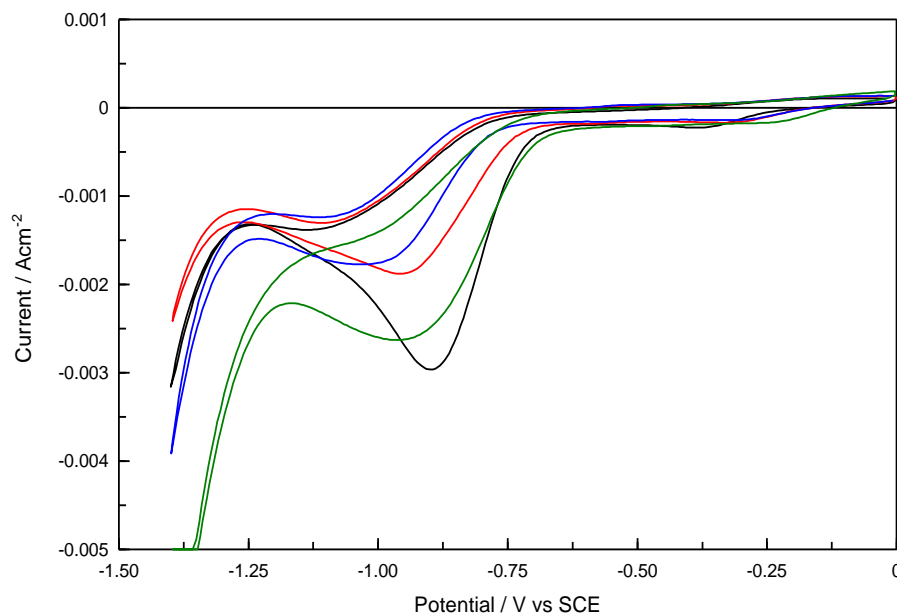


Figure 4.64a: Cyclic voltammograms at a scan rate of 50 mV s^{-1} in a solution of $5.0 \times 10^{-3} \text{ mol dm}^{-3} \text{ KNO}_3$ with different background electrolytes at a silver-modified GC electrode (silver deposited at $-0.50 \text{ V vs Ag/Ag}^+$ for 50 s), 0.1 mol dm^{-3} — LiClO₄, — KCl, — Na₂SO₄ and — Na₂CO₃.

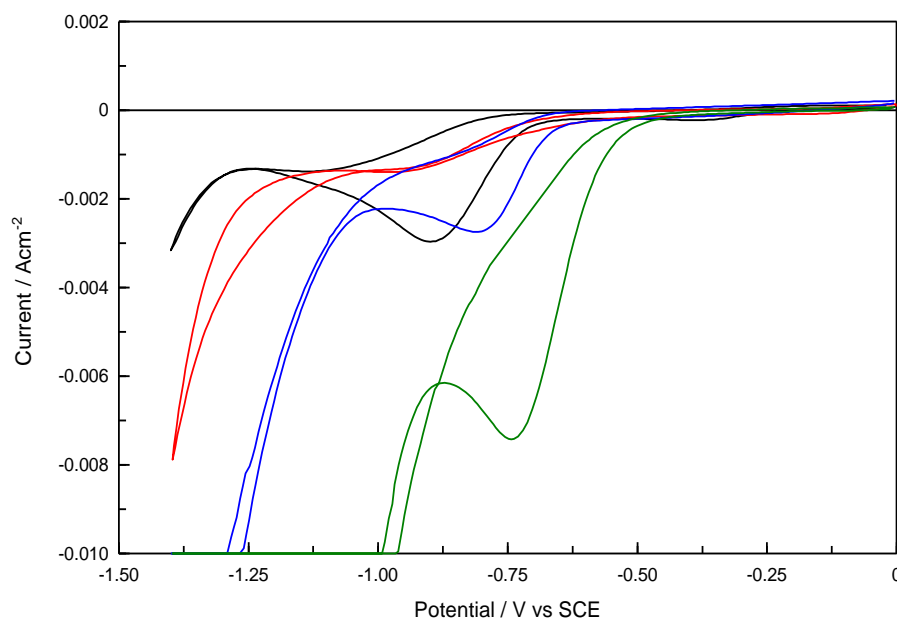


Figure 4.64b: Cyclic voltammograms at a scan rate of 50 mV s^{-1} in a solution of $5.0 \times 10^{-3} \text{ mol dm}^{-3} \text{ KNO}_3$ with different background electrolytes at a silver-modified GC electrode (silver deposited at $-0.50 \text{ V vs Ag/Ag}^+$ for 50 s), 0.1 mol dm^{-3} — LiClO₄, — H₂SO₄, — NaOH and — PBS solution.

Table 4.8: Peak reduction current (I_p^c) and potential (E_p^c) at the silver-modified GC electrode (silver deposited at -0.50 V vs Ag/Ag⁺ for 50 s) in a solution containing 5.0×10^{-3} mol dm⁻³ KNO₃ in various supporting electrolytes (0.1 mol dm⁻³) and the corresponding pH, background currents have been subtracted.

Electrolyte	pH	I_p^c / Acm^{-2}	$E_p^c / \text{V vs SCE}$
NaOH	12.6	-0.00107	-0.98
Na ₂ CO ₃	11.4	-0.00149	-1.03
Na ₂ SO ₄	5.3	-0.00161	-0.96
KCl	8.7	-0.00231	-0.97
PBS	6.7	-0.00244	-0.81
LiClO ₄	7.8	-0.00275	-0.89
H ₂ SO ₄	1.5	-0.00532	-0.74

Another point to note is the positive sweep in the NaOH-containing solution gives a similar peak current magnitude as the negative sweep. None of the other electrolytes display this characteristic. The KCl and Na₂SO₄ electrolytes show smaller currents compared to LiClO₄ and this is most likely due to the high adsorption properties of chloride and sulphate anions. The PBS solution displays a well-defined peak and the peak potential is observed at approximately -0.75 V vs SCE. However, the early onset of hydrogen evolution is a feature in this electrolyte. The highest current is observed in the H₂SO₄ solution, which indicates the importance of hydrogen ions in the reduction mechanism of nitrate. However, in these highly acidic conditions, there is poor separation from the hydrogen evolution reaction and the erratic nature of the peak current gives rise to poor reproducibility. The signal generally does not reach a steady state and this is most likely due to the evolution of hydrogen gas which disrupts the nitrate from effectively adsorbing at the surface. Molodkina and co-workers studied the kinetics and mechanism of nitrate and nitrite reduction at a platinum electrode with copper adatoms and showed that slightly adsorbed perchlorate anions do not hamper adsorption and reduction of nitrate⁽⁷⁹⁾. The same trend was observed in this study. The nitrate signal in LiClO₄ was well defined, stable and reproducible.

4.3.7 Kinetics and Reaction Mechanism of Nitrate Reduction

As discussed in the Introduction, the electrochemical reduction of nitrate is a complex reaction due to the large number of stable nitrogen oxidation states and potential products, NO_2^- , N_2O_4 , N_2 , NH_2OH , NH_3 , N_2O , N_2H_4 and NO . It is well accepted that in order for nitrate in solution to be reduced at any metal electrode surface, there must first be an interaction with the surface metal atom via an adsorption process. The metal atom provides the electrons for the reduction and consequently it is converted to the incipient hydrous oxide. The hydrous metal oxide is restored to its reduced state from the supply of electrons from the external current ⁽⁸⁰⁾. Cattarin has shown that nitrite is the main product for nitrate reduction at silver, while nitrogen gas and ammonia are mainly produced from the reduction reaction at Ni and Cu, respectively ⁽⁸¹⁾. In the following sections, attempts to gain an insight into the reaction mechanism of nitrate reduction at the silver-modified GC electrode are presented and discussed.

4.3.7.1 Influence of Scan Rate on Peak Current

The effect of scan rate was examined by cycling the silver-modified GC electrode in a $5.0 \times 10^{-3} \text{ mol dm}^{-3} \text{ KNO}_3$ solution at various scan rates in the range of 5 mV s^{-1} to 200 mV s^{-1} . Typical CV's are shown in Figure 4.65 and it is clear that the scan rate has a prominent effect on the nitrate signal. The most obvious trend from examining the voltammograms is that the current increases with increasing scan rate and the peak potential shifts to more negative potentials. This negative potential shift with increasing scan rate is typical for an irreversible reaction where electron transfer is slow.

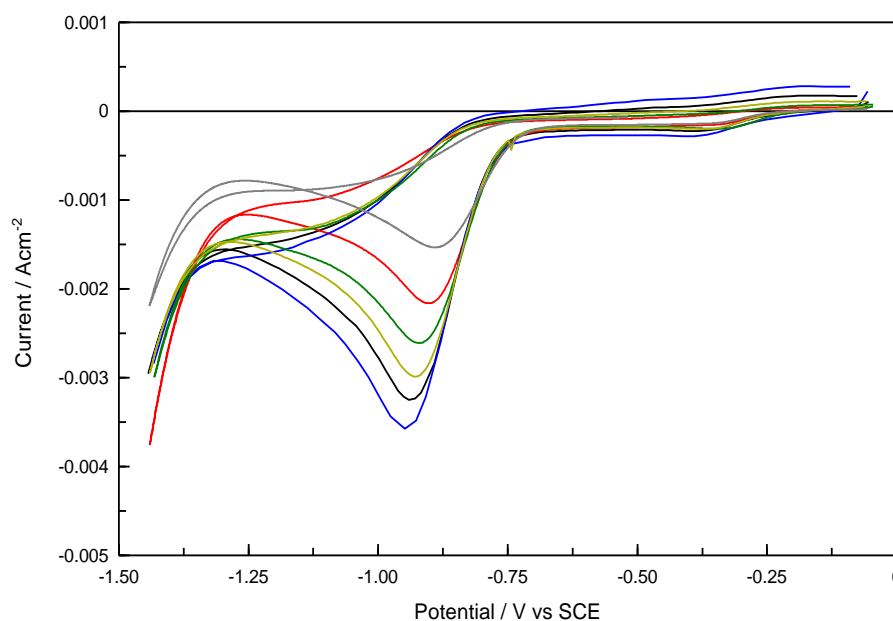


Figure 4.65: Cyclic voltammograms in a solution of $5.0 \times 10^{-3} \text{ mol dm}^{-3} \text{ KNO}_3$ and $0.1 \text{ mol dm}^{-3} \text{ LiClO}_4$ at a silver-modified GC electrode (silver deposited at $-0.50 \text{ V vs Ag/Ag}^+$ for 50 s) at a scan rate of — 5, — 10, — 25, — 50, — 100 and — 200 mV s^{-1} .

A linear response of the peak current to scan rate is indicative of an electrochemical reaction under diffusion control, as described by the Randles-Sevcik equation, Equation 4.9⁽⁸²⁾. In this version of the equation for an irreversible process, i_p is the peak current (A), n is the number of electrons, D is the diffusion coefficient ($\text{cm}^2 \text{ s}^{-1}$), v is the scan rate (V s^{-1}), C_o is the concentration (mol cm^{-3}), α is the charge transfer coefficient and n' is the number of electrons transferred up to and including the rate determining step.

$$i_p = -(2.99 \times 10^5)n(\alpha n')^{1/2}D^{1/2}v^{1/2}AC_o \quad 4.9$$

This equation is useful for the determination of the diffusion coefficient for a particular reaction. According to Equation 4.9, the current density is proportional to the square root of the scan rate and the slope of the resulting plot can be used to determine the diffusion coefficient provided $\alpha n'$ is known. In Figure 4.66, the peak current density is plotted as a function of the square root of the scan rate. A linear

response is obtained for scan rates below 50 mV s^{-1} , however, at higher scan rates the relationship deviates from linearity. De and Badea also showed that the relationship was not linear over the entire range ^(75,80). This, coupled with a non-zero intercept, indicates that the process is under some kinetic control possibly connected to the nitrate adsorption process. This adsorption process is essential prior to the reduction reaction and it appears to be time dependent. High sweep rates may not allow sufficient time for nitrate to adsorb.

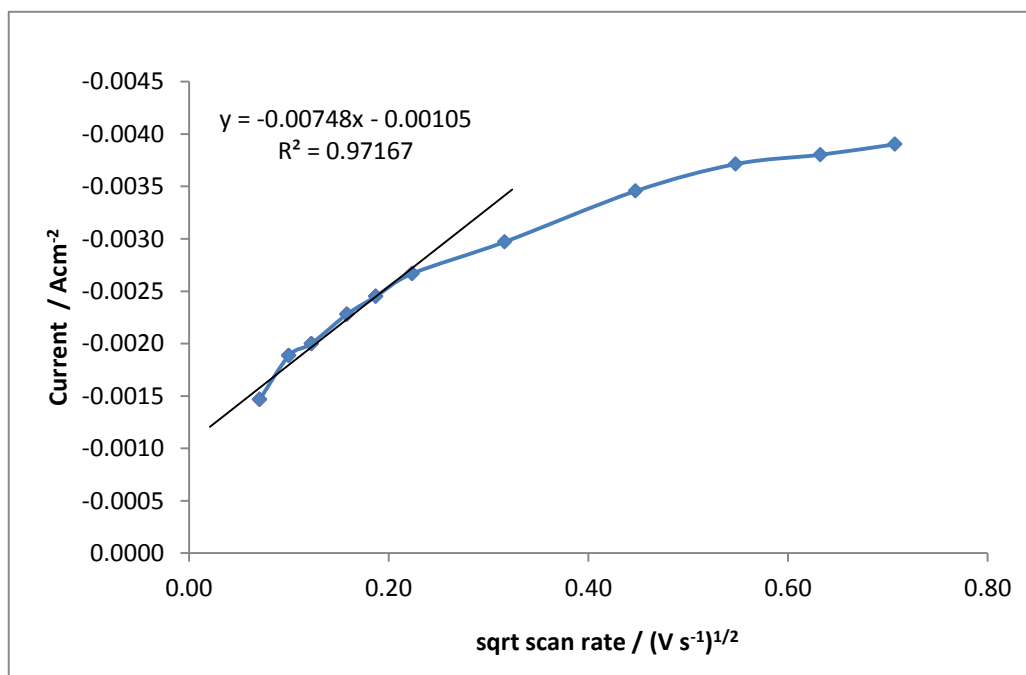


Figure 4.66: Peak reduction current plotted as a function of the square root of scan rate for the voltammograms presented in Figure 4.65. Background currents have been subtracted.

4.3.7.2 Evaluation of the Charge Transfer Coefficient

In order to determine the diffusion coefficient using the Randles-Sevcik equation, a value for $\alpha n'$ must be known. The following sections describe various methods to elucidate these parameters. The charge transfer coefficient, α , is a measure of the symmetry of the energy barrier during the transfer of an electron ⁽⁸³⁾. It lies between 0 and 1 but in most systems falls between 0.3 and 0.7 with 0.5 chosen as an approximation where no experimental data are available. The charge transfer coefficient can be determined using a number of equations applied to the appropriate data set.

4.3.7.2.1 Shape Factor

Equation 4.10 can be applied to an irreversible process in order to determine the value of $\alpha n'$ by measuring $|E_p - E_{p1/2}|$, which is also called the shape factor ⁽²⁴⁾. The potentials, E_p and $E_{p1/2}$, are indicated on the voltammogram in Figure 4.67, where E_p is the peak potential and $E_{p1/2}$ is the half-wave potential. The shape factor was calculated at different scan rates for the silver-modified GC electrode in solutions containing $5.0 \times 10^{-3} \text{ mol dm}^{-3} \text{ KNO}_3$. As shown in Figure 4.68, the shape factor drifts slightly with scan rate, varying from 100 mV at the lower scan rates to 125 mV at the higher scan rates. An average value of 113 mV was calculated for $|E_p - E_{p1/2}|$ and using Equation 4.10 the value of $\alpha n'$ was calculated as 0.422.

$$|E_p - E_{p1/2}| = 1.857 \frac{RT}{F\alpha n'} \quad (\text{V}) \quad 4.10$$

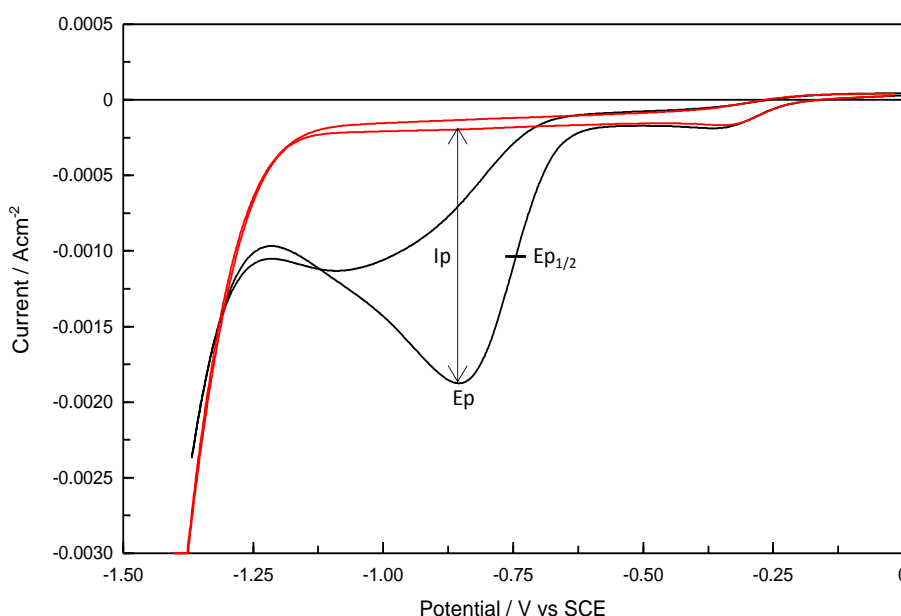


Figure 4.67: CV's in a solution of — $5.0 \times 10^{-3} \text{ mol dm}^{-3} \text{ KNO}_3$ and $0.1 \text{ mol dm}^{-3} \text{ LiClO}_4$ at a silver-modified GC electrode (silver deposited at $-0.50 \text{ V vs Ag/Ag}^+$ for 50 s) at a scan rate of 10 mV s^{-1} . — background scan in $0.1 \text{ mol dm}^{-3} \text{ LiClO}_4$.

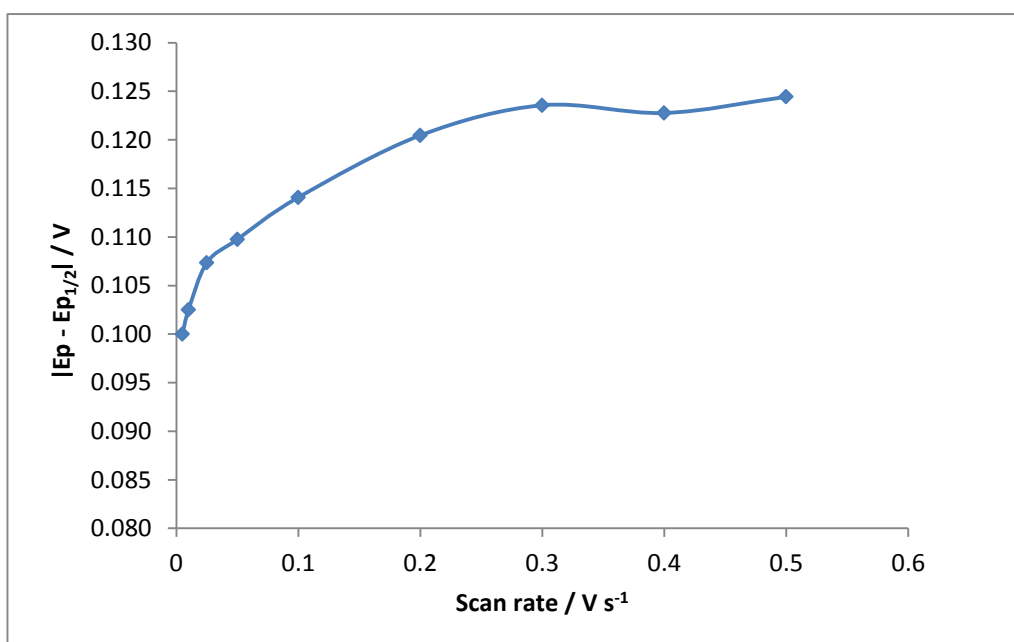


Figure 4.68: Plot of average $|E_p - E_{p1/2}|$ as a function of scan rate for 3 sets of experiments.

4.3.7.2.2 Peak Potential as a Function of log of Scan Rate

Another relationship commonly employed to determine the value of an' is Equation 4.11, where E_p is the peak potential and $\log v$ is the logarithm of the scan rate. As shown in Equation 4.11, the cathodic peak potential for an irreversible process shifts by $29.6/an'$ for each decade increase in scan rate.

$$\left| \frac{dE_p}{d \log v} \right| = \frac{29.6}{an'} \quad (\text{mV}) \quad 4.11$$

In Figure 4.69, a plot of the peak potential as a function of the logarithm of the scan rate is shown. Good linearity is obtained and the slope of the plot was used to give a value for an' of 0.451, which is in good agreement with the value of 0.422 obtained using the shape factor analysis. This type of plot is called a Laviron plot

(84). In addition to the determination of $\alpha n'$ from the slope, the intercept can be used to calculate the electrochemical rate constant, k^0 , through Equation 4.12.

$$\log K_{ET} = \alpha \log(1 - \alpha) + (1 - \alpha) \log \alpha - \log \left(\frac{RT}{n'Fv} \right) - \frac{\alpha(1 - \alpha)n'F\Delta E_p}{2.3RT} \quad 4.12$$

This equation can be reduced by applying the constraint of $\Delta E_p = 0$ to give Equation 4.13, where v_c is the x-intercept for the cathodic branch of the Laviron plot ^(85,86). The k^0 extracted from these experimental data was $9.79 \times 10^{-3} \text{ s}^{-1}$.

$$k^0 = \frac{\alpha n' F v_c}{RT} \quad 4.13$$

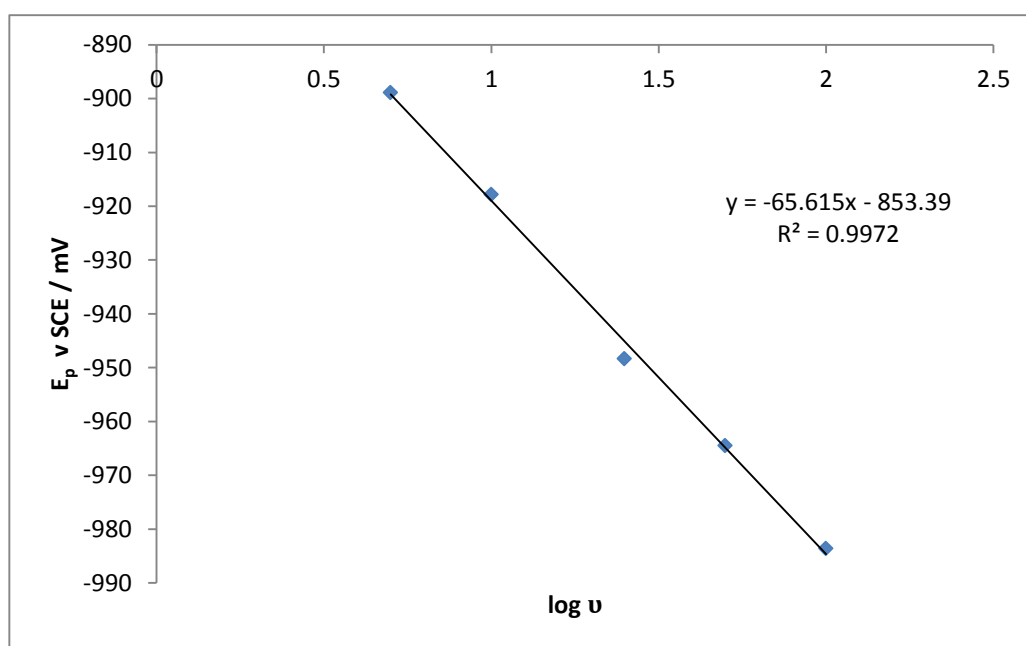


Figure 4.69: Dependence of the peak potential (E_p) on the logarithm of scan rate for a solution of $5.0 \times 10^{-3} \text{ mol dm}^{-3} \text{ KNO}_3$ and $0.1 \text{ mol dm}^{-3} \text{ LiClO}_4$ at a silver-modified GC electrode (silver deposited at -0.50 V vs Ag/Ag^+ for 50 s).

4.3.7.2.3 Tafel Analysis

The elucidation of the Tafel slope can be useful in differentiating between possible reaction mechanisms. The Tafel slope, Equation 4.14, is derived from the data of the rising portion of the plot where the logarithm of the current is plotted as a function of the logarithm of the potential at a low scan rate, typically 5 mV s^{-1} . The voltammogram recorded at a scan rate of 5 mV s^{-1} for the silver-modified GC electrode in $5.0 \times 10^{-3} \text{ mol dm}^{-3} \text{ KNO}_3$ is shown in Figure 4.70, while the corresponding logarithmic plot is presented in Figure 4.71. The region used to compute the Tafel slope is shown on the plots and extends between the linear potential region of -0.75 V and -0.80 V vs SCE. The Tafel slope was calculated as 140 mV and applying Equation 4.14 yields an $\alpha n'$, value of 0.423 , which is in good agreement with the values calculated in Sections 4.3.7.2.1 and 4.3.7.2.2. Using the three techniques to determine $\alpha n'$ an average value of 0.444 was obtained. This value was then used in Equation 4.9 to determine the diffusion coefficient.

$$\text{slope} = \frac{2.303 RT}{\alpha F n'} \quad 4.14$$

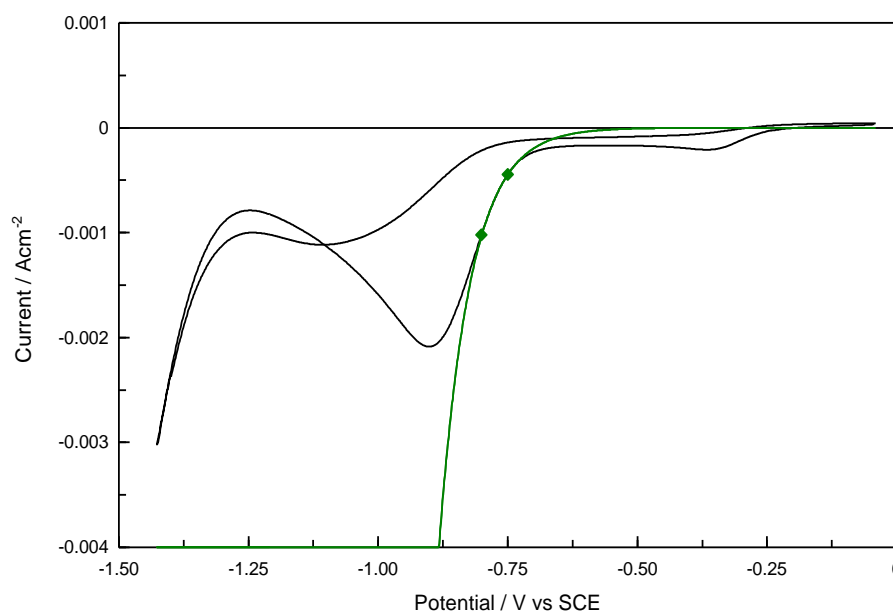


Figure 4.70: Tafel slope analysis, current as a function of potential for a CV at a scan rate of 5 mV s^{-1} in a solution of $5.0 \times 10^{-3} \text{ mol dm}^{-3} \text{ KNO}_3$ and $0.1 \text{ mol dm}^{-3} \text{ LiClO}_4$ at a silver-modified GC electrode (silver deposited at -0.50 V vs Ag/Ag^+ for 50 s).

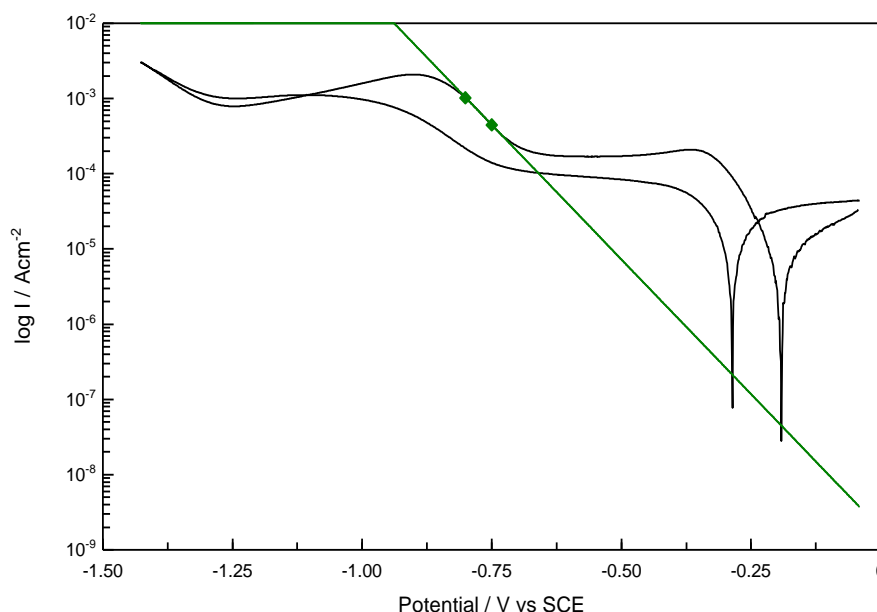


Figure 4.71: Tafel slope analysis with the logarithm of current plotted as a function of potential, for a CV at a scan rate of 5 mV s^{-1} in a solution of $5.0 \times 10^{-3} \text{ mol dm}^{-3} \text{ KNO}_3$ and $0.1 \text{ mol dm}^{-3} \text{ LiClO}_4$ at the silver-modified GC electrode (silver deposited at $-0.50 \text{ V vs Ag/Ag}^+$ for 50 s).

4.3.7.3 Diffusion Coefficient for Nitrate Reduction

With a value of $\alpha n'$ averaged from three different experimental approaches, the Randles-Sevick equation, Equation 4.9, was applied to determine the diffusion coefficient. The slope of the linear region in Figure 4.66 is given by Equation 4.15, where n is 2 since the nitrate to nitrite reduction is a two electron process, $\alpha n'$ is 0.444 and C_0 is $5.0 \times 10^{-6} \text{ mol cm}^{-3}$.

$$\text{slope} = -(2.99 \times 10^5)n(\alpha n')^{1/2}D^{1/2}C_0 \quad 4.15$$

The diffusion coefficient, D , was calculated as $1.41 \times 10^{-5} \text{ cm}^2 \text{ s}^{-1}$. This compares well with literature values for nitrate reduction at other electrode surfaces. Aouina obtained a value of $1.31 \times 10^{-5} \text{ cm}^2 \text{ s}^{-1}$ for nitrate reduction at a copper electrode in neutral NaClO_4 solutions⁽⁸⁷⁾. Gartia and co-workers reported a value at a silver microelectrode of $8.99 \times 10^{-6} \text{ cm}^2 \text{ s}^{-1}$ ⁽⁸⁸⁾, while other groups quote values in the range of 1.0×10^{-5} to $2.0 \times 10^{-5} \text{ cm}^2 \text{ s}^{-1}$ ⁽⁷³⁾.

4.3.7.4 Number of Electrons in Rate Determining Step of Nitrate Reduction

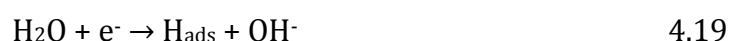
As discussed in the Introduction, most studies investigating the mechanism of the nitrate reduction reaction state that the rate determining step is a 2 e⁻ transfer step. This yields nitrite after an initial nitrate adsorption step, Equations 4.16 and 4.17 ^(78,89,90). Using the value of $\alpha n'$ of 0.444, obtained in Section 4.3.7.2, the number of electrons in the rate-determining step can be obtained if the α value is known.



As mentioned in 4.3.7.2, α lies between 0 and 1 and is often approximated to 0.5 if not known experimentally. However, in the system under investigation here, if n' is taken as 2, in order to satisfy the experimental results α must equal 0.222, which is somewhat low. If n' is 1, then α becomes 0.444, which is close to the quoted approximate value for α of 0.5.

In the literature, where groups have tried to understand the mechanism of nitrate reduction at various surfaces, a range of values for α and n' have been reported. Oznuluer and colleagues solved for $\alpha n'$ using the Randle-Sevcik equation with a diffusion coefficient of $2 \times 10^{-5} \text{ cm}^2 \text{ s}^{-1}$ and found $\alpha n'$ equal to 1.1 ± 0.5 for a graphene modified copper electrode. For two electrons in the rate-determining step, this gives $\alpha n'$ equal to 0.5 ⁽⁹¹⁾. Reyter and co-workers using Equations 4.10 and 4.11 found $\alpha n'$ equal to 0.98 ± 0.08 thus assuming a value for α of 0.5, and two electrons involved in the rate-determining step ⁽⁷³⁾. However, there are many examples of α values lower than 0.5. De reported a value of 0.25 for $\alpha n'$ from the Tafel slope for the reduction of $5.0 \times 10^{-3} \text{ mol dm}^{-3} \text{ NaNO}_3$ in $1.0 \text{ mol dm}^{-3} \text{ NaClO}_4$ at an iridium modified carbon fibre electrode ⁽⁹²⁾. The low value for the transfer coefficient, according to De, suggests that nitrate reduction on the surface of the modified carbon fibre is not a simple electron transfer reaction and that the adsorption process must be closely associated with the electron transfer. They also

calculated Tafel slopes using Temkin and Frumkin isotherms as a comparison and found excellent agreement. With a value for $\alpha n'$ of 0.25 they suggested n' was 1 and proposed the following mechanism for the rate-determining step, Equation 4.18. Additionally, this can be written as two reactions where the significance of the adsorbed hydrogen is illustrated, Equations 4.19 and 4.20.



Korgel and co-workers⁽⁹³⁾ also obtained a low value for α of 0.23 and also suggested a one-electron transfer step involving a short-lived intermediate, NO_3^{2-} , Equation 4.21



Dima and co-workers obtained a Tafel slope of 120 mV/dec or higher ($\alpha n' \sim 0.5$) for nitrate reduction at coinage and transition metal electrodes in acidic solution and suggested that the rate-determining step is the first electron transfer during the overall conversion to nitrite as in Equation 4.17⁽⁹⁴⁾. Others have reported α values larger than 0.5. Badea and co-workers obtained a value for α of 0.258 using coulometry data and determined n as 2 for the first electron transfer for nitrate reduction at a copper electrode in alkaline media, although the rate-determining step was not specified⁽⁸⁰⁾. Gartia and co-workers determined a value for α of 0.65 for nitrate reduction at a silver micro electrode⁽⁸⁸⁾.

4.3.7.5 The Current Function

The current function also gives an indication of what occurs at the electrode surface during the reduction process. The current function is shown in Figure 4.72, where the current function, $(i_p/v^{1/2})$, is plotted as a function of the scan rate.

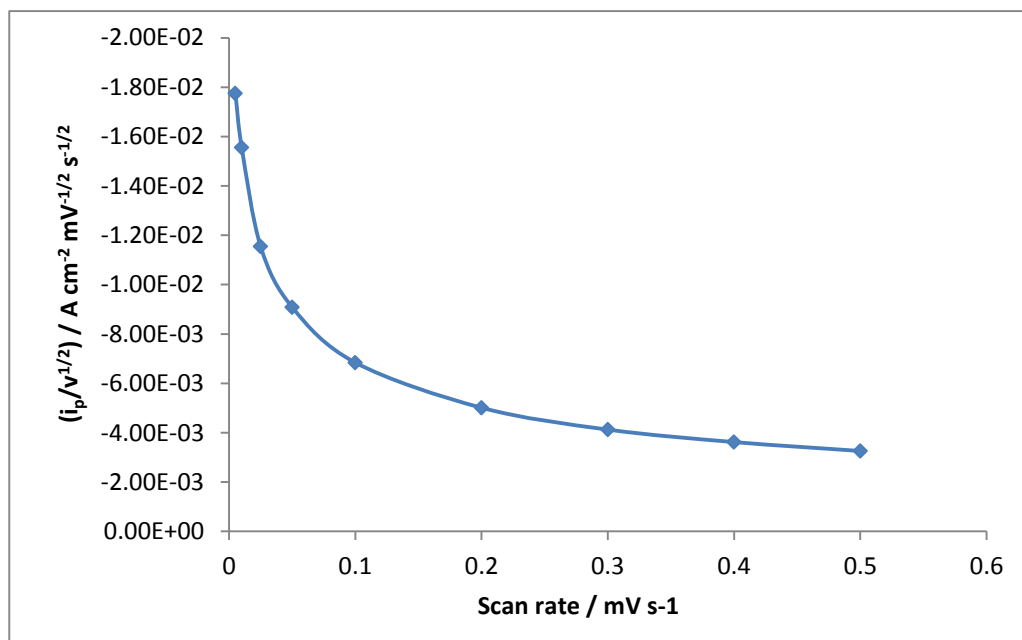


Figure 4.72: The current function $(i_p/v^{1/2})$ as a function of scan rate for a solution of $5.0 \times 10^{-3} \text{ mol dm}^{-3} \text{ KNO}_3$ and $0.1 \text{ mol dm}^{-3} \text{ LiClO}_4$ at the silver-modified GC electrode (silver deposited at -0.50 V vs Ag/Ag^+ for 50 s).

The current function decreases with increasing scan rate, decaying from $1.8 \times 10^{-2} \text{ A cm}^{-2} \text{ V}^{-1/2} \text{ s}^{1/2}$ to $4.0 \times 10^{-3} \text{ A cm}^{-2} \text{ V}^{-1/2} \text{ s}^{1/2}$ as the scan rate is increased. This indicates the presence of a chemical reaction coupled to the electron transfer (EC mechanism) ⁽⁸²⁾. Fedurco and co-workers, with the aid of voltammogram simulations generated using a computer program, found an ECE mechanism (electron-transfer, chemical, electron-transfer) for nitrate reduction with a slow first charge-transfer step, followed by the resulting intermediate being consumed in a fast homogeneous reaction with water molecules. The final nitrite product was assumed to form in a second electron-transfer step ⁽⁹⁵⁾. This simulated linear sweep voltammogram was in excellent agreement with the voltammogram observed for nitrate reduction at a silver electrode in neutral NaClO_4 solution. They suggested that this likely reaction pathway could be analogous to what occurs

under conditions of photoemission experiments when nitrate anions react with hydrated electrons to form $(\text{NO}_3^\bullet)^{2-}$ species, Equation 4.22. The $(\text{NO}_3^\bullet)^{2-}$ species combine with H_2O to form NO_2^\bullet radicals, Equation 4.23



This sequence of a slow electron-transfer step and a fast chemical step is consistent with the generated simulation. However, distinguishing between the two steps is difficult experimentally. Finally, the nitrite radical species is expected to reduce according to Equation 4.24. Reaction 4.24 is fast compared to the reaction in Equation 4.22, and its redox potential is quite positive, $E^0 = 0.895 \text{ V}$ vs NHE.



For silver nanoparticles deposited on a gold electrode, Fajerweg and co-workers kinetic analysis also supported this mechanism. A shape factor for cyclic voltammograms in a saline nitrate solution yielded an $\alpha n'$ of 0.57 and a monotonous decrease in $i_p/v^{1/2}$ with $v^{1/2}$ indicating a chemical reaction coupled with electron transfer ⁽⁹⁶⁾. Clearly, the mechanism is very complex and there are many conflicting theories in the literature. In this work, the data are consistent with a one-electron transfer step being a slow step followed by a fast second one-electron transfer step or a chemical reaction.

4.3.7.6 Standard Rate Constant for Nitrate Reduction

The standard rate constant, k_0 , is a measure of the kinetics of an electrochemical system, Equation 4.25. Large and small values of k_0 indicate fast and slow kinetics, respectively, and the type and complexity of the molecule undergoing the electron transfer influences the magnitude of k_0 . The standard rate constant was computed for the nitrate reduction reaction at the silver-modified GC electrode using the peak potentials and Equation 4.26. This theoretical treatment predicts that the peak potential for an irreversible reaction will vary with the scan rate.



$$E_p = E^0 - \frac{RT}{\alpha n' F} \left[0.780 + \ln \left(\frac{D^{1/2}}{k_s} \right) + \ln \left(\frac{\alpha n' F}{RT} v \right)^{1/2} \right] \tag{4.26}$$

As shown in Equation 4.26, the formal potential, E^0 , for a redox couple, which is a thermodynamic parameter, is required to compute the rate constant. However, Velasco eliminated the E^0 term to yield Equation 4.27^(97,98). In this equation, k_0 is expressed in cm s^{-1} , where D is the diffusion coefficient ($1.41 \times 10^{-5} \text{ cm}^2 \text{ s}^{-1}$), v is the scan rate (V s^{-1}) and $E_p - E_{p1/2}$ for each scan rate is the shape factor as determined from Section 4.3.7.2.1. From Equation 4.27, it is evident that k_0 is not constant but varies linearly with $v^{1/2}$.

$$k_0 = 1.11 D_0^{1/2} (E_p - E_{p/2})^{1/2} v^{1/2} \tag{4.27}$$

Velasco discussed this relationship, and concluded that sweep voltammetry at slower sweep rates was not a suitable method to determine k_0 for irreversible reactions. However, at higher sweep rates, k_0 tends to reach a constant value, which represents the true k_0 . The voltammograms were recorded at different scan rates and the rate constants, k^0 , were calculated using Equation 4.27. In Figure 4.73, the calculated standard rate constants are plotted as a function of the scan rate. A linear relationship is obtained and there is no evidence that the rate

constant reaches a limiting value at the higher scan rates. Even at a scan rate of 500 mV s^{-1} , the rate constants continued to increase. The standard rate constant was calculated as $8.9 \times 10^{-4} \text{ cm s}^{-1}$ at a scan rate of 5 mV s^{-1} and $8.3 \times 10^{-3} \text{ cm s}^{-1}$ for a scan rate of 500 mV s^{-1} . This suggests that the true k_0 value is higher than $8.3 \times 10^{-3} \text{ cm s}^{-1}$.

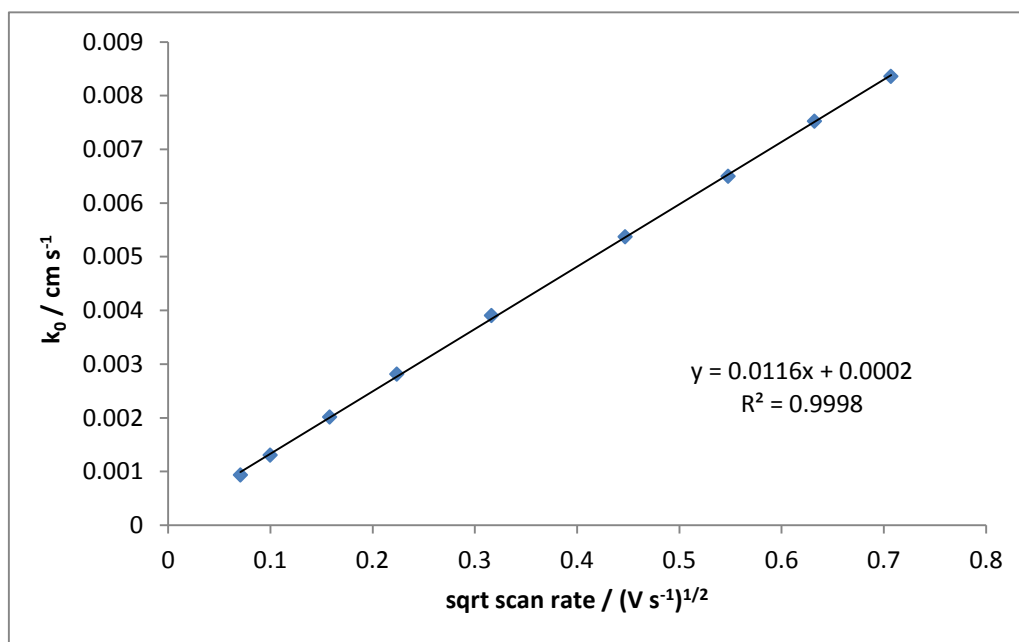


Figure 4.73: Plot of the standard rate constant as a function of $v^{1/2}$.

4.3.7.7 Reaction Order

In chemical kinetics, the rate law can be used to obtain the reaction order and the rate constant. Equation 4.28 is the proposed rate law for the nitrate reduction reaction, where the rate of the reaction is expressed as the peak reduction current. To determine the reaction order, n , the logarithm of this equation is taken, to give Equation 4.29. A logarithmic plot of the peak reduction current and the nitrate concentration is shown in Figure 4.74. A linear plot is obtained, indicating that the data can be used to elucidate n and the rate constant, k , from the slope and the inverse of the y-axis intercept, respectively.

$$\text{Rate} = \text{Current} = k[\text{KNO}_3]^n \quad 4.28$$

$$\log \text{Current} = n \log[\text{KNO}_3] + \log k \quad 4.29$$

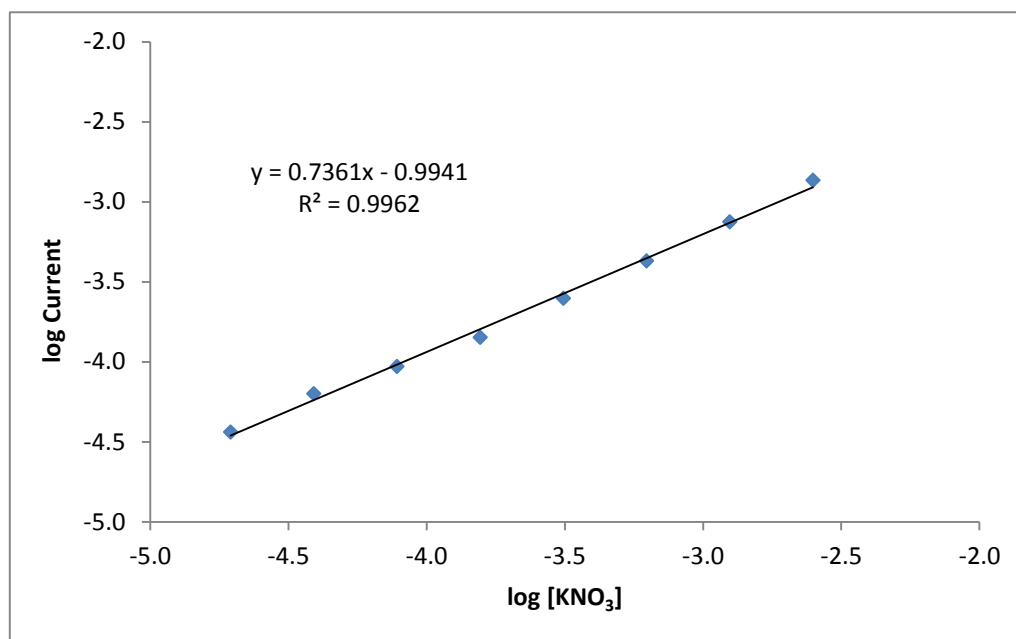


Figure 4.74: Plot of logarithm of the reduction current against the logarithm of KNO₃ concentration (mol dm⁻³) at the silver-modified GC electrode (silver deposited at -0.50 V vs Ag/Ag⁺ for 50 s). A background electrolyte of 0.1 mol dm⁻³ LiClO₄ was used for all solutions and voltammograms were recorded at 50 mV s⁻¹.

From these data, the reaction order was estimated to be 0.736 while an intercept of 0.9635 was obtained, and from Equation 4.29 this yields a rate constant of 9.87 A cm⁻² mol^{0.736} s^{-0.736}. The reaction order is in good agreement with previous literature values where Hague and Tariq⁽⁹⁹⁾ reported a reaction order of 0.747 at a solid titanium electrode and Casella and Gatta⁽⁷⁴⁾ reported a reaction order of 0.72 for the reduction of nitrate at a copper thallium composite and 0.70 for a pure copper electrodeposited film. Casella and Gatta suggest that this fractional reaction order supports the general hypothesis that the electrochemical reduction of nitrate is preceded by an initial adsorption step and that these values for the reaction order are typical of electrochemical processes that are under kinetic control. A reaction order as low as 0.26 was reported by Estudillo-Wong⁽¹⁰⁰⁾.

4.3.7.8 Reaction Hydrodynamics

Rotating disc voltammetry (RDV) was employed to monitor the hydrodynamics of the nitrate reduction reaction at the silver-modified GC electrode. The electrode was prepared as outlined in Section 4.3.1.2, where the silver was deposited using a single pulse of -0.50 V vs Ag/Ag⁺ for 50 s and cycled in a potential window of -0.05 to -1.45 V vs SCE at rotation speeds varying from 400 to 2000 rpm.

The Levich and Koutecky-Levich relationships, Equation 4.30 and 4.31, respectively, can be applied to the currents generated at different rotation speeds to give insight into the diffusional and kinetic limitations of a reaction at the electrode surface. A deviation of a plot of I vs $\omega^{1/2}$ (Levich plot) from a straight line intersecting the origin suggests that a kinetic limitation is involved in the electron-transfer reaction⁽⁸³⁾. When the electron-transfer process at the electrode exhibits sluggish kinetics the voltammograms appear stretched out along the potential axis and the shape of the sigmoidal wave can be slightly distorted. Also, the mass transport limiting current is shifted further away from the standard electrode potential. In summary, a reaction with sluggish kinetics at a rotating disc electrode (RDE) requires a larger overpotential to overcome the sluggish kinetics and reach the mass transport limited current.

$$i_L = (0.62)nFAD^{2/3}\omega^{1/2}\nu^{-1/6}C_o \quad 4.30$$

$$\frac{1}{i} = \frac{1}{i_k} + \frac{1}{0.62nFAD^{2/3}\omega^{1/2}\nu^{-1/6}C} \quad 4.31$$

Figure 4.75 shows the response of a silver-modified GC electrode to various rotation speeds. The CV's have indeed become more drawn out and the potential of the limiting current has shifted to higher reduction potentials, from -0.91 V at no rotation to -1.28 V vs SCE. As mentioned above, this is indicative of sluggish kinetics at the electrode.

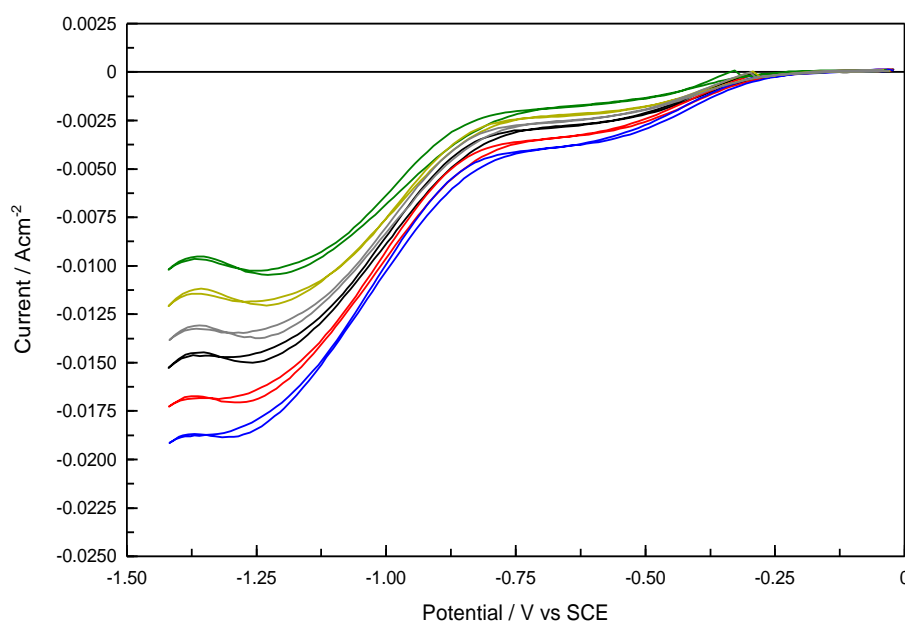


Figure 4.75: Rotating disc voltammograms in a solution of $5.0 \times 10^{-3} \text{ mol dm}^{-3} \text{ KNO}_3$ and $0.1 \text{ mol dm}^{-3} \text{ LiClO}_4$ at a silver-modified GC electrode (silver deposited at $-0.50 \text{ V vs Ag/Ag}^+$ for 50 s) at a rotation speed of — 400, — 600, — 800, — 1000, — 1500 and — 2000 rpm. Scan rate 50 mV s^{-1} .

The Levich and Koutecky-Levich plots are shown in Figures 4.76 and 4.77. The Levich plot deviates slightly from linearity at the higher rotation speeds, indicating there is a kinetic limitation to the reaction. By applying Equation 4.30 to the slope of the linear portion of the Levich plot, Figure 4.76, a diffusion coefficient of $1.66 \times 10^{-5} \text{ cm}^2 \text{ s}^{-1}$ is obtained when the number of electrons transferred, n , is taken as 2, F is the Faraday constant (96485 C mol^{-1}), A is the electrode area (cm^2), ν is the kinematic viscosity ($0.0086 \text{ cm}^2 \text{ s}^{-1}$ ⁽⁸⁷⁾) and C is the concentration of the reactant in the solution ($5.0 \times 10^{-6} \text{ mol cm}^{-3}$). This diffusion coefficient value is very close to the value obtained for the diffusion coefficient calculated by varying the scan rate ($1.41 \times 10^{-5} \text{ cm}^2 \text{ s}^{-1}$) in Section 4.3.7.3. Using the slope of Figure 4.77 and Equation 4.31, the Koutecky-Levich equation, a diffusion coefficient of $1.83 \times 10^{-5} \text{ cm}^2 \text{ s}^{-1}$ is obtained, which is in good agreement with other techniques discussed in this work. Aouina and co-workers obtained a value of $1.6 \pm 0.1 \times 10^{-5} \text{ cm}^2 \text{ s}^{-1}$ for the diffusion coefficient of nitrate using impedance measurements and the Levich plots also deviated from linearity at high rotation speeds ⁽⁸⁷⁾. Reduction

of nitrate at a cadmium RDE also showed deviation from a linearity at high rotation speeds ⁽¹⁰¹⁾.

The heterogeneous rate constant, k_0 , calculated from the intercept ($1/i_k$) of the Koutecky-Levich plot and Equation 4.32, gives a value of 0.11 cm s^{-1} .

$$i_k = nFAk_0C \quad 4.32$$

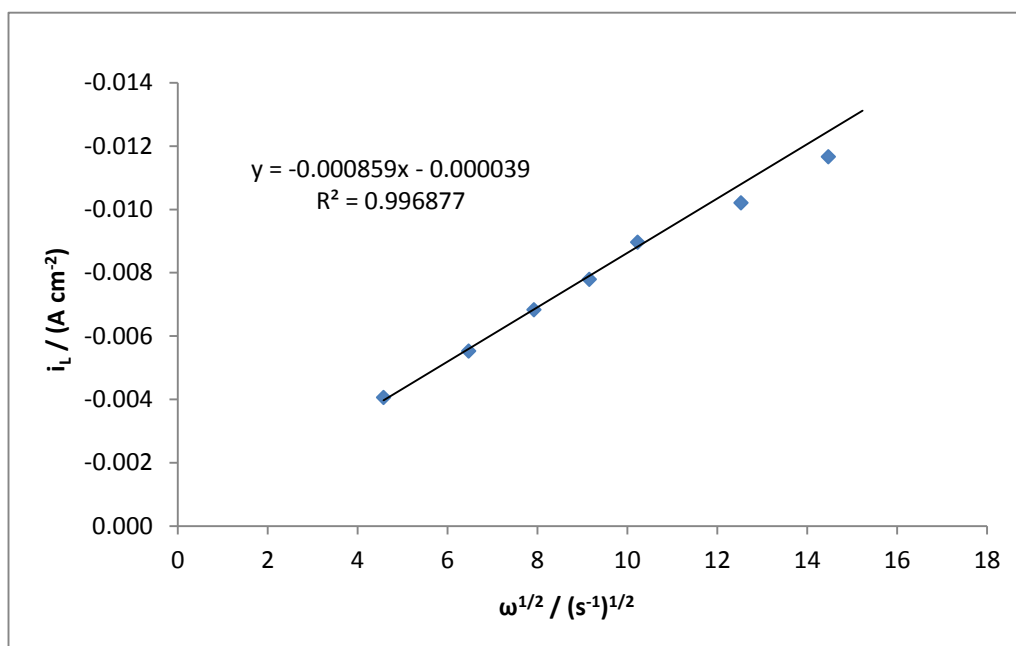


Figure 4.76: Levich plot for the limiting current (recorded at -1.28 V vs SCE) of the rotating disc voltammograms in Figure 4.75.

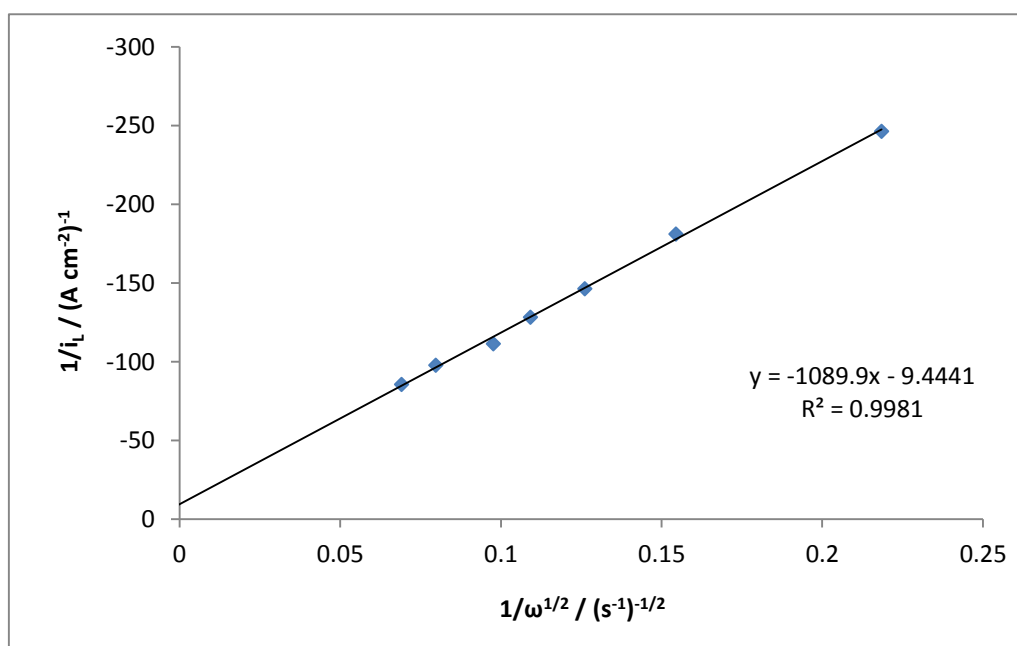


Figure 4.77: Koutecky-Levich plot for the limiting current (recorded at -1.28 V vs SCE) for the rotating disc voltammograms in Figure 4.75.

4.3.8 Shape of Nitrate Reduction Peak with Cycling

The process of nitrate reduction is complicated with many possible stable products formed at more or less the same potential. Also, the type of material and the condition of the surface dictates the products formed and plays a role in the profile of the CV's. Figure 4.78 is a typical CV (cycle 30) recorded for the silver-modified GC electrode in a solution containing $5.0 \times 10^{-3} \text{ mol dm}^{-3} \text{ KNO}_3$ and $0.1 \text{ mol dm}^{-3} \text{ LiClO}_4$ after 30 background cycles and 30 cycles in the nitrate solution. As mentioned earlier, Section 4.3.1.1, the onset of the reduction current occurs at -0.65 V vs SCE with a peak potential of -0.90 V vs SCE. The current then drops and increases again at -1.25 V vs SCE. On sweeping back in the positive direction, a reduction current is also observed, although with significant hysteresis. Cattarin suggested that the hysteresis between the two half cycles of the nitrate signal observed at a silver electrode indicates that surface modifications occur upon polarization at the negative potential limits⁽⁸¹⁾. Others suggest that the new reduction peak on the positive sweep is due to nitrate reduction on the "fresh" surface sites produced by hydrogen desorption⁽¹⁰²⁾. It is even more evident that

surface changes are occurring during voltammetric cycling when the shapes of the CV's are examined upon repetitive cycling, Figure 4.79.

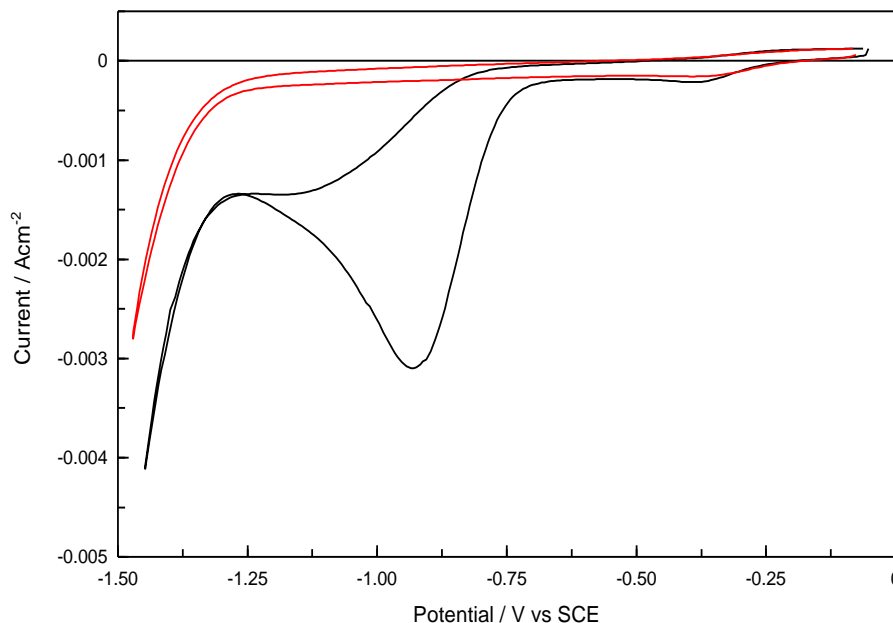


Figure 4.78: Cyclic voltammograms at a scan rate of 50 mV s^{-1} in a solution of — $5.0 \times 10^{-3} \text{ mol dm}^{-3} \text{ KNO}_3$ and $0.1 \text{ mol dm}^{-3} \text{ LiClO}_4$ and — $0.1 \text{ mol dm}^{-3} \text{ LiClO}_4$ only, at a silver-modified GC electrode (silver deposited at $-0.50 \text{ V vs Ag/Ag}^+$ for 50 s).

Initially, the nitrate reduction current has a peak potential of -1.179 V vs SCE in cycle 1, which gradually decreases in magnitude while simultaneously a second peak emerges with a peak potential of -0.90 V vs SCE . The peak current for this second peak continues to increase with repeated cycling and reaches a near steady state after about 30 cycles. At this point, the initial peak at -1.179 V vs SCE is no longer visible.

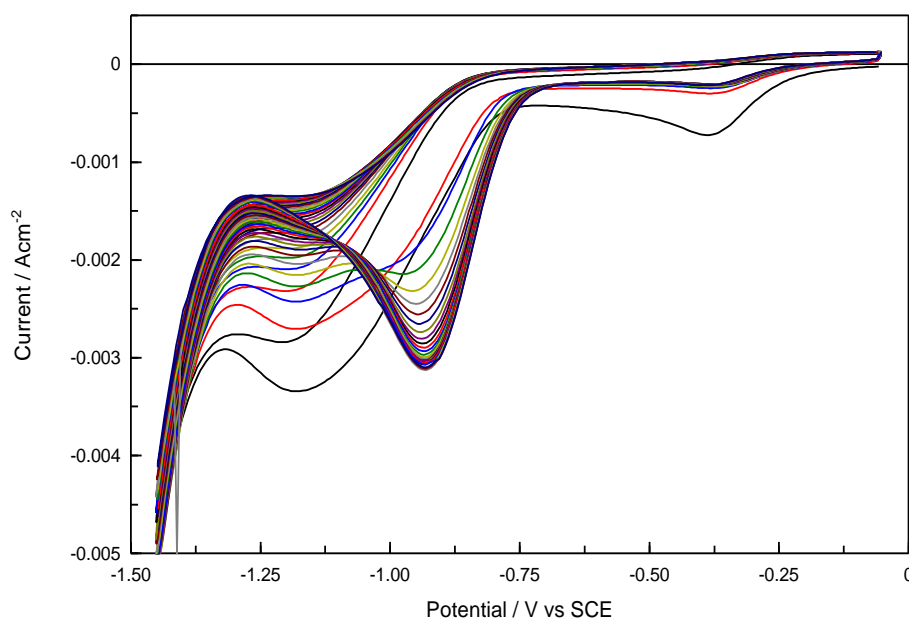


Figure 4.79: Cyclic voltammograms (30 cycles) recorded at a scan rate of 50 mV s^{-1} in a solution of $5.0 \times 10^{-3} \text{ mol dm}^{-3} \text{ KNO}_3$ and $0.1 \text{ mol dm}^{-3} \text{ LiClO}_4$ at a silver-modified GC electrode (silver deposited at $-0.50 \text{ V vs Ag/Ag}^+$ for 50 s).

In Figure 4.80, individual voltammograms from the 30 cycles are shown and these illustrate more clearly the significant changes observed upon repeated cycling. In cycle 1 and 2, there is no evidence of the second peak, however, the second peak emerges in cycle 5 and dominates the profile after approximately 15 cycles. On comparing cycle 1 with cycle 50, it is clear that there is a significant change in the voltammograms.

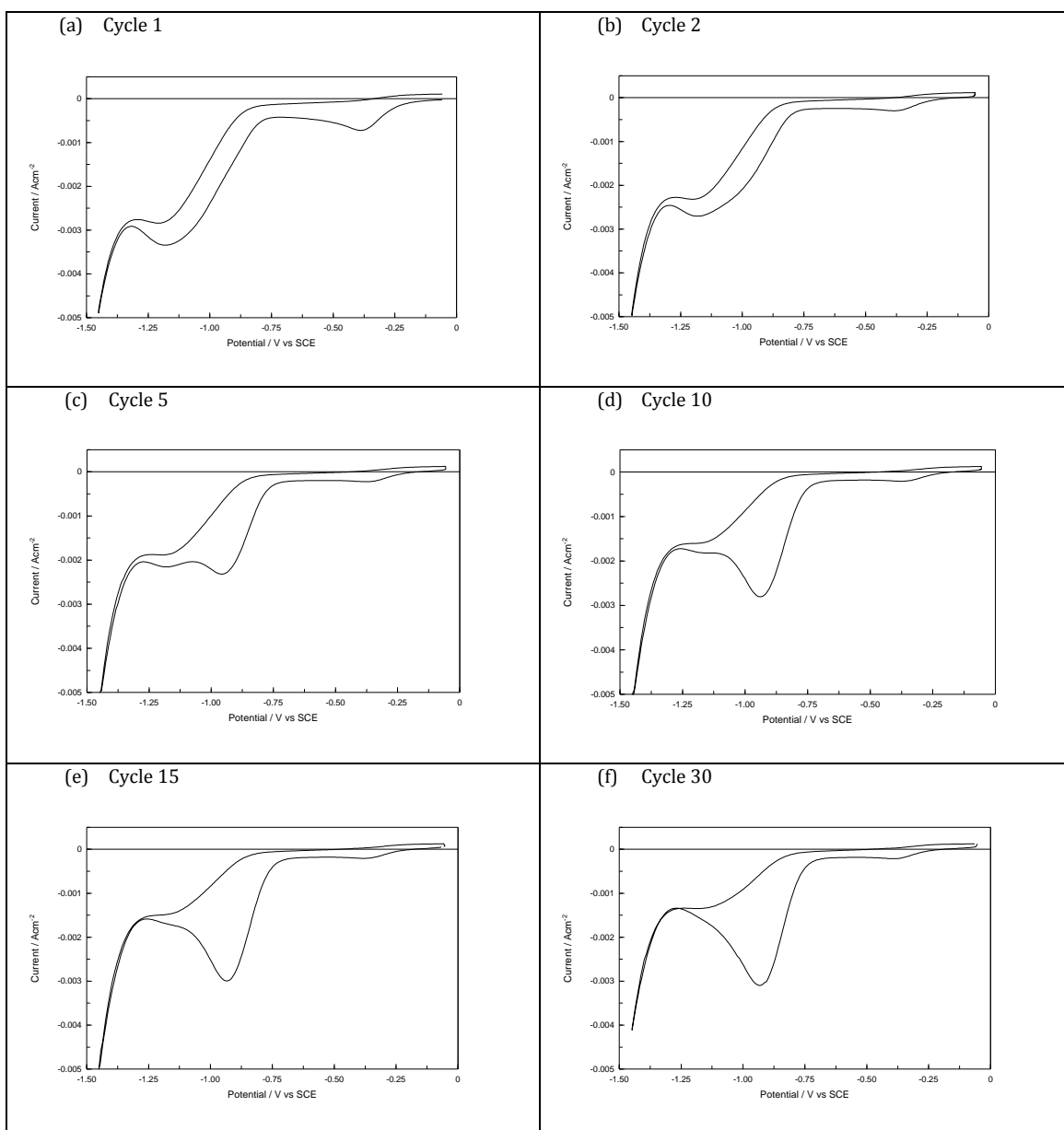


Figure 4.80: Cyclic voltammograms (cycles 1, 2, 5, 10, 15 and 30) at a scan rate of 50 mV s^{-1} in a solution of $5.0 \times 10^{-3} \text{ mol dm}^{-3} \text{ KNO}_3$ and $0.1 \text{ mol dm}^{-3} \text{ LiClO}_4$ at a silver-modified GC electrode (silver deposited at $-0.50 \text{ V vs Ag/Ag}^+$ for 50 s).

It is difficult to explain these significant changes in the voltammograms. Chebotareva and Nyokong observed the reduction of nitrate at a Cu phthalocyanine modified GC electrode and found one peak in the first scan and on second and subsequent scans this peak shifted to lower reduction potentials ⁽¹⁰³⁾. No real explanation for this was offered, only a reference to a paper published by Cattarin ⁽⁸¹⁾ which states that this observed changing peak shape upon cycling is not typical of a diffusion-limited process.

In order to determine if this was connected with the silver particles, the bulk silver electrode was cycled in a $5.0 \times 10^{-3} \text{ mol dm}^{-3} \text{ KNO}_3$ solution and the resulting CV are shown in Figure 4.81. A similar trend is observed at the bulk silver electrode although the initial peak at -1.25 V vs SCE is less prominent, as shown in Figure 4.81(a). In addition, it takes more cycling before the nitrate peak reaches a steady state. The peak current is plotted as a function of the cycle number in Figure 4.81(b). The current increases with cycle number and reaches a near steady state after approximately 30 cycles.

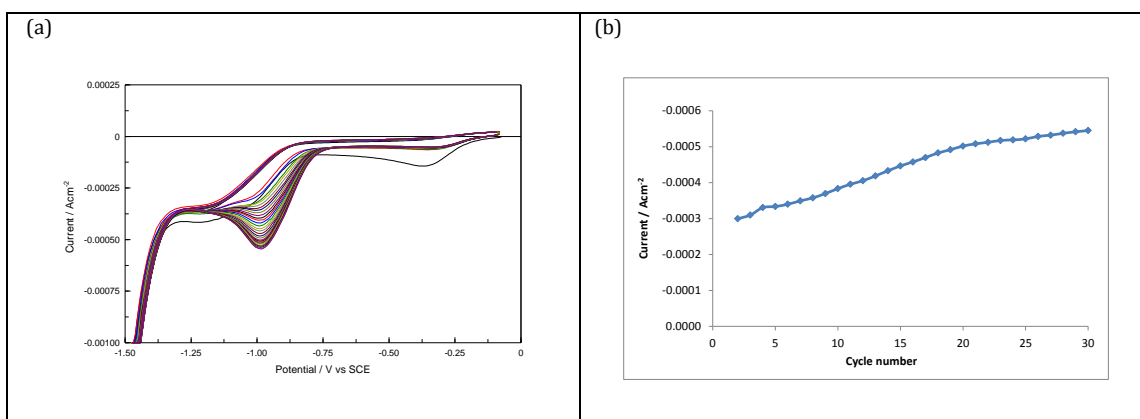


Figure 4.81: (a) Cyclic voltammograms (30 cycles) at a scan rate of 50 mV s^{-1} in a solution of $5.0 \times 10^{-3} \text{ mol dm}^{-3} \text{ KNO}_3$ and $0.1 \text{ mol dm}^{-3} \text{ LiClO}_4$ at a bulk silver electrode. (b) plot of peak current at -0.90 V vs SCE as a function of cycle number.

If this new emerging peak is due to new species being formed at the electrode surface then transferring the electrode to a fresh solution of nitrate should result in the peak potential returning to that observed in the first cycle. The silver-modified GC electrode was cycled in the $5.0 \times 10^{-3} \text{ mol dm}^{-3} \text{ KNO}_3$ solution for 30 cycles. This electrode was then transferred to a fresh $5.0 \times 10^{-3} \text{ mol dm}^{-3} \text{ KNO}_3$ solution and the CV's were recorded. The voltammograms recorded in the fresh solution are shown in Figure 4.82. Clearly, the same pattern is not observed as that seen in Figure 4.79. The emerging second peak is present from cycle 1 and the cycles reach a steady state after only a few cycles. This may point to changes to the electrode surface as the cause of the changing profile rather than the generation of any new species.

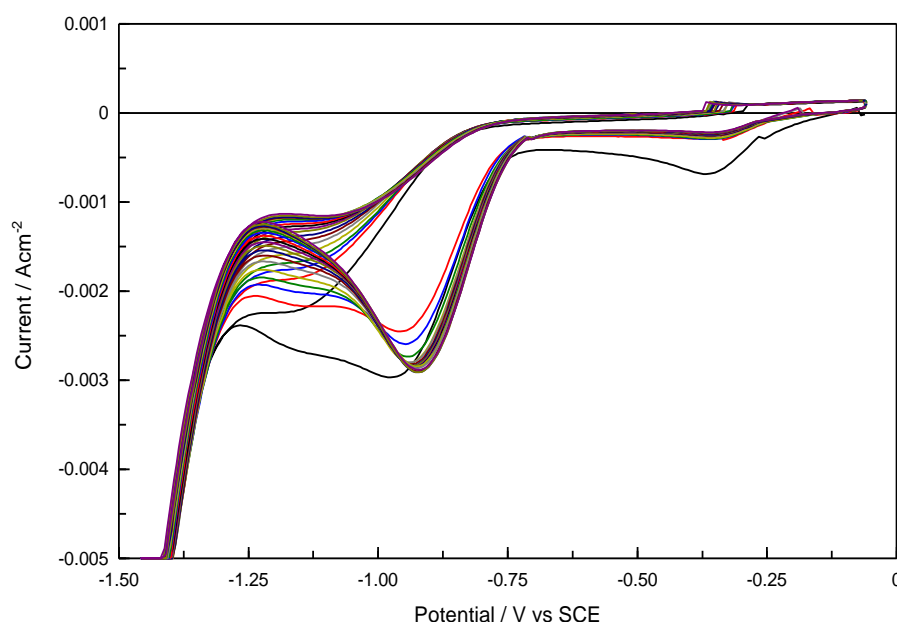


Figure 4.82: Cyclic voltammograms (30 cycles) at a scan rate of 50 mV s^{-1} in a fresh solution of $5.0 \times 10^{-3} \text{ mol dm}^{-3} \text{ KNO}_3$ and $0.1 \text{ mol dm}^{-3} \text{ LiClO}_4$ at a silver-modified GC electrode (silver deposited at $-0.50 \text{ V vs Ag/Ag}^+$ for 50 s).

This theory is further supported by the observed effect that cycling the electrode in the background solution ($0.1 \text{ mol dm}^{-3} \text{ LiClO}_4$) for different cycle numbers has on the subsequent developing nitrate profile. The silver-modified GC electrode was cycled in the background electrolyte for different cycle numbers and then transferred to the nitrate solution.

With no background cycling in LiClO_4 , Figure 4.83 (a), the emerging peak at -0.90 V vs SCE become larger in current than the initial peak at -1.17 V vs SCE after 15 cycles in the nitrate solution. However, after 30 background cycles, Figure 4.83 (b), the emerging peak dominates after only 5 cycles and after 60 background cycles, the second emerging peak is the major peak at cycle 1, Figure 4.83 (c). This is more clearly evident in Figure 4.83 (d) where the peak current for the second emerging nitrate reduction peak is plotted as a function of the number of cycles in the background electrolyte. The peak current reaches a near constant value of $3.0 \times 10^{-3}\text{ A cm}^{-2}$, however, this is achieved within a few cycles following 60 background cycles and requires approximately 15 cycles after the electrode is first cycled in the background electrolyte for 30 cycles.

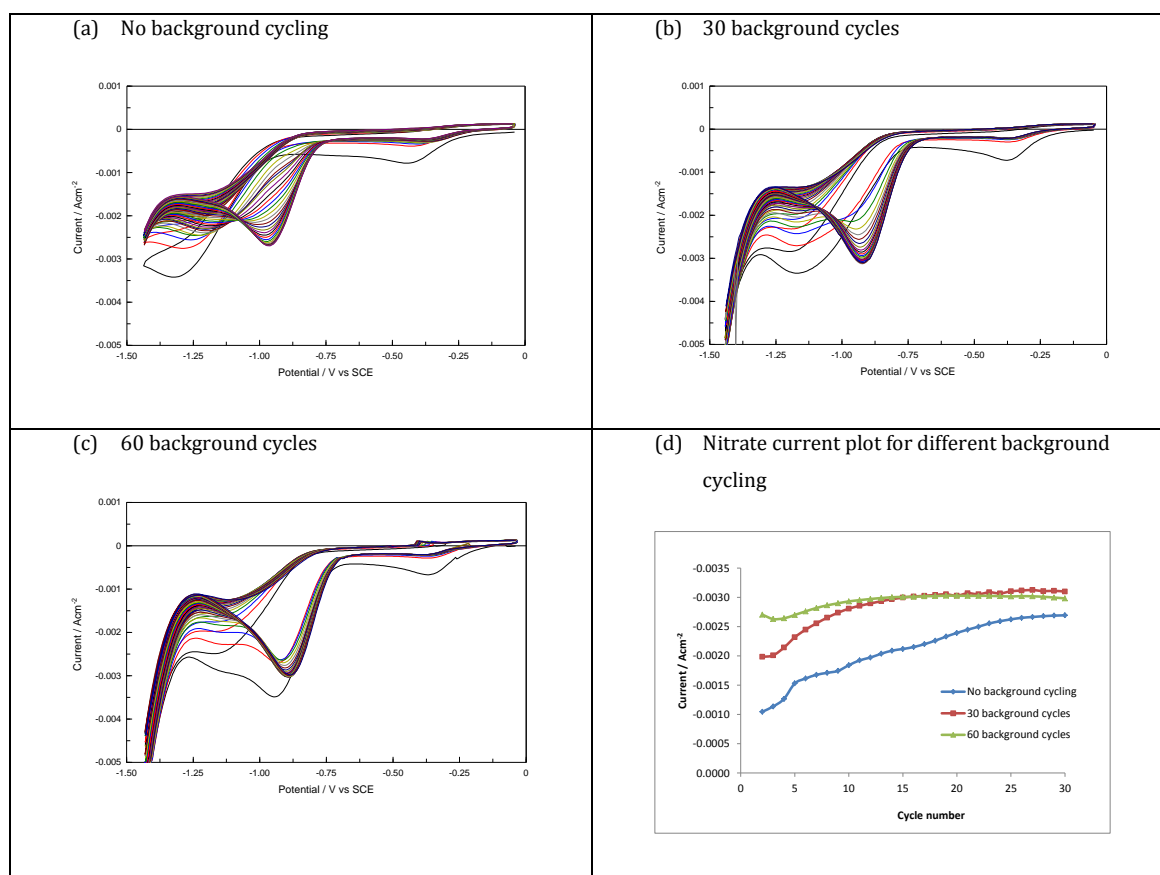


Figure 4.83: Cyclic voltammograms at a scan rate of 50 mV s^{-1} in a solution of $5.0 \times 10^{-3}\text{ mol dm}^{-3}\text{ KNO}_3$ and $0.1\text{ mol dm}^{-3}\text{ LiClO}_4$ at a silver-modified GC electrode (silver deposited at -0.50 V vs Ag/Ag^+ for 50 s) after different number of background cycles in $0.1\text{ mol dm}^{-3}\text{ LiClO}_4$.

It is clear that cycling the electrode through a reductive window influences the surface and consequently the nitrate peak. This type of 'activation' of the electrode surface has been used in other studies involving nitrate sensors. Shariar pre-treated a copper electrode by applying consecutive anodic and cathodic potential pulses to strip and redeposit copper atoms ⁽¹⁰⁴⁾. This resulted in a more defined nitrate reduction peak at much lower reduction potentials.

Next, the voltammograms were cycled between different potential limits to determine if the lower potential limit had any influence on the nitrate reduction wave. The silver-modified GC electrode was cycled from -0.05 V vs SCE to reductive potential limits of -1.25 V and -1.45 V vs SCE, as shown in Figure 4.84. It was found, as illustrated in Figure 4.84(a), that when the potential limit was reversed at -1.25 V vs SCE the emerging peak at -0.90 V vs SCE was slow to resolve, and even after 60 cycles in the background electrolyte and 30 cycles in the nitrate-containing solution the magnitude of the nitrate peak current was low. On reversing the potential at -1.45 V vs SCE, Figure 4.84(b), much higher peak currents are obtained for the second emerging peak. Indeed, if Figures 4.84(a) and (b) are compared, it is clear that the peak current for the emerging wave is only 52% of that obtained when the electrode is cycled to -1.45 V vs SCE. However, this effect of enhanced current with increased reductive limit is not permanent and, as shown in Figure 4.84(c), as the limit is returned to -1.25 V vs SCE, the peak current decays. In this case, the electrode was initially cycled to -1.45 V vs SCE to observe the emerging peak at -0.90 V vs SCE, and then the electrode was cycled to -1.25 V vs SCE. Figure 4.84 (d) traces the current magnitude for each of the potential windows to illustrate more clearly the changes in the peak current with cycle number.

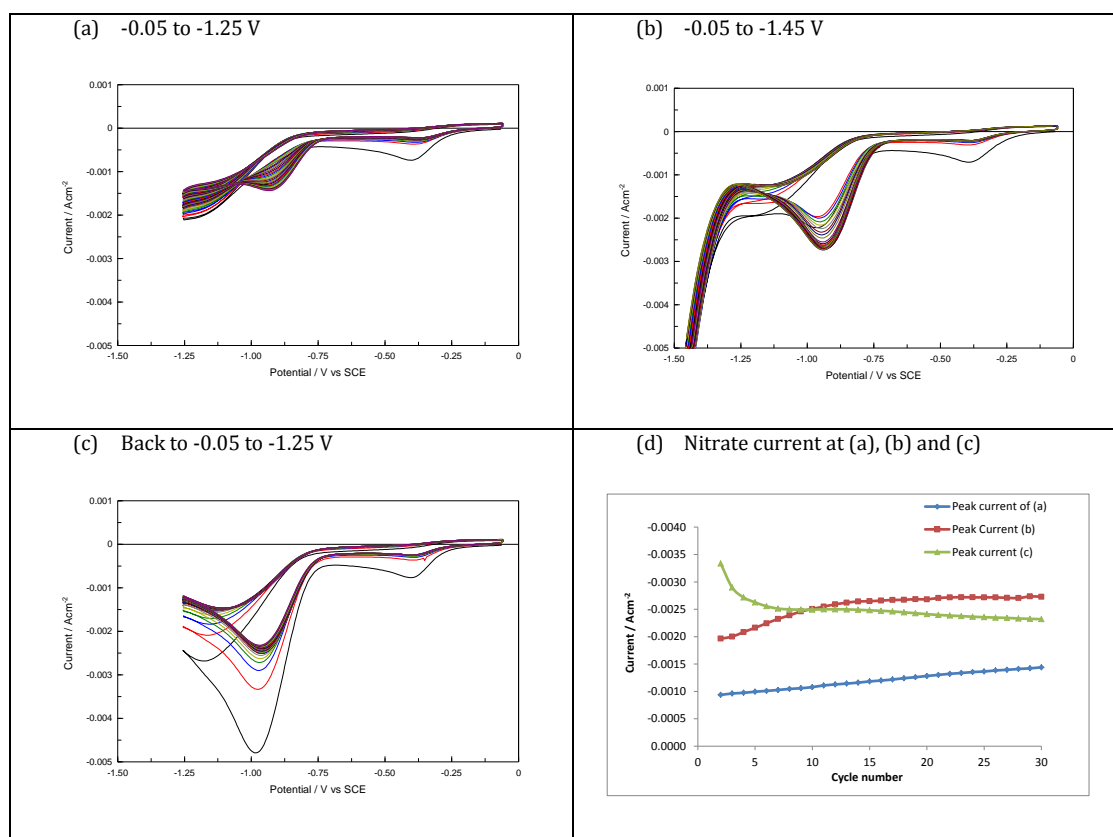
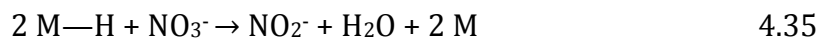
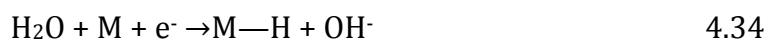


Figure 4.84: Cyclic voltammograms at a scan rate of 50 mV s⁻¹ in a solution of 5.0 × 10⁻³ mol dm⁻³ KNO₃ and 0.1 mol dm⁻³ LiClO₄ at a silver-modified GC electrode (silver deposited at -0.50 V vs Ag/Ag⁺ for 50 s) with different reductive potential limits.

It is often commented in the literature that hydrogen adsorption passivates the surface and hinders the cathodic process, but the observations in this work, and others, show that in order to reach a steady state and maximum current response it is essential to scan into the hydrogen evolution region. Nitrate reduction at precious metal cathodes generally corresponds to where hydrogen adsorption takes place. Since the heterogeneous reduction of nitrate with hydrogen gas involves adsorbed hydrogen atoms as a key intermediate as described by the reactions in Equations 4.33, 4.34 and 4.35, an analogous mechanism may be occurring electrochemically⁽¹⁰⁵⁾.



The scope of this work is limited to the analytical attributes of the silver-modified GC electrode and the mechanism involved is still speculative. As mentioned above, it is suggested in several reports that hydrogen inhibits the nitrate reduction due to competitive adsorption for active sites. However, it appears that scanning into the region of the hydrogen evolution reaction is important for maximum current output for nitrate. Indeed, as illustrated in Figure 4.85, the application of a constant potential of -1.45 V vs SCE for 2 min is sufficient to observe high currents for the nitrate peak at -0.90 V vs SCE.

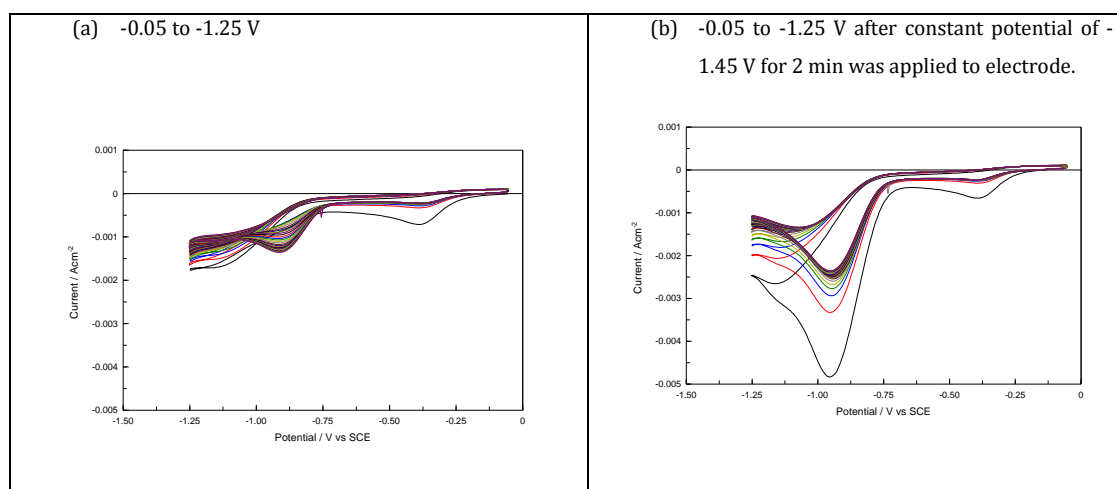


Figure 4.85: Cyclic voltammograms at a scan rate of 50 mV s⁻¹ in a solution of 5.0 × 10⁻³ mol dm⁻³ KNO₃ and 0.1 mol dm⁻³ LiClO₄ at a silver-modified GC electrode (silver deposited at -0.50 V vs Ag/Ag⁺ for 50 s). (a) electrode scanned from -0.05 to -1.25 V for 30 cycles, (b) electrode was first exposed to a constant potential of -1.45 V for 2 min and then cycled between -0.05 to -1.25 V vs SCE.

It may be concluded from Figures 4.85 and 4.86 that exposure to reduction potentials corresponding to hydrogen evolution are important for a good nitrate current response. As a result, the lower potential limit was extended further into the hydrogen evolution region and the upper potential was also varied. These experiments are summarised in Figure 4.86. The voltammograms recorded on cycling the electrode to potential limits of -1.25 V, -1.45 V, -1.65 V and -1.85 V vs SCE are shown in Figure 4.86(a), while the peak currents are plotted as a function of the lower potential limit in Figure 4.86(b). Clearly, further extension of the reductive potential limit does not enhance the signal further and if extended too far, the hydrogen evolution reaction becomes vigorous and the silver particles are destroyed (not shown). The influence of the upper potential limit is shown in Figure 4.86s (c) and (d). The silver-modified GC electrode was cycled between -1.25 V and upper potential limits of -0.05 V, -0.25 V, -0.45 V and -0.65 V vs SCE. The oxidative potential limit has a significant influence on the nitrate reduction peak at -0.90 V vs SCE and the peak current decreases in magnitude as the upper potential limit is varied from -0.05 V to -0.65 V vs SCE.

A similar change was observed by Casella and co-workers at a composite copper thallium electrode. They found that the signal disappeared almost completely with values more reductive than -0.60 V vs SCE ⁽⁷⁴⁾. The general interpretation of this observation is that the overall reduction process involves a preliminary adsorption step in the potential region between 0.0 V and -0.50 V vs SCE before a multi-step reduction process occurs at the more negative potentials. Therefore, the maximum peak current was achieved by selecting a potential window of -0.05 V to -1.45 V vs SCE.

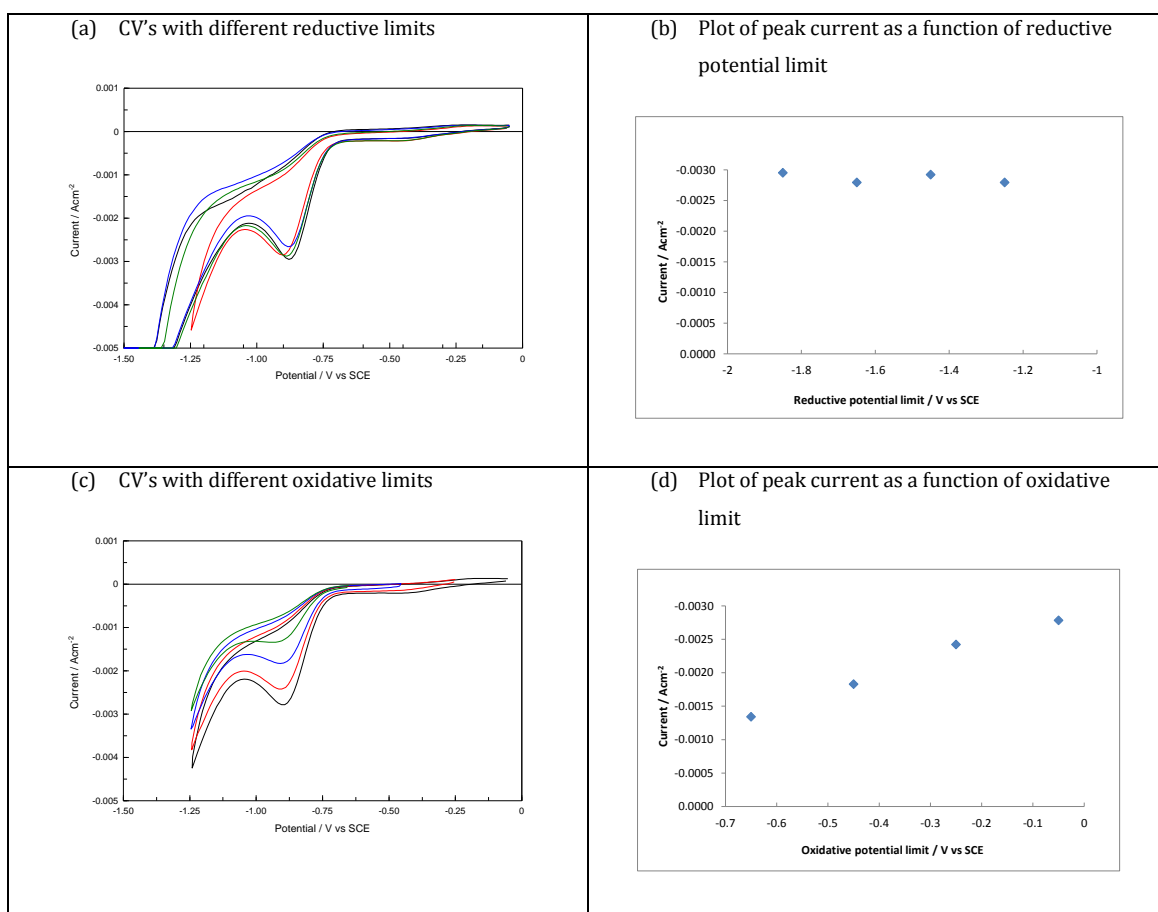


Figure 4.86: Cyclic voltammograms at a scan rate of 50 mV s^{-1} in a solution of $5.0 \times 10^{-3} \text{ mol dm}^{-3} \text{ KNO}_3$ and $0.1 \text{ mol dm}^{-3} \text{ LiClO}_4$ at a silver-modified GC electrode (silver deposited at $-0.50 \text{ V vs Ag/Ag}^+$ for 50 s) (a) and (b) oxidative limit fixed at -0.05 V vs SCE and reductive limit varied. (c) and (d) reductive limit fixed at -1.25 V vs SCE and oxidative limit varied.

4.3.9 Long-term Cycling

Figure 4.87 shows how the silver-modified GC electrode performs under extended periods of cycling, with the peak current plotted as a function of cycle number. Some of the CV's are shown in Figure 4.88. Initially, the current increases, but as the cycles progress the peak potential shifts and the current decreases before eventually reaching a near constant value of $2.2 \times 10^{-3} \text{ A cm}^{-2}$. The peak current remains fairly stable after 200 cycles with only small increases. Kim and colleagues noted that the peak current at a silver electrode decreases appreciably with repetitive cycling, indicating nitrate depletion ⁽²⁶⁾.

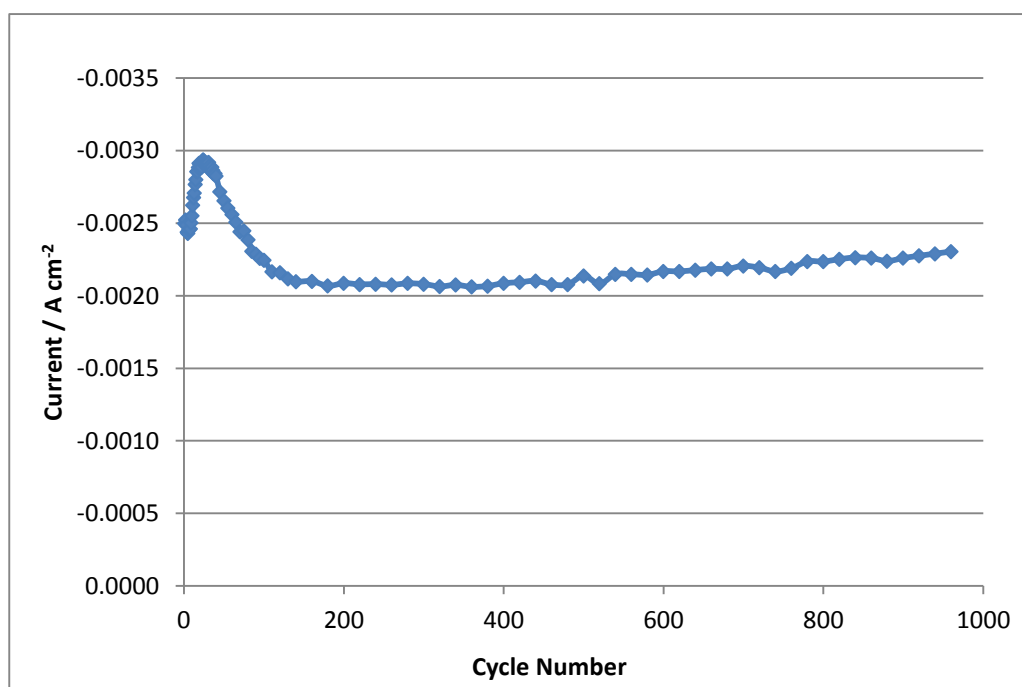


Figure 4.87: Peak current of cyclic voltammograms at a scan rate of 50 mV s^{-1} in a solution of $5.0 \times 10^{-3} \text{ mol dm}^{-3} \text{ KNO}_3$ and $0.1 \text{ mol dm}^{-3} \text{ LiClO}_4$ at a silver-modified GC electrode (silver deposited at -0.50 V vs Ag/Ag^+ for 50 s) over 1000 cycles.

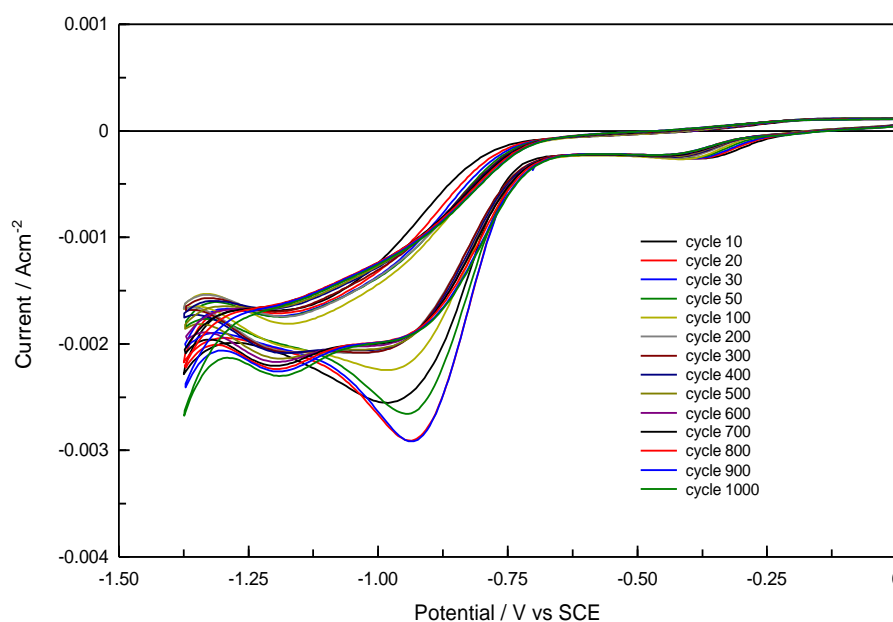


Figure 4.88: Cyclic voltammograms at a scan rate of 50 mV s^{-1} in a solution of $5.0 \times 10^{-3} \text{ mol dm}^{-3} \text{ KNO}_3$ and $0.1 \text{ mol dm}^{-3} \text{ LiClO}_4$ at a silver-modified GC electrode (silver deposited at -0.50 V vs Ag/Ag^+ for 50 s) 1000 cycles.

4.3.10 Interferences

A number of common interference species was chosen and their electrochemical behaviour at the silver-modified GC electrode was studied. Possible effects on the nitrate signal were examined over the potential window of the nitrate reduction reaction.

4.3.10.1 Nitrite Interference

Nitrite, the first product of the nitrate reduction reaction at almost any electrode, is an obvious choice as an interferent. The CV's, recorded in $5.0 \times 10^{-3} \text{ mol dm}^{-3} \text{ KNO}_3$ or $5.0 \times 10^{-3} \text{ mol dm}^{-3} \text{ NaNO}_2$, are shown in Figure 4.89. It is clear that silver is a poor catalyst for the nitrite reduction reaction compared to the reduction of nitrate. The peak for the nitrite reduction in the forward scan is centred around -1.12 V vs SCE with some reduction on the reverse wave. However, the peak current is considerably lower than that observed for the nitrate reduction reaction. The onset of the nitrite reduction clearly occurs at more reductive potentials than that observed for nitrate at silver.

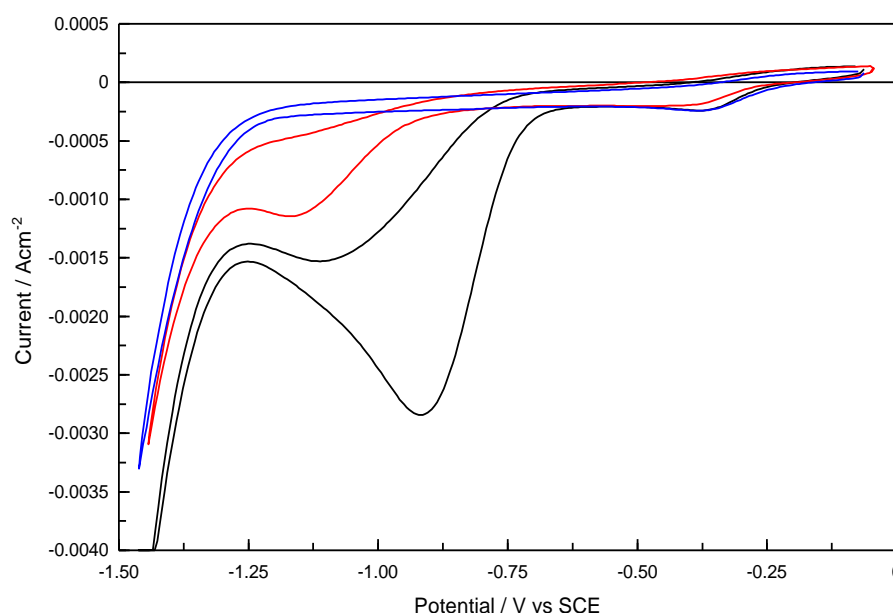


Figure 4.89: Cyclic voltammograms in a solution of — $5.0 \times 10^{-3} \text{ mol dm}^{-3} \text{ KNO}_3$, — $5.0 \times 10^{-3} \text{ mol dm}^{-3} \text{ NaNO}_2$ and — $0.1 \text{ mol dm}^{-3} \text{ LiClO}_4$ (background electrolyte) at a silver-modified GC electrode (silver deposited at -0.50 V vs Ag/Ag^+ for 50 s). Scan rate 50 mV s^{-1} .

However, depending on the concentrations of nitrite and nitrate, the signals may overlap which likely means differentiating between the two signals in a mixture of the compounds is problematic. Figures 4.90 and 4.91 show the effects on the nitrate reduction peak to increasing concentrations of NaNO_2 . The nitrite concentration was varied from $5.0 \times 10^{-4} \text{ mol dm}^{-3}$, which is lower than the nitrate concentration ($5.0 \times 10^{-3} \text{ mol dm}^{-3}$), to a higher concentration of $5.0 \times 10^{-2} \text{ mol dm}^{-3}$. At the lower concentrations of nitrite, there is a decrease in the nitrate reduction current possibly due to competitive adsorption for surface sites between the nitrate and nitrite. As the nitrite concentration is increased, the peak current for the nitrate reduction reaction increases, reaching a value of approximately $4.0 \times 10^{-3} \text{ A cm}^{-2}$ in the presence of $5.0 \times 10^{-2} \text{ mol dm}^{-3}$ nitrite. There is also a significant change in the position of the peak potential, varying from -0.90 V vs SCE in the absence of nitrite to -1.22 V vs SCE in the presence of $5.0 \times 10^{-2} \text{ mol dm}^{-3}$ nitrite. Clearly, the nitrite is an interferent.

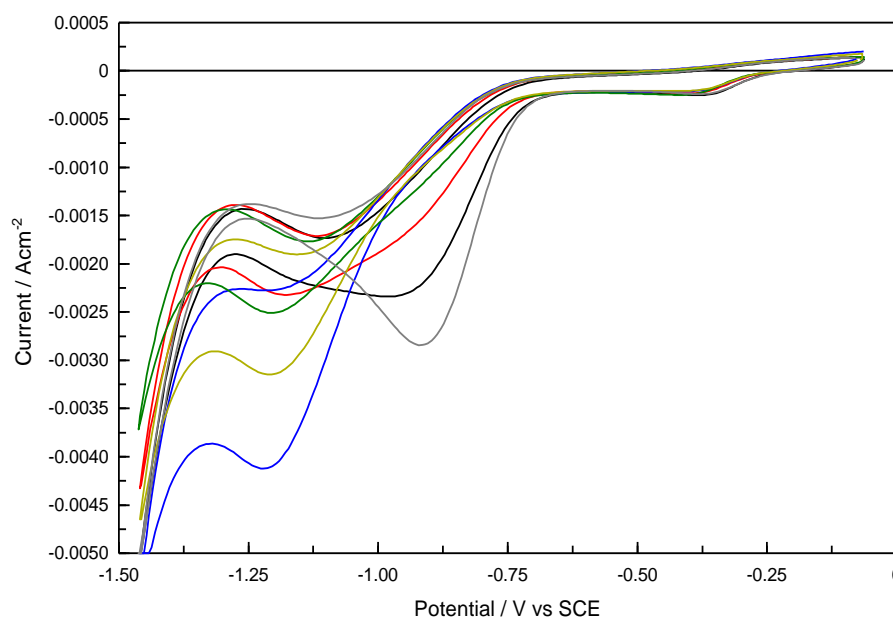


Figure 4.90: Cyclic voltammograms in a solution of $5.0 \times 10^{-3} \text{ mol dm}^{-3} \text{ KNO}_3$ and $0.1 \text{ mol dm}^{-3} \text{ LiClO}_4$ only and with increasing concentrations of NaNO_2 . — $5.0 \times 10^{-4} \text{ mol dm}^{-3}$, — $2.5 \times 10^{-3} \text{ mol dm}^{-3}$, — $5.0 \times 10^{-2} \text{ mol dm}^{-3}$, — $2.5 \times 10^{-2} \text{ mol dm}^{-3}$ and — $5.0 \times 10^{-2} \text{ mol dm}^{-3} \text{ NaNO}_2$ at a silver-modified GC electrode (silver deposited at $-0.50 \text{ V vs Ag/Ag}^+$ for 50 s). Scan rate 50 mV s^{-1} .

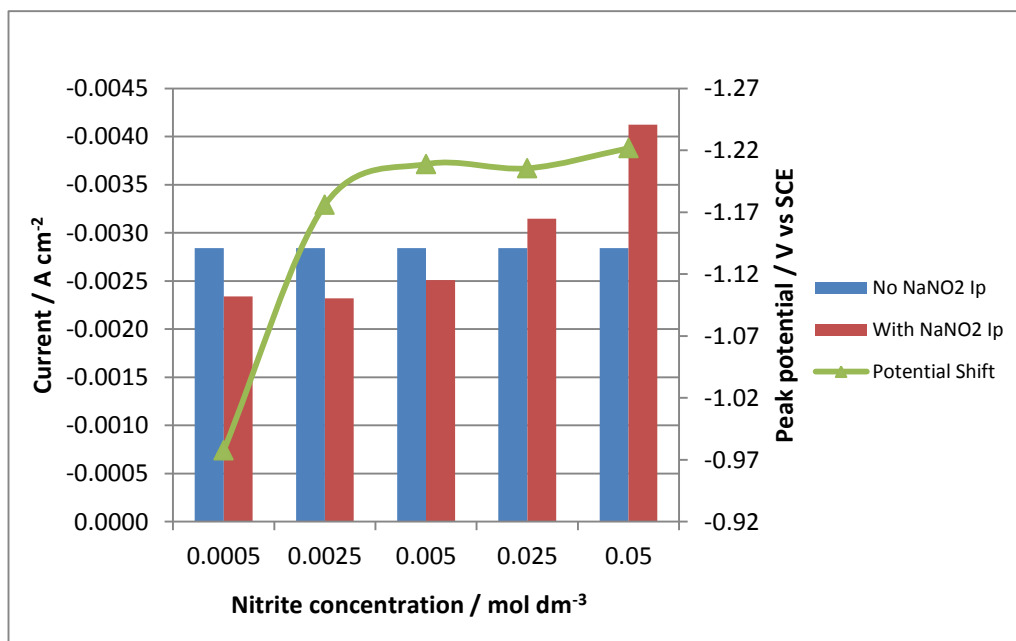


Figure 4.91: Peak currents from the CV's in Figure 4.90 in the ■ absence and ■ presence of various amounts of NaNO₂. The green trace represents the peak potential shift as a function of NaNO₂ concentration.

4.3.10.2 Chloride Interference

Chloride is another common interferent. Due to its strong adsorption properties it readily blocks the surface of the electrode to the intended analyte. Since an initial adsorption step is essential for nitrate reduction and given that chloride is a common anion found in most aquatic environments, its role as a possible interferent in the sensing of nitrate was studied.

In Figure 4.92, the CV's recorded for the silver-modified GC electrode in 5.0×10^{-3} mol dm⁻³ nitrate in the presence of chloride anions, with concentrations varying from 5.0×10^{-4} mol dm⁻³ to 5.0×10^{-2} mol dm⁻³, are shown. The effect of the chloride anion is shown more clearly in Figure 4.93, where the peak currents for the nitrate reduction reaction are plotted as a function of the chloride concentration and the peak potential is also shown as a function of the chloride concentration. It is clear from Figures 4.93 and 4.94 that even at low chloride concentrations, 10 times lower than the nitrate concentration, the peak current and potential of the nitrate reduction peak are significantly affected.

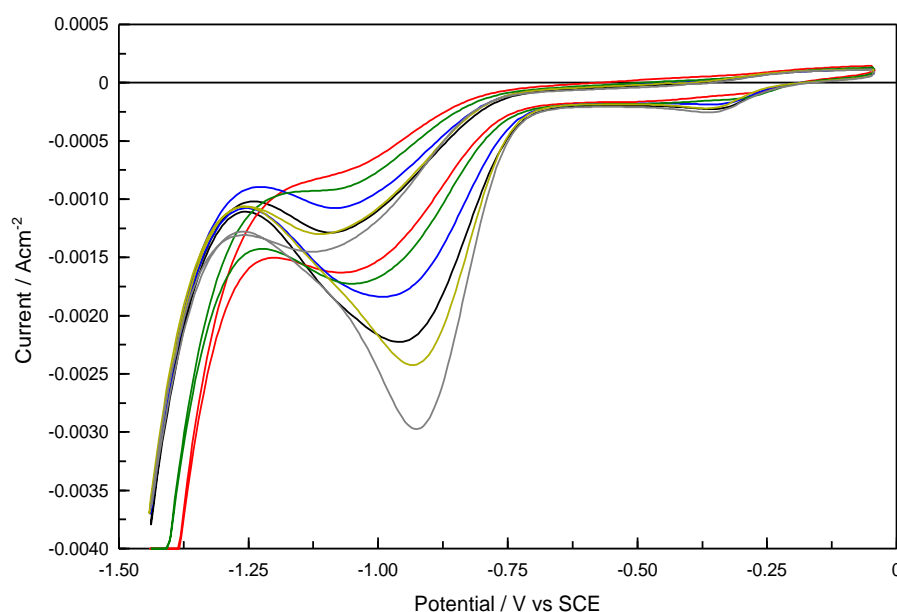


Figure 4.92: Cyclic voltammograms in a solution of $5.0 \times 10^{-3} \text{ mol dm}^{-3} \text{ KNO}_3$ and $0.1 \text{ mol dm}^{-3} \text{ LiClO}_4$ only and with increasing concentrations of KCl — $5.0 \times 10^{-4} \text{ mol dm}^{-3}$, — $2.5 \times 10^{-3} \text{ mol dm}^{-3}$, — $5.0 \times 10^{-2} \text{ mol dm}^{-3}$, — $2.5 \times 10^{-2} \text{ mol dm}^{-3}$ and — $5.0 \times 10^{-2} \text{ mol dm}^{-3}$ KCl at a silver-modified GC electrode (silver deposited at -0.50 V vs Ag/Ag^+ for 50 s). Scan rate 50 mV s^{-1} .

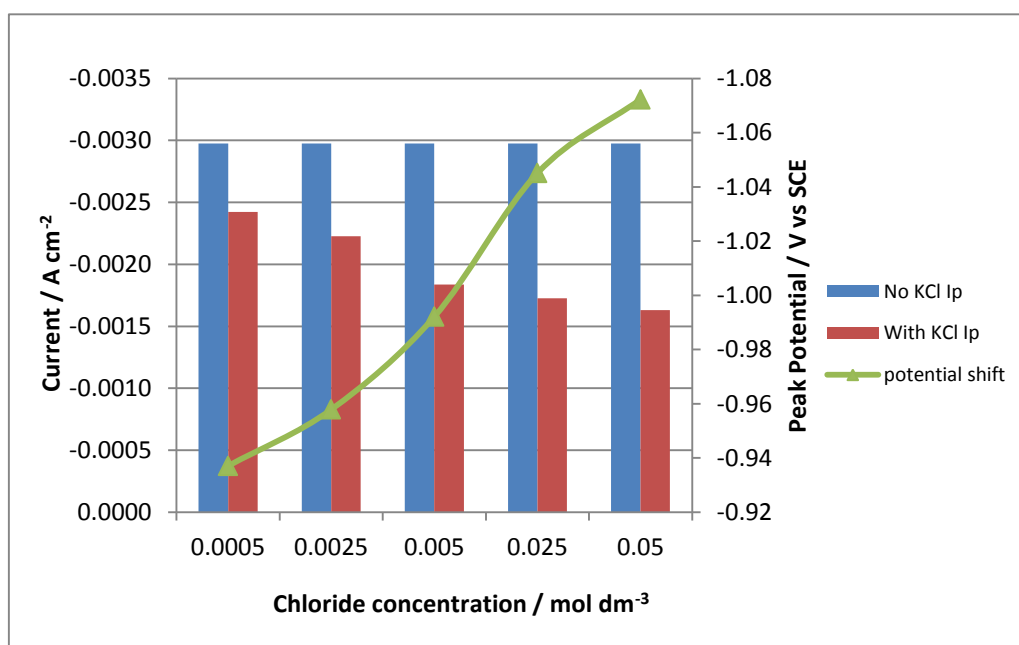


Figure 4.93: Peak currents from the CV's in Figure 4.92 in the ■ absence and ■ presence of various amounts of KCl. The green trace represents the peak potential shift as a function of KCl concentration.

Chloride interference during nitrate detection at other silver and copper electrodes has been examined by other groups and similar decreases have been observed (26,106). Inspection of the silver reduction peak at the beginning of the potential sweep, Figure 4.94, indicates that the silver itself is altered by the presence of the chloride anion as the peak is diminished in the presence of increasing amounts of chloride. Likely a layer of AgCl is formed on the surface of the particles.

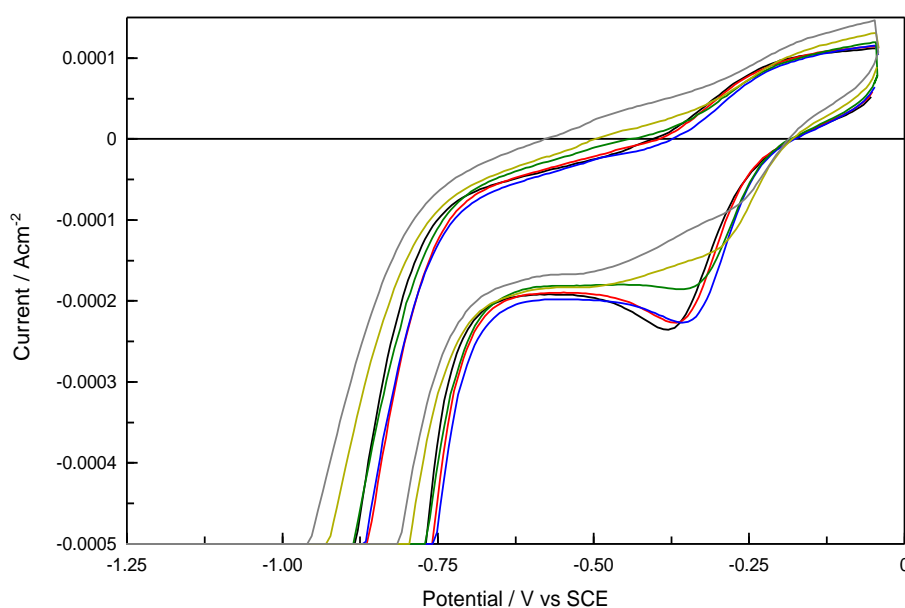


Figure 4.94: Figure 4.92 magnified to view the silver reduction peaks.

4.4 Summary of Results

In this chapter, silver nanoparticles were successfully deposited at a GC electrode (GC) and this electrode was used in the electrochemical detection of nitrates. The GC substrate was selected as the nitrate reduction reaction is not observed at a bare GC electrode.

The silver nanoparticles were deposited on a GC electrode using an electrochemical pulse technique. A double pulse technique was first employed as a means of achieving particles with a high degree of homogeneousness. An oxidation pulse of 1.0 V vs Ag/Ag⁺ was applied to clean the electrode, and then the double pulse was applied. The first step involved the application of a short pulse, E₁, for a short period of time to instantaneously nucleate nanoparticle seeds. Subsequently, a longer growth pulse, E₂, at a lower reduction potential was applied in order to grow these seeds into more established particles without further nucleation at fresh sites on the GC electrode. It appeared from the SEM micrographs that although many seed particles were produced during the nucleation pulse at E₁, many of these particles did not mature into stable particles during the growth pulse and most likely redissolved and deposited on more stable sites. Longer growth pulses not only resulted in larger particles but a lower density of particles. As E₁ was varied from -0.25 V to -1.00 V vs Ag/Ag⁺ the total number of particles increased and a relatively high level of polydispersity was observed.

The electrochemical detection of nitrates was studied at the silver particles deposited at the GC electrode using a 5.0 x 10⁻³ mol dm⁻³ KNO₃ solution. A broad peak was observed at approximately -0.90 V vs SCE indicating the reduction of nitrate at the silver-modified GC electrode. Longer growth pulses did not translate into higher reduction currents. For example, particles deposited at a longer growth pulse of 100 s, which are expected to have significantly more silver on the electrode compared to an electrode subjected to a growth pulse of 50 s, showed no improvement in the magnitude of the reduction current. It appears that the number or density of silver nanoparticles is more important than the quantity of silver in the detection of nitrates. Although the double pulse method results in a

well-defined nitrate reduction peak, the particles had a wide distribution of sizes and a single pulse method was applied in an attempt to lower the size distribution of the silver particles.

In the single pulse method, a cleaning pulse of 1.0 V vs SCE was also applied and the electrode was immersed, under open-circuit conditions, in the silver-containing solution for 60 min. Then, the reduction potential was applied and this was varied from -0.25 V, -0.50 V, -0.75 V to -1.0 V vs Ag/Ag⁺. This procedure, incorporating the immersion step, gave very good reproducibility. Furthermore, a high density of silver particles was observed at potentials from -0.50 V to -1.0 V vs Ag/Ag⁺. These applied potentials are sufficient for nucleation to occur during the entire pulse, giving progressive nucleation. Very few large particles were evident on the surface and the narrowest size distribution was achieved using the single pulse of -0.50 V vs Ag/Ag⁺ for 50 s.

However, similar CV's were recorded for the electrochemical detection of nitrates at the silver particles deposited using the single and double pulse methods. This indicates that the morphology of the silver deposited on the surface of the GC electrode has little influence on the catalytic ability of silver to reduce the nitrate ion. Stripping voltammograms were recorded to estimate the amount of silver deposited and, again, similar stripping voltammograms were recorded for the single and double pulse methods. However, as the single pulse method of -0.50 V vs Ag/Ag⁺ for 50 s gave excellent reproducibility, coupled with a homogenous deposition of silver with a narrow size distribution, this method was selected for the formation of the silver particles.

The current-time transients for the single pulse method recorded during the deposition of silver were analysed using the Scharifker and Hills model for two and three dimensional nucleation. The experimental and theoretical plots were compared and it was concluded that the experimental data agreed well with the progressive nucleation and 3D growth model.

The surface area of the electrodeposited particles was estimated using the underpotential deposition of lead and the reduction of surface oxides using cyclic voltammetry. For the underpotential deposition of lead, a full monolayer coverage was achieved using a $10.0 \times 10^{-3} \text{ mol dm}^{-3}$ solution of PbCl_2 dissolved in 0.1 mol dm^{-3} HCl and the potential was cycled between -0.49 V and -0.20 V vs SCE at a scan rate of 20 mV s^{-1} . Very good agreement was obtained between the surface areas computed using the oxide charges and lead underpotential deposition experiments. For example, the real surface area of a 2 mm diameter bulk silver electrode was calculated as 0.0543 cm^2 for the lead underpotential deposition and 0.0542 cm^2 for the charge of the oxide reduction reaction, giving a roughness factor of 1.73. The surface areas of the silver-modified GC electrode were calculated as 0.034 cm^2 following a 25 s deposition period, 0.069 cm^2 for a 50 s deposition period and increasing to 0.087 cm^2 and 0.104 cm^2 for deposition periods of 75 s and 100 s , respectively, using a single pulse of -0.50 V vs Ag/Ag^+ . These surface areas were used to normalise the currents recorded for the reduction of nitrates.

Cyclic voltammetry and constant potential amperometry experiments were used to generate calibration curves for the detection of nitrates at bulk silver and the silver-modified GC electrode. The silver particles were deposited at -0.50 V vs Ag/Ag^+ for 50 s to give the silver-modified GC electrode. Using the peak currents from the CV's of the bulk silver electrode, the linear regression equation was obtained as, $I_{\text{pc}} = -0.1094c_{\text{NO}_3^-}$, with a correlation coefficient of 0.9923 and a limit of detection of $3.9 \times 10^{-5} \text{ mol dm}^{-3}$. A limit of detection of $2.0 \times 10^{-5} \text{ mol dm}^{-3}$ and a much larger slope value of $-0.5312 \text{ A mol}^{-1} \text{ dm}^3$ was obtained for the silver-modified GC electrode, indicating that the silver deposited on a GC electrode is more sensitive to nitrate levels than a bulk crystalline silver electrode. The sensitivity of the sensor was increased 10 fold using constant potential amperometry and the limit of detection was calculated as $9.8 \times 10^{-6} \text{ mol dm}^{-3}$ for the silver-modified GC electrode. This level of detection falls well below the maximum concentration of $8.0 \times 10^{-4} \text{ mol dm}^{-3}$ of nitrate as set out by the EPA under the Nitrate Directive (91.676/EEC).

The influence of pH and the effects of different electrolytes on the reduction of nitrate were studied at the silver-modified GC electrode. Small changes in the magnitude of the peak currents were observed between pH values of 4.0 and 12.0, however, much higher peak currents were observed at lower pH values between 2.0 and 4.0. This was attributed to the adsorbed H⁺ ions on the surface, which are necessary for the reduction of nitrates. As the pH is increased, hydroxide ions occupy the active sites giving rise to lower peak currents for the reduction of nitrate. Similarly, alkaline solutions, such as NaOH and Na₂CO₃, exhibit low nitrate reduction currents, while KCl and Na₂SO₄ electrolytes show smaller currents compared to LiClO₄, which is probably due to the high adsorption properties of chloride and sulphate anions. The highest current was obtained in the acidic H₂SO₄ solution, however, the hydrogen reduction reaction observed with this solution gives rise to poor reproducibility.

The kinetics of the nitrate reduction reaction was studied at the silver-modified GC electrode. Using the Randles-Sevcik equation, the diffusion coefficient was calculated as $1.41 \times 10^{-5} \text{ cm}^2 \text{ s}^{-1}$. A non-zero intercept was obtained, consistent with the adsorption of the nitrate anion. The shape factor, $|E_p - E_{p1/2}|$, was computed as 113 mV to give a value for an' as 0.422. The value of an' was also computed using Tafel analysis, giving a value for an' of 0.423. A linear relationship between the peak potential and the logarithm of the scan rate was obtained, and using these data the rate constant for the reduction of nitrate was calculated as $9.79 \times 10^{-3} \text{ s}^{-1}$. The reaction order for the nitrate reduction reaction was obtained by plotting the logarithm of the peak current as a function of the logarithm of the nitrate concentration, to give a rate law with a reaction order of 0.736. This fractional reaction order is consistent with the adsorption of the nitrate anion. Rotating disc voltammetry was employed to study the hydrodynamics of the nitrate reduction reaction. Linear Levich plots were obtained; however, some deviation was noted at higher rotation rates. Using the slope of the linear portion of the Levich plot, the diffusion coefficient was calculated as $1.66 \times 10^{-5} \text{ cm}^2 \text{ s}^{-1}$, which was in excellent agreement with the value obtained using variations in the scan rate. The rate constant was calculated from the intercept of the Koutecky-Levich plot to give a value of 0.11 cm s^{-1} .

The CV's recorded in the nitrate solution were examined upon repetitive cycling, and surface changes were detected. Initially, the nitrate reduction peak potential occurs at about -1.179 V vs SCE in cycle 1, but this peak gradually decreases in magnitude while, simultaneously, a second peak emerges with a peak potential of -0.90 V vs SCE. The peak current for this second peak continues to increase with repeated cycling and reaches a near steady state after about 30 cycles. This was attributed to surface changes as opposed to variations in solution composition as a result of the nitrate reduction reaction. It was also found that it was necessary to scan into the hydrogen evolution region in order to obtain a maximum current for the nitrate reduction reaction.

The influence of nitrite and chloride anions on the electrochemical detection of nitrates was studied by adding nitrite or chloride anions of different concentrations to a nitrate solution. The addition of nitrites gave rise to lower peak currents and a significant change in the position of the peak potential, varying from -0.90 V vs SCE in the absence of nitrate to -1.22 V vs SCE in the presence of 5.0×10^{-2} mol dm⁻³ nitrate. Similarly, interference was observed in the presence of chloride anions. Significant changes in the peak potential and the peak currents were observed on the addition of chloride anions and this was attributed to the formation of AgCl on the surface of the silver nanoparticles.

4.5 References

1. M. Ueda, H. Dietz, A. Anders, H. Knepe, A. Meixner, W. Plieth, "Double-pulse technique as an electrochemical tool for controlling the preparation of metallic nanoparticles", *Electrochimica Acta*, **48**, 377, (2002).
2. J.T. Matsushima, L.C.D. Santos, A.B. Couto, M.R. Baldan, N.G. Ferreira, "Electrodeposition of Cu Nanoparticles on BDD Electrodes: Reactions and Nucleation Mechanism", *Journal of the Electrochemical Society*, **159**, D246, (2012).
3. Y. Wang, E. Laborda, C. Salter, A. Crossley, R.G. Compton, "Facile in situ characterization of gold nanoparticles on electrode surfaces by electrochemical techniques: average size, number density and morphology determination", *Analyst*, **137**, 4693, (2012).
4. A. Abbaspour, F. Norouz-Sarvestani, "High electrocatalytic effect of Au–Pd alloy nanoparticles electrodeposited on microwave assisted sol–gel-derived carbon ceramic electrode for hydrogen evolution reaction", *International Journal of Hydrogen Energy*, **38**, 1883, (2013).
5. A.A. Isse, S. Gottardello, C. Maccato, A. Gennaro, "Silver nanoparticles deposited on glassy carbon. Electrocatalytic activity for reduction of benzyl chloride", *Electrochemistry Communications*, **8**, 1707, (2006).
6. J. Ustarroz, U. Gupta, A. Hubin, S. Bals, H. Terryn, "Electrodeposition of Ag nanoparticles onto carbon coated TEM grids: A direct approach to study early stages of nucleation", *Electrochemistry Communications*, **12**, 1706, (2010).
7. A.O. Solak, P. Gülser, E. Gökm, F. Gökmeşe, "A New Differential Pulse Voltammetric Method for the Determination of Nitrate at a Copper Plated Glassy Carbon Electrode", *Microchimica Acta*, **134**, 77, (2000).
8. R. Sivasubramanian, M.V. Sangaranarayanan, "Detection of lead ions in picomolar concentration range using underpotential deposition on silver nanoparticles-deposited glassy carbon electrodes", *Talanta*, **85**, 2142, (2011).
9. V. Hernández-Ramírez, A. Alatorre-Ordaz, M.D.L. Yépez-Murrieta, J.G. Ibanez, C. Ponce-De-León, F.C. Walsh, "Oxidation of the Borohydride Ion at Silver Nanoparticles on a Glassy Carbon Electrode (GCE) Using Pulsed Potential Techniques", *ECS Transactions*, **20**, 211, (2009).
10. C.M. Welch, C.E. Banks, A.O. Simm, R.G. Compton, "Silver nanoparticle assemblies supported on glassy-carbon electrodes for the electro-analytical detection of hydrogen peroxide", *Analytical and Bioanalytical Chemistry*, **382**, 12, (2005).
11. A. Sheludko, G. Bliznakov, "Initial Stages of electrodeposition of metals. II", *Bulg. Acad. Sci. Phys. Inst.*, **2**, 227, (1952).
12. H. Liu, R.M. Penner, "Size-Selective Electrodeposition of Mesoscale Metal Particles in the Uncoupled Limit", *The Journal of Physical Chemistry B*, **104**, 9131, (2000).
13. H. Liu, F. Favier, K. Ng, M.P. Zach, R.M. Penner, "Size-selective electrodeposition of meso-scale metal particles: a general method", *Electrochimica Acta*, **47**, 671, (2001).
14. G. Gunawardena, G. Hills, I. Montenegro, "Electrochemical nucleation: Part II. The electrodeposition of silver on vitreous carbon", *Journal of Electroanalytical Chemistry and Interfacial Electrochemistry*, **138**, 241, (1982).
15. G.D. Adžić, D.M. Dražić, A.R. Despić, "A method of obtaining a small number of nucleation sites and growing large crystal grains", *Journal of Electroanalytical Chemistry and Interfacial Electrochemistry*, **239**, 107, (1988).
16. M. Miranda-Hernández, M. Palomar-Pardavé, N. Batina, I. González, "Identification of different silver nucleation processes on vitreous carbon surfaces from an ammonia electrolytic bath", *Journal of Electroanalytical Chemistry*, **443**, 81, (1998).

17. J.V. Zoval, R.M. Stiger, P.R. Biernacki, R.M. Penner, "Electrochemical deposition of silver nanocrystallites on the atomically smooth graphite basal plane", *Journal of Physical Chemistry*, **100**, 837, (1996).
18. G. Sandmann, H. Dietz, W. Plieth, "Preparation of silver nanoparticles on ITO surfaces by a double-pulse method", *Journal of Electroanalytical Chemistry*, **491**, 78, (2000).
19. M. Palomarpardave, M.T. Ramirez, I. Gonzalez, A. Serruya, B.R. Scharifker, "Silver electrocrystallization on vitreous carbon from ammonium hydroxide solutions", *Journal of the Electrochemical Society*, **143**, 1551, (1996).
20. Z.-B. Lin, B.-G. Xie, J.-S. Chen, J.-J. Sun, G.-N. Chen, "Nucleation mechanism of silver during electrodeposition on a glassy carbon electrode from a cyanide-free bath with 2-hydroxypyridine as a complexing agent", *Journal of Electroanalytical Chemistry*, **633**, 207, (2009).
21. T. Rapecki, A.M. Nowicka, M. Donten, F. Scholz, Z. Stojek, "Activity changes of glassy carbon electrodes caused by their exposure to OH center dot radicals", *Electrochemistry Communications*, **12**, 1531, (2010).
22. F.R. Bento, L.H. Mascaró, "Analysis of the initial stages of electrocrystallization of Fe, Co and Fe-Co alloys in chloride solutions", *Journal of the Brazilian Chemical Society*, **13**, 502, (2002).
23. B. Scharifker, G. Hills, "Theoretical and experimental studies of multiple nucleation", *Electrochimica Acta*, **28**, 879, (1983).
24. R. Greef, L.M. Peter, D. Pletcher, J. Robinson, *Instrumental Methods in Electrochemistry*; Horwood Publishing Limited, 1985.
25. G. Chang, J. Zhang, M. Oyama, K. Hirao, "Silver-Nanoparticle-Attached Indium Tin Oxide Surfaces Fabricated by a Seed-Mediated Growth Approach", *The Journal of Physical Chemistry B*, **109**, 1204, (2005).
26. D. Kim, I.B. Goldberg, J.W. Judy, "Chronocoulometric determination of nitrate on silver electrode and sodium hydroxide electrolyte", *Analyst*, **132**, 350, (2007).
27. O. Ghodbane, M. Sarrazin, L. Roué, D. Bélanger, "Electrochemical Reduction of Nitrate on Pyrolytic Graphite-Supported Cu and Pd-Cu Electrocatalysts", *Journal of the Electrochemical Society*, **155**, F117, (2008).
28. S. Trasatti, O.A. Petrii, "Real Surface Area Measurements in Electrochemistry", *Pure and Applied Chemistry*, **63**, 711, (1991).
29. D.a.J. Rand, R. Woods, "Determination of real surface area of palladium electrodes. Electrochemical oxidation of thin palladium films on gold. Comments", *Analytical Chemistry*, **47**, 1481, (1975).
30. A.J. Motheo, S.a.S. Machado, M.H. Van Kampen, J.R. Santos, "Electrochemical Determination of Roughness of Silver Electrode Surface", *Journal of the Brazilian Chemical Society*, **4**, 122, (1993).
31. M.O. Finot, G.D. Braybrook, M.T. Mcdermott, "Characterization of electrochemically deposited gold nanocrystals on glassy carbon electrodes", *Journal of Electroanalytical Chemistry*, **466**, 234, (1999).
32. S. Dong, Q. Qiu, "Novel deposition of lead on a glassy carbon electrode and its electrocatalytic reduction of dioxygen", *Journal of Electroanalytical Chemistry and Interfacial Electrochemistry*, **314**, 331, (1991).
33. V. Sudha, M.V. Sangaranarayanan, "Underpotential deposition of metals – Progress and prospects in modelling", *Journal of Chemical Sciences*, **117**, 207, (2005).
34. D.M. Kolb, M. Przasnyski, H. Gerischer, "Underpotential deposition of metals and work function differences", *Journal of Electroanalytical Chemistry and Interfacial Electrochemistry*, **54**, 25, (1974).

35. P. Delahay, C.W. Tobias, H. Gerischer, *Advances in Electrochemistry and Electrochemical Engineering*; Wiley, 1978.
36. L.-L. Fang, Q. Tao, M.-F. Li, L.-W. Liao, D. Chen, Y.-X. Chen, "Determination of the Real Surface Area of Palladium Electrode", *Chinese Journal of Chemical Physics*, **23**, 543, (2010).
37. E.A. Streltsov, S.K. Poznyak, N.P. Osipovich, "Photoinduced and dark underpotential deposition of lead on selenium", *Journal of Electroanalytical Chemistry*, **518**, 103, (2002).
38. A.H. Creus, P. Carro, S. González, R.C. Salvarezza, A.J. Arvia, "A New Electrochemical Method for Determining the Fractal Dimension of the Surface of Rough Metal Electrodeposits: Its Application to Dendritic Silver Surfaces", *Journal of the Electrochemical Society*, **139**, 1064, (1992).
39. E. Kirowa-Eisner, Y. Bonfil, D. Tzur, E. Gileadi, "Thermodynamics and kinetics of upd of lead on polycrystalline silver and gold", *Journal of Electroanalytical Chemistry*, **552**, 171, (2003).
40. G.A. Ragoisha, A.S. Bondarenko, N.P. Osipovich, E.A. Streltsov, "Potentiodynamic electrochemical impedance spectroscopy: lead underpotential deposition on tellurium", *Journal of Electroanalytical Chemistry*, **565**, 227, (2004).
41. E. Kirowa-Eisner, D. Tzur, E. Gileadi, "Underpotential dissolution of metals under conditions of partial mass-transport control", *Journal of Electroanalytical Chemistry*, **621**, 146, (2008).
42. V. Bansal, V. Li, A.P. O'mullane, S.K. Bhargava, "Shape dependent electrocatalytic behaviour of silver nanoparticles", *CrystEngComm*, **12**, 4280, (2010).
43. D.F. Yancey, L. Zhang, R.M. Crooks, G. Henkelman, "Au@Pt dendrimer encapsulated nanoparticles as model electrocatalysts for comparison of experiment and theory", *Chemical Science*, **3**, 1033, (2012).
44. J. Sackmann, A. Bunk, R.T. Pötzschke, G. Staikov, W.J. Lorenz, "Combined in situ SPM and EIS studies of Pb UPD on Ag(111) and Ag(100)", *Electrochimica Acta*, **43**, 2863, (1998).
45. U. Schmidt, S. Vinzelberg, G. Staikov, "Pb UPD on Ag(100) and Au(100) — 2D phase formation studied by in situ STM", *Surface Science*, **348**, 261, (1996).
46. E. Kirowa-Eisner, R. Gepshtein, E. Gileadi, "Effect of diffusion in underpotential deposition: Simulated and experimental results", *Journal of Electroanalytical Chemistry*, **583**, 273, (2005).
47. Y. Bonfil, M. Brand, E. Kirowa-Eisner, "Characteristics of subtractive anodic stripping voltammetry of Pb and Cd at silver and gold electrodes", *Analytica Chimica Acta*, **464**, 99, (2002).
48. J.T. Hupp, D. Larkin, M.J. Weaver, "The influence of lead underpotential deposition on the capacitance of the silver-aqueous interface", *Journal of Electroanalytical Chemistry and Interfacial Electrochemistry*, **131**, 299, (1982).
49. M. Łukaszewski, A. Czerwiński, "Electrochemical preparation and characterization of thin deposits of Pd-noble metal alloys", *Thin Solid Films*, **518**, 3680, (2010).
50. E.B. Yeager, A.J. Salkind, *Techniques of Electrochemistry*; John Wiley & Sons Canada, Limited, 1972.
51. A. Hamelin, S. Morin, J. Richer, J. Lipkowski, "Adsorption of pyridine on the (311) face of silver", *Journal of Electroanalytical Chemistry and Interfacial Electrochemistry*, **285**, 249, (1990).
52. S. Trasatti, O.A. Petrii, "Real surface area measurements in electrochemistry", *Journal of Electroanalytical Chemistry*, **327**, 353, (1992).

53. V.D. Jovic, B.M. Jovic, "Underpotential deposition of cadmium onto Cu(111) and Cu(110) from chloride containing solutions", *Journal of the Serbian Chemical Society*, **66**, 345, (2001).
54. N.P. Osipovich, S.K. Poznyak, "Underpotential deposition of cadmium adatoms on Te and CdTe", *Electrochimica Acta*, **52**, 996, (2006).
55. V.D. Jović, B.M. Jović, "Underpotential deposition of cadmium onto (111) face of silver from chloride containing solution", *Electrochimica Acta*, **47**, 1777, (2002).
56. F.W. Campbell, R.G. Compton, "Contrasting Underpotential Depositions of Lead and Cadmium on Silver Macroelectrodes and Silver Nanoparticle Electrode Arrays", *International Journal of Electrochemical Science*, **5**, 407, (2010).
57. M. Innocenti, C. Zafferoni, A. Lavacchi, L. Becucci, F. Di Benedetto, E. Carretti, F. Vizza, M.L. Foresti, "Electroactivation of Microparticles of Silver on Glassy Carbon for Oxygen Reduction and Oxidation Reactions", *Journal of the Electrochemical Society*, **161**, D3018, (2014).
58. C.-L. Lee, Y.-L. Tsai, C.-H. Huang, K.-L. Huang, "Performance of silver nanocubes based on electrochemical surface area for catalyzing oxygen reduction reaction", *Electrochemistry Communications*, **29**, 37, (2013).
59. M.C. Dos Santos, S.a.S. Machado, "Electrochemical deposition of the first Cd monolayer on polycrystalline Pt and Au electrodes. An Upd study", *Journal of the Brazilian Chemical Society*, **9**, 211, (1998).
60. Y. Tang, T.E. Furtak, "Study of underpotential deposition of metals using the quartz crystal microbalance", *Electrochimica Acta*, **36**, 1873, (1991).
61. D.A. Skoog, F.J. Holler, S.R. Crouch, *Principles of Instrumental Analysis*; Thomson Brooks/Cole, 2007.
62. M.J. Moorcroft, J. Davis, R.G. Compton, "Detection and determination of nitrate and nitrite: a review", *Talanta*, **54**, 785, (2001).
63. J. Davis, M.J. Moorcroft, S.J. Wilkins, R.G. Compton, M.F. Cardosi, "Electrochemical detection of nitrate and nitrite at a copper modified electrode", *Analyst*, **125**, 737, (2000).
64. D. Quan, J.N. Shim, J.D. Kim, H.S. Park, G.S. Cha, H. Nam, "Electrochemical determination of nitrate with nitrate reductase-immobilized electrodes under ambient air", *Analytical Chemistry*, **77**, 4467, (2005).
65. K.M. Miranda, M.G. Espey, D.A. Wink, "A Rapid, Simple Spectrophotometric Method for Simultaneous Detection of Nitrate and Nitrite", *Nitric Oxide*, **5**, 62, (2001).
66. I.M.P.L.V.O. Ferreira, S. Silva, "Quantification of residual nitrite and nitrate in ham by reverse-phase high performance liquid chromatography/diode array detector", *Talanta*, **74**, 1598, (2008).
67. A. González-Bellavista, J. Macanás, M. Muñoz, E. Fabregas, "Sulfonated poly(ether ether ketone), an ion conducting polymer, as alternative polymeric membrane for the construction of anion-selective electrodes", *Sensors and Actuators B: Chemical*, **125**, 100, (2007).
68. G. Jiao, S.H. Lips, "Nitrate Assay by Multiple Wavelength Spectroscopy and Analysis of Kinetic Parameters of Net Nitrate Uptake by Barley Seedlings", *Journal of Plant Nutrition*, **23**, 79, (2000).
69. S. Kage, K. Kudo, N. Ikeda, "Determination of nitrate in blood by gas chromatography and gas chromatography-mass spectrometry", *Journal of Chromatography B: Biomedical Sciences and Applications*, **742**, 363, (2000).
70. S.-E. Bae, K.L. Stewart, A.A. Gewirth, "Nitrate Adsorption and Reduction on Cu(100) in Acidic Solution", *Journal of the American Chemical Society*, **129**, 10171, (2007).

71. B.K. Simpson, D.C. Johnson, "Electrocatalysis of Nitrate Reduction at Copper-Nickel Alloy Electrodes in Acidic Media", *Electroanalysis*, **16**, 532, (2004).
72. L. Mattarozzi, S. Cattarin, N. Comisso, P. Guerriero, M. Musiani, L. Vázquez-Gómez, E. Verlato, "Electrochemical reduction of nitrate and nitrite in alkaline media at CuNi alloy electrodes", *Electrochimica Acta*, **89**, 488, (2013).
73. D. Reyter, D. Bélanger, L. Roué, "Study of the electroreduction of nitrate on copper in alkaline solution", *Electrochimica Acta*, **53**, 5977, (2008).
74. I.G. Casella, M. Gatta, "Electrochemical reduction of NO_3^- and NO_2^- on a composite copper thallium electrode in alkaline solutions", *Journal of Electroanalytical Chemistry*, **568**, 183, (2004).
75. D. De, J.D. Englehardt, E.E. Kalu, "Cyclic voltammetric studies of nitrate and nitrite ion reduction at the surface of iridium-modified carbon fiber electrode", *Journal of the Electrochemical Society*, **147**, 4224, (2000).
76. L. Taniguchi, N. Nakashima, K. Yasukouchi, "Reduction of nitrate to give hydroxylamine at a mercury electrode using cobalt(III)-and nickel(II)-cyclams as catalysts", *Journal of the Chemical Society, Chemical Communications*, 1814, (1986).
77. Y. Wang, J. Qu, R. Wu, P. Lei, "The electrocatalytic reduction of nitrate in water on Pd/Sn-modified activated carbon fiber electrode", *Water Research*, **40**, 1224, (2006).
78. M.T. De Groot, M.T.M. Koper, "The influence of nitrate concentration and acidity on the electrocatalytic reduction of nitrate on platinum", *Journal of Electroanalytical Chemistry*, **562**, 81, (2004).
79. E.B. Molodkina, I.G. Botryakova, A.I. Danilov, J. Souza-Garcia, J.M. Feliu, "Kinetics and mechanism of nitrate and nitrite electroreduction on Pt(100) electrodes modified by copper adatoms", *Russian Journal of Electrochemistry*, **49**, 285, (2013).
80. G.E. Badea, "Electrocatalytic reduction of nitrate on copper electrode in alkaline solution", *Electrochimica Acta*, **54**, 996, (2009).
81. S. Cattarin, "Electrochemical reduction of nitrogen oxyanions in 1 M sodium hydroxide solutions at silver, copper and CuInSe₂ electrodes", *Journal of Applied Electrochemistry*, **22**, 1077, (1992).
82. A.J. Bard, L.R. Faulkner, *Electrochemical Methods: Fundamentals and Applications*; Masson, 1982.
83. A.J. Bard, Faulkner L.R., *Electrochemical methods: Fundamentals and Applications*; 2nd ed. ed.; Wiley, 2000.
84. E. Laviron, "General expression of the linear potential sweep voltammogram in the case of diffusionless electrochemical systems", *Journal of Electroanalytical Chemistry and Interfacial Electrochemistry*, **101**, 19, (1979).
85. A.L. Eckermann, D.J. Feld, J.A. Shaw, T.J. Meade, "Electrochemistry of redox-active self-assembled monolayers", *Coordination Chemistry Reviews*, **254**, 1769, (2010).
86. I. Taurino, S. Carrara, M. Giorcelli, A. Tagliaferro, G. De Micheli, "Comparison of two different carbon nanotube-based surfaces with respect to potassium ferricyanide electrochemistry", *Surface Science*, **606**, 156, (2012).
87. N. Aouina, H. Cachet, C. Debiemme-Chouvy, T.T.M. Tran, "Insight into the electroreduction of nitrate ions at a copper electrode, in neutral solution, after determination of their diffusion coefficient by electrochemical impedance spectroscopy", *Electrochimica Acta*, **55**, 7341, (2010).
88. M.R. Gartia, B. Braunschweig, T.-W. Chang, P. Moinzadeh, B.S. Minsker, G. Agha, A. Wieckowski, L.L. Keefer, G.L. Liu, "The microelectronic wireless nitrate sensor network for environmental water monitoring", *Journal of Environmental Monitoring*, **14**, 3068, (2012).

89. B. Hafezi, M.R. Majidi, "A sensitive and fast electrochemical sensor based on copper nanostructures for nitrate determination in foodstuffs and mineral waters", *Analytical Methods*, **5**, 3552, (2013).
90. M. Li, C. Feng, Z. Zhang, X. Lei, R. Chen, Y. Yang, N. Sugiura, "Simultaneous reduction of nitrate and oxidation of by-products using electrochemical method", *Journal of Hazardous Materials*, **171**, 724, (2009).
91. T. Öznülüer, B. Özdurak, H. Öztürk Doğan, "Electrochemical reduction of nitrate on graphene modified copper electrodes in alkaline media", *Journal of Electroanalytical Chemistry*, **699**, 1, (2013).
92. D. De, J.D. Englehardt, E.E. Kalu, "Electroreduction of nitrate and nitrite ion on a platinum-group-metal catalyst-modified carbon fiber electrode - Chronoamperometry and mechanism studies", *Journal of the Electrochemical Society*, **147**, 4573, (2000).
93. B.A. Korgel, H.G. Monbouquette, "Quantum confinement effects enable photocatalyzed nitrate reduction at neutral pH using CdS nanocrystals", *Journal of Physical Chemistry B*, **101**, 5010, (1997).
94. G.E. Dima, A.C.A. De Voos, M.T.M. Koper, "Electrocatalytic reduction of nitrate at low concentration on coinage and transition-metal electrodes in acid solutions", *Journal of Electroanalytical Chemistry*, **554–555**, 15, (2003).
95. M. Fedurco, P. Kedzierzawski, J. Augustynski, "Effect of multivalent cations upon reduction of nitrate ions at the Ag electrode", *Journal of the Electrochemical Society*, **146**, 2569, (1999).
96. K. Fajerweg, V. Ynam, B. Chaudret, V. Garçon, D. Thouron, M. Comtat, "An original nitrate sensor based on silver nanoparticles electrodeposited on a gold electrode", *Electrochemistry Communications*, **12**, 1439, (2010).
97. A. Sivanesan, P. Kannan, S. Abraham John, "Electrocatalytic oxidation of ascorbic acid using a single layer of gold nanoparticles immobilized on 1,6-hexanedithiol modified gold electrode", *Electrochimica Acta*, **52**, 8118, (2007).
98. J.G. Velasco, "Determination of standard rate constants for electrochemical irreversible processes from linear sweep voltammograms", *Electroanalysis*, **9**, 880, (1997).
99. I.U. Haque, M. Tariq, "Voltammetry of Nitrate at Solid Cathodes", *ECS Transactions*, **16**, 25, (2009).
100. L.A. Estudillo-Wong, E.M. Arce-Estrada, N. Alonso-Vante, A. Manzo-Robledo, "Electroreduction of nitrate species on Pt-based nanoparticles: Surface area effects", *Catalysis Today*, **166**, 201, (2011).
101. Davenport R. J, D.C. Johnson, "Voltammetric Determination of Nitrate and Nitrite ions using a Rotating Cadmium disk Electrode", *Analytical Chemistry*, **45**, 1979, (1973).
102. S. Ureta-Zañartu, C. Yáñez, "Electroreduction of nitrate ion on Pt, Ir and on 70:30 Pt:Ir alloy", *Electrochimica Acta*, **42**, 1725, (1997).
103. N. Chebotareva, T. Nyokong, "Metallophthalocyanine catalysed electroreduction of nitrate and nitrite ions in alkaline media", *Journal of Applied Electrochemistry*, **27**, 975, (1997).
104. S.M. Shariar, T. Hinoue, "Simultaneous Voltammetric Determination of Nitrate and Nitrite Ions Using a Copper Electrode Pretreated by Dissolution/Redeposition", *Analytical Sciences*, **26**, 1173, (2010).
105. C. Milhano, D. Pletcher In *Modern Aspects of Electrochemistry*, No. 45; White, R.E., Ed.; Springer New York: 2009; Vol. 45, p 1.
106. D. Pletcher, Z. Poorabedi, "The reduction of nitrate at a copper cathode in aqueous acid", *Electrochimica Acta*, **24**, 1253, (1979).

Chapter 5

Conclusions

5.1 Conclusion

The objective of the research work presented in this thesis was the electrochemical synthesis of silver nanoparticles. Once formed, the silver nanoparticles were characterised using scanning electron microscopy (SEM) coupled with energy dispersive X-Ray analysis (EDX) and UV-Vis spectroscopy. The potential applications of the silver nanoparticles in the electrochemical detection of nitrates and as a heterogeneous catalyst for the reduction of 4-nitrophenol were investigated. Finally, the antibacterial activity of the silver nanoparticles was measured.

In Chapter 3, the electrochemical synthesis of poly(N-vinylpyrrolidone) (PVP) protected silver nanoparticles is described. The colloidal silver nanoparticles were generated in solutions containing AgNO_3 , KNO_3 and PVP. The optimum conditions were found as $0.05 \text{ mol dm}^{-3} \text{ AgNO}_3$, $0.1 \text{ mol dm}^{-3} \text{ KNO}_3$, $423.75 \text{ g dm}^{-3} \text{ PVP}$ with an electrochemical pulse of -6.0 V vs Ag^+/Ag applied until a total charge of 180 C was reached. Using UV-Vis spectroscopy, the diameter of the PVP-protected silver nanoparticles was calculated as 5.73 nm . The application of lower potentials resulted in a significant decrease in the concentration of the silver nanoparticles. Similarly, an increase in the PVP concentration gave rise to a decrease in the rate of formation of the silver nanoparticles as the PVP-containing solution is viscous, particularly at concentrations higher than 423.75 g dm^{-3} . Agglomeration of the silver nanoparticles was observed on increasing the pulse period to 1200 s , indicating that the PVP was no longer able to protect the particles. The observed agglomeration is consistent with Ostwald ripening, where the smaller particles dissolve in solution to generate silver ions which are then deposited on larger particles in order to reach a more thermodynamically stable state. Alternatively, the formation of large clusters at longer deposition times can be explained using the theory of suspended electrodes. In this analysis, charged silver particles extend the area of the cathode and facilitate the electrodeposition of silver ions, and as a result the particles become larger. However, if the pulse period is maintained below 1200 s the nanoparticles show excellent stability. Indeed, the absorbance of

the nanoparticles was monitored over a 30 day period and excellent stability was observed, consistent with the stabilising properties of PVP.

The addition of AgNO₃ and KNO₃ gave rise to changes in the absorbance band, indicating that the Ag⁺ or NO₃⁻ ions alter the stability of the PVP-protected silver nanoparticles. This was attributed to the presence of additional cations in the diffuse double layer which neutralises the electrostatic forces that prevent aggregation. Furthermore, the nitrate anion may lead to the oxidation and degradation of the PVP chains, giving rise to the observed instability of the silver particles upon addition of nitrate anion.

The PVP-protected silver nanoparticles were immobilised in a polyacrylamide hydrogel and then employed for the reduction of 4-nitrophenol and the electrochemical detection of nitrates. This hydrogel matrix was selected as it is biocompatible, insoluble in aqueous solutions and highly porous, making it an ideal matrix for the nanoparticles. The porous nature of the polyacrylamide hydrogel allows good contact between the silver nanoparticles and the 4-nitrophenol molecules. Furthermore, the composite is easily recoverable once the reduction of the 4-nitrophenol is complete. Indeed, the reduction of 4-nitrophenol was observed at the immobilised silver nanoparticles. In the presence of NaBH₄, the 4-nitrophenol was completely reduced after a 60 min period. The rate constant for the reduction reaction was calculated as $7.4 \times 10^{-4} \text{ s}^{-1}$. However, higher rates were observed by increasing the number of hydrogel discs, giving a higher surface area for the reduction of 4-nitrophenol. The reusability of the composite was excellent, showing similar rate constants for repeated reactions. Furthermore, the activity of the composite was maintained on dehydrating and rehydrating. However, the PVP-protected silver nanoparticles immobilised in the polyacrylamide matrix showed poor detection of nitrates. Diffusion of nitrate was limited within the hydrogel matrix and indeed this was confirmed using the ferrocyanide/ferricyanide electrochemical probe.

The anti-bacterial activity of the polyacrylamide-PVP-protected silver nanoparticles was tested using *Staphylococcus aureus*, MRSA, *Escherichia coli* and two strains of *Pseudomonas aeruginosa*. In addition, the hydrogel was loaded with

a solution of AgNO_3 to give the presence of mobile Ag^+ ions. The greatest zones of inhibition were observed for the composites containing the Ag^+ ions, consistent with the view that the silver ion is biologically active and readily binds to cell surface receptors and proteins. The hydrogels containing silver nanoparticles offer a means of slow release of Ag^+ ions as the nanoparticles dissolve over time which is a significant advantage of these materials.

In Chapter 4, silver nanoparticles were successfully deposited at a GC electrode and this electrode was used in the electrochemical detection of nitrates. The GC substrate was selected as the nitrate reduction reaction is not observed at a bare GC electrode and any current generated for the reduction of nitrate can be attributed to the deposited particles and not to the underlying electrode material. The parameters that influence the electrodeposition process and consequently how the electrochemical detection of nitrate is affected were explored.

The silver nanoparticles were electrodeposited on a GC electrode using either a double pulse technique or a single pulse technique. In both approaches, an oxidation pulse of 1.0 V vs Ag/Ag^+ was applied to clean the electrode. For the double pulse technique, a pulse at E_1 was applied for a short period of time to instantaneously nucleate nanoparticle seeds. Then, a longer growth pulse at E_2 , at a lower reduction potential, was applied to grow the seeds into established particles without further nucleation at fresh sites. In the single pulse method, the electrode was immersed under open-circuit conditions in the silver-containing solution for 60 min. Then, the reduction potential was applied. Using scanning electron microscopy, the sizes of the particles were obtained. A high density of seed particles was produced during the nucleation pulse at E_1 , however, many of these particles did not mature into stable particles during the growth pulse. Instead, the particles redissolved and then deposited on more stable particles to give rise to larger particles with a lower density. Furthermore, a relatively high level of polydispersity was observed for the double pulse. A much higher density of silver particles was achieved using the single pulse technique. Potential pulses from -0.50 V to -1.0 V vs Ag/Ag^+ are sufficient for nucleation to occur during the entire pulse, giving progressive nucleation. Very few large particles were evident

on the surface and a narrow size distribution was achieved. Using the Scharifker and Hills model for two and three dimensional nucleation, the nucleation was consistent with the progressive nucleation and a 3D growth model.

The electrochemical detection of nitrates was studied at the silver particles using the single and double pulse methods. Similar cyclic voltammograms were recorded for the silver particles deposited using the single and double pulse methods. This indicates that the morphology of the silver deposited on the surface of the GC electrode has little influence on the catalytic activity of silver for the reduction of the nitrate ion. In both cases, a broad nitrate reduction peak was observed at approximately -0.90 V vs SCE, indicating the reduction of nitrate.

Cyclic voltammetry and constant potential amperometry experiments were used to generate calibration curves for the detection of nitrates at bulk silver and the silver-modified GC electrode. The surface areas of the deposited silver particles were calculated as 0.034 cm² following a 25 s deposition period, 0.069 cm² for a 50 s deposition period and increasing to 0.087 cm² and 0.104 cm² for deposition periods of 75 a and 100 s, respectively, using a single pulse of -0.50 V vs Ag/Ag⁺. These surface areas were used to normalise the currents for the nitrate reduction reaction and much higher normalised nitrate reduction currents were obtained for the silver-modified GC electrode compared to a bulk silver electrode. Indeed, using the peak currents from the cyclic voltammograms, the limit of detection at the bulk silver electrode was computed as 3.9×10^{-5} mol dm⁻³, compared to the limit of detection of 2.0×10^{-5} mol dm⁻³ for the silver nanoparticles. Furthermore, a much higher sensitivity was obtained for the silver-modified GC electrode, indicating that the deposited silver nanoparticles are more sensitive to nitrate detection. The sensitivity of the sensor was increased 10 fold using constant potential amperometry and the limit of detection was calculated as 9.8×10^{-6} mol dm⁻³ for the silver-modified GC electrode. This level of detection falls well below the maximum concentration of 8.0×10^{-4} mol dm⁻³ of nitrate as set out by the EPA under the Nitrate Directive (91.676/EEC).

The kinetics of the nitrate reduction reaction was studied at the silver-modified GC electrode. The term an' was computed as 0.422 using the shape factor, $|E_p - E_{p1/2}|$, and Tafel analysis. The rate constant for the reduction of nitrate was calculated as $9.79 \times 10^{-3} \text{ s}^{-1}$. The reaction order for the nitrate reduction reaction was obtained by fitting the electrochemical data to the rate law, to give a rate law with a reaction order of 0.736. This fractional reaction order is consistent with an adsorption step, where the adsorption of the nitrate anion is the rate-determining step. Rotating disc voltammetry was employed to study the hydrodynamics of the nitrate reduction reaction. Linear Levich plots were obtained at lower rotation rates. The diffusion coefficient was calculated as $1.66 \times 10^{-5} \text{ cm}^2 \text{ s}^{-1}$, and the rate constant was calculated from the intercept of the Koutecky-Levich plot as 0.11 cm s^{-1} .

The influence of pH, the effects of different electrolytes and the addition of nitrites and chlorides on the reduction of nitrate were studied at the silver-modified GC electrode. Higher peak currents were observed at lower pH values between 2.0 and 4.0, consistent with the adsorption of H^+ ions at the surface, which appears to facilitate the reduction of nitrates. As the pH is increased, hydroxide ions occupy the active sites giving rise to lower peak currents. Similarly, alkaline solutions or solutions with anions which adsorb on the surface show smaller nitrate reduction currents. Significant interference was observed on the addition of nitrites and chloride anions. The formation of AgCl on the surface of the silver nanoparticles occurred on addition of the chloride anions, giving rise to lower peak currents and a significant change in the position of the peak potential.

Overall, the main goals of this thesis were achieved. The silver nanoparticles were successfully synthesised, and these were used in the electrochemical detection of nitrates, by modifying a GC electrode with the silver particles, while the reduction of 4-nitrophenol was observed for the particles immobilised within the hydrogel matrix. Finally, the hydrogel immobilised particles and, in particular, the hydrogel immobilised Ag^+ ions, showed very good and promising antibacterial activity.